LEABHARLANN CHOLÁISTE NA TRÍONÓIDE, BAILE ÁTHA CLIATH | TRINITY COLLEGE LIBRARY DUBLIN
Ollscoil Átha Cliath | The University of Dublin

Terms and Conditions of Use of Digitised Theses from Trinity College Library Dublin

Copyright statement

All material supplied by Trinity College Library is protected by copyright (under the Copyright and Related Rights Act, 2000 as amended) and other relevant Intellectual Property Rights. By accessing and using a Digitised Thesis from Trinity College Library you acknowledge that all Intellectual Property Rights in any Works supplied are the sole and exclusive property of the copyright and/or other IPR holder. Specific copyright holders may not be explicitly identified. Use of materials from other sources within a thesis should not be construed as a claim over them.

A non-exclusive, non-transferable licence is hereby granted to those using or reproducing, in whole or in part, the material for valid purposes, providing the copyright owners are acknowledged using the normal conventions. Where specific permission to use material is required, this is identified and such permission must be sought from the copyright holder or agency cited.

Liability statement

By using a Digitised Thesis, I accept that Trinity College Dublin bears no legal responsibility for the accuracy, legality or comprehensiveness of materials contained within the thesis, and that Trinity College Dublin accepts no liability for indirect, consequential, or incidental, damages or losses arising from use of the thesis for whatever reason. Information located in a thesis may be subject to specific use constraints, details of which may not be explicitly described. It is the responsibility of potential and actual users to be aware of such constraints and to abide by them. By making use of material from a digitised thesis, you accept these copyright and disclaimer provisions. Where it is brought to the attention of Trinity College Library that there may be a breach of copyright or other restraint, it is the policy to withdraw or take down access to a thesis while the issue is being resolved.

Access Agreement

By using a Digitised Thesis from Trinity College Library you are bound by the following Terms & Conditions. Please read them carefully.

I have read and I understand the following statement: All material supplied via a Digitised Thesis from Trinity College Library is protected by copyright and other intellectual property rights, and duplication or sale of all or part of any of a thesis is not permitted, except that material may be duplicated by you for your research use or for educational purposes in electronic or print form providing the copyright owners are acknowledged using the normal conventions. You must obtain permission for any other use. Electronic or print copies may not be offered, whether for sale or otherwise to anyone. This copy has been supplied on the understanding that it is copyright material and that no quotation from the thesis may be published without proper acknowledgement.

TRINITY COLLEGE DUBLIN



Investigation of factors affecting dissolution under biorelevant low velocity hydrodynamic conditions, using in vitro and in-silico methods

Bo Liu, M. Pharm. Eng.

Being a thesis submitted for the degree of

Doctor of Philosophy in Pharmaceutics

Under the supervision and direction of

Deirdre M. D'Arcy,

B.Sc. (Pharm.), M. (Pharm.), Dip. (Clin. Pharm.), Dip. (Stat. Q.I.), Ph.D., M.P.S.I.

and

Professor Owen I. Corrigan,

B.Sc. (Pharm) (N.U.I.), M.A., Ph.D. (N.U.I.), F.T.C.D., F.P.S.I.

October 2011

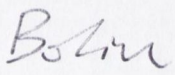
TRINITY COLLEGE
2 3 AUG 2012
LIBRARY DUBLIN

Thesis 9533

DECLARATION

This thesis is submitted by the undersigned to the University of Dublin, Trinity College, for examination for the degree of Doctor of Philosophy. It has not been submitted for a degree at any other university. I myself carried out all the practical work except where duly acknowledged. The library of University of Dublin, Trinity College, may lend or copy this thesis on request. This manuscript was written by me with the help of editorial advice from Dr. D.M. D'Arcy and Prof. O.I Corrigan

Bo Liu



Summary

The goals of the current study were to investigate the effect of hydrodynamics on the dissolution of non-disintegrating compacts in a low velocity environment. This work also studies the impact of hydrodynamics on the dissolution of immediate release tablets in a flow-through apparatus, where a model was developed to simulate particulate dissolution.

The dissolution of Benzoic Acid (BA) compacts was carried out in the flow-through apparatus at different inflow rates in order to determine the effect of low fluid velocity on the dissolution rate. The dissolution rates of BA were not significant different under different inflow rates in the flow-through cell with a diameter of 22.6 mm. Hydrodynamics at different inflow rates was studied in the flow-through apparatus using a 3-D Computational Fluid Dynamics (CFD) model in order to interpret the effect of flow velocity, shear stress and shear rate on dissolution rate. The simulated result indicated that the flow reversal resulting from boundary separation may weaken the effect of the bulk flow rate on the dissolution rate of BA.

In the low velocity environment, density gradients resulting from dissolution of compounds of different solubilities can also affect the hydrodynamics. Therefore, freely soluble lactose monohydrate (LM) and slightly soluble benzoic acid (BA) were used to study the effect of density gradients on the dissolution rate. A 2-D species transfer model was developed to simulate how the downward flow resulting from LM dissolution counteracted the upward forced flow. Hydrodynamics were significantly different in the flow-through apparatus for the freely soluble LM due to downward flow induced by density gradients. Additionally, a forced-natural convection combination (FNCC) model was used to predict the dissolution rate of BA and LM in the flow-through apparatus.

However, the FNCC method could not predict accurately the dissolution rate of the freely soluble LM in the low velocity environment. As the LM affected the local hydrodynamics in a low velocity environment, the effect of LM on the dissolution rate of BA from BA-LM composition was investigated. An investigation was carried out to predict the dissolution rate of BA and LM in the dissolution apparatus using the theory of dissolution of poly phase mixtures developed by Higuchi and co-workers (Higuchi, Mir et al. 1965) . In the low velocity environment of the flow-through apparatus and the free convection system, the freely soluble LM increased the dissolution rate of slightly soluble BA. This effect increased with

increasing LM content. The theory from Higuchi and coworkers needed to be modified to reflect this effect.

A low velocity environment of 16 ml min^{-1} in the 22.6 mm diameter cell in the flow-through apparatus, using an open system with water as the dissolution medium, was selected to establish an *IVIVC*, using the published drug plasma concentration data from carbamazepine formulations. The *IVIVC* used was comparable to the published *IVIVC* using a high agitation rate of 75 rpm, and a high concentration of surfactant in the paddle apparatus.

A particulate dissolution model was used to simulate the dissolution rate of comprehensive particles from the disintegrated tablets in the flow-through apparatus. Particle size, effective local volume and velocity parameters were relevant to the accuracy of the simulation. The simulated result was close to the observed result at 16 and 32 ml min^{-1}, but not at 8 ml min^{-1}.

In conclusion, factors affecting dissolution rates in a low velocity environment were studied in detail, and a biorelevant dissolution test environment was generated. It is vital to account for effects such as density gradients, flow reversal, and particle distribution in the cell when conducting dissolution tests in the low velocity environment of the flow-through apparatus.

Table of Contents

DECLARATION ii

Summary iii

Table of Contents v

Acknowledgements xi

Publications and Presentations associated with this thesis xii

Publications: xii

Oral presentations: xii

Posters: xii

Abbreviations and Symbols xiii

Origin & Scope xviii

Chapter 1 Introduction 1

1.1 Fundamentals of fluid mechanics 2

1.1.1 The principles governing fluids in motion 2

1.1.2 Laminar and turbulent flows 3

1.1.3 Boundary layers 4

1.1.3.1 The boundary layer on a planar surface 4

1.1.3.2 Boundary layer separation 5

1.1.4 Computational fluid dynamics (CFD) 6

1.1.4.1 Creating an initial mesh using Gambit™ 7

1.1.4.2 Fluent™, as the solver 8

1.2 Dissolution theory 10

1.2.1 Effective diffusion boundary layer theory 10

1.2.2 Convective diffusion theory 13

1.3 *In vitro* dissolution testing 14

1.3.1 Dissolution testing and USP 1 and 2 dissolution apparatuses 15

1.3.2 Flow-through dissolution apparatus (USP4) 16

1.3.3 Using CFD to study the hydrodynamics in the USP 1, USP 2 and USP 4 dissolution apparatuses 18

1.4 *In vivo* and *in vitro* correlation (IVIVC) 20

1.4.1 Correlation Levels 20
1.4.2 Deconvolution and convolution correlation technique 21
1.4.3 Using the Biopharmaceutics Classification System (BCS) to estimate *IVIVC* 25
1.4.4 Effect of Physiological features of the GI tract on *In Vivo* drug dissolution and absorption 26
1.4.5 Biorelevant *in vitro* dissolution 27
Chapter 2 Materials and Methods 30
2.1 Materials and Equipment 31
2.1.1 Materials 31
2.1.2 Equipment 31
2.1.2.1 Software 31
2.1.2.2 Computational Resources 31
2.1.2.3 Instruments 31
2.2 Methods 32
2.2.1 Computational fluid dynamics- geometrical model construction and flow simulation 32
2.2.1.1 2-D and 3-D models generated by Gambit™ 32
2.2.1.2 Determination of the input flow rate in the flow through apparatus 38
2.2.1.3 Solver and inlet flow conditions defined for the 2-D flow through apparatus, 2-D free convection system and 3-D flow-through apparatus 38
2.2.1.4 Species transfer and defining materials 39
2.2.1.5 Horizontal lines created in the 2-D and 3-D models for profiling hydrodynamic data 40
2.2.1.6 Determination of pressure gradients within the CFD simulated flow field 42
2.2.2 Dissolution rate studies 43
2.2.2.1 Dissolution rate studies of BA and LM 43
2.2.2.2 Dissolution rate studies of carbamazepine (CBZ) in the paddle and flow-through apparatuses. 46
2.2.2.3 The f_2 factor (similarity factor) 46
2.2.3 Solubility measurements 47
2.2.4 Diffusion coefficient determination 48
2.2.5 Analysis of BA, LM and CBZ 50
2.2.6 Particle size reduction and partide size measurement of BA, LM and CBZ. 51

2.2.6.1 Measurement of BA and LM 51
2.2.6.2 Measurement of CBZ 51
2.2.7 Measurement of solution density 52
2.2.8 Statistical methods 53
2.2.9 Code used to simulate the *in vitro* dissolution profile 53
2.2.10 The observed plasma concentration of Tegretol IR and CR 54
2.2.11 The model used in the Gastroplus™ to predict plasma concentration 54
2.2.12 Validating uniform mixing of non-interacting compounds 54
Chapter 3 Hydrodynamics in the flow-through apparatus. 55
3.1 Introduction 56
3.2 Dissolution studies of BA and LM in the flow-through apparatus 57
3.3 Simulated hydrodynamic features in the flow-through apparatus 59
3.3.1 Flow profile at the cell inlet at different flow rates 59
3.3.2 Velocity magnitude, wall shear stress and pressure distribution generated at different flow rates in the flow-through apparatus. 59
3.3.3 Pressure distribution in the flow-through cell 65
3.3.4 Wall shear stress and shear rate distribution on the compact surface at different flow rates. 68
3.3.4.1 Wall shear stress distribution 69
3.3.4.2 Analysis of shear rate distribution 71
3.3.4.3 Shear rate at the compact surface 74
3.3.5 Relationship between observed hydrodynamic phenomena and observed dissolution rate 75
3.4 Prediction of dissolution rate under different flow rates in the flow-through apparatus. 76
3.4.1 Physicochemical property 76
3.4.1.1 Solubility of BA and LM 76
3.4.1.2 Diffusion coefficient of BA and LM 76
3.4.2 Prediction of dissolution rate 78
3.5 Conclusion 84
Chapter 4: Hydrodynamics and species transfer in the flow-through apparatus and free convection system: investigating variation in hydrodynamics with solubility of model drug ... 85
4.1 Introduction 86

4.2 Physicochemical properties and dissolution studies 87
4.2.1 Measurement of particle size of BA and LM 87
4.2.2 Measurement of density 88
4.2.3 Dissolution profile and dissolution rate 88
4.3 Comparison of 3-D simulation model to 2-D simulation in the region of interest 90
4.4 Hydrodynamic analysis of simulated 2-D hydrodynamic models including LM and BA species transfer in the flow-through apparatus and free convection system 91
4.4.1 Steady state of the BA and LM species transfer model in the flow-through apparatus and free convection system 91
4.4.2 Hydrodynamics simulations including BA species transfer in the flow-through apparatus and free convection system from simulation including BA species transfer model 94
4.4.3 Hydrodynamics simulations including LM species transfer in the flow-through apparatus and free convection system from simulation including LM species transfer model. 100
4.4.4 The effective diffusion boundary layer for BA and LM in the flow-through apparatus and free convection system 105
4.4.5 Further consideration for practical dissolution 107
4.5 Prediction of dissolution rates of BA and LM in the flow-through apparatus based on the shear rate generated by Fluent™. 108
4.6 Conclusion 110
Chapter 5 Investigation of dissolution rate of two-component compact systems of freely soluble component and slightly soluble component under low velocity conditions 112
5.1 Introduction 113
5.2 Validating composition and non-interacting of mixture systems 113
5.3 Dissolution rate of BA and LM mixture systems in the different dissolution apparatuses 114
5.4 Investigation of factors affecting the dissolution rate of two-component systems. 118
5.4.1 Predicting dissolution rate from non-interacting two component systems 118
5.4.2 Modification of the theory from Higuchi and coworkers by an empirical method to account for differing h value 127
5.4.3 The steady state assumption in the theory from Higuchi and coworkers 131
5.4.4 Using the adapted Higuchi equation to predict dissolution rate in the free convection system 135

5.5 Conclusion..... 139
Chapter 6 *IVIVC* study of carbamazepine using the flow-through apparatus..... 140
6.1 Introduction 141
6.2 *In vitro* dissolution study of Tegretol IR and CR tablets 142
6.2.1 The *in vitro* dissolution test of Tegretol IR in the paddle apparatus. 142
6.2.2 Dissolution of Tegretol IR in the flow-through apparatus..... 146
6.3 Using *in vitro* dissolution data to generate *IVIVC*. 147
6.3.1 Deconvolution of observed plasma concentration profile of Tegretol IR based on Wagner-Nelson method 147
6.3.2 *IVIVC* result based on simulated result of Gastroplus™ and observed *in vivo* result. 151
6.4 Conclusion..... 153
Chapter 7 Simulation of particle dissolution in the flow-through apparatus 154
7.1 Introduction 155
7.2 Dissolution of Tegretol IR in the open and close loop configurations of the flow-through apparatus. 156
7.3 Hydrodynamics considerations for Tegretol in the flow-through apparatus 157
7.4 Prediction of dissolution rate of Tegretol IR..... 159
7.4.1 Particle size analysis..... 159
7.4.2 Consideration of effects from other parameters during the simulation. 162
7.4.2.1 Absolute and relative velocity..... 162
7.4.2.2 Effective volume in the CBZ dissolution 166
7.4.3 Simulated dissolution results..... 166
7.5 Conclusion..... 170
Chapter 8 General discussion..... 172
8.1 Comparing of particulate dissolution theories..... 173
8.2 Comparing hydrodynamics effects in USP 2 and USP 4 174
8.3 The dissolution of multi-component systems in a low velocity environment..... 176
8.4 Comparing hydrodynamics in the USP4 dissolution apparatus to simulation of gastric hydrodynamics..... 178
8.5 Dissolution of particles under physiological based hydrodynamic condition. 180
8.6 Conclusion and Future work. 182
8.6.1 Conclusion 182

8.6.2 Future work 183
References 184
Appendices 204
Appendix 1 Calibration curve 204
Appendix 2 Dissolution data from J. Parojcic group (Provided by J. Parojcic). 207
Appendix 3 Code used to calculate ΔS in paddle apparatus, flow-through apparatus and free convection system 208
A3.1. The Code used to calculate ΔS in paddle apparatus 208
A3.2. The Code used to calculate ΔS in flow-through apparatus 211
A3.3. The Code used to calculate ΔS in free convection system 214

Acknowledgements

I would like to express my sincere gratitude to my supervisors, Dr. Deirdre D'Arcy and Professor Owen Corrigan for their support and assistance over the last four years.

Thank you to Dr. Deirdre D'Arcy for her highly valuable advice, guidance, encouragement, patience, ingenious thought and for making both her time and expertise so readily available during this project.

Thank you to Professor Owen Corrigan for his direction, experience and assistance.

I would also like to thank the assistance from Dr. Tim Persoons for his work on applying *in silico* simulation of dissolution theories, Dr. Geoff Bradley for his support on applications of Fluent™ software and Professor Jelena Parojcic for her support on *in vitro* data of Tegretol and application of Gastroplus™.

Thanks to the sponsors for the financial support provided by the Irish Research Council for Science, Engineering and Technology (IRCSET), which supported my PhD degree at Trinity College, Dublin.

I also like to thank Dr. Lidia Tajber and Dr. Ahmed Barham Shawqi for carrying out the particle size measurement and SEM, respectively.

Thank you to Dr. Xue Li, Geoff Burne, Stephany Micallef, Vincent Curtin and Christine Grossjohann for the "painful" proof reading and for your friendship and encouragement.

I should not forget to thank Dr. Yongheng Liu, Dr. Rong Hu, Dr. Yong Chen, Dr. Hongxun Hao, Dr. Xiaowei Jiang, Hao Liu, Qian Dai, Nian Shen and Simon Dowling for the assistance in mathematics, engineering and programming, and also your friendship and encouragement.

Thanks also to all of students and staff in school of Pharmacy and Pharmaceutical sciences, Trinity College, Dublin for all of their help for last few years.

Finally, special thanks to my mother Minggui Li and my father Lixin Liu who have always been a constant source of inspiration to me.

Publications and Presentations associated with this thesis

Publications:

D.M. D'Arcy, B. Liu, O.I. Corrigan, 2011. Investigating the effect of solubility and density gradients on local hydrodynamics and drug dissolution in the USP 4 dissolution apparatus. International Journal of Pharmaceutics. (Accepted)

D.M. D'Arcy, B. Liu, R. G. Bradley, A.M. Healy, O.I. Corrigan, 2010. Hydrodynamic and species transfer simulations in the USP 4 dissolution apparatus: considerations for dissolution in a low velocity pulsing flow, Pharmaceutical Research, 27(2):246-258

Oral presentations:

B. Liu, D. M. D'Arcy and O. I. Corrigan, 2009, Use of high performance computing to predict dissolution relevant to in vivo drug absorption, All-Ireland Schools of Pharmacy Research Conference in Dublin

Posters:

B. Liu, D. D'Arcy, I. Kovacevic, J. Parojcic, O. Corrigan, 2010. Investigating the role of the flow-through dissolution apparatus (USP 4) in in vitro in vivo correlation (IVIVC) using a BCS class II model drug. AAPS Journal 12(S2)

B. Liu, D. M. D'Arcy and O. I. Corrigan, 2009, Can a soluble excipient increase drug dissolution under mild hydrodynamic conditions by enhancing natural convection? 2nd PharmSciFair (Pharmaceutical Sciences Fair & Exhibition) in Nice

D.M. D'Arcy, B. Liu, R. O'Dwyer, G. Bradley, O.I. Corrigan, 2008. Dissolution in the flow-through apparatus- use of computational fluid dynamics (CFD) to investigate hydrodynamic effects. AAPS Journal 10(S2)

B. Liu, D. M. D'Arcy and O. I. Corrigan, 2008, investigating dissolution rates in regions of low forced convection- the effect of natural convection caused by a freely soluble excipient. 30th All Ireland Schools of Pharmacy Research Seminar in Cork

Abbreviations and Symbols

1-D	1-Dimensional
2-D	2-Dimensional
3-D	3-Dimensional
A_t	amount of absorbed at time t
A_{cross}	the pipe cross-sectional area
A_n	the absorption number
A_A	the amount per unit volume of A
A_B	the amount per unit volume of B
$(A_2-A_1)_{sample}$	absorbance difference of the corresponding sample
$(A_2-A_1)_{blank}$	absorbance difference of the blank
A	the length of the plate
B	the width of the plate
C_S	the solubility of solute
C	the concentration of solute at time t
$C_\delta(t)$	the intravenous drug concentration at time t
C_t	plasma concentration at time t
C_A	the saturated solubility of A
C_B	the saturated solubility of B
C_{BA}	the solubility of BA
C_{LM}	the solubility of LM
D	the diffusion coefficient
D_A	the diffusion coefficient of A
D_B	the diffusion coefficient of B
D_n	the dissolution number
D_{BA}	the diffusion coefficient of BA
D_{LM}	the diffusion coefficient of LM
d_p	diameter of the particle
d_{light}	light path
dV_z	differential of the fluid velocity in the radial direction

dY	differential of distance between two mesh points
E_t	total energy
F(t)	drug release fraction at time t
F_{abs}	the fraction of absorption
F_{drag}	drag force
F_{buoy}	buoyancy
$F_{fluidacc}$	fluid acceleration force
F_{Basset}	the resistance due to flow field unsteadiness
f_2	similarity factor
G_i	body force
$grad\ c$	concentration gradient
G	acceleration due to Earth's gravity
$h_{c,WF}$	diffusion layer thickness using in Wang and Flanagan Equation
$h_{i\%BA}$	the thickness of effective diffusion boundary layer for BA at different BA-LM composition system
$h_{100\%LM}$	the thickness of effective diffusion boundary layer for LM at 100 % LM system
h	the diffusion layer thickness
h_{eff}	effective diffusion boundary thickness
h'	the adapted h according to observed value
$\vec{J_i}$	the diffusion flux of species i
K_s	the rate constants of gastric emptying
K_t	the rate constants of small intestinal transit
K_a	the rate constants of intrinsic absorption
K_e	elimination constant
k_i	the correction factor used to adapt the thickness of effective diffusion boundary
k_{mass}	mass transfer coefficient
L_T	the length of the tube
L_w	diameter of compact
L_{line}	a characteristic linear dimension
M_s	the amount of drug in the stomach
M_c	the amount of drug in the colon
M_n	the amount of drug in the n th compartment

MW	molecular weight of the substance to be assayed
m_p	the apparent particle mass
N_u	Nusselt number, the ratio of convective to conductive heat transfer across the boundary
N_A	the amount of A in the mixture
N_B	the amount of B in the mixture
N_{BA}	the original amounts of BA
N_{LM}	the original amounts of LM
P_{eff}	the permeability
Q	heat added
Q_F	the volumetric flow rate
Q_{cell}	the flow rate in the flow-through cell
R	dissolution rate
RC_i	the net rate of production of species
R_T	the radius of the tube
R_{BA}	the dissolution rate of BA
R_{LM}	the dissolution rate of LM
R_t	mean percent of reference
R_A	the dissolution rate of A
R_B	the dissolution rate of B
R_{forced}	dissolution rate in the forced convection
R_{whole}	dissolution rate over the whole pulse
R_{FNCC}	dissolution rate of forced-natural convection combination
r_p	the particle radius
R	the radius of round plate
Sh	Sherwood number
Sc	Schmidt number
SA	surface area
S_1	the coordinate value representing the boundary between phase A and solution
S_2	the coordinate value representing the boundary between bulk mixture and phase A
S_i	the rate of creation by addition from the dispersed phase

T_t	mean percent of test sample
T	time
U_f	fluid velocity
U_p	particle velocity
$\vec{V}$ or V	velocity
V_{app}	apparent distribution volume
Vol_p	the effective volume of each particle during zero flow pattern
V_c	the apparent volume of the central compartment
V_p	descent rate of particles
V_{Final}	Final volume of solution
V_{LM}	Sample volume of lactose
V_{abs}	absolute velocity
V_{rel}	relative velocity
W	work done
w_0	initial particle weight
W	particle weight at time t
X	the amount of undissolved drug
$(X_p)_t$	the amount of drug in the peripheral compartment as a function of time after oral administration
X	the ratio of BA in the mixture
Y_i	mass fraction
ρ	Density
$\delta\vec{F}$	net force
M	the dynamic viscosity of the fluid
ν	the kinematic viscosity
ω	angular velocity
A	shear rate
α_i	shear rate at each 0.01s (Fluent™)
ϵ	extinction coefficient of NADH at: 340 nm = 6.3 [l × mmol^{-1} × cm^{-1}]
τ_w	shear stress
$\Delta\rho$	the difference between the density of the saturated solution of the solute in the

	solvent and the density of the pure dissolution medium (bulk density)
ρ_s	solution density
ρ_f	density of fluid
ρ_{BA}	the density of BA
ρ_p	the density of particle
ε	Porosity
ε_{LM}	the porosity of LM
τ_{BA}	the tortuosity of BA
τ	Tortuosity
τ_{ij}	stress tensor

Origin & Scope

Before a drug can be absorbed in the gastro-intestinal (GI) tract, it should be completely dissolved in *in vivo*. Two important factors determine this *in vivo* dissolution process: the dissolution medium and hydrodynamics. FaSSIF and FeSSIF dissolution medium have been used to simulate *in vivo* fasted and fed situations and developments in the area of biorelevant dissolution media (Galia, Nicolaides et al. 1998; Nicolaides, Symillides et al. 2001). Hydrodynamics, in particular, computational fluid dynamics (CFD) has been used to simulate hydrodynamics, is the other important factor affecting the dissolution process, and has recently gained more attention in the literature relevant to dissolution testing (Kukura, Arratia et al. 2002; Kukura, Arratia et al. 2003; McCarthy, Kosiol et al. 2003; Kukura, Baxter et al. 2004; McCarthy, Bradley et al. 2004; Baxter, Kukura et al. 2005; D'Arcy, Corrigan et al. 2005; D'Arcy, Corrigan et al. 2006). Although these works suggest CFD could be used to study *in vivo* and *in vitro* hydrodynamics, none have suggested a biorelevant hydrodynamic environment for *in vivo* dissolution testing.

Due to the low velocity fluid motion determined in the GI tract (Katori, Aoyagi et al. 1995; Pal, Indireshkumar et al. 2004; Bradshaw, Irimia et al. 2006), a low velocity *in vitro* dissolution environment is desirable for achieving biorelevant dissolution conditions. The flow-through apparatus (USP 4 dissolution apparatus) produces a different flow type to that of paddle apparatus (USP 2 dissolution apparatus) and basket apparatus (USP 1 dissolution apparatus), and can be used to investigate dissolution under a low velocity environment (Qureshi, Caille et al. 1994; Nicolaides, Hempenstall et al. 2000). The flow-through apparatus has a low velocity pulsing flow, while the paddle and basket apparatus have rotary flow. Furthermore, the dissolution in the flow through apparatus can be used while applying sink or non-sink conditions, and combining higher and lower flow rates (Ikegami, Tagawa et al. 2003). Therefore, the flow-through apparatus may be a more suitable method to forecast *in vivo* release behaviour in humans than the paddle apparatus which has higher velocities at standard operating speeds (50-150 rpm).

Computational fluid dynamics (CFD) has been used to study hydrodynamics in the USP 1 and 2 dissolution apparatus (Kukura, Arratia et al. 2002; Kukura, Arratia et al. 2003; McCarthy, Kosiol et al. 2003; Kukura, Baxter et al. 2004; McCarthy, Bradley et al. 2004; Baxter, Kukura et al. 2005; D'Arcy, Corrigan et al. 2005; D'Arcy, Corrigan et al. 2006; Swichtenberg 2006). These

CFD simulations could easily be used to investigate different factors inducing variability and provide comprehensive data on velocity, shear stress and pressure distribution. CFD also can be used to simulate the hydrodynamics in the flow-through apparatus. The factors determining the dissolution rate of a drug in the flow-through apparatus can be observed in the simulated model in order to identify aspects affecting the drug dissolution rate in the GI tract.

Based on a study of hydrodynamics in the flow-through apparatus, it should be possible to select biorelevant dissolution conditions to develop a correlation between *in vitro* dissolution and *in vivo* absorption.

The general approach of the study is as follows. First, the dissolution of model compounds in a low velocity environment was studied using a slightly soluble compound benzoic acid (BA) and a highly soluble compound, lactose monohydrate (LM). Second, the insights gained from this experiment are applied to investigate hydrodynamics in the flow-through apparatus in order to determine the main factors affecting the dissolution rate in a low velocity environment and to attempt to predict the dissolution rate of immediate release tablets in the flow-through apparatus. These studies referred to the model drug are used to determine the dissolution conditions of the post-market drug Tegretol and to predict its dissolution rate in the flow-through apparatus. The new *IVIVC* will be created in order to find out how *in vitro* dissolution in the flow-through apparatus affects *in vivo* absorption based on the existed *pharmacokinetics* data combined with new dissolution test data in the flow-through apparatus.

Finally, through study of dissolution in a biorelevant hydrodynamic environment, and knowledge of hydrodynamic and physicochemical parameters involved, it should be possible to simulate a dissolution profile from a selected model drug within this biorelevant environment.

Studies performed in the current work include: simulation of hydrodynamic effect on the non-disintegrating compact of BA (slightly soluble) and (highly soluble) LM in low flow velocity conditions; examination of the dissolution of mixture compacts of BA and LM; prediction of the dissolution rate of mixture compacts under different hydrodynamic conditions based upon a polyphase mixtures equation; development of *in vitro* biorelevant dissolution methods

of Tegretol using USP 4 flow-through apparatus and prediction of dissolution rate of Tegretol in the flow-through apparatus.

Chapter 1 Introduction

1.1 Fundamentals of fluid mechanics

"A fluid is matter in a readily distortable form, so that the smallest unbalanced external force on it causes an infinite change of shape, if applied for a long enough time (Francis 1975)."
Fluid mechanics is the field of study where this fundamental principle is applied to liquid and gaseous systems. It includes area such as the study of different flow types, boundary conditions and solid dissolution under laminar flow.

1.1.1 The principles governing fluids in motion

The fundamental laws used to describe properties of fluid flow include: conservation of mass (continuity), Newton's second law of motion and conservation of energy (first law of thermodynamics).

Mass conservation:

The continuity equation is a mathematical statement of the principle of the conservation of mass (Equation 1.1) (Massey and Ward-smith 2006).

The rate at which mass enters the region = the rate at which mass leaves the region + the rate of accumulation of mass in the region

Equation 1. 1

If the flow is steady, parameters do not change with time and the rate at which mass is accumulated within the region is zero. The expression then reduces to:

The rate at which mass enters the region= The rate at which mass leaves the region

Equation 1. 2

General form of Newton's second law (conservation of momentum) (Post 2009):

$$m d\vec{V} = \vec{F} dt$$

Equation 1. 3

Where $\vec{V}$ is the velocity, t is the time, $\vec{F}$ is the net force.

First law of thermodynamics (Post 2009):

The conservation of energy (first law of thermodynamics equation) is illustrated in Equation 1.4.

$$dE_t = dQ + dW$$

Equation 1. 4

Where E_t is the total energy, Q is the heat added and W is work done on the system.

When Newton's second law (momentum conservation) is applied to fluid, the Navier-Stokes equation was yielded and the Navier-Stokes equation defines the principal conditions to be satisfied by a fluid as it flows (Currie 2003).

The Navier-Stokes law of motion can be written as follows considering an infinitesimal fluid particle (Sonin 2001),

$$\rho \frac{dV_i}{dt} = \frac{\partial \tau_{ij}}{\partial x_j} + \rho G_i$$

Equation 1. 5

Where i is the direction, V_i is the velocity in the i direction, τ_{ij} is the stress tensor, G_i is the body force and x_j is direction x.

1.1.2 Laminar and turbulent flows

There are two basic flow types: laminar flows and turbulent flows. The difference between them was investigated by Osborne Reynolds (1842-1912) (Reynolds, Brightmore et al. 1900; O'Connor and Robertson 2011). Laminar flow , which occurs at lower velocities, may be considered as moving in layers or laminate (Batchelor 1956; Gary 1993; Massey and Ward-smith 2006). In turbulent flow, the paths of individual particles of fluid are in a disorderly manner instead of straight line (Reynolds, Brightmore et al. 1900; Dodge and Metzner 1959; O'Connor and Robertson 2011).

The Reynolds number (Re) (Equation 1.6) is a dimensionless number that is used to determine the different flow types (Stokes 1851; Reynolds 1883; Rott 1990).

$$Re = \frac{\rho V L_{line}}{\mu} = \frac{V L_{line}}{\nu} = \frac{Q_F L_{line}}{\nu A_{cross}}$$

Equation 1. 6

where L_{line}: is a characteristic linear dimension, (traveled length of fluid); ν: is the kinematic viscosity ($\nu = \mu / \rho$, μ is the viscosity);

In pipes:

Where Q_F: is the volumetric flow rate and A_{cross}: is the pipe surface area.

When a fluid flows in a pipe, experimental observations have determined that laminar flow occurs when Re<2300 and turbulent flow occurs when Re>4000. In the interval between 2300 and 4000, both laminar and turbulent flows are possible (Merzkirch 2005).

1.1.3 Boundary layers

The friction of a fluid on a surface causes a reduction of speed in the adjacent layer and this layer is called a hydrodynamic boundary layer (Francis 1975) . The theory of hydrodynamic boundary layer is based on the recognition that the effect of the friction on a solid surface is confined within a thin layer of fluid adjacent to the surface. Beyond this layer, the fri ction has no effect (Prandtl 1904; Francis 1975; Sayers 1992; Anderson 2005; Massey and Ward-smith 2006). Different aspects of velocity, shear stress and gradient determine the thickness of the boundary layer. At the same time, within the boundary layer, both laminar and turbulent flow can occur (Schlichting and Gersten 2000).

1.1.3.1 The boundary layer on a planar surface

Due to the retarding force from the planar surface, the boundary layer starts at the leading edge. The effect of the retarding force passes from one layer of liquid to another layer. Hence, more and more of the fluid is slowed down, while the fluid passes the plane. It is conventionally considered that the thickness of the layer may be taken as the distance from the surface to that at which the velocity reaches 99% of the velocity of the main stream (Francis 1975; Sayers 1992; Massey and Ward-smith 2006). However, with an increase of thickness of layer, the laminar flow becomes unstable as the Reynolds number of the boundary zone increases with the distance from the leading edge. The motion of fluid becomes disturbed and turbulent flow develops when the Reynolds number reaches the

critical value of approximately 1500(Levich 1962). There is a transition region in which the laminar flow changes to turbulent flow. As reported, the boundary layer is thinner when the Reynolds number is higher (Schlichting and Gersten 2000). Viscous sublayer is the region of a mainly-turbulent flow that is near a boundary and in which the flow is laminar (Francis 1975). The zone outside the viscous sublayer region is called the buffer zone, a zone where most turbulent fluctuations are generated (Holland and Bragg 1995).

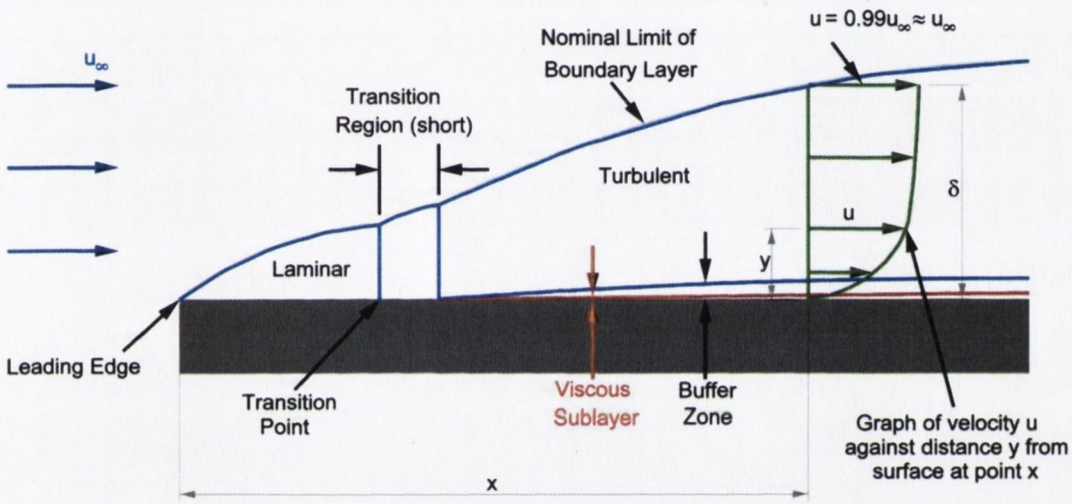


Figure 1. 1 Boundary layer on flat plate (Cortana Corporation 2011)

1.1.3.2 Boundary layer separation

Boundary layer separation is a phenomenon that occurs when an adverse pressure gradient develops. The pressure acts to the local flow and decelerates the flow velocity along the body. Thus the boundary layer thickness rapidly increases (Graebel 2007). An adverse pressure gradient occurs when the static pressure increases in the direction of the flow. The flow reversal then occurs. The point at which the flow reversal starts is called the separation point (Gad-el-Hak 2000).

Separation of a boundary was first reported by Prandtl (Prandtl L. 1904). As shown in Figure 1.2, the pressure is increased from S_1 to S_3. The adverse pressure gradient is positive (from S_2 to S_3, $\frac{dP}{dx} > 0$). Such a pressure gradient counteracts to some extent the "slow down" effect of the boundary on the fluid (Francis 1975; Sayers 1992; Massey and Ward-smith 2006). Beyond S_1, the pressure increases, and hence the net pressure in the boundary layer decreases the

velocity of the forward flow. Furthermore, at position S_3, the flow close to the surface has been reversed. The fluid cannot follow the contour of the surface, because of the reduction of velocity in the boundary layer caused by an adverse pressure gradient. Separation occurs within both laminar and turbulent boundary layers. However, the flow is more prone to separate in laminar layers than in turbulent layers. This is because the increase of velocity with distance from the surface is less in laminar flow than in the turbulent flow.

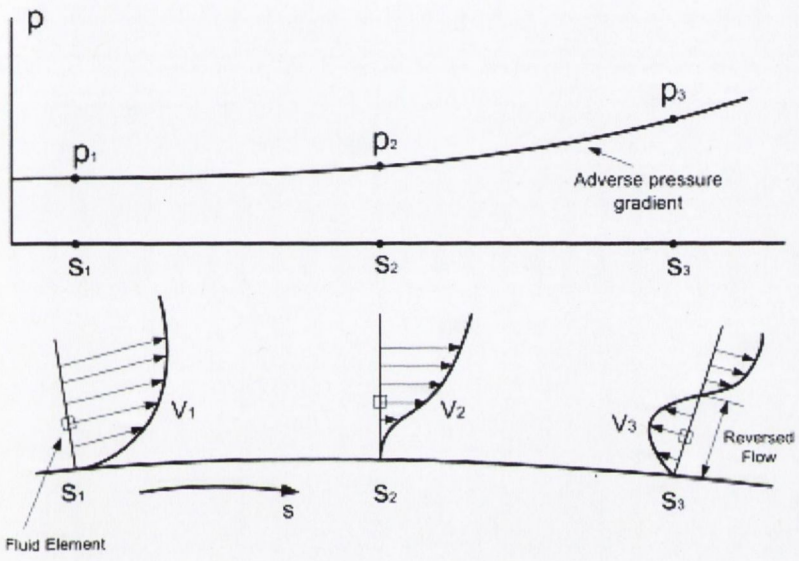


Figure 1. 2 Separation of streamline on the plate surface (Claes and Hoffman 2011)

Most flow types need to be solved by Navier-Stokes equations using a numerical method. As the pressure gradient varies semi-sinusoidally with time in a pulsed flow, the trend of the velocity becomes flatter rather than parabolic (White 1991).

1.1.4 Computational fluid dynamics (CFD)

CFD, is a branch of fluid mechanics that uses numerical methods and algorithms to solve problems that involve fluid flow. The basis of almost all CFD problems is the Navier–Stokes equations, which define any single-phase fluid flow. CFD can be used to numerically solve the Navier-Stokes equations in 1-D, 2-D and 3-D flow fields.

Fluent™ is a popular commercial CFD software package which was used in the current work to solve the equations relevant to hydrodynamics within the flow field. Additionally, the pre-processing package Gambit™ was used to create the meshed fluid domain. The sequence of

using Gambit™ and Fluent™ to solve a fluid problem is as follows (Fluent Inc 2004; Fluent Inc 2006).

(1) Gambit™ is used to generate the initial mesh outside of the solver. The objective flow field can be divided into thousands of small mesh cells by Gambit™ and then the boundary condition can be defined in Gambit™.

(2) Fluent™ is used to simulate fluid flow in complex geometries by solving the flow problems based on structured and unstructured meshes generated by Gambit™.

1.1.4.1 Creating an initial mesh using Gambit™

GAMBIT™ is a meshing software package which provides the basic steps of building, meshing, and assigning zone types to a simple and intuitive model (Fluent Inc 2004). The vertices, edges, faces and volumes are used to produce 2-D or 3-D grids (Fluent Inc 2004). Compared to 3-D grids, 2-D grids consume much less memory and take much less time to run. The types of 2-D grids can be mapped or be paved with triangles or quadrilaterals. 3-D grids are used to generate a full 3-D simulation of the flow which obviously consumes more memory and takes longer to solve. Furthermore, the grids can be divided into structured and unstructured grids. The structured grid is topologically rectangular which means that the mesh volume is a quadrilateral in 2-D or a hexahedron in 3-D, and the mesh volume is linked only to its immediate neighbours. The structured grids can reduce storage and CPU requirements. Unstructured grids are composed of two types: Tgrid and Cooper mesh (Fluent Inc 2004). The Tgrid unstructured grids use a 3-D paving algorithm with tetrahedral and pyramidal shaped grids, which are very easy to use to generate a grid for a complex geometry (Fluent Inc 2004). The Cooper mesh projects a set of face meshes, being mapped or paved, from one side of the domain to another. The Cooper mesh leads to very small mesh volumes at flow constrictions (Fluent Inc 2004).

A high quality mesh is supposed to have smooth variations in grid spacing, minimal grid skewness (cell interior angles equal); and be graded towards boundaries and other areas where rapid variations in parameters occur (Fluent Inc 2004). Boundaries conditions also can be defined in Gambit™, after creating the meshes. There are different boundary types including wall, outflow and mass flow inlet in the Gambit™. Additionally, a further flexible change of boundaries conditions is allowed in Fluent™.

1.1.4.2 Fluent™, as the solver

Fluent™ is a state-of-the-art computer program for modeling fluid flow and heat transfer in complex geometries (Fluent Inc 2006) . The steps using Fluent™ to solve a fluid dynamics problem are as follows:

(1). Start the appropriate solver for 2-D or 3-D modeling.

(2). Import and check the grid (mesh file).

(3). Select the solver formulation and choose the basic and additional equations: laminar or turbulent (or inviscid) flow, chemical species or reactions, heat transfer models, etc. Identify any additional models required: fans, heat exchangers, porous media, etc.

When the laminar or turbulent models are selected, the corresponding laminar or turbulent equations are applied in the simulation. These parameters of laminar and turbulent models are defined in the viscous model panel of Fluent™ software.

When the model is selected, it can be implicit or explicit. In the implicit formulation, an unknown value in each cell uses existing and unknown values from neighboring cells in implicit formulation, whereas an unknown value in each cell computed from rel ations that include only existing values are used in the explicit formulation (Fluent Inc 2006). Additionally, the implicit formulation must solve the equations simultaneously. Furthermore, the 1st-Order implicit formulation is sufficient for most of the problems. The 2nd-Order Implicit formulation can be used instead of the 1st-Order implicit formulation in order to improve accuracy. With the 1st-order scheme, any cell average variable is obtained from the corresponding calculated value at the center of a cell. The 2^{nd}-order implicit is more complicated which has a higher order accuracy for the value of any variable at the cell face.

Fluent™ can model the mixing and transport of chemical species by solving conservation equations describing convection, diffusion, and reaction sources for each component species (Fluent Inc 2006). General species transfer can be solved using the following equation (Equation 1.7) (Fluent Inc 2006). In species transfer without reactions, the net rate of production of species (RC_i) is 0, S_i is the defined sources by the user.

$$\frac{\partial}{\partial t}(\rho Y_i) + \nabla \cdot (\rho \vec{V} Y_i) = -\nabla \cdot \vec{J_i} + RC_i + S_i$$

Equation 1. 7

Where Y_i is the mass fraction, RC_i is the net rate of production of species i by chemical reaction, S_i is the rate of creation by addition from the dispersed phase plus any user-defined sources and $\vec{J_i}$ is the diffusion flux of species i.

(4). Specify physicochemical properties and then adjust the solution control parameters. After the selection of the solver, it is required that the material properties and boundaries are specificed. For a normal hydrodynamic model, the material physicochemcial properties are defined in the materials panel including: density, heat capalcity, thermal conductivity and viscosity. For species transport, the mixture material template is selected. As two or more than two components are simulated in the species transport models, the density of each template must be defined.

After building the meshes in Gambit™, further refining can be done in Fluent™. As important fluid interactions often occur in the boundary zones, the cells in these regions are required to be refined. Boundary adaption is allowed to mark or refine cells in the proximity of the selected boundary zones, whereas this procedure cannot increase the resolution of a curved surface (Fluent Inc 2006). Therefore, if more cells are required on a curved surface where the shape of the surface is important, it is necessary to create the mesh with sufficient surface nodes before reading it into the solver(Fluent Inc 2006). For example, boundary zone can be adapted to put more refined mesh.

(5). Initialize the flow field and calculate a solution.

(6). Examine and save the results.

1.2 Dissolution theory

1.2.1 Effective diffusion boundary layer theory

Planar surface:

The widely used theory for predicting dissolution rate was proposed by Noyes and Whitney in 1897 and subsequently developed by Nernst and Brunner. An unstirred diffusion layer concept was added into the original theory as illustrated in Equation 1.8 (Qiu, Chen et al. 2009). This model assumes that a rapid equilibrium is produced at the solid-liquid interface and subsequently diffusion occurs across a thin layer of solution into a bulk flow, which is termed a diffusion layer. This process of diffusion across the diffusion layer controls the dissolution rate in most cases. According to Equation 1.8, the dissolution rate is inversely proportional to the thickness of the diffusion boundary layer.

$$\frac{dX}{dt} = \frac{SAD}{h}(C_s - C)$$

Equation 1. 8

Where C is the concentration of solute at time t; C_s is the solubility of solute; D is the diffusion coefficient; h is the thickness of the diffusion layer; SA is the surface area and X is the amount of undissolved drug.

Higuchi applied the diffusion boundary layer theory in biopharmaceutics to predict drug release rates from a planar surface (Higuchi 1967). Based on the diffusion boundary layer theory, Higuchi also developed mixture models to predict the dissolution rate of separated components in a mixture (Higuchi 1967).

Particulate systems:

Considering the dramatic change of surface area of particles as the dissolution proceeds, a "cube-root law" was proposed by Hixson and Crowell (Hixson and Crowell 1931; Wang and Flanagan 1999; Wang and Flanagan 2002) to predict the dissolution rate of particles, which assumes a constant thickness of the diffusion boundary layer over the whole dissolution process as illustrated in Equation 1.9.

$$(\frac{4\pi\rho}{3})^{1/3}\frac{DC_S}{\rho h}t = w_0^{1/3} - w^{1/3} \text{ (cube-root law)}$$

Equation 1. 9

Where w is the particle weight at time t, w_0 is the initial particle weight, ρ is the density of the particle.

Actually, the thickness of the effective diffusion boundary layer could not be constant over the entire course of the dissolution process especially when poly –disperse powders are used and an initial phase of poor disaggregation of granules or poor wetting of formulation is encountered (Macheras and Iliadis 2006). Furthermore, the relationship between the effective thickness of the diffusion boundary layer and the surface area is reported in many studies (Higuchi 1963; Higuchi, Rowe et al. 1963).

As the concentration gradient on a curved surface is non-linear relationship (Wang and Flanagan 1999), the "cube-root law" was further developed by Wang and Flanagan based on effective diffusion boundary layer thickness (h_{eff}), and therefore the dissolution rate, depends on the diffusion boundary layer thickness ($h_{c,WF}$) and particle radius (Wang and Flanagan 1999; Wang and Flanagan 2002). In the theory of Wang and Flanagan, it was assumed that the thickness of the diffusion layer ($h_{c,WF}$) is independent of the particle size (Equation 1.10).

$$\frac{1}{h_{eff}} = \frac{1}{r_p} + \frac{1}{h_{c,WF}}$$

Equation 1. 10

Where h_{eff} is the effective diffusion boundary layer thickness, r_p is the particle radius and $h_{c,WF}$ is the diffusion layer thickness.

The predicted result of h_{eff} using Wang and Flanagan's model is sensitive to the change of thickness of diffusion layer ($h_{c,WF}$) based on an empirical value of diffusion layer estimated to be 110 μm (Wang and Flanagan 1999; Wang and Flanagan 2002). When the value of $h_{c,WF}$ was decrease from 110 to 30 μm, the predicted result based on Wang and Flanagan equation would be more similar to the calculated result using a fluid dynamic model (Sugano 2008). Under constant convective flow, the diffusion layer thickness could be considered as an

independent constant. However, the strength of flow could change in most cases. Consequently the thickness of the diffusion layer would not remain constant under a changing flow, as the changing of the thickness of hydrodynamic boundary layer could squeeze or expand the thickness of the diffusion layer. Thus, Wang and Flanagan's model may not accurately predict the dissolution rate in an unsteady hydrodynamic diffusion boundary layer situation. Also, as particle size changes, relative velocity of particle will change.

Thus, it is required to add a parameter, representing the fluid dynamic characteristics (Re), into the equation in order to obtain an accurate estimate of thickness of effective diffusion boundary layer. The Sherwood number (Sh) represents the fluid dynamic characteristics of mass transfer by diffusion and convective flow as illustrated in Equation 1.11. The Sherwood number is proportional to the mass transfer coefficient and inversely proportional to the thickness of the diffusion boundary layer (Equation 1.12). A new model based on the fluid dynamic theory was developed (Levins and Glastonbury 1972; Levins and Glastonbury 1972).

$Sh = 2 + 0.6Re^{1/2}Sc^{1/3}$ (Ranz-Marshall Correlation)

Equation 1. 11

$$k_{mass} = \frac{DSh}{2r_p} = \frac{D}{h_{eff}}$$

Equation 1. 12

Where k_{mass} is the mass transfer coefficient, Sh is the Sherwood number, Sc is the Schmidt number.

In a low agitation system, as Re is negligible, the Sh (Equation 1.11) is 2 for small particles (diameter ≤ 30μm) and the degree of agitation does not affect the dissolution rate for these small particles (Sugano, Okazaki et al. 2007). The thickness of the effective diffusion boundary layer becomes less than the radius when the particle size increases (Sugano, Okazaki et al. 2007). However, the thickness of the effective diffusion boundary layer remains almost constant when the particle diameter is greater than 100 μm, as the increase in Sh is counteracted by the increase of particle size in the denominator of the Equation 1.12 (Sugano 2008).

1.2.2 Convective diffusion theory

The convective diffusion theory demonstrates that the transfer of the solid to solution is controlled by a combination of liquid flow and diffusion (Levich 1962). The convective diffusion theory is based on first principles. However, the fluid dynamic model is based on an empirical method. The convective diffusion theory is illustrated in Equation 1.13.

$$\frac{\partial c}{\partial t} = Dgrad\ c - Vgrad\ c$$

Equation 1. 13

Where $grad\ c$ is the concentration gradient and V is velocity.

The first part on the right side of Equation 1.13 is the diffusion contribution, whereas the second part represents convection.

Subsequently, Levich developed the integrated version of Equation 1.14, focusing on different situations (Levich 1962).

With respect to rotation speed, Equation 1.13 was developed by Levich to solve the diffusion of the rotary disk.

$$R = 0.62D^{2/3}\nu^{1/6}\omega^{1/2}c_s$$

Equation 1. 14

Where ω is the angular velocity, R is the dissolution rate (mass per time) and v is kinematic viscosity.

As the angular velocity may affect the velocity on the compact surface, the angular velocity appears in the equation. The concentration gradient and velocity distributed on the compact surface will affect the dissolution rate according to Equation 1.14.

Equation 1.15 was proposed by Levich to solve the dissolution rate of free-falling solid particles. The particle size could be affected by the flow conditions surrounding it. Thus the particle size and dissolution rate can be evaluated using Equation 1.15.

$$R = 7.98D^{2/3}V_p^{1/3}d^{4/3}c_s$$

Equation 1. 15

Where V_p is descent rate of particles, d is the diameter of the particle.

The dissolution rate from a plate in a situation of flow over the surface of the plate is solved by Levich as illustrated in Equation 1.16 (Levich 1962).

$$R = 0.68Dc_s b(\frac{\nu}{D})^{1/3}\sqrt{\frac{Va}{\nu}}$$

Equation 1. 16

Where a is the length of the plate, b is the width of the plate and V is velocity.

The convective diffusion theory then was developed by Bird et al. who give a more accurate description of flow changes on a plate surface (Bird, Stewart et al. 2007). Based on the contribution of Levich and Bird et al., Nelson and Shah presented a convective-diffusion equation integrated for both a rectangular and round dissolving surface as illustrated in Equation 1.17 and 1.18 (Nelson and Shah 1975; Shah and Nelson 1975; Shah and Parrott 1976; Nelson and Shah 1977).

$$R = 0.808D^{2/3}c_s\alpha^{1/3}bL^{2/3}$$

Equation 1. 17 (Rectangular plate)

$$R = 2.157D^{2/3}c_s\alpha^{1/3}r^{5/3}$$

Equation 1. 18 (Round plate)

Where α is the shear rate, r is the radius of round plate.

1.3 *In vitro* dissolution testing

Because dissolution is often the rate determining step of absorption for many low solubility compounds, *in vitro* dissolution testing can be used to investigate the in vivo absorption

characteristics. Furthermore, *in vitro* dissolution testing, as a quality control tool in pharmaceutical manufacturing, is widely used to evaluate the consistency of drug release between batches. Therefore, the *in vitro* dissolution test is very important in different phases of drug development.

1.3.1 Dissolution testing and USP 1 and 2 dissolution apparatuses.

The USP 1 (basket) and 2 (paddle) dissolution apparatuses were introduced by the USP-NF Joint Panel on Physiological Availability as official testing apparatuses in order to address the insufficiency of the disintegration test. The disintegration test was adopted in 1945 by the British Pharmacopoeia and in 1950 by the USP (Grady 1980; The United States Pharmacopeial Convention 2007).

The USP 1 and 2 dissolution apparatuses are widely used in new formulation development (Gray, Kelly et al. 2009), Quality Control (QC) (FDA CDER 1997; FDA CDER 1997; FDA CDER 2003; Dokoumetzidis and Macheras 2006) and *In Vitro* and *In Vivo* bioequivalence (FDA CDER 1997; FDA CDER 2000; Federal Register 2000). It is a requirement to carry out a dissolution test on most solid formulations.

In the case of formulation development, USP 1 and 2 dissolution apparatuses are used to investigate different factors affecting the dissolution rate including formulation factors such as surface area (Sunada, Shinohara et al. 1989) and excipients (Adebayo and Itiola 2003; Nerurkar, Jun et al. 2005; Alvarez 2006; Gohel, Parikh et al. 2007), processing factors such as compression force (Levy, Antkowiak et al. 1963; Khan and Rooke 1976), hardness (Chowhan and Palagyi 1978), packaging type (Urdinola, Gray et al. 1981) and storage conditions (Urdinola, Gray et al. 1981). In addition, the dissolution test has been used as an indicator of stability of a solid formulation (FDA CDER 2003).

In the case of QC testing in pharmaceutical industry, dissolution testing determines the product batch release (FDA CDER 1997; Dokoumetzidis and Macheras 2006), the stability of the product (Khan, Karnachi et al. 2000; Fitzpatrick, McCabe et al. 2002; Phadnis and Suryanarayanan 2002; FDA CDER 2003; Marchais, Cayzeele et al. 2003), the manufacturing changes (FDA CDER 1995; FDA CDER 1997; FDA CDER 2000; Federal Register 2000) and the similarity of release of drug release (Moore and Flanner 1996; O'Hara, Dunne et al. 1998; Shah, Tsong et al. 1998).

Different internal and external factors determine the variability present in USP Apparatus 1 and 2 (Healy, McCarthy et al. 2002; Kukura, Baxter et al. 2004; Achanta, Gray et al. 2005; Burmicz 2005; Crist and Spisak 2005; Foster and Brown 2005; Mirza, Joshi et al. 2005; Scott 2005; Buhse 2006). Firstly, the height of the shaft in the vessel and rotation speed would bring about a variance in the results of a dissolution test. Secondly, the calibration of the apparatus and the different hydrodynamics when a tablet is placed at different locations would bring about variability. Finally, factors involved in apparatus manufacture, such as shaft wobble, could result in variability in dissolution results. Those factors could result in inconsistent dissolution test results in the USP dissolution apparatuses.

1.3.2 Flow-through dissolution apparatus (USP4)

The flow-through apparatus is one of the dissolution apparatuses documented in the different official pharmacopoeias. The use of flow-through cells for dissolution testing of the tablets and capsules was developed in the laboratories of the United States Food and Drug Administration (FDA) over 40 years ago (Vliet 1957; Langenbucher, Benz et al. 1989). The flow-through apparatus was published, as an official dissolution apparatus, in the USP, the European Pharmacopoeia and the Japanese Pharmacopoeia nearly 30 years ago (Langenbucher, Benz et al. 1989). Compared to the paddle apparatus, the flow-through apparatus can expose the different dosage forms to a more consistent laminar flow and less variation in the cell, avoiding the effect of turbulent flow related to the rotation mechanism. The flow-through cell is composed by an upper cylindrical part and a lower conical part. Although the pump operation mechanism and a change in input flow rate range would affect the flow pattern inside the flow-through cell (Lerk and Zuurman 1970; Tingstad, Dudzinski et al. 1973; Tingstad, Gropper et al. 1973; Langenbucher, Benz et al. 1989), the 1mm glass beads filled in the lower conical part of the flow-through cell which "break" the upward flow, can increase the range of useful flow rates (Tingstad, Dudzinski et al. 1973).

There are two different sized cells for dissolution testing in the flow-through apparatus, of 22.6 and 12 mm in diameter. The volume for the upper cylindrical part is 12 ml in the 22.6 mm cell. If the flow rate is under 16 ml min^{-1}, only 1 minute is required for the liquid to completely change in the 22.6 mm flow-through cell. In order to avoid backward flow, a red glass bead is inserted in the flow inlet hole of the lower conical part. A piston pump is used to push the liquid into the flow-through cell. When the pump is in a suction phase, the fluid is

drawn from the reservoir and when the pump is in a discharge phase, no fluid is drawn from the reservoir. Therefore, a "semi-sinusoidal" flow is produced.

In each minute, the piston pump can produce 120 pulses. When the system is in the "semi-sinusoidal" inflow, the mechanical flow will push the red bead upwards and fresh dissolution medium enters the flow-through cell. When the system is in the "zero" inflow phase, the red bead can fall down and block the inlet flow hole. Thus, the fluid in the flow-through cell does not move backwards into the pipe. During the dissolution test in the flow-through apparatus, the dissolution medium fills the cell and the dosage form is completely exposed to the dissolution medium.

An advantage of the flow-through apparatus is that the dissolution media and flow rate can be changed during the dissolution test. Furthermore, floating dosage forms can be fixed in the centre of the cell of the flow-through apparatus, which enables full contact between the dosage form and the dissolution medium. Compared to the basket and paddle apparatuses, USP apparatus 1 and 2, the flow-through apparatus can maintain theoretical sink conditions easily, especially for poorly soluble drugs, as an unlimited amount of dissolution media may be used. The effects of variation in local concentration, over the course of the pulse, on dissolution rate are likely to be more complex than a simpler picture of constant sink conditions.

The flow-through apparatus can be run in two configurations: an open loop system and a closed loop system as shown in Figure 1.3. In the closed system, the dissolution medium is pumped from the medium reservoir to the bottom of flow-through cell. After the dissolution medium fully fills the cell of the flow-through apparatus, the dissolution medium with solute exits the cell and returns to the medium reservoir again. A magnetic stirrer is used to thoroughly mix the solution of solute and the remaining dissolution medium to produce a new solution. The new solution will return to the cell to finish the circulation route of the closed system. For the each cell, there is a separate reservoir to collect the dissolution medium.

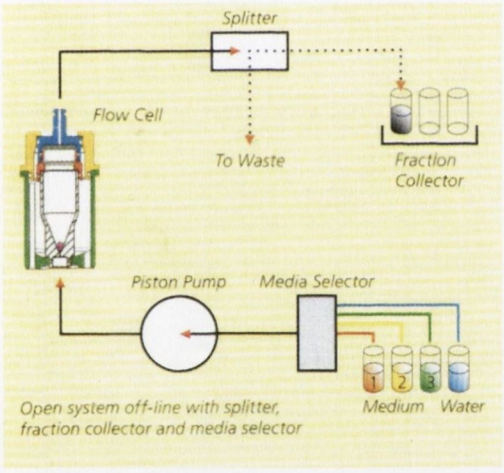
In the case of the open loop system, fresh dissolution medium can pass through the flow-through cell and be collected in a collection flask, while fresh dissolution media is pumped from the reservoir to the flow-through cell.



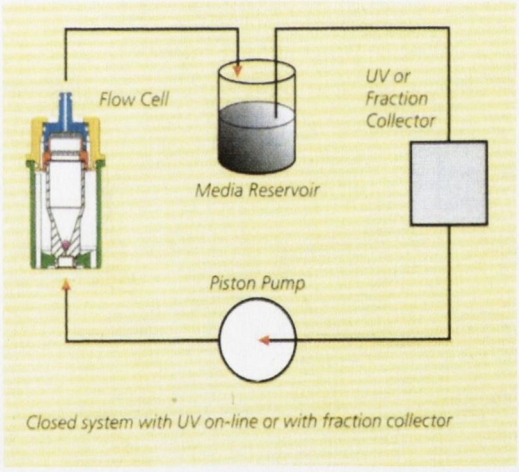
A



B



C.



D.

Figure 1. 3 The image of the flow-through apparatus and two operation configurations. A. Sotax CE6 flow-through apparatus; B. the 22.6 mm diameter cell of flow-through apparatus C. Open system in the flow-through apparatus D. Closed system of the flow-through apparatus (Sotax Inc 2006).

1.3.3 Using CFD to study the hydrodynamics in the USP 1, USP 2 and USP 4 dissolution apparatuses

CFD can be used to predict the effect of hydrodynamic environment on dissolution rate within the pharmacopoeial dissolution apparatuses.

The location of a dissolving dosage form in the vessel of the USP dissolution test apparatus 2 has been investigated in several studies using CFD tools (McCarthy, Kosiol et al. 2003; Kukura, Baxter et al. 2004; D'Arcy, Corrigan et al. 2005). The observed dissolution rate of a benzoic acid compact at the centre base position of the vessel was significantly lower than when the compact was placed on the curved side of the vessel (D'Arcy, Corrigan et al. 2005). The simulated maximum flow velocity at a rotation speed of 50 rpm was approximately 0.03 m s^{-1} (D'Arcy 2007) which is lower than that of 0.067 m s^{-1} at the curved side of the vessel (D'Arcy, Corrigan et al. 2005). The lower flow velocity on the compact surface results in a greater thickness of the hydrodynamic boundary layer on the compact surface when located at the centre of the vessel base. Thus, the dissolution rates were lower at the central position than from the compact placed on the curved side, despite a constant rotation speed. Furthermore, a lower strain rate has been determined at the centre of the vessel base than along the curved side (Baxter, Kukura et al. 2005). The strain rates relating to the strength of convective flow affects the mass transfer rate from solid to liquid. A lower strain rate at the centre of the vessel base means that a lower dissolution rate will be observed if the compact is placed in this location (Kukura, Baxter et al. 2004).

The simulation of hydrodynamics in the USP 1 dissolution test apparatus (basket apparatus) was investigated by D'Arcy et al (D'Arcy, Corrigan et al. 2006). For the velocity distribution around the basket, the flow velocity on the basket surface is approximately 0.0422 m s^{-1} at 50 rpm. The radial and axial flow velocities inside basket were estimated to be about 0.001 to 0.004 m s^{-1} and 0.0075 to 0.0275 m s^{-1}, respectively, at 100 rpm. This suggested that a low velocity region is present inside basket compared to that of the centre position of the vessel base in the paddle apparatus. The simulated fluid velocity is lower in the basket apparatus than that of the centre position of the vessel base in the paddle apparatus at 50 rpm (D'Arcy, Corrigan et al. 2005; D'Arcy, Corrigan et al. 2006).

A comprehensive fluid dynamics analysis using CFD of hydrodynamics in the USP 4 would assist in determining the effects of hydrodynamics on the dissolution rate, as has been carried out previously for USP 1 and 2 apparatuses. In terms of hydrodynamics within a flow-through system, studies investigating the effect of flow rates in different flow-through systems on dissolution rates have been widely reported (Zhang, Vadino et al. 1994; Cammarn and Sakr 2000; Bhattachar, Wesley et al. 2002; Sunesen, Pedersen et al. 2005; Stevens and Missel

2006). Considering the low average velocities present in the large 22.6 mm diameter cell, the very low Reynold's number present under flow rates of 4 to 50 ml min^{-1} (Cammarn and Sakr 2000), has previously resulted in little difference in dissolution rates observed across this flow velocity range, for a non-disintegrating system of salicylic acid dissolving in a media of pH 7.4 phosphate buffer (Cammarn and Sakr 2000). Moreover, studies have been previously presented using numerical models which included the effect of density gradients in a very low-velocity flow-through environment, where the effect of gravity on natural convection increased with increasing solubility of the solute (Stevens and Missel 2006).

1.4 *In vivo* and *in vitro* correlation (IVIVC)

The term *IVIVC* refers to the establishment of a rational relationship between a biological property, or a parameter derived from a biological property produced by a dosage form (e.g. plasma concentration or amount of drug absorbed), and a physicochemical property or characteristic of the same dosage form (usually the extent or rate of drug release) (The United States Pharmacopeial Convention 2007).

1.4.1 Correlation Levels

The *IVIVC* is divided into four categories of Level: A, B, C and Multiple level C by the FDA. The correlation levels are based on the ability to correlate the plasma drug concentration to the administration of the given dosage form.

Level A

A Level A correlation is usually estimated by deconvolution followed by comparison of the fraction of drug absorbed to the fraction of drug dissolved (FDA CDER 1997). A Level A correlation is linear with a point-to-point relationship between *in vitro* dissolution and *in vivo* input rate.

Level B

A Level B correlation relies on the principles of statistical moment analysis, where the mean *in vitro* dissolution time is compared either to the mean residence time or to the mean *in vivo* dissolution time.

Level C

A Level C *IVIVC* establishes a single point relationship between a dissolution parameter which does not reflect the complete shape of the plasma concentration time curve, which is the critical factor that defines the performance of extended release products.

Multiple level C

A Multiple level C represents the relationship between the amount of the product dissolved at several time points and one or several pharmacokinetic parameters of interest (The United States Pharmacopeial Convention 2008).

Level A represents a point to point relationship between *in vitro* release and *in vivo* absorption from the dosage from, which should be developed with at least two formulations demonstrating different *in vivo* profiles. Level B and Level C are normally used for several purposes including selecting excipients, optimising manufacturing processes, quality control and investigating release patterns.

1.4.2 Deconvolution and convolution correlation technique

Convolution and deconvolution are the main methods used to establish an *IVIVC*. Convolution is developed based on the superposition principle. A linear relationship (convolution) between drug release and drug concentration *in vivo* can be expressed using the following equation (Emami 2006):

$$C_t = C_\delta(t)F(t) = \int_0^t C_\delta(u)F(t-u)du$$

Equation 1. 19

Where $C_\delta(t)$ is the intravenous drug concentration at time t, C_t is the drug concentration following oral administration of a solid dosage form at time t and F(t) is the drug release

fraction at time t. The in vivo drug concentration can be estimated from an *in vitro* release profile using the convolution method.

Deconvolution techniques are required to estimate the *in vivo* absorption or dissolution time course for the development of a level A correlation. The main deconvolution method is numerical deconvolution. Wagner-Nelson method and the Loo-Riegelman method are used used for one-compartment model and two-compartment model, respectively.

The deconvolution method of Wagner-Nelson is illustrated in Equation 1.20. The advantage of Wagner-Nelson method is (1) the absorption and elimination processes can be quite similar and accurate determinations of absorption rate (Ka) can be made (Wagner and Nelson 1963). (2) The absorption process doesn't have to be first order (Wagner and Nelson 1963). This method can be used to investigate the absorption process.

$$A_t = V_{app}(C_t + K_e \int_0^t C_d dt)$$

Equation 1. 20

Where A_t is the amount of drug absorbed at time t, V_{app} is the apparent distribution volume, K_e is the elimination constant and C_d is drug concentration.

When time is extended to infinity, A_∞ is identical to the bioavailable dose and can be describe in Equation 1.21.

$$A_\infty = V_{app}K_e \int_0^\infty C_d dt$$

Equation 1. 21

The fraction of amount absorbed is equal to the amount absorbed at time t divided by dose as illustrated in Equation 1.22

$$Fabs_t = \frac{A_t}{A_\infty} = \frac{V_{app}(C_t + K_e \int_0^t C_d dt)}{Dose}$$

Equation 1. 22

The difference in fraction of amount absorbed with time is calculated using Equation 1.23

$$\Delta F_{abs} = F_{abst+1} - F_{abst} = \frac{V_{app}\left(C_{t+1} + K_e \int_0^{t+1} C_d dt\right) - V_{app}\left(C_t + K_e \int_0^t C_d dt\right)}{Dose}$$

$$= \frac{V_{app}\left[(C_{t+1} - C_t) + K_e \frac{1}{2}(C_{t+1} + C_t)(t_{t+1} - t_t)\right]}{V_{app} K_e \int_0^\infty C_d dt}$$

$$= \frac{(C_{t+1} - C_t) + K_e \frac{1}{2}(C_{t+1} + C_t)(t_{t+1} - t_t)}{K_e \int_0^\infty C_d dt}$$

Equation 1. 23

Where F_{abs} is the fraction absorbed.

The deconvolution method of Loo-Riegelman for two-compartment systems is more complicated than the Wager-Nelson method, as there is a requirement for intravenous data to estimate the amount of drug present in the peripheral compartment (Emami 2006). The Loo-Riegelman method requires drug concentration time data after both oral and intravenous administration of the drug to the same subject and the fraction absorbed at any time t is given by Emami (Equation 1.24 (Emami 2006)):

$$Fabs_t = \frac{C_t + k_e \int_0^t C_d dt + (X_p)_t / V_c}{k_e \int_0^\infty C_d dt}$$

Equation 1. 24

Where $(X_p)_t$ is the amount of drug in the peripheral compartment as a function of time after oral administration and V_c is the apparent volume of the central compartment.

Gastroplus is a programme to model the time course of drug absorption, which can be used to study convolution and deconvolution. Gastroplus is based on the Advanced Compartmental Absorption and Transit (ACAT) model. This model was suggested by Yu et al (Yu and Amidon

1999). The original Compartmental Absorption and Transit (CAT) model assumed that the GI tract was divided into 3 segments i.e. stomach, small intestine and colon. The small intestine was described by 7 compartments according to the change of transit flow as illustrated in Figure 1.4. The equations used to predict plasma concentration in different compartments are given by Equations 1.25 to 1.27.

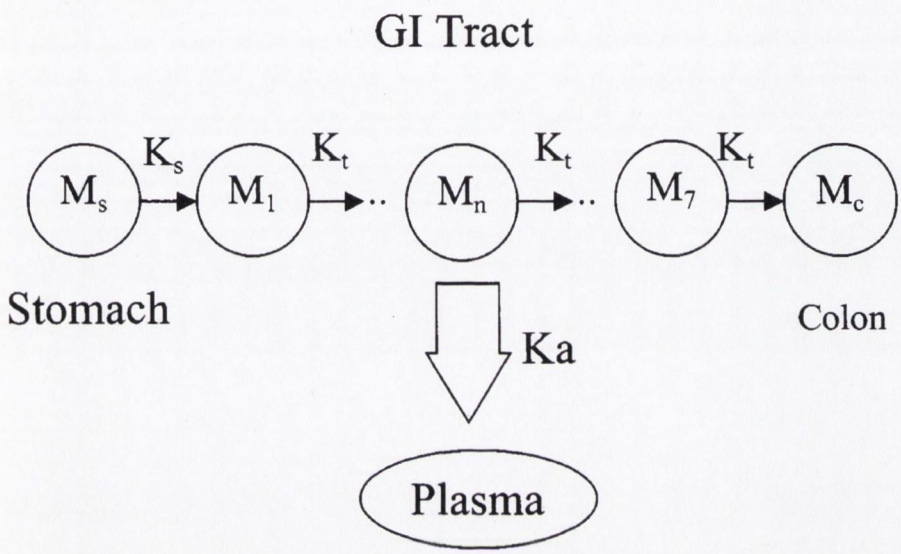


Figure 1. 4 A schematic diagram of the CAT model with linear transit and passive absorption kinetics. This model accounts for the transit in the stomach, duodenum, jejunum, and ileum, and the absorption in the duodenum, jejunum, and ileum (Yu and Amidon 1999)

$\frac{dM_s}{dt} = -K_s M_s$ (Stomach(Yu and Amidon 1999))

Equation 1. 25

$\frac{dM_n}{dt} = K_t M_{n-1} - K_t M_n$ n=1, 2, 3, ..., 7. (Small intestine(Yu and Amidon 1999))

Equation 1. 26

$\frac{dM_c}{dt} = K_t M_N$ (Colon(Yu and Amidon 1999))

Equation 1. 27

M_s: the amount of drug in the stomach;

M_c: the amount of drug in the colon;

M_n: the amount of drug in the n th compartment;

K_s, K_t, and K_a are the rate constants of gastric emptying, small intestinal transit, and intrinsic absorption, respectively.

1.4.3 Using the Biopharmaceutics Classification System (BCS) to estimate *IVIVC*

The BCS was first proposed by Amidon et al (Amidon, Lennnernas et al. 1995). According to the solubility and permeability of the drugs, the BCS is divided into four classes, as illustrated in Table 1.1.

According to the dissolution and permeability of each BCS drug class, the expectation for *IVIVC* for immediate and extended release formulations is shown in Table 1.1 (Sirisuth and Eddington ; Galia, Nicolaides et al. 1998; Emami 2006). As most drugs of Class I and II are dissolution rate controlled, *IVIVC* is expected for these drugs.

Table 1. 1 Expected IVIVC for different BCS class drugs.

Class	Solubility	Permeability	*IVIVC*
I	High	High	Correlation (if dissolution is rate-controlling step)
II	Low	High	*IVIVC* expected
III	High	Low	Little or no *IVIVC*
IV	Low	Low	Little or no *IVIVC*

Additionally, the BCS can be used as the basis of biowavier applications. The Food and Drug Administration (FDA) have stated that solubility, intestinal permeability and dissolution rate area governing factors of the rate and extent of oral drug absorption from IR solid oral-dosage forms, when considering a biowaiver (FDA CDER 2000). The BCS guidelines recommend that a drug fulfills the following conditions when applying for a biowavier: 1. the drug must be stable in the GI tract; 2. excipients used in the IR dosage form have no obvious effect on the rate and extent of oral drug absorption; 3. the product will not be absorbed in the oral cavity.

The extension of biowaiver to BCS classes II-IV based on the BCS framework have been investigated in many studies (Yu, Amidon et al. 2002; Manzo, Olivera et al. 2006; Kovacevic,

Parojcic et al. 2008; Tsume and Amidon 2010). Due to the low solubility and high permeability of a class 2 drugs, the oral absorption of a class 2 drug is controlled by the *in vivo* dissolution rate of the drug. If the *in vivo* dissolution rate can be estimated *in vitro*, an *in vivo in vitro* correlation could be established. Although many *in vitro* dissolution methods are used to mimic *in vivo* dissolution, those *in vitro* methods are difficult to validate due to the numerous *in vivo* process involved (Oberle and Amidon 1987). Furthermore, the solubility in the absorbing region determines the intestinal absorption rate. Thus, *in vitro* dissolution testing of dosage forms containing low solubility drugs may require the addition of surfactant such as sodium lauryl sulfate (SLS) to the dissolution relative to mimic the dissolution process *in vivo* and for maintenance of sink conditions.

1.4.4 Effect of Physiological features of the GI tract on *In Vivo* drug dissolution and absorption

The dissolution rate of low solubility drugs in the GI tract is affected by two main factors, dissolution medium and hydrodynamics. Bio-relevant dissolution media have been widely investigated in many studies (Horter and Dressman 2001; Nicolaides, Symillides et al. 2001; Wei and Lobenberg 2006). The hydrodynamics in the GI tract is affected by gastric emptying, gastrointestinal transit and many other factors. As transit time in the esophagus is about 5-15s, it will not notably affect the absorption of solid dosage forms (Dressman and Lennernas 2000).

Generally, the gastric emptying time affects fast dissolving drugs and the intestinal transit time impacts the absorption of the dissolution-rate-limited drugs assuming a first order process. The half-life of gastric emptying for fasted stomach is approximately 15.8 min with 300 ml water (Steingoetter, Fox et al. 2006). For the fed stomach, the situation is more complicated due to effect of liquid concentration and solid particle size. The time for complete emptying of the fed stomach has been estimated to be around 40 mins (Marciani, Cox et al. 2010). The intestine is usually the main absorption region for most drugs. The transit time of coated pellets through the entire small intestine is approximately 192 minutes (Steingoetter, Fox et al. 2006). Estimates of *in vivo* fluid velocity values vary widely, from 2.0×10^{-4}-8.0×10^{-4} ms^{-1} from intestinal fluid transit times (Diebold 2005), to a maximum of 7.5×10^{-3} ms^{-1} simulated in CFD simulations of a 2-D stomach (Pal, Indireshkumar et al. 2004). Although velocity spikes of up to ~0.25-0.5 ms^{-1} of a non-disintegrating tablet (particularly

during the gastric emptying and colon arrival periods) has been observed, this was against a background profile of much lower tablet velocities. This illustrated both inter-patient variability and intra-patient variability over the time, as measured by magnetic marker monitoring.

1.4.5 Biorelevant *in vitro* dissolution

Hydrodynamics and dissolution media are two important factors to determine the birorelevance of an *in vitro* dissolution test for some low solubility drugs such as BCS II drug. In this case, surfactant can be added in the dissolution medium in order to ensure biorelevant *in vitro* dissolution conditions and consequently establish a desirable *IVIVC* (Meyer, Straughn et al. 1992; Jung, Milan et al. 1997; Lake, Olling et al. 1999; Marchais, Cayzeele et al. 2003; Lee, Park et al. 2005; El-Massik, Abdallah et al. 2006). However, compendial dissolution media often fail for *IVIVC* of poorly soluble compounds as these dissolution media does not consider the physiological environment of the GI tract (Dressman, Amidon et al. 1998; Horter and Dressman 2001). FASSIF and FESSIF dissolution media were developed to simulate *in vivo* fasted and fed conditions (Nicolaides, Symillides et al. 2001; Scholz, Abrahamsson et al. 2002).

The hydrodynamics of the *in vitro* dissolution apparatus is another factor for consideration when developing an *IVIVC* (Scholz, Abrahamsson et al. 2002; Diebold 2005; Dressman and Kramer 2005). However, the current biorelevant hydrodynamic tests can be limited by the hydrodynamics of USP 1 and 2 dissolution apparatuses. Although the application dissolution testing of USP 1 and 2 dissolution apparatuses in *IVIVC* could reduce development time and costs for new productions, the USP 1 and 2 dissolution apparatuses in *in vitro* dissolution testing may not be the best way to establish the *IVIVC* (Hussain 2004; Qureshi 2004; Woodcock 2004; Zhang and Yu 2004; Buhse 2005; Muzzio and Armenante 2005 ; Swichtenberg 2006). The method set up in the USP 1 and 2 dissolution apparatuses may not relate well to *in vivo* performance. This is mainly because the vortex and higher velocity range produced in the dissolution test of USP 1 and 2 dissolution apparatuses may not represent all *in vivo* flow types. The dissolution results obtained from the USP 1 and 2 dissolution apparatuses are often not relevant to the results *in vivo*, since the geometry and operational conditions of these dissolution systems are different to *in vivo* conditions considering the physiological conditions in the gastrointestinal lumen. Furthermore, there are notable differences in these *in vivo* velocity estimates. CFD simulations of hydrodynamics in the

paddle apparatus predict the maximum velocities relative to a compact at the centre of the base of the paddle apparatus (50 rpm) to range from 0 to 0.03 ms^{-1} (D'Arcy, Corrigan et al. 2005). These velocities are higher than most estimates of average *in vivo* fluid velocity values. Therefore, the selection of a low flow rate in the flow-through apparatus is considered appropriate when trying to generate a bio-relevant environment. A flow rate of 8 ml min^{-1} in the 22.6 mm diameter cell combined with a biorelevant dissolution medium, has been found to correlate with the *in vivo* result for a poorly soluble drug of danazol (Sunesen, Pedersen et al. 2005). Therefore, it is possible to get *IVIVC* with low velocity considerations such as in the flow-through apparatus.

The hydrodynamics in the USP 4 dissolution apparatus are notably different to the USP 1 and USP 2 apparatuses, as the pulsing flow is the main flow type instead of the rotatory flow in the USP 4 dissolution apparatus and an open loop system can be applied ensuring sink conditions. Additionally, CFD has been effectively applied in the hydrodynamic study in the USP 1 and USP 2 apparatuses, indicating that CFD can also be used to study hydrodynamics in the USP 4 apparatus. Moreover, the low velocity study in the USP 4 dissolution apparatus is more meaningful. This may suggest more meaningful flow field to that in the *in vivo* environment. The effect of density gradient and local concentration on the dissolution rate is inevitable in the low velocity environment (Stevens and Missel 2006). The species transfer provided by Fluent™ can investigate the effect of the above factors on the hydrodynamics in the USP 4 dissolution apparatus. It is necessary to predict dissolution rate in the USP 4 apparatus based on the above flow field analysis in the USP 4 apparatus, as the dissolution rate is the controlling rate for the absorption of the most low solubility drug such as BCS II drug. The theoretical predict dissolution rate of the BCS II drug in the USP 4 apparatus under low velocity environment may be relevant to the observed *in vivo* dissolution rate.

Overall Aim:

1. To simulate (using CFD) the fluid hydrodynamics in the USP 4 dissolution apparatus under different inflow rates in order to examine the effect of different flow rates on the flow velocity in the low velocity environment of the 22.6 mm cell.

2. To investigate the effect, under the low velocity conditions in the USP 4 flow-through apparatus, of the dissolution of slightly and freely soluble compounds and the resulting

density gradients on the local hydrodynamics, and consequently on the dissolution rates of compacts made from single components and mixtures of different solubility.

3. To develop an *IVIVC* for BCS II drug, under the low velocity conditions in the USP 4 dissolution apparatus.

4. To simulate particulate dissolution of a class 2 model drug, in the low velocity conditions in the USP 4, and from this to predict *in vivo* absorption profiles.

Chapter 2 Materials and Methods

2.1 Materials and Equipment

2.1.1 Materials

Materials	Manufacturer/Supperlier
Benzoic Acid	VWR International Ltd (Poole, England)
Lactose Monohydrate	Sigma-Aldrich (The Netherlands)
Hydrochloric acid 37% w/v	Riedel-de Haen (Seezle, Germany)
Potassium Chloride	Merck KGaA (Darmstadt, Germany)
Lactose/D-galactose kit	Boehringer Mannheim/ R-Biopharm (Darmstadt, Germany)
Carbamazepine (Tegretol 200mg)	Novartis (Surrey, England)
Carbamazepine (Tegretol Retard 400mg)	Novartis (Surrey, England)
Carbamazepine	Sigma-Aldrich (MO, USA)
Membrane filters, 0.45 µm	Pall (Life Sciences)(Mexico)

2.1.2 Equipment

2.1.2.1 Software

Fluent™ version 6.3.26	ANSYS, Inc. (NH, USA)
Gambit™ version 2.4.6	ANSYS, Inc. (NH, USA)
Minitab version 14	Minitab Inc. (PA, USA)
Microsoft Excel (office 2003)	Microsoft (WA, USA)
Matlab version 7.4	The MathWorks, Inc. (MA, USA)
WinNonlin version 5.2	Pharsight®, a Certara™ company (MO, USA)
Gastroplus version 5.3.0	Simulations Plus, Inc. (CA, USA)

2.1.2.2 Computational Resources

Dell Precision T5400 workstation	Dell (Limerick, Ireland)
Linux operating platform	Scientific linux (Tønsberg,Norway)

2.1.2.3 Instruments

Hydraulic press	Perkin-Elmer (CA, USA)

CE7 smart flow-through apparatus	Sotax (Basel, Switzerland)
DT 6 Dissolution Test Apparatus	Erweka (West Germany)
Glass jars (free convection studies)	Lennox (TN, USA)
Hitachi S-3500N scanning electron microscope	Hitachi (Tokyo ,Japan)
UV spectrophotometry 1700	Shimadzu (Suzhou China)
Malvern Mastersizer 2000 with Scirocco attachment	Malvern Instruments Ltd (Worcestershire, UK)
Malvern Mastersizer 2000 with Hydro attachment	Malvern Instruments Ltd (Worcestershire, UK)
Magnetic stirrer hotplate	Stuart Scientific (Staffordshire, UK)
Pycnometer bottle (Density bottle)	MBL (MA, USA)
Sartorius Balance BP121S	Sartorius (Gottingen, Germany)
Waterbath	B.Braun (Melsungen AG, West Germany)

2.2 Methods

2.2.1 Computational fluid dynamics- geometrical model construction and flow simulation

The diameter and thickness of the compact used in the dissolution test was 13 and 3 mm, respectively. The curved side and one planar surface were coated with paraffin wax so that only one planar surface was exposed to the dissolution medium. In the flow-through apparatus, the area of interest for the current work is the upper cylindrical part of the flow cell with a 30 mm height and 22.6 mm diameter. In the free convection system (glass jar), the main chamber section is 54 mm in diameter and 50.7 mm in height, and the upper lip section (where the lid screws onto the jar externally) is 46.8 mm in diameter and 12.2 mm in height.

2.2.1.1 2-D and 3-D models generated by Gambit™

(1). Construction of the 2-D flow-through apparatus with the compact in the centre of the cell

Gambit™ software was used to build a 2-D model of the cell of the USP 4 dissolution apparatus. The flow-through cell of the USP 4 comprises two parts i.e. a lower circular cone

and an upper cylinder. When the dissolution rate was tested in the USP 4, the lower circular cone was filled with small glass beads. The axial velocity of the flow was decreased since the flow needed to penetrate though the glass beads (diameter: 1mm) layer and the flow path width of the lower cone increased from the bottom to the top of the cone. The 2-D model of the upper cylindrical part was as shown in Figure 2.1. The compact in the 2-D model was a projection of its curved side in order to analyse the drug release from the exposed planar surface of the compact.

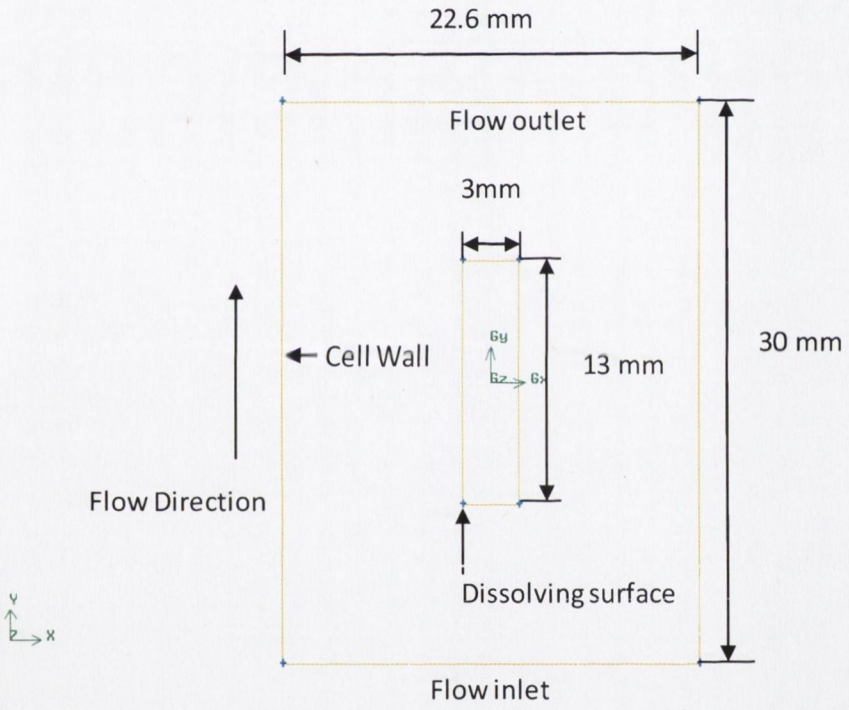


Figure 2. 1 Geometry of the 2D flow-through apparatus containing the compact constructed in the Gambit™ pre-processor.

The mesh was created within the flow-through model following the creation of the geometry of the flow-through apparatus. The quadrilateral meshing tool provided by Gambit™ was used to create a structured rectangular mesh. In order to ensure a regular structured rectangular mesh, the "Map" mesh type was enabled in the mesh module. A fine mesh was created by reducing the interval spacing of the vertices distributed in each line. A fine mesh will facilitate the generation of an accurately simulated model. The surface subtract tool was used to create a new "cell cylinder" without the rectangular compact. The mesh is shown in

the Figure 2.2. A more dense mesh of approximately 6×10^{-6}m width per mesh cell was generated on the compact surface.

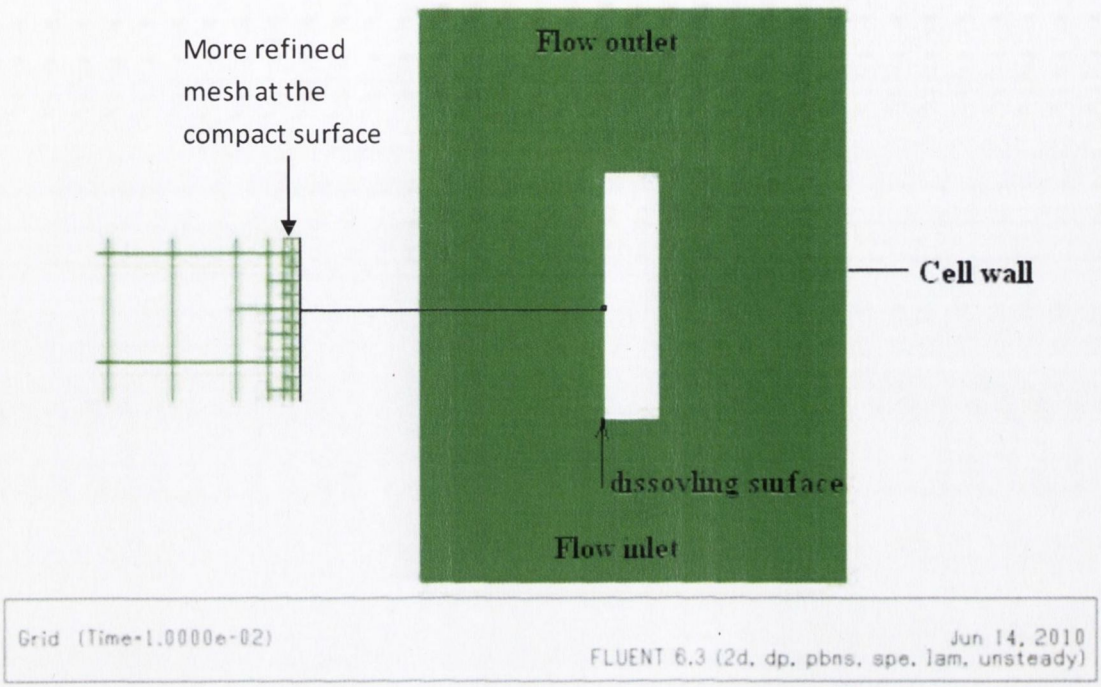


Figure 2. 2 Geometry of the 2-D flow-through apparatus containing the compact with regular structured rectangular mesh generated by Gambit™.

(2). Construction of the 2-D free convection apparatus with the compact suspended from the upper surface.

Gambit™ software was used to create the 2-D model of the free convection system, as illustrated in Figure 2.3. The free convection system was applied in a cylindrical glass jar. The 2-D free convection system created in Gambit™ was composed of three rectangles. The lower rectangle has the same height and width as the main section of the jar, the upper rectangle has the height and width of the upper lip section of the jar. The small rectangle in the center is the projection of the curved side of the compact with the same width (diameter) and height as the compact.

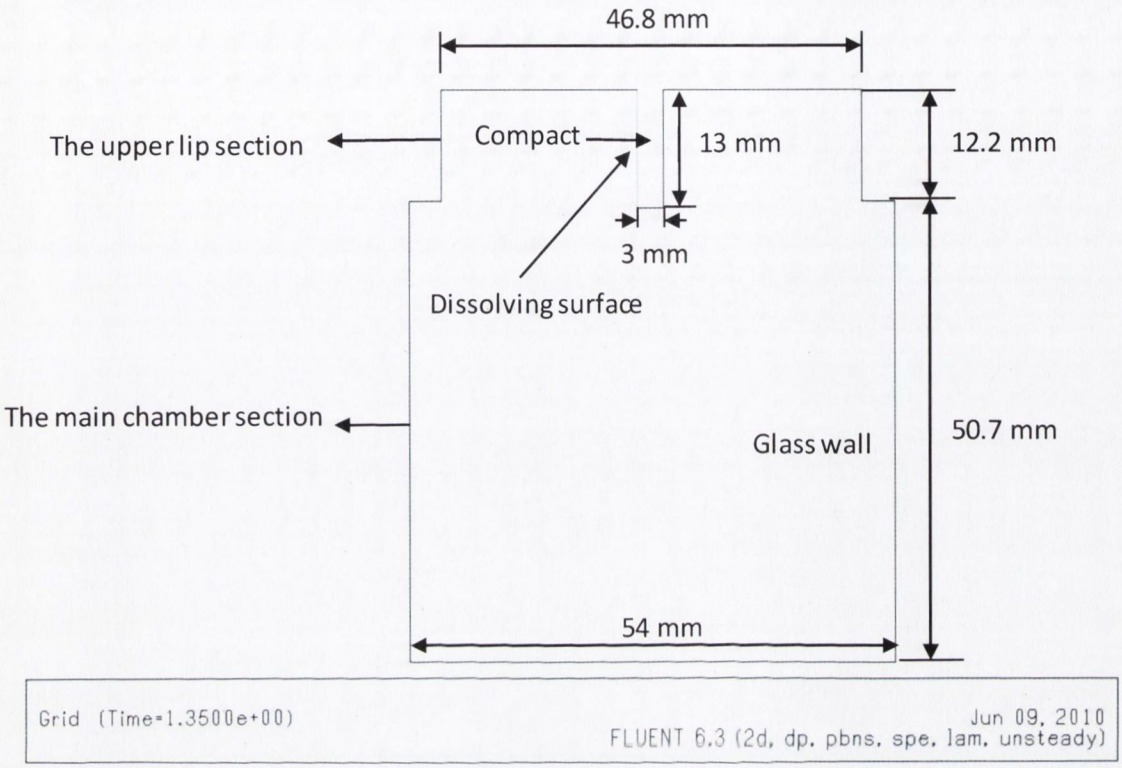


Figure 2. 3 Geometry of 2D free convection system containing the compact constructed in the Gambit™ pre-processor.

The method to create the mesh for the 2-D free convection system is the same as the above description of the flow-through apparatus. A regular structured rectangular mesh was generated in the Gambit™ as illustrated in Figure 2.4. Furthermore, a more dense mesh of approximately 3.25×10^{-6} m width for each mesh cell was generated on the compact surface. The surface subtract tool was used to create a new "free convection system" without the rectangular compact.

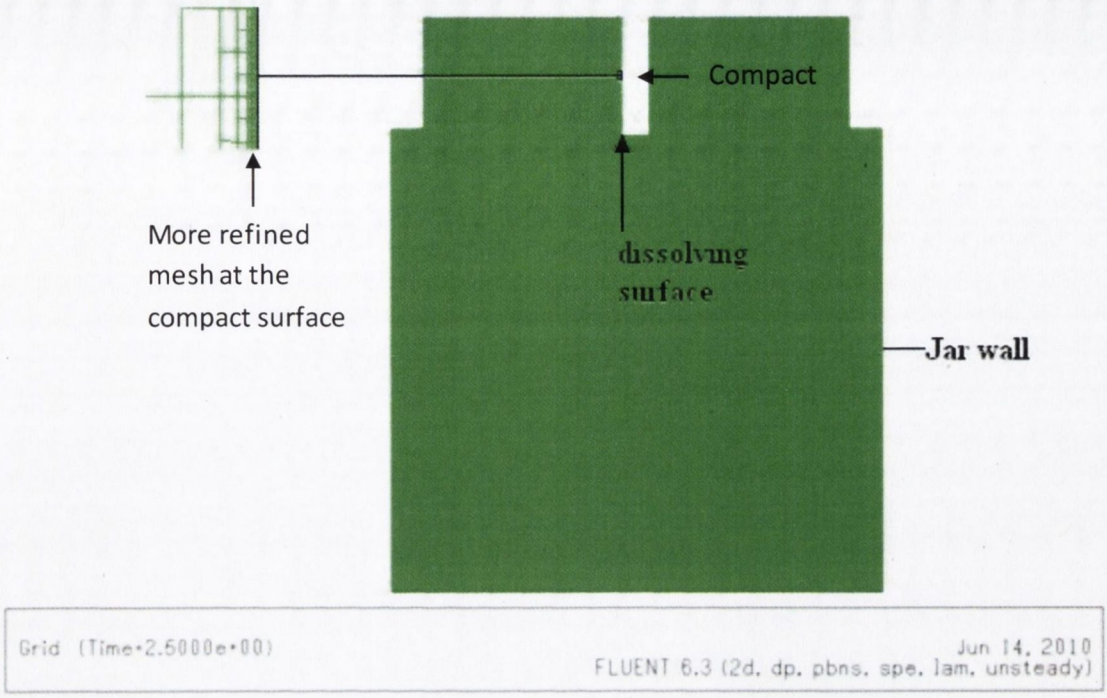


Figure 2. 4 Geometry of 2D free convection system containing the compact with regular structured rectangular mesh generated by Gambit™.

(3). Construction of the 3-D flow-through apparatus

The 3-D model of flow-through apparatus is illustrated in Figure 2.5. The geometry tool in Gambit was used to create the cylinders. The dimension parameters were input in the cylinder volume tool under the geometry tool. It was required to subtract the volume of compact cylinder from the total volume, since the liquid only occupies the space surrounding the compact, and not the compact itself. The volume subtract tool was used to create a new "cell cylinder" without the compact cylinder.

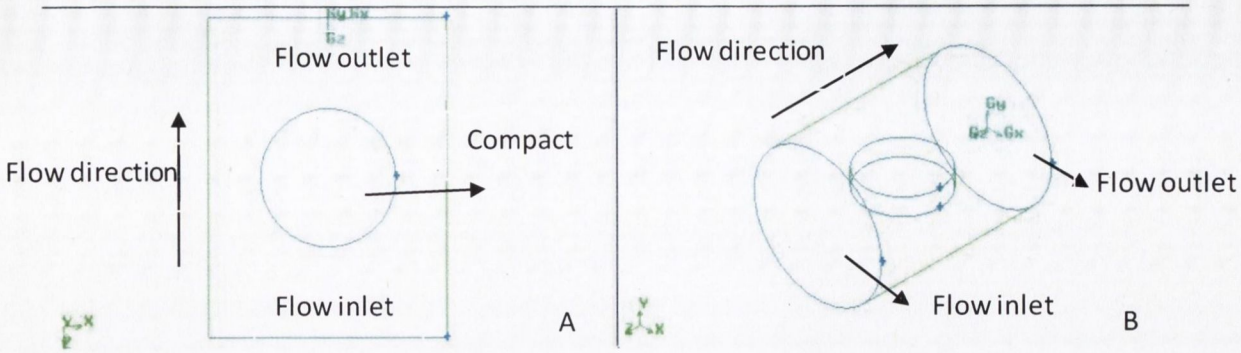


Figure 2. 5 Geometry of 3-D flow-through apparatus containing the compact constructed in the Gambit™ pre-processor view in a different orientation. A. planform viewed from the Y coordination. B. side view in operation, cell is orientated as described in A.

The mesh in the 3-D model is different to the 2-D model. The volume mesh tool was used to create a mesh in the cell cylinder part. The tetrahedral/hybrid scheme was used with TGrid type mesh elements. A total of 244825 elements were created in the model. A refined mesh of approximately 1.4×10^{-5} m width for each mesh cell was generated on the compact surface.

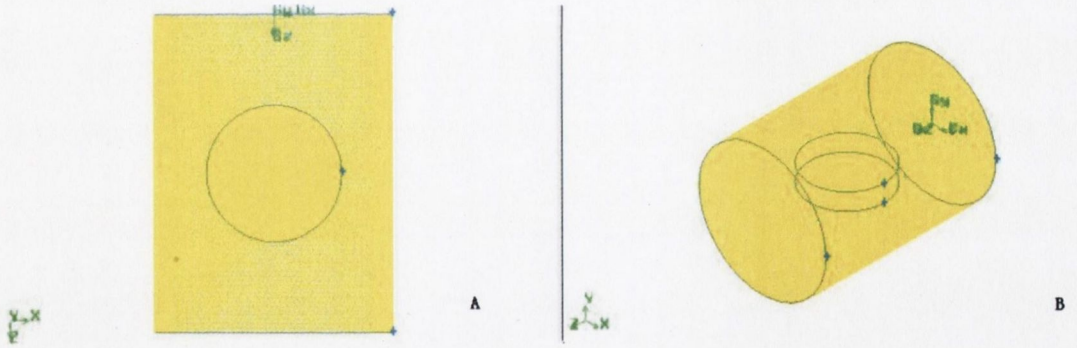


Figure 2. 6 Geometry of 3-D flow-through apparatus containing the compact generated by Gambit™ view from different orientation. A. platform viewed from the Y coordination. B. side view.

(4). Boundary definition

Different boundary types were specified in Gambit. In the 2-D and 3-D models of the flow-through apparatus, the bottom of the cell cylinder was added as a velocity inlet, and the top of the cell cylinder was defined as the out flow (Figure 2.1 and 2.5). The remaining surfaces were defined as wall in both the 2-D and 3-D flow-through apparatus models. In the 2-D model of a free convection system, all of surfaces were defined as wall.

2.2.1.2 Determination of the input flow rate in the flow through apparatus

As a piston pump is used in the flow through apparatus, the flow is a pulsing flow. The equations simulating the pulsing flow under different flow rates have different amplitudes. In the current study, different flow rates were employed. The flow profile in each pulse is divided into two parts: a semi-sinusoidal flow profile in the first half of the pulse (0 to 0.25s) and zero flow in the second half of the pulse (0.26 to 0.5s). Therefore, the amplitude of the profile of the semi-sinusoidal curve is different at different inflow rates as shown in Table 2.1. Each pulse lasts for 0.5s in total.

Table 2. 1 The different flow rate profile equations in the first half of the pulse of each pulse at 8, 16 and 43 mlmin^{-1}

System flow rate (ml min^{-1})	Equations	Range of t
8	$Q_{cell} = 0.00104 \int_0^t \sin(4\pi t)$	0 to 0.25s in each pulse
16	$Q_{cell} = 0.00208 \int_0^t \sin(4\pi t)$	0 to 0.25s in each pulse
43	$Q_{cell} = 0.00561 \int_0^t \sin(4\pi t)$	0 to 0.25s in each pulse

2.2.1.3 Solver and inlet flow conditions defined for the 2-D flow through apparatus, 2-D free convection system and 3-D flow-through apparatus.

The 2-D and 3-D meshed model generated by Gambit™ was imported into Fluent™ as a case file. The solver was based on the unsteady time and 1st – order implicit unsteady formulation. The laminar model was selected as a viscous model. The direction of flow was from the cell bottom to the top. The pulsing flow profile was created using a user defined function. The function written using C Language was compiled in Fluent™ and loaded into the program. The code written in the C Language was obtained from the Trinity Centre for High Performance Computing (TCHPC). As the change of flow profile with time is investigated in the current study, an unsteady time model was enabled. The length of each time step is 0.01 second and the max iterations per time step were 600.

The solver was the same as the above in the free convection system. However, there was no flow inlet in the free convection system, and therefore no need to define a flow rate.

In the simulation of the 3-D flow through apparatus, the species transfer was not enabled. Three different flow rates of 8, 16 and 43 ml min^{-1} were simulated using the 3-D model.

2.2.1.4 Species transfer and defining materials

The species transport option without reactions was applied in all 2-D models in order to simulate the effect of dissolution on local hydrodynamics. The specified mass fraction of solute to form a saturated solution was applied at the nodes of the boundary which represented the planar surface of the compact, simulating the effect of dissolution on fluid density adjacent to this surface. This was the user defined source of the second species (Equation 1.8). The maximum mass fraction was calculated from compound solubility. Thus the maximum mass fraction of BA and LM is 0.0045 and 0.219, respectively. No-slip conditions were applied as boundary conditions. The diffusion coefficient was entered in the "material properties" of Fluent™ for either BA or LM as appropriate. A laminar model was used, and the operating conditions consisted of a fluid with viscosity of water at 37°C (6.943×10^{-4}kg $m^{-1}s^{-1}$) with gravitational acceleration of 9.8 m s^{-2}. The general conservation Equation 1.8 was used to predict the species transfer. The mixture template was selected in the species transport model. The BA and LM properties were added into the material properties and dissolution medium property was added into the mixture template.

Table 2. 2 The values of BA input into the simulation of Fluent™

Property	Units	Method	Value(s)
Density	kg/m^3	constant	1320 (Parr Instrument Company 2008)
Molecular Weight	kg/kgmol	constant	122.22

Table 2. 3 The values of LM input into the simulation of Fluent™

Property	Units	Method	Value(s)
Density	kg/m^3	constant	1580
Molecular Weight	kg/kgmol	constant	360.2

Table 2. 4 The values of 0.1 M HCl input into the simulation of Fluent™

Property	Units	Method	Value(s)
Density	kg/m^3	constant	995
Viscosity	kg/m s	constant	0.000694
Molecular Weight	kg/kgmol	constant	18.0152

2.2.1.5 Horizontal lines created in the 2-D and 3-D models for profiling hydrodynamic data

In order to obtain the velocity magnitude and shear rate distribution in different positions inside the flow-through apparatus and free convection system, three horizontal lines were created at different horizontal positions, at regular intervals along the compact surface. The distribution of the lines in the 2-D flow-through apparatus and free convection system are illustrated in Figure 2.7 and Figure 2.8, respectively. The lines were 6 mm apart in the 2D flow-through apparatus and free convection system. The output profile of shear rate and velocity magnitude distribution with location can be plotted in EXCEL.

In the 2-D models of the flow-through apparatus and free convection systems, the velocity data on the upper and lower horizontal lines were used to judge whether the system in the steady state. The velocity distribution present at the location of these horizontal lines was calculated over consecutive pulses, at a range of time points during each pulse. If the velocity distribution was, or was close to, overlapping at these times, it was considered that the system had come to steady state.

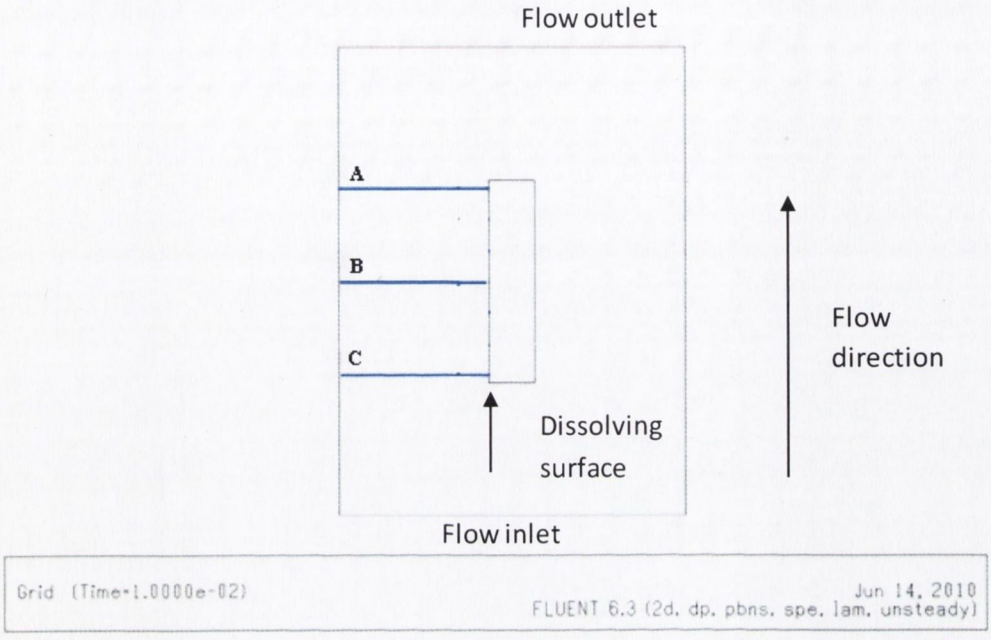


Figure 2. 7 The horizontal lines for profiling hydrodynamic data in the flow-through apparatus 2-D model: A. line A is just below the top of the compact; B. line B is in centre of the compact; C. line C is just above the bottom of the compact.

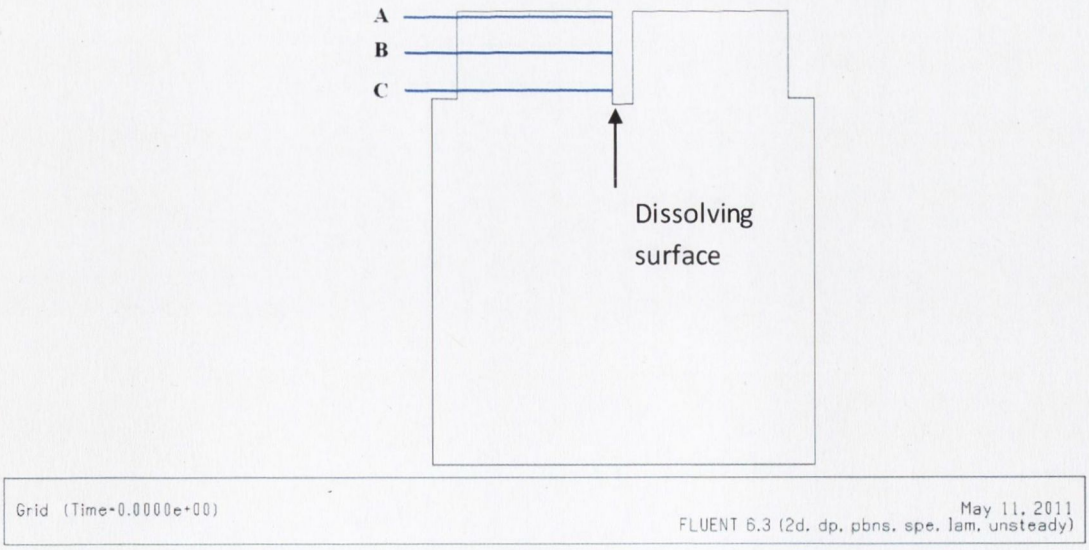


Figure 2. 8 The horizontal lines for profiling hydrodynamic data in the free convection system 2-D model: A. line A is just below the top of the compact; B. line B is in the centre of the compact; C. line C is just above the bottom of the compact.

The Lines A, B and C in the 3-D flow-through apparatus are illustrated in Figure 2.9. The shear rates and velocity magnitude at 0.06, 0.13 and 0.21s from simulations at 8, 16 and 43 ml min^{-1} were extracted from those lines.

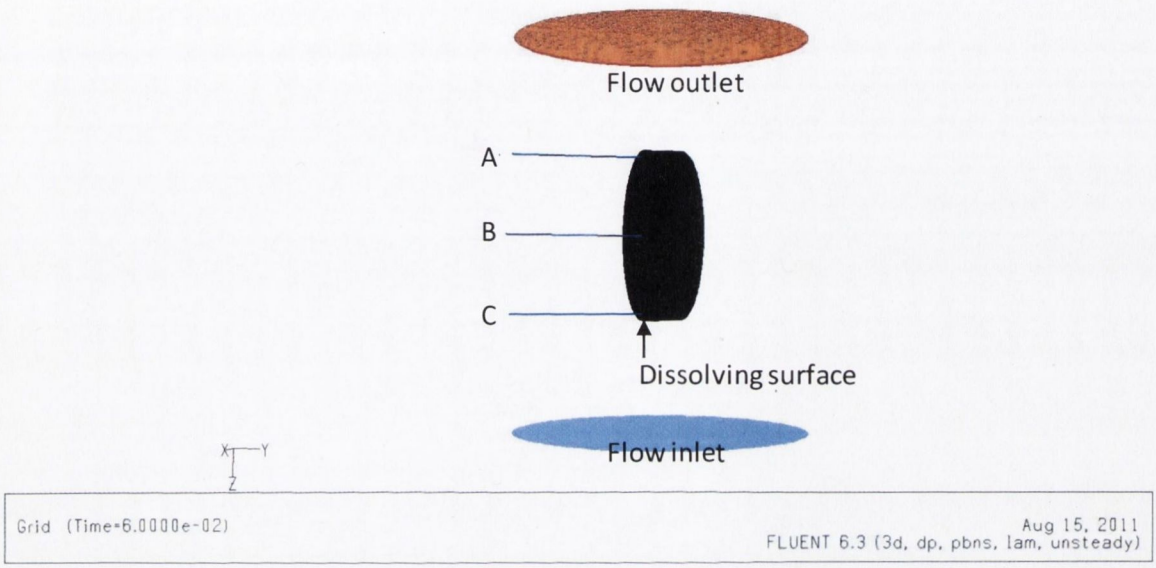


Figure 2. 9 The horizontal lines for profiling hydrodynamic data in the flow-through apparatus 3-D model: A. line A is perpendicular to the compact surface close to the upper edge; B. line B is perpendicular to the compact surface on the central position; C. line C is perpendicular to the compact surface close to the lower edge

The thickness of the diffusion boundary layer was estimated as the distance from the compact surface to the first point at which the concentration is lower than 1% of saturated solubility. The data was obtained from Line B in the flow-through apparatus (Figure 2.7) and Line B in the free convection system (Figure 2.8).

2.2.1.6 Determination of pressure gradients within the CFD simulated flow field

The change of flow direction in the system is caused by differences in pressures. The pressure gradients are also an important index to judge the hydrodynamic changes in the simulated model. The static pressure, dynamic pressure and total pressure were data available from the CFD simulations in Fluent. The static pressure refers to the pressure of a fluid at a nominated depth in the fluid. The dynamic pressure is related to the flow motion. The total pressure was determined by the combined effect of the static pressure and the dynamic pressure.

2.2.2 Dissolution rate studies

2.2.2.1 Dissolution rate studies of BA and LM

(1) Compact preparation and coating

A Perkin-Elmer 13 mm hydraulic punch and die set and a Perkin-Elmer hydraulic press were used to compress the compacts, which were 13 mm in diameter and approximately 3 mm in height by a compressive stress of 10 tons for 5 minutes (100% LM compacts was pressed of 5 tons for 5 minutes). All dissolution studies were performed using compacts containing 6 different ratios of BA: LM, as follows: 100:0, 75:25, 50:50, 25:75, 15:85 and 0:100.

The coating method involved placing the compact on a glass slide with the planar surface facing downward. A small amount of molten paraffin wax was then put on the compact, and the mould quickly placed over the compact. As the wax rapidly hardened, the mould was removed, and the glass slide removed from the planar surface, which then remains exposed for dissolution. The wax was further pared down to reach a coating of approximately 1mm thickness.

Each compact was then examined to ensure integrity of the coating. A coated 100% BA compact, to be placed in the vertical position of the free convection system, is shown in Figure 2.10. In order to fix the coated compacts vertically to the underside of the lid of the jar of the free convection system, part of the wax coating was left as a flat surface as shown in Figure 2.10. This flat surface was fixed to the underside of the lid of the jar. The wax coating on the compacts for use in the paddle apparatus and flow-through apparatus had no flat section- i.e. had a smooth curved surface.

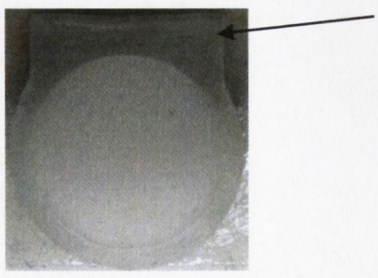


Figure 2. 10 Coated compact for the free convection system.

(2) Dissolution test in different apparatuses

All compacts were coated with paraffin wax leaving only one planar surface exposed to the dissolution medium. The dissolution tests in the paddle apparatus were carried out using 900 ml 0.1 M HCl as the dissolution medium with a paddle rotation speed of 50rpm (Figure 2.11). The dissolution medium was degassed at 37 °C. In the current study, the samples were measured in three separated glass vessels in order to generate three replicate results.

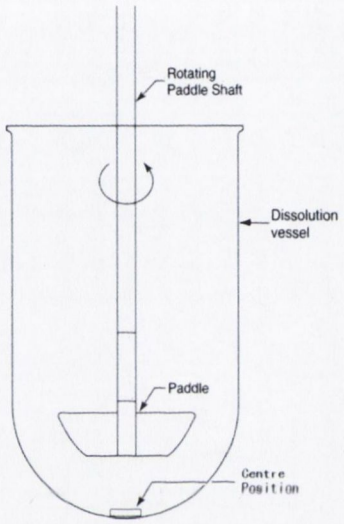


Figure 2. 11 Dissolution test in the paddle apparatus with the compact at the center of the vessel base.

The dissolution test using a Sotax CE-7 flow-through apparatus, as shown in the Figure 1.3, was used to measure the dissolution rate of BA compacts, LM compacts and the compact consisting of mixtures of BA and LM. The compact was fixed in a vertical orientation in the middle of a cylindrical cell by the "V" shape metal compact holder. The flow rates selected in this investigation were 8, 16 and 43 ml min^{-1}. The piston pump connected to the flow-through apparatus induced a pulsing flow. Three samples were measured in three separate flow-through cells in order to generate three replicate results.

The free convection system consisted of a jar with the compact fixed to the underside of the lid, with the exposed planar surface orientated vertically. A diagram of this free convection system is presented in Figure 2.12. In order to ensure that the dissolving surface was fully immersed in the medium, a needle was inserted through the lid and excess dissolution medium introduced. The volume of medium in each jar was approximately 124 ml. The

sampling procedure involved careful removal of the lid of the jar with the compact attached. A second lid was then placed on the jar, the medium mixed well and sampled. For the 100% BA compact only, fresh medium was then introduced to the jar to replace the sampled volume.

As the sampling process may affect the dissolution rate in the free convection system through involuntary agitation of the static medium, independent dissolution tests were carried out for each sampling time point in the free convection system for all compacts except those of 100% BA. It had previously been demonstrated that the sampling process did not impact on the dissolution rate for 100% BA. Dissolution experiments were conducted in parallel, in several jars simultaneously. At each sampling time point, samples were obtained from 3 of these jars to generate 3 replicate results.

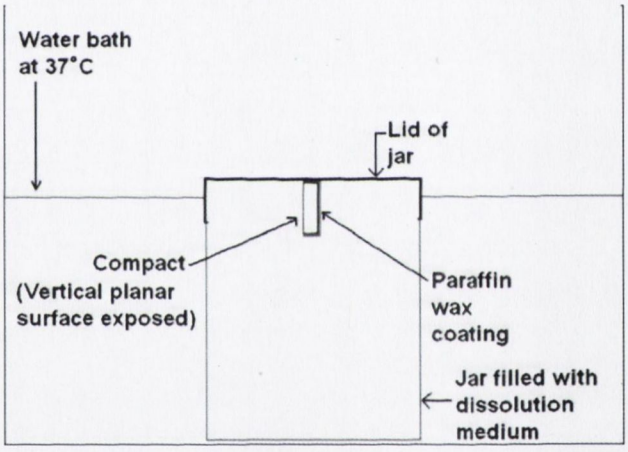


Figure 2. 12 Apparatus used in the determination of the dissolution rate from the planar surface, free convection system.

(3) Sampling time

With the exception of the compacts containing 15% BA, sampling times of BA in the paddle and flow-through dissolution apparatus were 15, 30, 60, 90 and 120 minutes. These times were also used for the 100% BA compact in the free convection system. All time points were used to determine the BA dissolution rate. Due to fast disintegration of compacts with a higher ratio of LM in the mixture, the sampling time points for the 15% BA compact were at 5, 10, 15, 30 and 40 minutes for the 15% BA compact in the paddle apparatus and flow-through apparatus. The sample time points for 75%, 50% and 25% BA compacts were 10, 20, 30, 40

and 50 mins in the free convection system. For the 15% BA compact, sampling times were 5, 10 and 15 minutes

As disintegration was observed at later time points for LM from the 100% LM compact, only the 15 minute point was used to calculate the dissolution rate. The 15 minutes sampling time point for LM was therefore used in dissolution testing of all other compacts containing the LM-BA mixture, to correspond with the sampling time for the 100% LM compact.

2.2.2.2 Dissolution rate studies of carbamazepine (CBZ) in the paddle and flow-through apparatuses.

The CBZ tablets were tested in the flow-through apparatus and paddle apparatus. The CBZ formulations used were Tegretol IR 200mg and CR 400mg tablets. In each test, three replicates were carried out.

The dissolution test of CBZ in the paddle apparatus was carried out at 25, 50 and 75 rpm with three replicates. The dissolution media used were pure water, 0.1% and 1% sodium lauryl sulphate at 37 °C. The sampling time points were: 10, 20, 30, 45, and 60 minutes. The dissolution test of Tegretol IR in the flow-through apparatus was tested at 8, 16 and 32 ml min^{-1}. The tablet was fixed in the tablet holder, in the center of the cell. Tegretol CR was tested at 8 and 16 ml min^{-1} only, as the tablet excipient clogged the outlet filter at 32 ml min^{-1} making the testing condition impossible. The temperature was 37 °C. Both open and closed loop system configurations were used, for the IR tablets.

The test duration in the closed and open loop system was 1 and 10 hours, respectively. The dissolution medium was pure water. In the closed loop configuration, sampling times were every 10 minutes during the first 30 minutes and every 15 minutes from 30 to 60 minutes. In the open close loop configuration, sampling times were every 10 minutes during the first 1 hour and every 30 minutes from 1 to 3 hours. The samples were taken each hour from 3 to 8 hours and the last sample was taken at 10 hours.

2.2.2.3 The f_2 factor (similarity factor)

The dissolution profiles were compared using the f_2 factor (FDA CDER 2000; Ansari, Kazemipour et al. 2004). The f_2 factor is given by the following equation.

$$f_2 = 50log\left\{\left(1 \div \frac{1}{n}\sum_{t=1}^{n}(R_t - T_t)^2\right)^{-0.5} \times 100\right\}$$

Equation 2. 1

Where n is the number of dissolution sample times, and R_t and T_t are the mean percent of reference and test sample dissolved at each time point, t.

2.2.3 Solubility measurements

Solubility was measured using the equipment shown in the Figure 2.13. To determine the solubility of LM in 0.1 M HCl, an excess (15g) of LM was added to 0.1 M HCl, and sampled regularly until the amount dissolved was no longer increasing (4 hours). Three replicates solubility experiments were carried out in the current study. Circulating water was pumped from the water bath through the water jacket of the cells. The water bath was kept at a constant temperature of 37°C. A magnetic stirrer was placed in the cell to increase the dissolution rate by vigorous agitation.

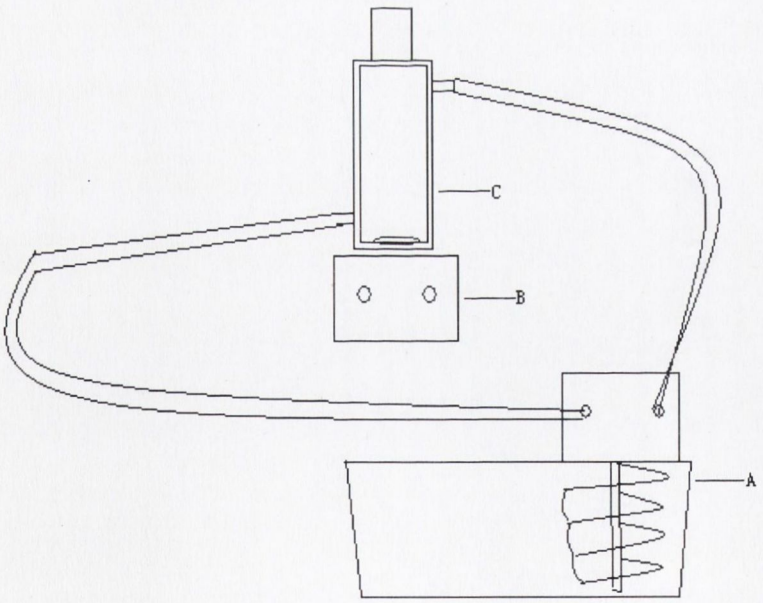


Figure 2. 13 Schematic diagram of cell used to determine solubility. Key: A, water bath; B, magnetic stirrer; C, Cell were used in order to generate two replicates of each solubility experiment at a time.

To determine the solubility of LM in a saturated BA solution using the same above method, the LM was dissolved, in 90%, 80% and 75% w/v saturated BA solution at 37 °C. The concentration of saturated BA solution was 4.564 g/L at 37°C (Ramtoola and Corrigan 1987).

The same method was used to determine the solubility of BA in a saturated LM solution. BA was dissolved in 90%, 80% and 75% w/v saturated LM solution at 37 °C.

2.2.4 Diffusion coefficient determination

The diffusion coefficient in water was determined using the silver membrane filter method, described in detail by Goldberg and Higuchi (Goldberg and Higuchi 1968). In brief, it involved measuring the rate of diffusion of the drug across a silver membrane filter. A conical flask (flask 1) containing a degassed aqueous solution was stirred by a magnetic stirrer. Flask 1 was modified to incorporate a glass side-arm. A second 250 ml conical flask, also modified to incorporate a glass side-arm, containing distilled water, was the receptor flask (flask 2) for the diffusing drug. The side glass side-arms between the flasks are clamped together, and the filter is located at this junction between two Teflon washers. 250 ml of either the solution or water were added to both flasks simultaneously. When the water addition to flask 2 was completed, flask I was quickly filled to the top and a glass Y adapter was placed in position. More solution was added through one of the arms, keeping the stopcock of the other arm open for air displacement. The contents of flask 2 were sampled at intervals of 30 min, and analyzed by U.V. spectrophotometry at 295 nm to determine the diffusion rate of salicylic acid from flask 1.

The precision of the apparatus was determined using BA at 30 °C by comparing the measured diffusion coefficient with the known value of 1.113×10^{-5} cm^2s^{-1} (Goldberg and Higuchi 1968). In order to calculate an unknown D value, it is necessary to first calculate the cell constant, using a compound which has a known D value.

The CBZ diffusion coefficient was obtained from the published data of 8.689×10^{-6} cm^2s^{-1} (Kovacevic, Parojcic et al. 2008).

Measurement of cell constant

The diffusion coefficient for 0.1 M KCl at 30 °C is $1.873\times10^{-5}cm^2s^{-1}$ (Goldberg and Higuchi 1968). KCl solution was used to measure the cell constant according to the method of

Goldberg and Higuchi (Goldberg and Higuchi 1968). The calculation of the cell constant is given as:

$L_{cell}=G/(D(C_2-C_1))$

Equation 2. 2

L_{cell}: cell constant

G: the rate of transport from conical flask 1 and 2;

D: diffusion coefficient;

C_1: concentration in conical flask 1;

C_2: concentration in conical flask 2.

A calibration curve of KCl was constructed using a conductivity meter. As KCl solution is an electrolyte solution there is an increase in conductivity with increasing concentration of KCl. The conductivity is proportional to the KCl concentration in the solution. Solutions with concentrations of 0, 6, 12, 18 and 24 mg ml^{-1} of KCl were used to construct a calibration curve.

To calculate the cell constant, 0.1 M degassed KCl solution was put into flask 2 as shown in the Figure 2.14. The whole apparatus was kept at 30 °C in a water bath. 10 ml samples were taken from flask 1 and replaced with 10 ml water. The sampling times were 0, 0.5, 1 and 2 hours. The concentration of KCl in each sample was plotted against time. The slope of the line was used to calculate the rate of transport from flask 1 to flask 2, used in Equation 2.2 to calculate the cell constant. As the cell constant is not affected by the small temperature changes, this cell constant was used to determined the diffusion coefficient at 37 °C

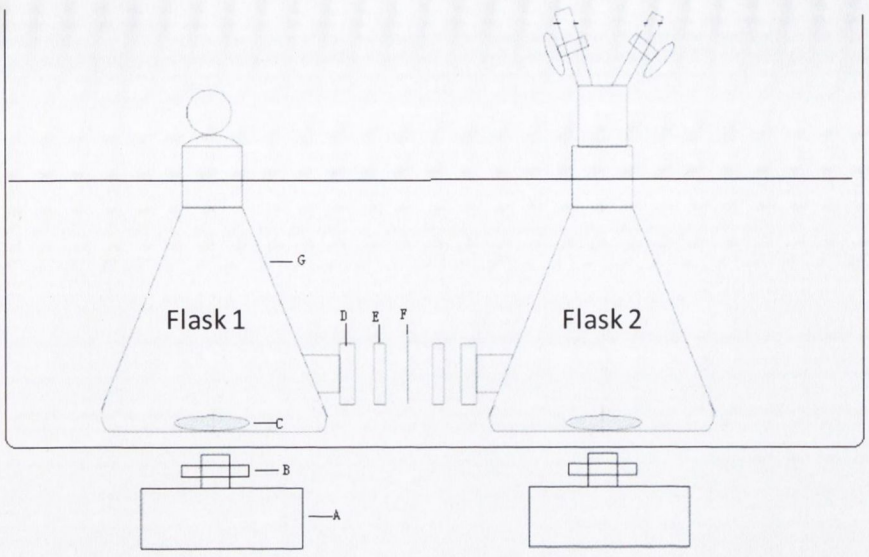


Figure 2. 14 Schematic diagram of apparatus used to determine the diffusion coefficients. Key: A, synchronous motor; B, stirrer; C, Teflon-coated stirring bar; D, ground-glass end; E, Teflon washer; F, silver membrane; G, 250 ml conical flask.

2.2.5 Analysis of BA, LM and CBZ

In order to construct a calibration curve of BA, the absrobance of BA solution of 0.1, 0.4, 1, 2, 5, and 10 mg per 100 ml 0.1 M HCl was measured. The BA solution absorbance was measured using UV spectrophotometry at a wavelength of 274 nm.

To construct a calibration curve of CBZ, concentrations of CBZ solutions of 0.5, 1, 1.5, 2 and 2.5 mg per 100 ml dissolution media were prepared. The dissolution media were pure water, 0.1% sodium lauryl sulphate and 1% sodium lauryl sulphate. The CBZ solution absorbance was measured using UV spectrophotometry at 285 nm.

The LM concentration was determined using a Lactose/D-galactose enzymatic assay kit. The principle to determine the concentration of LM present was to measure the amount of NADH formed from the reaction of LM and galactose dehydrogenase. The absorbance of the NADH solution was measured by UV spectrophotometry at 340 nm. The following equation was used to calculate the amount of LM (Product Documentation, Boehringer Mannheim/R-Biopharm, Darmstadt, Germany). The absorbance of $(A_1)_{sample}$ is the absorbance of lactose solution without reaction to galactose dehydrogenase. The absorbance of $(A_2)_{sample}$ is the

absorbance of NADH after the reaction of lactose and galactose dehydrogenase. The increase in NADH can indicate the amount of LM in the solution.

$$\Delta A = (A_2 - A_1)_{sample} - (A_2 - A_1)_{blank}$$

Equation 2. 3

$$c = \frac{V_{Final} \times MW}{\epsilon \times d_{light} \times V_{LM} \times 1000} \times \Delta A \ (g/L)$$

Equation 2. 4

$(A_2\text{-}A_1)_{sample}$: absorbance difference between the corresponding sample, ;

$(A_2\text{-}A_1)_{blank}$: absorbance difference between the blank;

V_{Final}: Final volume of solution 3.3 ml being analysed after reagent added;

V_{LM}: sample solution containing LM 0.1 ml;

MW: molecular weight of LM to be assayed;

d_{light}: light path;

ϵ = extinction coefficient of NADH at: 340 nm = 6.3 [l × mmol^{-1} × cm^{-1}]

2.2.6 Particle size reduction and particle size measurement of BA, LM and CBZ.

2.2.6.1 Measurement of BA and LM

The particle size measurements of BA and LM were carried out using a Malvern Mastersizer 2000 with Scirocco attachment. The compound powder was put in the Scirocco dry powder feeder until it covered the tray of feeder. The air pressure was set at 2 bar. The particle size of the BA and LM powder, have been passed through a 250 μm size sieve, was measured.

A ball-mill was then used to decrease the particle size of the LM for 10 to 15 minutes. The milled LM particle size, after sieving through a 53 μm size sieve, was measured.

2.2.6.2 Measurement of CBZ

The original Tegretol particle size distribution was measured after the tablet disintegrated in 30 ml water, after 1 minute. The sample was measured under 2000 rpm rotation using a

Malvern Mastersizer 2000 with Hydro attachment. The measurement in the particle size was the same as for Tegretol particles. Samples were also measured after raising the ultrasound level to 50% for approximately 1s three times, and to 100% for approximately 1 second three times.

The excipients in the Tegretol IR tablets are silica colloidal anhydrous, micro crystalline cellulose, magnesium stearate and carmellose sodium (Medicines.ie 2011). As the silica colloidal anhydrous and magnesium stearate are usually used as lubricants in a formulation, and the carmellose sodium is used as disintegrant, it is likely that these three excipients are present as a small quantity of the total excipient mass. Thus it is speculated that the microcrystalline cellulose (MCC) as diluent was the major excipient in the Tegretol IR formulation.

Since the majority of the excipient in the CBZ mixture is thought to be microcrystalline cellulose, it cannot be dissolved by ethanol. The disintegrated tablet was put in the ethanol and subsequently the particle size was measured in Malvern Mastersizer 2000 with Hydro attachment. After the ethanol solution was filtered, the solid part was retained on the filter and was washed with water. This operation was repeated until the CBZ was fully dissolved in the ethanol. The remaining solid was dried in the oven over night. The samples were sieved and measured using the same method as that used to measure the original Tegretol particles size distribution.

2.2.7 Measurement of solution density

The 0.1M HCl solution density was measured in a density bottle. The mass of the empty bottle was measured on a balance. Afterwards the bottle was completely filled with pure water. The mass of the water is calculated by subtracting the mass of the bottle from the total mass at 37 °C. Using a known value of the density of pure water (Lide 2009), the volume of the bottle is calculated from the density and the mass. The density of 0.1 M HCl solution can be calculated using the mass of the 0.1 M HCl solution and bottle volume at 37 °C.

The density of LM and BA saturated solution in 0.1 M HCl was measured in the same density bottle, using the calculated bottle volume and the measured solution mass. The LM and BA solution, and the density bottle were maintained at 37 °C.

2.2.8 Statistical methods

A two sample T-test is used to perform a hypothesis test and compute a confidence interval of the difference between two populations (MINITAB® 2003). In this work, a two sample t-test was used to detect whether there was a significant difference in dissolution rates from the compacts composed of different ratios of BA. The p-value was used to determine the appropriateness of rejecting the null hypothesis in a hypothesis test. The p-values can range from 0 to 1. The smaller the p-value obtained, the smaller the probability that rejecting the null hypothesis is a mistake. Before conducting any analyses, a commonly used p-value associated with significance is 0.05. In the current study, if the p-value is smaller than 0.05, it means the dissolution rates are different. If it is bigger than 0.05, it means the dissolution rates are similar and the hypothesis of similarity is established. Therefore, the null hypothesis was that the dissolution rates were not significantly different.

2.2.9 Code used to simulate the *in vitro* dissolution profile

The equations used to predict the dissolution rate of Tegretol IR tablets in the flow-through apparatus were solved numerically in Matlab. The method used was published by D'Arcy and Persoons (D'Arcy and Persoons 2011) based on Equation 1.12, using Sh and Re, with Re calculation from the input flow profile (Table 2.1) using either an absolute or relative velocity configuration. The code written in the C Language was obtained from Dr. Tim Persoons. Different parameters were required to input into the programme as shown in the Table 2.5.

Table 2. 5 The property of CBZ particles input into the particle dissolution simulation code solved in Matlab.

Property	Units	Method	Value(s)
CBZ Particle Density (Kovacevic, Parojcic et al. 2008)	kg/m3	constant	1200
Fluid Density	kg/m3	constant	995
Fluid Dynamic Viscosity	Pa.s	constant	7e-4
Diffusion Coefficient (Kovacevic, Parojcic et al. 2008)	m^2/s	constant	8.7e-10
Solubility (Lee, Park et al. 2005)	kg/m^3	constant	0.23

2.2.10 The observed plasma concentration of Tegretol IR and CR

The observed *in vivo* result of Tegretol IR and CR was obtained from previously reported data (Kovacevic, Parojcic et al. 2008). The Tegretol IR tablets administrated to 18 healthy volunteers of both sexes with average age of 33 and average body weight of 72 kg. Each volunteer received a 400 mg dose of Tegretol IR with a 20 day washout period. Blood samples after dosing were taken at 0.5, 1, 2, 4, 6, 8, 10, 12, 24, 36, 48, 72, 96 and 120 h. Tegretol CR tables were tested in 24 healthy volunteers of both sexes with average age of 31.8 and average weight of 69.8. The sampling time points were 0.5, 1, 2, 4, 6, 8, 10, 12, 24, 36, 48, 72, 120 and 144 h after dosing.

2.2.11 Model for drug plasma concentration prediction in Gastroplus™

The simulation of plasma concentration was performed by Parojcic et al. The ACAT model was used to predict the plasma concentration based on the *in vitro* dissolution profile. Compared to single- or dual-compartment pharmacokinetic models, the ACAT model is a physiologically-based pharmacokinetics (PBPK) model and divides the GI tract into nine compartments based on their different structure and functions. The remaining body parts are divided into central and peripheral compartments. The drug is absorbed from those nine compartments rather than following a single compartment first order absorption. In addition, the pharmacokinetics simulation was carried out in the two-compartment model.

2.2.12 Validation of uniform mixing of non-interacting compounds

The content of BA was measured in different ratio mixture compacts including 25%, 50% and 70% BA. The mixture compacts were ground so that the particles dissolved in the dissolution media. The measurement method is the same as described in section 2.2.5.

Chapter 3 Hydrodynamics in the flow-through apparatus.

3.1 Introduction

The predicted dissolution rate in a laminar flow cell or similar flow-through system has been investigated in many studies (Nelson and Shah 1975; Shah and Nelson 1975). These studies tried to predict the dissolution rate of benzocaine (very slightly soluble in water) in a rectangular laminar flow cell, by calculating the shear rate from flow rate and cell dimensions. The reported dissolution rate was proportional to the cubic root of the inflow rate (Nelson and Shah 1975; Shah and Nelson 1975). However, a change in flow velocity by varying the flow rate has been shown previously not to significantly affect the dissolution rate of salicylic acid tablets in the 22.6 mm cell within the flow-through apparatus (Cammarn and Sakr 2000). This contradiction will be clarified in the current study.

Different flow rates may result in variation of the shear rate, shear stress, pressure and other factors. These factors may be of interest to interpret the dissolution rate in the flow-through apparatus. A change of shear rate close to the compact surface has resulted in a change in dissolution rate of the model drug (Dressman and Kramer 2005; Bird, Stewart et al. 2007), as the thickness of hydrodynamic and concentration boundary layers decreases with an increase in shear rate close to the compact surface. Consequently, the dissolution rate of a model drug will increase.

BA (slightly soluble) and LM (freely soluble) compacts were studied in the flow-through apparatus in the current study.

The objectives of this chapter were:

- to examine the effect of different flow rates on dissolution rates of BA compacts, and the dissolution rate of LM compacts at 8 ml min^{-1} in order to study the effect of hydrodynamics on the dissolution rate of compounds with different solubilities.
- to investigate hydrodynamic features, including boundary layer separation and flow reversal, using simulated hydrodynamics in the flow-through apparatus;
- to interpret the relationship between dissolution rates and flow rates in the flow-through apparatus and to attempt to predict the dissolution rate using simulated shear rate data.

3.2 Dissolution studies of BA and LM in the flow-through apparatus

The dissolution studies were carried out in the in the flow-through apparatus at 8, 16 and 43 ml min^{-1}. The profile of BA dissolution in the flow-through apparatus is shown in Figure 3.1. The dissolution profiles are similar for BA at the different flow rates. Although the measured concentrations from 0 to 60 minutes are nearly overlapping under different inflow rates, the dissolution profile determined a lightly increasing trend from 8 to 43 ml min^{-1}.

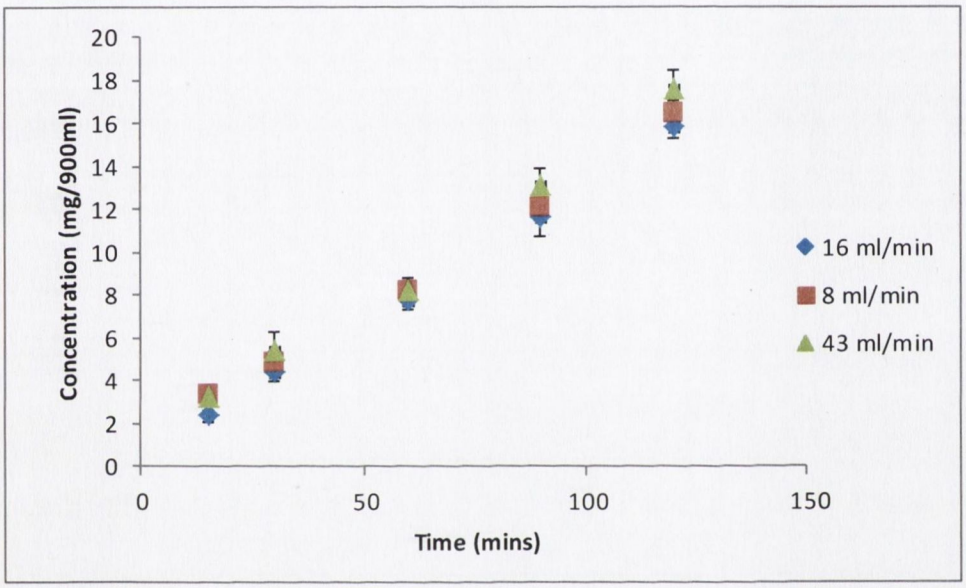


Figure 3. 1 Dissolution profile of BA at different flow rates of 8, 16 and 43 ml min^{-1}

The average dissolution rates of BA at 8, 16 and 43 ml min^{-1} and LM at 8 ml min^{-1} are shown in Table 3.1. Results which fall within 1 standard deviation could be considered to be similar i.e. there is no difference between observed dissolution rates at the different flow rates investigated. The amount of dissolving divided surface area and total solution volume can generate the dissolution rate. The dissolution rate in the following chapters was calculated using the same procedure.

Table 3. 1 The average dissolution rate obtained from BA at different flow rates and LM at 8 ml min^{-1}.

Compounds	Flow rate (ml min^{-1})	Average dissolution rate (mg min^{-1} cm^{-2})
	8	0.094 +/- 0.008
BA	16	0.095+/- 0.007
	43	0.102+/- 0.003
LM	8	3.240 +/- 0.680

Statistical analysis using a 2-sample t-test was also used to estimate the difference between different flow rates as illustrated in Table 3.2. In each case, the p values were greater than 0.05. Therefore, at a significance level of 0.05, any difference in flow rate in the 22.6 mm cell is shown to be insignificant. Therefore, the dissolution rates in the flow-through apparatus were not proportional to the flow rates, despite an increasing trend with increasing of flow rates, - an increase of flow rate cannot lead to a significant increase in the dissolution rate. This observation was not in agreement with the relationship between flow rate and dissolution rate studied of Benzocaine in water for the rectangular channel type of flow through system (Nelson and Shah 1975; Shah and Nelson 1975). However, the lack of increase in dissolution rate with flow rate in the 22.6 mm cell used in the current system has been noted before by Cammarn and Sakr (Cammarn and Sakr 2000).

Table 3. 2 Results of the 2-sample t-test comparing the dissolution rates of BA compacts at 8, 16 and 43 ml min^{-1} in the flow through apparatus

	P value from 2 sample t-test		
Flow rate (ml min^{-1})	8 vs 16	8 vs 43	16 vs 43
8	0.81	0.217	-
16	-	-	0.242

The CFD simulations of hydrodynamics in the flow-through apparatus were therefore investigated to determine why the dissolution rate does not increase despite the increase in input flow rate.

3.3 Simulated hydrodynamic features in the flow-through apparatus.

3.3.1 Flow profile at the cell inlet at different flow rates

According to the input profile equations described in chapter 2.2.1, inlet velocities at different flow rates in the flow-through apparatus were as shown in Figure 3.2. The maximum inlet flow velocities at 8, 16 and 43 ml min^{-1} in the flow-through apparatus are approximately 1.1×10^{-3}, 2.1×10^{-3} and 5.7×10^{-3} m s^{-1}, indicating that the maximum flow velocity is proportional to the flow rates. Although the maximum input flow velocity does not represent actual velocity distribution in 22.6 mm cell, it indicates that the flow velocity in the flow-through apparatus could be extremely low compared to the maximum velocity of approximately 0.1 m s^{-1} at 50 rpm in in the curve side of the vessel of the paddle apparatus (D'Arcy, Corrigan et al. 2005).

At the same time, due to the "semi-sinusoidal" flow input into the flow-through cell, the hydrodynamics in the flow-through cell change with time. This changing inlet flow velocity with time results in a changed flow environment occurring with time in the flow-through cell. This changing flow environment may affect the overall dissolution rate in the flow-through apparatus.

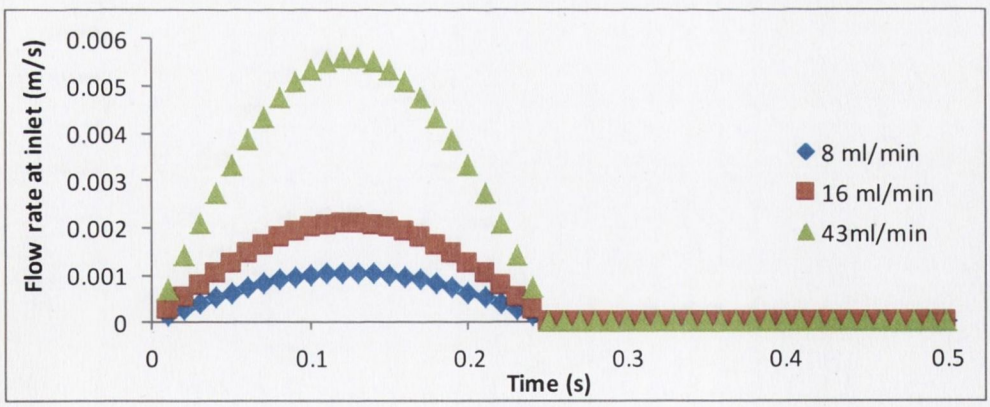


Figure 3. 2 The input flow profile in the flow-through apparatus at 8, 16 and 43 ml min^{-1}

3.3.2 Velocity magnitude, wall shear stress and pressure distribution generated at different flow rates in the flow-through apparatus.

The velocity vectors, wall shear stress and pressure distribution are investigated in this section in order to determine the effect of the hydrodynamics on the dissolution rate at different input flow rates. The input flow profile demonstrated a similar velocity at 0.06 and

0.20s as the velocities at those time points were almost symmetrically distributed on the "semi-sinusoidal" curve (Figure 3.2). However, the velocity at 0.06s was in the growth stage of the "semi-sinusoidal" curve whereas the velocity at 0.20s was during the decreasing velocity section.

The observed fluid velocity vectors at 8, 16 and 43 ml min^{-1}, as illustrated in Figure 3.3, 3.4 and 3.5, demonstrated a different distribution at 0.06 and 0.20s. The simulated velocity vectors at 8 ml min^{-1} are shown in Figure 3.3. The direction of velocity vector near the curved and planar surfaces at 0.06s was upward. However, the direction of velocity vector near the curved and planar surface at 0.20s is divided into two parts: the direction of the inner velocity vectors close to the compact surface was downward; the outer velocity vectors were upward. This change in direction illustrated by the velocity vectors demonstrates that separation occurred in the boundary, which resulted in flow reversal. In addition, the boundary separation was first observed at 0.20s at 8 ml min^{-1}.

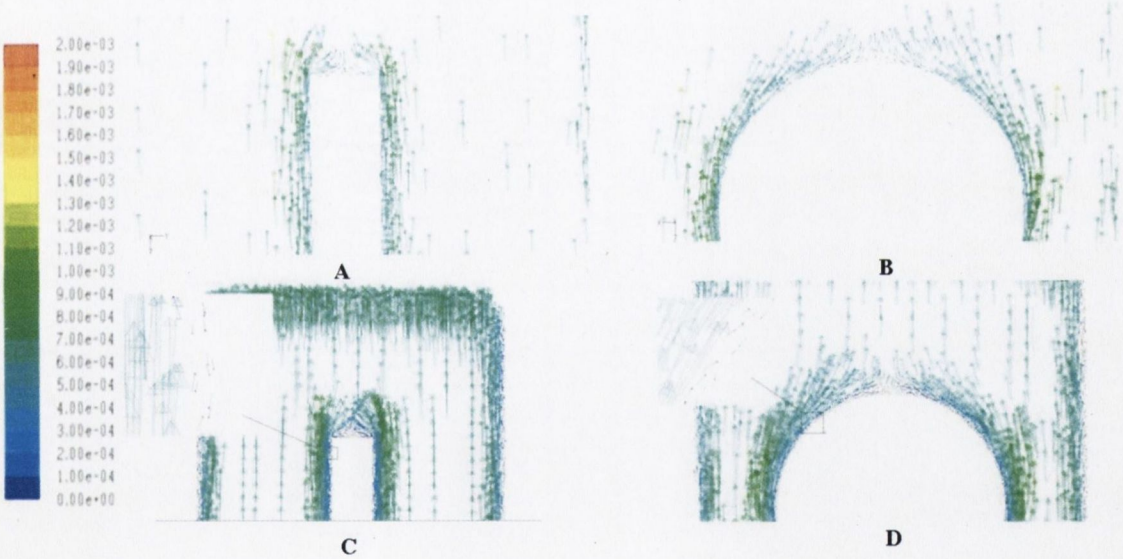


Figure 3.3 Simulated velocity vectors at 8 ml min^{-1}. A: the vectors coloured by velocity magnitude through the centre of the compact, perpendicular to the planar surface at 0.06s; B: the vectors coloured by velocity magnitude parallel with planar surface at 0.06s; C: the vectors coloured by velocity magnitude through the centre of the compact, perpendicular to the planar surface at 0.20s; D: the vectors coloured by velocity magnitude parallel with planar surface at 0.20s.

The corresponding simulated velocity vectors coloured by velocity magnitude in the flow-through apparatus at 16 ml min^{-1} are shown in Figure 3.4. Boundary separation had also occurred by 0.20s at 16 ml min^{-1}.

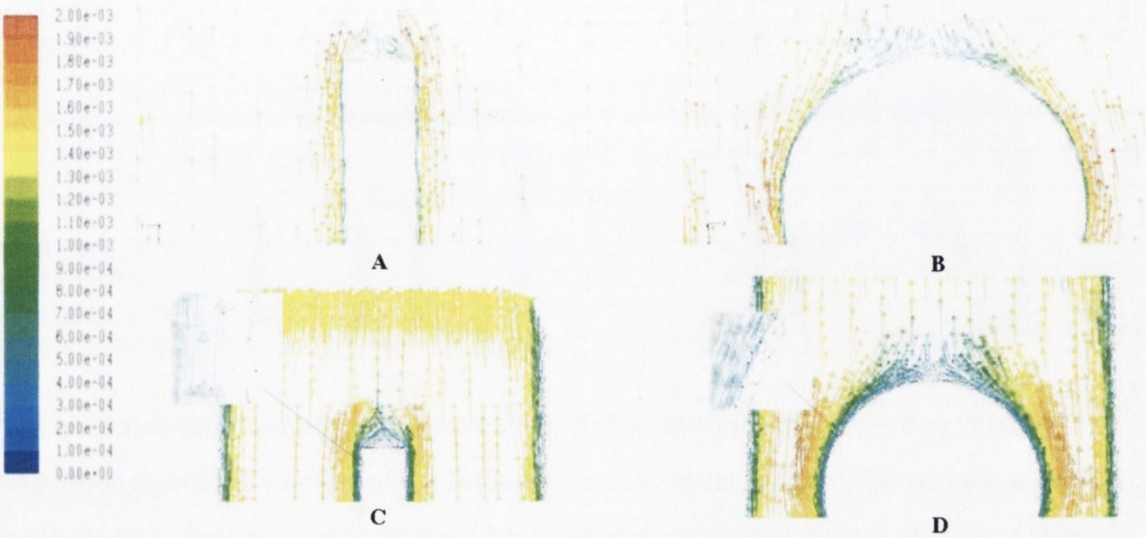


Figure 3.4 Simulated velocity vectors at 16 ml min^{-1}. A: the vectors coloured by velocity magnitude through the centre of the compact, perpendicular to the planar surface at 0.06s; B: the vectors coloured by velocity magnitude parallel with planar surface at 0.06s; C: the vectors coloured by velocity magnitude through the centre of the compact, perpendicular to the planar surface at 0.20s; D: the vectors coloured by velocity magnitude parallel with planar surface at 0.20s.

The simulated velocity vectors coloured by velocity magnitude in the flow-through apparatus at 43 ml min^{-1} are shown in Figure 3.5. The results are similar to the other velocity conditions in that the boundary separation had occurred by 0.20s at 43 ml min^{-1}. The scale of 0 to 0.008 m s^{-1} displayed in Figure 3.5 was larger than that of 0 to 0.002 m s^{-1} in Figure 3.3 and Figure3.4, for clarity of the image.

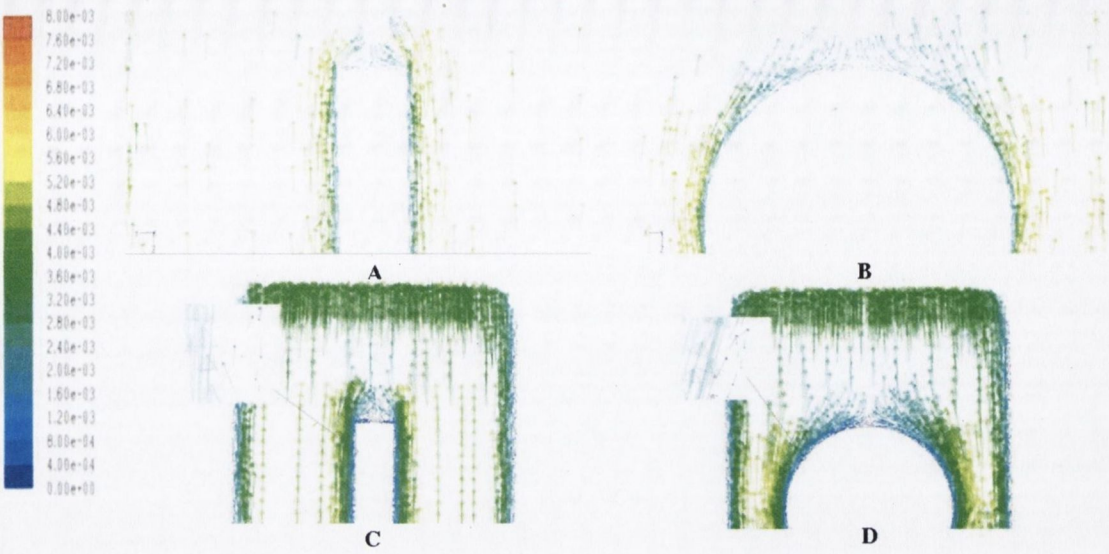


Figure 3.5 Simulated velocity vectors at 43 ml min^{-1}. A: the vectors coloured by velocity magnitude through the centre of the compact, perpendicular to the planar surface at 0.06s; B: the vectors coloured by velocity magnitude parallel with planar surface at 0.06s; C: the vectors coloured by velocity magnitude through the centre of the compact, perpendicular to the planar surface at 0.20s; D: the vectors coloured by velocity magnitude parallel with planar surface at 0.20s.

Although the input flow velocities were similar at 0.06s and 0.20s as illustrated in Figure 3.5, the simulated velocity range in the cell demonstrated the difference in hydrodynamics at 0.06 and 0.20s at each flow rate. As the flow reversal was observed at 0.20s, it indicated that the fluid boundary had separated. The retarding force from wall friction (both the cell wall and the compact surface) as well as the fluid moving against an adverse pressure gradient would reduce the flow velocity. When this retarding force was large enough, the inner layer of fluid close to compact surface could deviate away from the main stream direction and reverse the flow direction (Kakhi 2009).

It is interesting that the boundary separation was first observed at the same time of 0.20s at each flow rate. Although the maximum simulated flow velocity at 8, 16 and 43 ml min^{-1} were approximately 1.2×10^{-3}, 1.8×10^{-3} and 4.8×10^{-3} m s^{-1}, respectively, the corresponding retardation could dramatically reduce the flow velocity in the inner layer close to the compact surface and flow reversal occurred at 0.20s at each flow rate investigated. In accordance with a fixed wall

friction on the compact surface, the correspondent adverse pressure gradient increase d with increasing input flow rates, resulting in a boundary separation at the same time point at different flow rates.

As described in chapter 2, section 2.2.1, three different horizontal lines were generated from the compact surface to the wall of the cell as shown in Figure 3.6, in order to investigate the simulated hydrodynamics near the compact surface over the course of the pulse. The shear rate and velocity magnitude were obtained at 0.06, 0.13 and 0.21s.

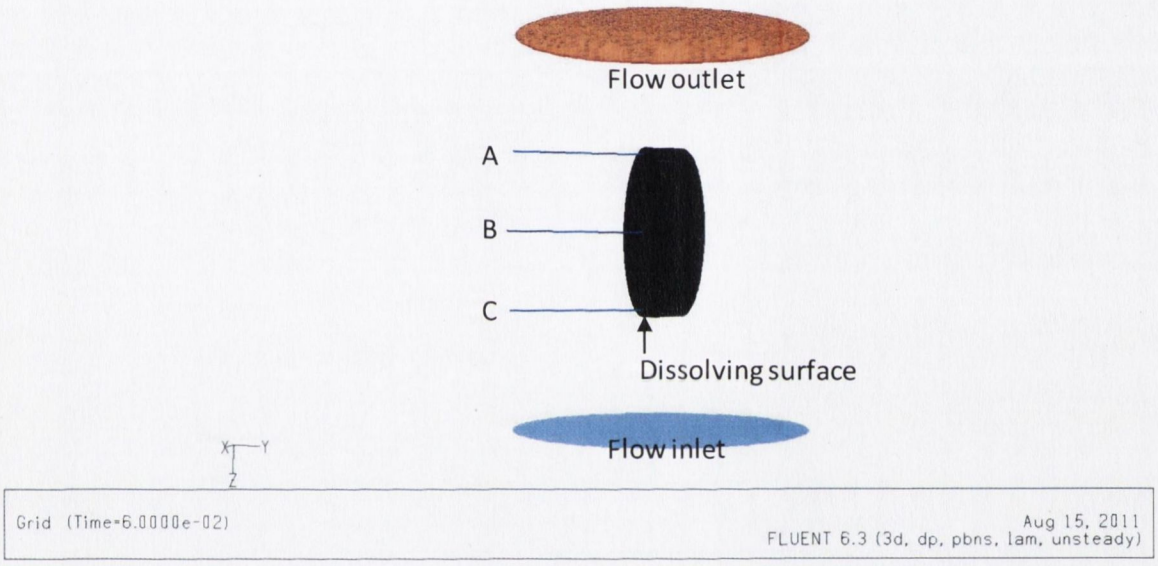


Figure 3. 6 The horizontal lines for profiling hydrodynamic data in the flow-through apparatus 3-D model: A. line A is perpendicular to the compact surface close to the upper edge; B. line B is perpendicular to the compact surface on the central position; C. line C is perpendicular to the compact surface close to the lower edge

In addition, the maximum input velocity was around 0.13s. Therefore, the velocity distribution at 0.13s was also investigated. The velocity magnitude distribution on the central line at 8 ml min^{-1} at 0.06, 0.13 and 0.21s in the flow through apparatus is shown in Figure 3.7. The shape of the velocity magnitude distribution profiles was symmetrical. The velocity magnitude distribution profile decreased sharply close to the compact surface and cell wall. At the same time, the velocity magnitude distribution profile varies little in the main stream area. This sharp decrease in velocity close to both the cell wall and the compact surface indicates that the retarding forces from the compact surface and the cell wall are similar.

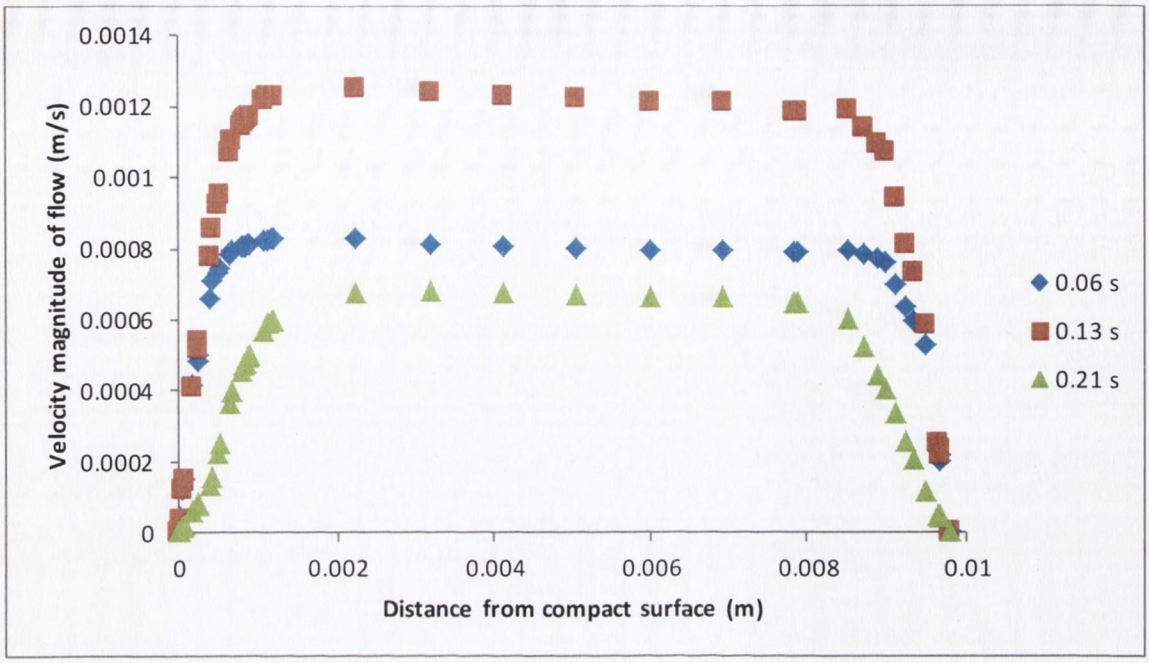


Figure 3. 7 The velocity magnitude distribution on the Line B (central line) at 8 ml min^{-1} at 0.06, 0.13 and 0.21s.

As illustrated in Figure 3.7, the bulk flow velocity distributed on Line B at 8 ml min^{-1} was slightly higher at 0.06s than that at 0.21s. As the highest input velocity appeared at 0.125s in each pulse as illustrated in Figure 3.2, a slightly higher bulk flow velocity would be expected to occur at 0.06s than at 0.21s as the inflow velocity at 0.06s is marginally closer to the peak inflow velocity. As expected, the bulk flow velocity of approximately 1.2×10^{-3} m s^{-1} was highest at 0.13s, as illustrated in Figure 3.8. Furthermore, the velocity distributions in Figure 3.7 and 3.8 demonstrated that hydrodynamic boundary is estimated to be approximately 1 mm from the compact surface, for example bulk flow velocity is reached at this point. The bulk flow velocity at 16 ml min^{-1} was nearly twice of that at 8 ml min^{-1}, and the bulk flow velocity at 43 ml min^{-1} was nearly 5 times of that at 8 ml min^{-1}. This indicated that the bulk flow velocities were approximately proportional to the input flow rates.

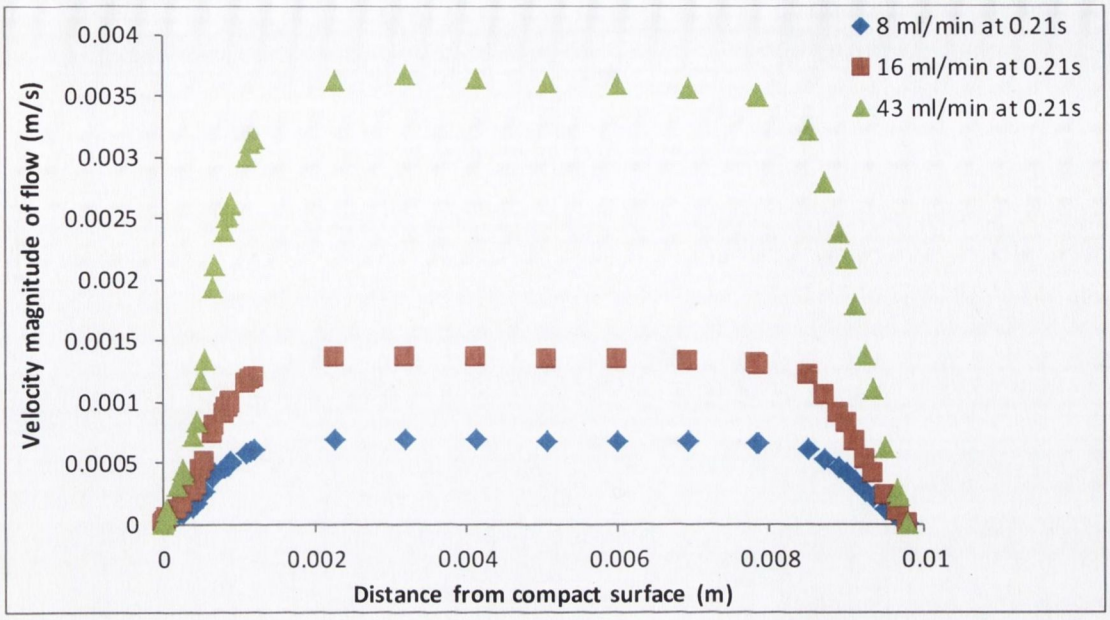


Figure 3. 8 The simulated velocity magnitude distribution on the Line B (central line) at 0.21s at 8, 16 and 43 ml min^{-1}

3.3.3 Pressure distribution in the flow-through cell

As an adverse pressure gradient has been shown to result in boundary separation (Kakhi 2009; D'Arcy, Liu et al. 2010), the effects of pressure gradient at different flow rates on boundary separation and flow reversal were investigated.

Static pressure in a fluid refers to the pressure of a fluid at a nominated depth in the fluid. Although the gauge pressure was used in a previously published report on hydrodynamics in the flow-through apparatus (Kakhi 2009), static pressure was investigated in the current work. Gauge pressure is equal to the static pressure plus dynamic pressure. Dynamic pressure can be neglected in the current work compared to static pressure. As velocity and dynamic pressure have a similar distribution as illustrated in Figure 3.9 A and B. The dynamic pressure ranged from 0- 9.62×10^{-4} Pascal which was much lower than the static pressure of -0.10-0.176 Pascal at 8 ml min^{-1} illustrated in Figure 3.9.

Therefore, compared to the static pressure, the dynamic pressure could be neglected. The total pressure was nearly equal to the static pressure. Thus, the following discussion is based on the static pressure.

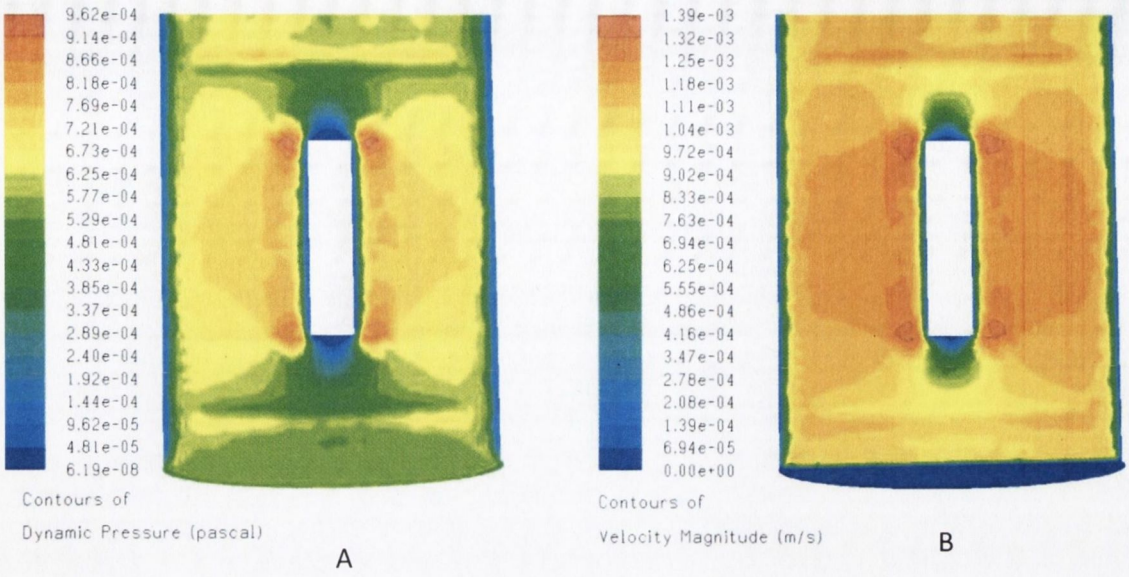


Figure 3. 9 The simulated dynamic pressure and velocity magnitude distribution at 0.13s at 8 ml min^{-1}. A. Dynamic pressure distribution (Pascal), B Velocity magnitude distribution (ms^{-1}).

Contours of static pressure at flow rates of 8, 16 and 43 ml min^{-1} are shown in Figure 3.10, Fig 3.11 and Fig 3.12, respectively. At 0.06s, the static pressure is higher at the bottom of the cell and the direction of the pressure gradient is the same at the different flow rates. At all flow rates at 0.20s, however, as the first half pulse is almost finished, the static pressure is higher at the top of the cell and the static pressure close to bottom has changed to negative pressure. Thus the pressure gradient was opposite to the direction of bulk flow, and is therefore described as an adverse pressure gradient, as previously illustrated in the same cell at 16 ml min^{-1} (Kakhi 2009; Kakhi 2009; D'Arcy, Liu et al. 2010). Therefore, boundary separation would be expected at all flow rates at 0.20s followed by flow reversal. In the work presented by Kakhi (2009), boundary separation occurred at 0.1875s in the flow-through apparatus at 16 ml min^{-1} (Kakhi 2009). The input flow was in the decreasing section of the semi-sinusoidal inflow curve. The adverse pressure gradient from -1.45 to zero Pascal at 16 ml min^{-1} (Kakhi 2009) was opposite to the velocity gradient, and the flow in the hydrodynamic boundary cannot overcome the negative pressure "barrier", due to the strong friction forces on the compact surface (Kakhi 2009). Following this, flow reversal could occur on the compact surface, and consequently, the boundary layer thickness grows rapidly. The boundary layer separation was first observed at 0.20s in the current study, while the flow was in the decreasing part of

the semi-sinusoidal inflow curve, similar to the results presented by Kakhi 2009. The simulated static pressure range at 16 ml was from -1.13 to zero Pa. As the input flow velocity at 0.20s would be close to that at 0.1875s, the simulated adverse pressure gradient was comparable to the reported value of range from zero to -1.45 Pascal (Kakhi 2009). The boundary separation at 8, 16 and 43 ml min^{-1} occurred at 0.20s, even though the adverse pressure range of -0.01 to -0.196, -0.01 to -1.13 and -0.01 to -1.87 Pascal are quite different at 8, 16 and 43 ml min^{-1}, respectively. Therefore it can be considered that the change in adverse pressure ranges at different flow rates did not affect the boundary separation time point.

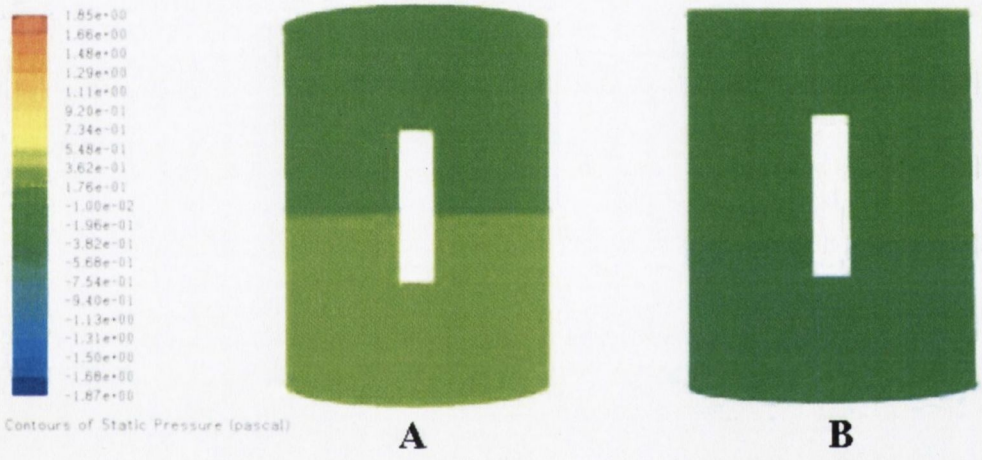


Figure 3. 10 Simulated contours of static pressure at 8 ml min^{-1} at: A. 0.06s; B. 0.20s.

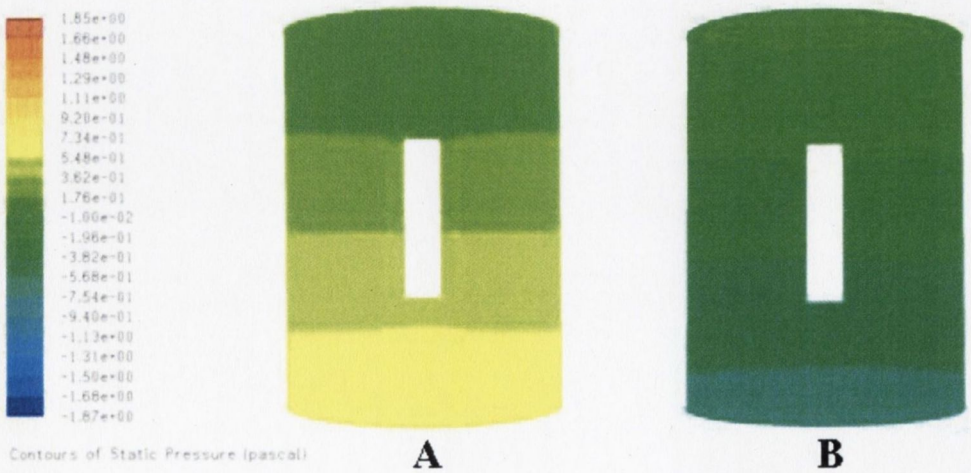


Figure 3. 11 Simulated contours of static pressure at 16 ml min^{-1} at: A. 0.06s; B. 0.20s.

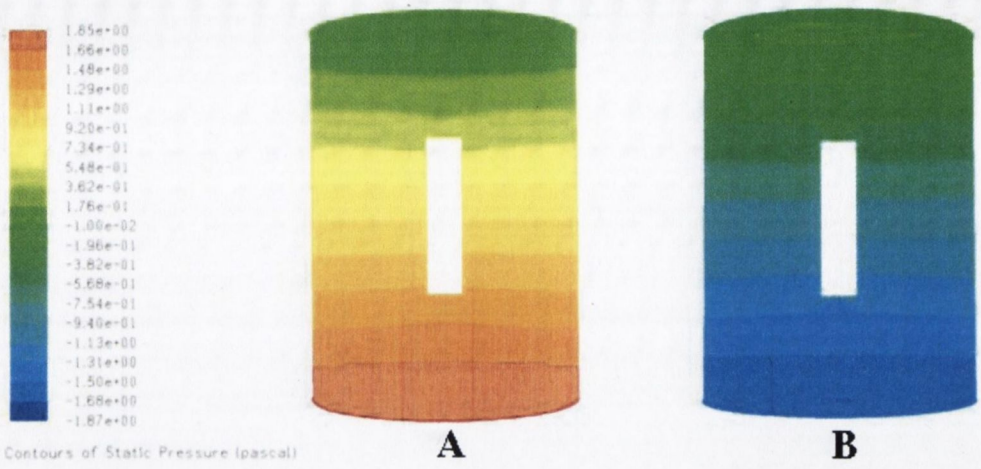


Figure 3. 12 Simulated contours of static pressure at 43 ml min^{-1} at: A. 0.06s; B. 0.20s.

3.3.4 Wall shear stress and shear rate distribution on the compact surface at different flow rates.

It has been established from section 3.2 that the velocity in the cell does increase with increasing flow rate, however the local velocity near the compact surface varies over the course of the pulse. This variation has been shown to be affected by the pulsing inflow and by the altered hydrodynamics following flow reversal, produced by the adverse pressure gradient present in the cell at 0.20s at all flow rates. Nevertheless, as the dissolution rate did not increase with increasing flow rate, wall shear stress and shear rates were investigated to interpret the effect of flow rate on dissolution rate.

The wall shear stress was determined by the following Equation 3.1.

$$\tau_w = \mu(\frac{\partial V}{\partial y})_{y=0}$$

Equation 3. 1

τ_w: shear stress

The wall shear stress is zero at the boundary separation point as the velocity gradient perpendicular to the wall vanishes at the wall (Schlichting and Gersten 2000).

3.3.4.1 Wall shear stress distribution

The simulated wall shear stress distribution on the compact surface is illustrated in this section. The contours of wall shear stress at 8, 16 and 43 ml min^{-1} at 0.06s and 0.20s were as shown in Figures 3.13, 3.14 and 3.15, respectively. The maximum shear stresses at 0.06s are estimated to be 7.50×10^{-3}, 1.25×10^{-2} and 2.50×10^{-2} Pascal at 8, 16 and 43 ml min^{-1}, respectively. Conversely, the shear stresses over most of the compact surface were zero at 8 and 16 ml min^{-1} at 0.20s. However the wall shear stress ranged from 3.75×10^{-3} to 7.50×10^{-3} Pascal at 43 ml min^{-1} which was not in agreement with the concept that the wall shear stress is zero at boundary layer separation. Compare shear rate at 0.2s at 43 ml min^{-1} with 0.06s at 8 ml min^{-1}, although similar maximum shear rate, majority of surface is at lower shear stress at 43 ml min^{-1}, 0.2s. Further investigation of the results from the 43 ml min^{-1} simulation showed that the surface shear stress was actually marginally lower at 0.19s than 0.2s, but boundary separation had not occurred across the surface at 0.19s. The presence of shear stress at 43 ml min^{-1} suggested that unsteady boundary separation occurred at 43 ml min^{-1}. When unsteady boundary separation occurs, the point of vanishing wall shear stress does not coincide with separation (Gad-el-Hak 2000).

The wall shear stress at all flow rates in the flow-through apparatus was much higher at 0.06s than 0.20s. On the other hand, the velocity magnitude ranges of 1.0×10^{-4}-1.3×10^{-3}, 1.0×10^{-4}-2.0×10^{-3} and 4.0×10^{-4}-5.2×10^{-3} m s^{-1} at 8, 16 and 43 ml min^{-1}, respectively at 0.06s were similar to those of 0-1.1×10^{-3}, 0-$1.8\times10^{-3}$and 0-4.8×10^{-3}m s^{-1} at 8, 16 and 43 ml min^{-1}, respectively at 0.2s.

A zero wall shear stress was simulated at 0.1875s (the point of boundary separation) on the compact surface (Kakhi 2009). The simulated wall shear stress at 0.20s at 16 ml min^{-1} in the current study was also zero at the point of boundary separation, further indicating that the current simulation was comparable to the previously reported simulation (Kakhi 2009) , and supporting the use of the same simulation technique to assess hydrodynamics at the other flow rates investigated in the current work (8 and 43 ml min^{-1}).

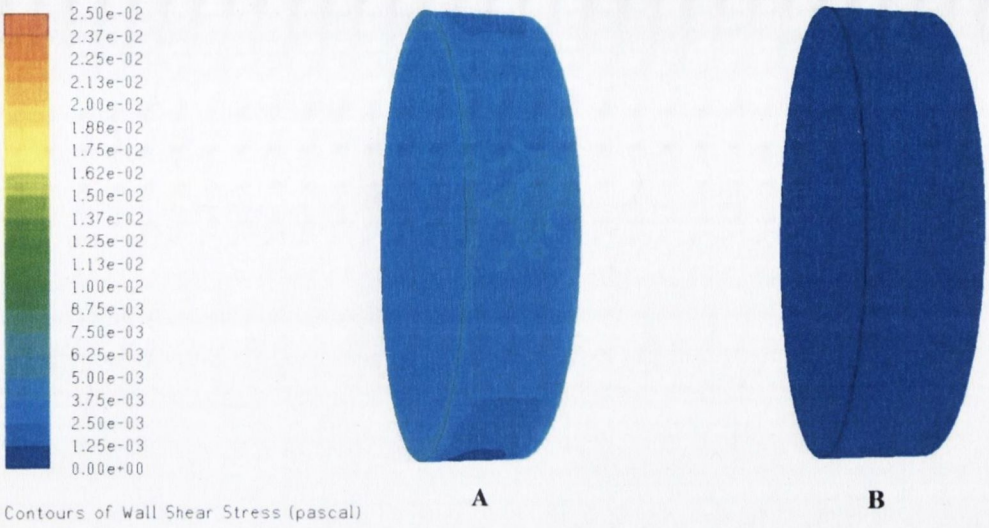


Figure 3. 13 The simulated contours of wall shear stress on the compact surface at 8ml min^{-1} in the flow-through apparatus at A: 0.06s, B:0.20s.

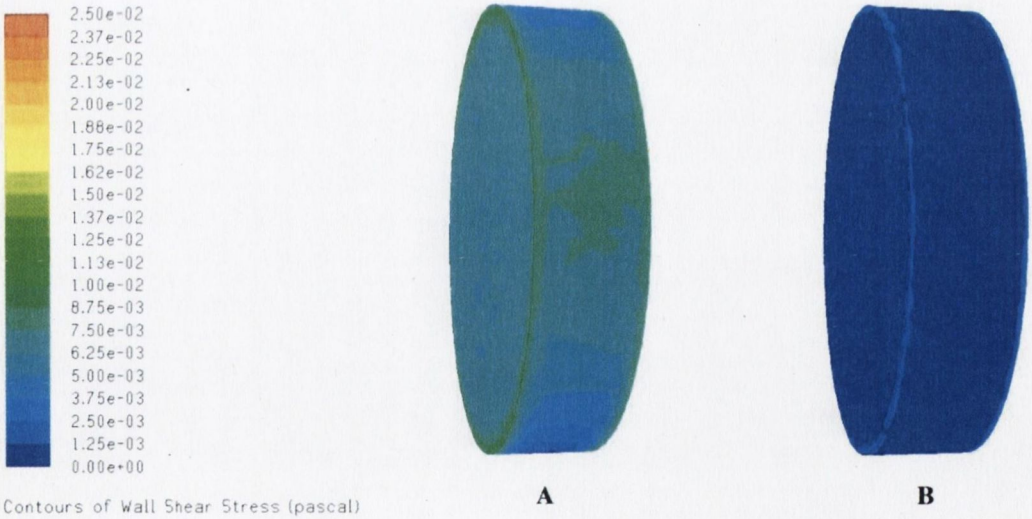


Figure 3. 14 The simulated contours of wall shear stress on the compact surface at 16ml min^{-1} in the flow-through apparatus at A: 0.06s, B:0.20s.

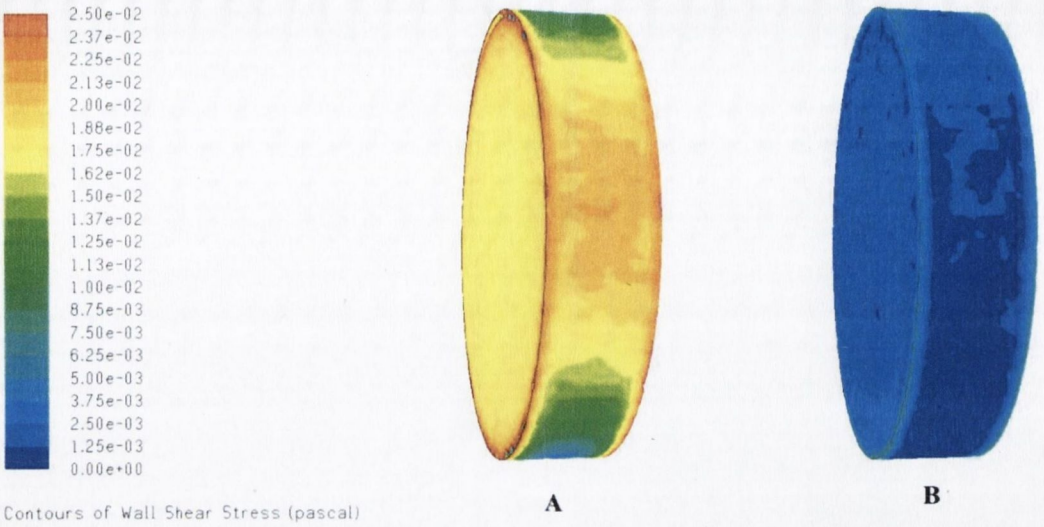


Figure 3. 15 The simulated contours of wall shear stress on the compact surface at 43 ml min^{-1} in the flow-through apparatus at A: 0.06s, B:0.20s.

The simulated shear stress demonstrated a higher shear stress profile on the edge of the compacts at different flow rates in the flow-through apparatus than in the more central areas of the surfaces, suggesting that the parts of compacts may dissolve faster than the other parts over time.

The notable difference between shear stresses on the compact surface at 0.06s and 0.20s, despite similar velocities in the region, suggests that shear stress may be a factor influencing the dissolution rate. Following from this, shear rate distribution in the region of the dissolving surface was investigated.

3.3.4.2 Analysis of shear rate distribution

The shear rate (α) was defined by equation 3.2. The dissolution rate can be considered to be determined by liquid velocity and concentration gradient (Nelson and Shah 1975). As the liquid velocity is associated with shear rate, the shear rate can affect the dissolution rate. Thus, the shear rate in the radial direction was investigated in the current study, as flow was primarily in the axial direction.

$$\alpha = \frac{dV_z}{dY}$$

Equation 3. 2

dV_z: differential of the fluid velocity in the radial direction;

dY: differential of distance between two mesh points in the radial direction from the compact surface

The maximum shear rates were determined from the lines illustrated in Figure 3.6, from the point closest to the compact surface to the cell wall. The shear rate distribution on Line B at 0.06, 0.13 and 0.21s are illustrated in Figure 3.16. In addition, the shear rates of the bulk flow were zero, as the difference in bulk flow velocity is zero, as illustrated in Figure 3.17.

The shear rates distributed on Line A, B and C demonstrated a similar profile at 0.06s and 0.13s, indicating that the direction of flow at 0.06 and 0.13s was similar. The increase in shear rate at 0.13 s and at higher flow rates, moving away from the compact surface, illustrates the increase in velocity gradient from the compact surface to the bulk. The decreasing shear rate approaching the bulk illustrates the decreasing velocity gradient, similar to a flatter flow profile, on approaching the mainstream velocity. Considering the boundary separation at 0.21s, the flow direction in the hydrodynamic boundary at 0.21s was different to that at 0.06 and 0.13s. As there was a negative velocity region from 0 to 1.74×10^{-4}m close to the compact surface at 0.21s, this velocity decreased from 0 to maximum negative value of -1.94×10^{-5} m s^{-1} and then increased to 1.69×10^{-5} m s^{-1}. Thus the shear rate at 0.21s begun from the negative value.

The change from negative to positive shear rate close to the compact surface at 0.21 s reflects the point at which the velocity direction changes from negative to positive. Similar trends at 0.21s were predicted at 16 and 43 ml min^{-1} (Figure 3.17).

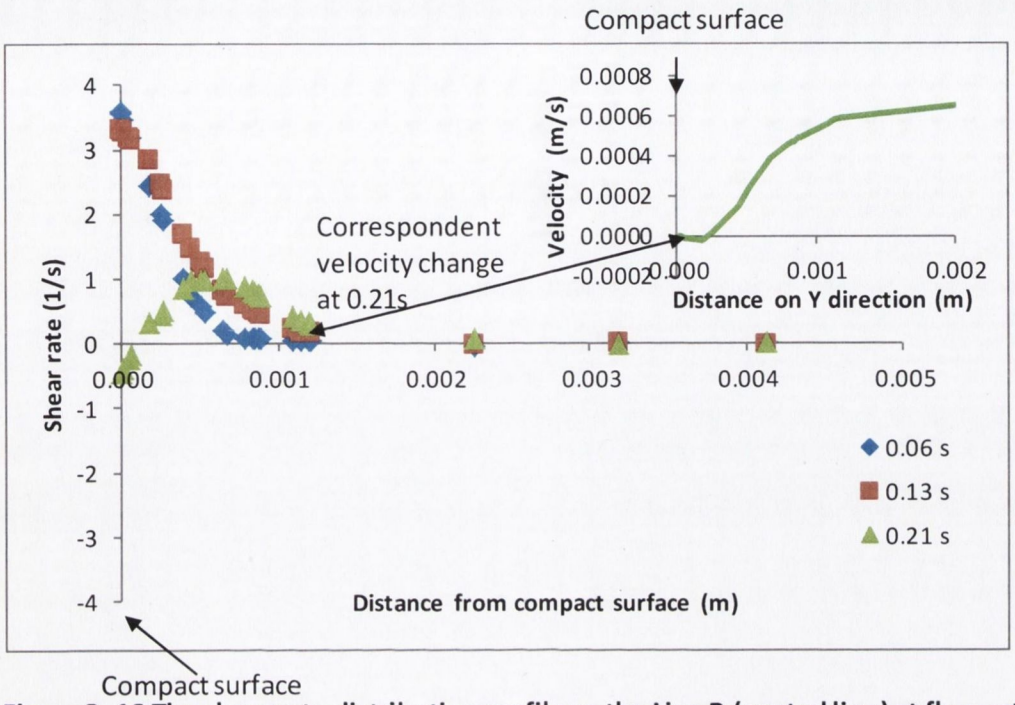


Figure 3. 16 The shear rate distribution profile on the Line B (central line) at flow rate 8 ml min^{-1} at 0.06, 0.13 and 0.21s. Inset image velocity distribution plotted against distance in Y direction at 0.21s.

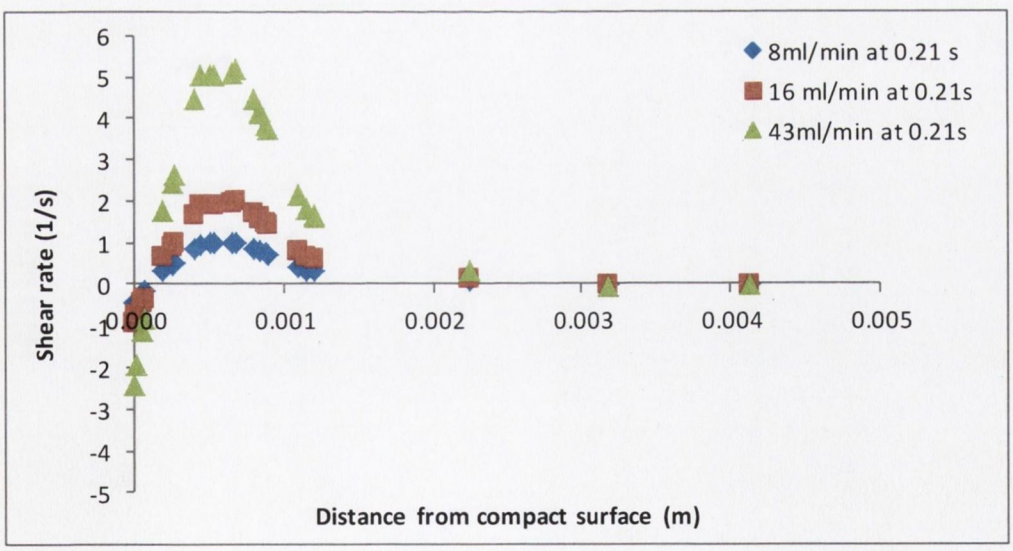


Figure 3. 17 The shear rate distributed on the Line B (central line) at 0.21 s at 8, 16 and 43 ml min^{-1}.

3.3.4.3 Shear rate at the compact surface

As the distance of the closest mesh point to the compact surface is extremely small (1.40×10^{-11}m), the shear rate at this point was taken as the surface shear rate. Furthermore, compact surface shear rate as calculated by the Fluent™ software, is integrated from the velocities of X, Y and Z direction rather than from the main stream axial direction.

The shear rates on the compact surface were as illustrated in Figure 3.18, a negative shear rate was observed after approximately 0.2s. This was evidence of the boundary separation at 0.2s at different flow rates. At 0.2s, the velocity difference on the compact surface was zero due to the boundary separation, thus the shear rate approached zero. After 0.2s, reversed (downward) flow was the dominant flow type in the hydrodynamic boundary. Therefore, the shear rates were negative (as the boundary condition defines zero velocity on the surface, the velocity differentials calculated must reflect either overall positive or negative flow). The negative shear rate distribution from 0.2 to 0.5s indicated that the flow direction at the compact surface was opposite to that from 0 to 0.2s. As there is no input flow during the second half of the pulse from 0.25 to 0.5s, the shear rate was close to zero at 0.5s. 0.25s was the transit point of "semi-sinusoidal" section of the inlet flow profile and the section with zero inflow (Figure 3.2). In addition, the maximum shear rate occurred of around 0.09s which was earlier than maximum velocity occurring at 0.13s of "semi-sinusoidal flow" part.

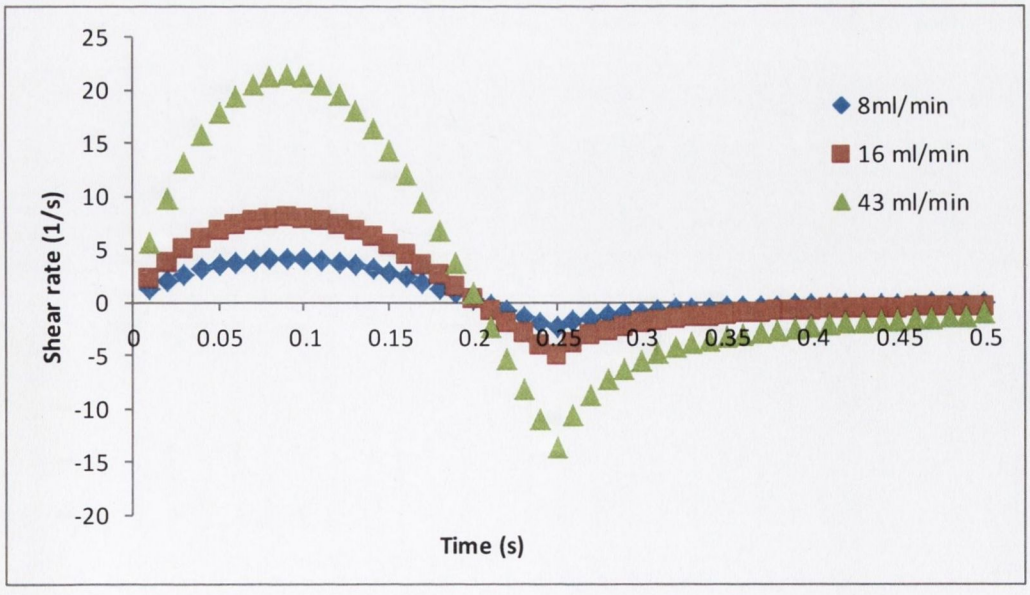


Figure 3. 18 The simulated shear rate on the compact surface over 1 pulse.

3.3.5 Relationship between observed hydrodynamic phenomena and observed dissolution rate.

The wall shear stress increased with increasing flow rate at 0.06s, but was close to zero at 0.2s despite similar fluid velocities being present in the cell at this time point, resulting from a similar inflow velocity at both time points.

Despite shear rates on the compact surface varying at each flow rate from 0 to 0.20s (Figure 3.18), as the cubic roots of shear rates are proportional to dissolution rate (Nelson and Shah 1975; Nelson and Shah 1977; Nelson and Shah 1987; Shah and Nelson 1987), this variation in shear rates may not notably affect the dissolution rates at different flow rates from 0 to 0.20s at each pulse. The shear rate at 0.21s is obviously lower than that at 0.13 and 0.06s at each flow rate, on the upper, central and lower lines (Figure 3.16).

The lack of correlation of input flow velocity and wall shear stress distribution at 0.06 and 0.20s indicated flow reversal resulting from boundary separation could apparently affect the wall shear stress distribution on the compact surface. The downward flow reversal counteracted upward flow which may increase the thickness of the diffusion film. Thus the dissolution rate may be lower than that before boundary separation. The similar wall shear stresses at 8, 16 and 43 ml min^{-1} at 0.20s suggest a similar effect from each flow rate on the diffusion boundary at this time point. Consequently, the dissolution rate may be similar from 0.20 to 0.25s in each pulse after boundary separation at different flow rates in the 22.6 mm cell.

As the input flow profile was divided into two parts, it was obvious that the dissolution rate in the second half of the pulse (0.25-0.5s) without flow input would not be the same as that of the first half of the pulse (0-0.25s). The dissolution rate in the second half of the pulse without forced convection may be similar at different flow rates, as the dissolution process is controlled by the natural convection.

Overall, the boundary separation from 0.20 to 0.25s obviously reduced the dissolution rate and had a similar effect at different flow rates. Difference in shear rate not adequate to produce a significant difference in cubic root of shear rate from 0 to 0.19s on dissolution rate, along with natural convection controlled dissolution rate from 0.26 to 0.5s combined to contribute to dissolution rates not varying with the flow rates investigated. Due to the

limitation of 3D simulation at different flow rates without enabling species transfer, the current simulation may not accurately simulate the effect of the density gradient from the dissolving species on the thickness of hydrodynamic boundary in this low velocity flow environment. Thus further investigation is required to study the density and concentration gradient effect on the dissolution rate. This will be explored further in chapter 4.

3.4 Prediction of dissolution rate under different flow rates in the flow-through apparatus.

3.4.1 Physicochemical property

The solubility and diffusion coefficients are used in the convection-diffusion model (Equation 1.18) used to predict dissolution rate in flow-through apparatus.

3.4.1.1 Solubility of BA and LM

The solubility of LM was measured in 0.1 M HCl at 37°C, and was determined to be 219.64 ± 22.2 g L^{-1}. The saturated solubility of BA in 0.1M HCl was taken to be 4.56 g L^{-1} (Ramtoola and Corrigan 1987).

3.4.1.2 Diffusion coefficient of BA and LM

The diffusion coefficients of 0.1M KCl and 0.01 M BA at 30°C were used to determine the cell constant. The diffusion of KCl and BA is shown in Figure 3.19 and 3.20, respectively. There was time for some diffusion before the first sample, and thus the value of the first sample point was not zero. The observed cell constant based on KCl was 94.23 +/- 9.74 cm. The cell constant was calculated by BA, using this previously published D value of 1.113×10^{-5} cm^2s^{-1} (Goldberg and Higuchi 1968), as 92.35 +/-0.44 cm, which is not significantly different to the experimental value from KCl, validating the method used to measure the diffusion coefficient. Additionally, The calculated D value of $(1.087+/-0.005)\times10^{-5}$ cm^2s^{-1} was similar to the reported value of 1.113×10^{-5} cm^2s^{-1}.

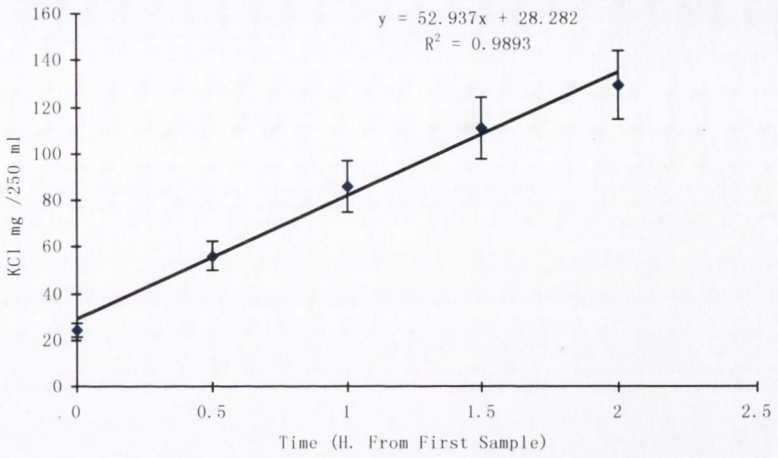


Figure 3. 19 Diffusion of 0.1 M KCL with the apparatus at 30 °C, cell constant equal to 94.23 +/- 9.74 cm.

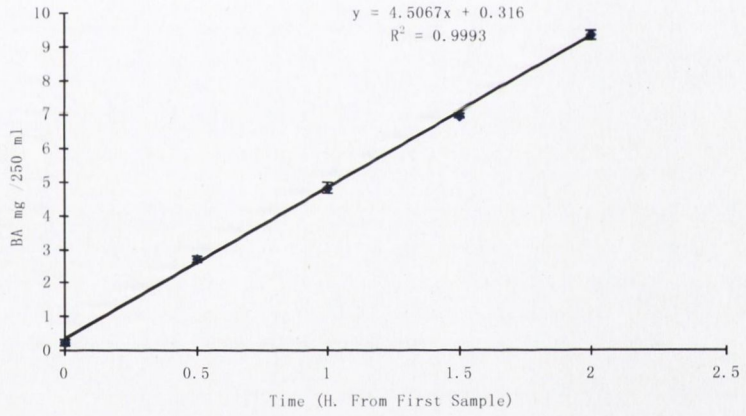


Figure 3. 20 Diffusion of 0.01 M BA at 30 °C, cell constant equal to 92.35 +/-0.44 cm

The diffusion of LM in saturated BA solution at 37 °C is shown in Figure 3.21, with a calculated D value of $3.189\times10^{-6} \pm 0.815\times10^{-6}$ cm^2s^{-1} (Table 3.3), which was comparable with the reported value of 5-5.5x 10^{-6} cm^2s^{-1}, for LM in water at 30°C (Venancio and Teixeira 1997). The calculated D value from the line fitting from 1 to 2 hours was $4.504\times10^{-6} \pm 0.241\times10^{-6}$, which is close to the reported value (Venancio and Teixeira 1997). Although the result in Figure 3.21 was variable over time, the reason for the variability was unclear, therefore a line fitted through all points was used as an approximation of the D value of $3.189\times10^{-6} \pm 0.815\times10^{-6}$

cm^2s^{-1}. The D value of BA at 37 °C was taken to be 1.236×10^{-5} cm^2s^{-1} (Ramtoola and Corrigan 1987).

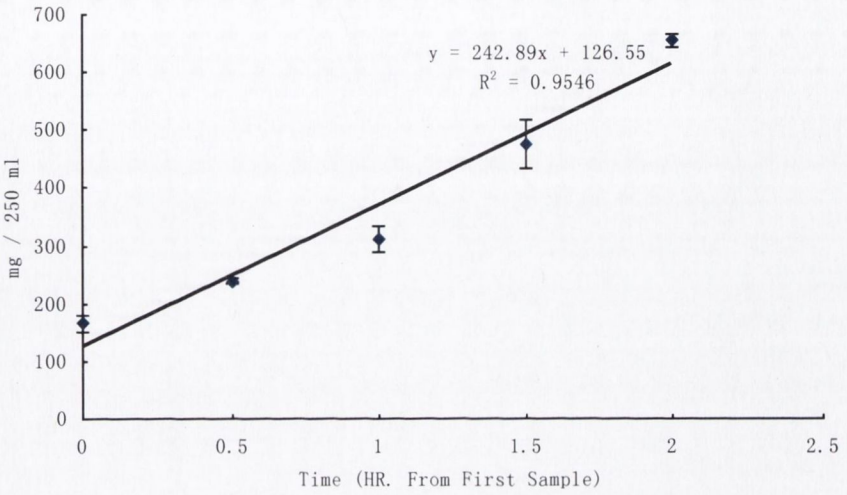


Figure 3. 21 Diffusion of LM in saturated BA solution at 37 °C.

Table 3. 3 Diffusion coefficient of BA, LM and LM in saturated BA solution

Solute/Solvent system	Diffusion coefficient(cm^2s^{-1})
LM in saturated BA solution at 37 °C	$3.189\times10^{-6} \pm 0.815\times10^{-6}$
BA at 37 °C from reference (Ramtoola and Corrigan 1987)	1.236×10^{-5}
LM at 30 °C from reference (Venancio and Teixeira 1997)	$5\text{-}5.5\times 10^{-6}$

3.4.2 Prediction of dissolution rate

The concentration gradient is the force promoting the drug diffusion and therefore the dissolution rate. The effective diffusion boundary theory assumes a saturated solution at the compact surface (Equation 1.8), when the sink condition is achieved. The shear rate could affect the concentration gradient, in that a higher shear rate could shorten the effective diffusion boundary layer

The shear rate in the original published equation (Equation 1.17), which related shear rate and dissolution rate, was estimated using the flow rate and cell dimension parameters

(Nelson and Shah 1975; Nelson and Shah 1977; Nelson and Shah 1987; Shah and Nelson 1987). The original prediction was based on a constant flow rate in one direction. However, the input flow rate in the flow-through apparatus is a pulsing flow with each 0.5s pulse divided into 50 time steps in the current CFD model, therefore it was assumed that the flow at each time step was constant, and the dissolution rate at each time step was calculated. Furthermore, as the flow reversal occurred in the flow-through apparatus, the fluid flow was not in one direction over the whole pulse.

Based on the above differences between velocity profile in the first half pulse and the second half pulse of the pulse, two aspects were considered in the current study. The first aspect is that the use of magnitude of shear rate predicts the dissolution rate. The second aspect assumes that the part of pulse can be predicted by a natural convection, as part of pulse has a low or zero velocity.

According to the shear rate distribution in Figure 3.18, the shear rate was affected by the residual flow, after the point of zero inflow (0.25s), with this effect decreasing with time from 0.25 to 0.5s. Thus the shear rates from 0.25 to 0.5s were investigated to predict dissolution rate and the maximum shear rates on the compact surface were used to predict the dissolution rate over the whole pulse (including both the zero inflow velocity section).

On the other hand, as there is no inflow from 0.26 to 0.5s of each pulse, natural convection may be the main flow type in the cell, despite residual flow affecting the hydrodynamics in the cell (Figure 3.18). In addition, the assumption used in Equation 3.5, is that the fluid flow is only in the Z direction and there are no convective flows on X and Y directions (Nelson and Shah 1975). However, the simulated velocity vectors, as illustrated in Figure 3.22, demonstrated a disordered distribution at 0.31s without forced convection, despite the shear rate value at 0.31s being similar to that at 0.21s (Figure 3.18), suggesting that Equation 3.5 may not be suitable from 0.26 to 0.5 s of each pulse. Thus, a method combining a natural convection model (from 0.26 to 0.5 s) (Equation 3.4) and the convective-diffusion model (from 0 to 0.25 s) (Equation 3.5) was used to predict the dissolution rate. This method will be termed the forced-natural convection combination (FNCC) method (Equation 3.7).

The calculated shear rate values (i.e. including positive/negative sign) arising from upward flow or flow reversal are shown in Figure 3.22. However, the calculated shear rate based on

single estimates from unidirectional flow was used to predict the dissolution rate in previous studies(Shah and Nelson 1975; Nelson and Shah 1987; Shah and Nelson 1987). Therefore, there was no situation of shear rate changing from positive to negative with changing flow direction. Thus, both calculated shear rate values and absolute shear rate values (i.e. value of shear rate excluding positive/negative sign –the positive modulus of the shear rate) were investigated to predict the dissolution rate in the current study.

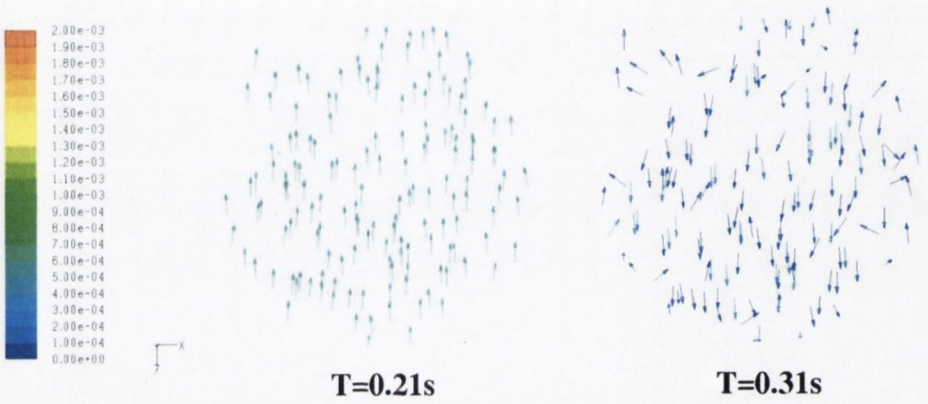


Figure 3. 22 Flow direction on the surface 1mm from the compact surface at 8 ml min^{-1}.

Equation 3.3 and 3.4 were used to predict dissolution rate in the free convection system.

$N_u = 0.673\left(\frac{g L_w^3 \Delta\rho}{D v \rho_s}\right)^{\frac{1}{4}}$ (Radziemaska and Lewandowski 2001)

Equation 3. 3

$$R_{natual} = NuC_s\frac{D}{L_w}$$

Equation 3. 4

Equation 3.5 was used to predict dissolution rate in the forced convection (Nelson and Shah 1975; Nelson and Shah 1977).

$$R_{forced} = \frac{4.32 \cdot D^{\frac{2}{3}} C_s r^{\frac{5}{3}}}{\pi r^2}\sum_{i=1}^{n}\alpha_i^{\frac{1}{3}}$$

Equation 3. 5

When n was equal to 50, the equation 3.5 could be used to predict dissolution rate over the whole pulse.

$$R_{whole} = \frac{4.32 \cdot D^{\frac{2}{3}} C_S r^{\frac{5}{3}}}{\pi r^2} \sum_{i=1}^{50} \alpha_i^{\frac{1}{3}}$$ (convection-diffusion over the whole pulse);

Equation 3. 6

When n was equal to 25, the combination of equation 3.4 and 3.5 could be used to predict dissolution rate using the FNCC method as follows:

$$R_{FNCC} = \frac{4.32 D^{\frac{2}{3}} C_S r^{\frac{5}{3}}}{\pi r^2} \sum_{i=1}^{25} \alpha_i^{\frac{1}{3}} + 0.5 Nu C_S \frac{D}{L_w}$$ (forced-natural convection combination);

Equation 3. 7

Where Nu (Nusselt number) is the ratio of convective to conductive heat transfer across the boundary; α is shear rate; L_w is diameter of compact; g is acceleration due to gravity; $\Delta\rho$ is the difference between the density of the saturated solution of the solute in the solvent and the density of the pure dissolution medium (bulk density); ρ_s is solution density; R_{forced} is dissolution rate per unit surface area per second in the forced convection; R_{whole} is dissolution rate per unit surface area per second over the whole pulse and R_{FNCC} is dissolution rate per unit surface area per second of forced-natural convection combination.

The predications based on calculated shear rate values over the whole pulse at different flow rates notably underestimated the dissolution rate (Table 3.4), since the density gradient effect on hydrodynamics was not presented in the current model, which may reduce the overall dissolution rate. Moreover, cubic roots magnified the shear rates value when the shear rates were between 0 and 1. Although the total positive shear rates were higher than that of the total negative shear rates, the predicted dissolution rates based on the calculated shear rate values were negative (Table 3.4).

Thus, the predicted dissolution rate in the free convection system was used to substitute the dissolution rates based on the simulated shear rates from 0.25 to 0.5s of each pulse (FNCC method). The predicted results based on calculated shear rate values using the FNCC method demonstrated a better agreement with the observed results (Table 3.4), indicating that free convection controlled the dissolution in the second half of each pulse. Furthermore, the

calculated shear rate values can represent the effect of flow reversal on the dissolution rate under forced convection conditions in the first half of the pulse.

The prediction based on the absolute velocity ignored the effect of flow direction on the shear rate. The predicted dissolution rate of LM based on absolute shear rate values over the whole pulse at 8 ml min^{-1} was lower than the observed result. However, the predicted dissolution rate of BA based on absolute shear rate values over the whole pulse at 8 ml min^{-1} was higher than the observed result. These predictions indicated that the effect of shear rate on the dissolution is overestimated in the BA case, particularly at higher flow rates, and underestimated in the LM case. Furthermore, although the dissolution rate is predicted to increase with flow rate, the predicted results are not directly proportional to flow rates. Therefore, although the prediction overestimates the dissolution rate for BA at each flow rate, and predicts an increasing dissolution rate with flow rate, the prediction does not suggest a large increase in dissolution rate with flow rate. For example, the dissolution rate is not even predicted to double when flow rate is increased from 8 to 43 ml min^{-1}. In addition the prediction based on absolute shear rate values from the FNCC method overestimates the dissolution rate at different flow rates, compared to that based on calculated shear rates values using the FNCC method. The overestimation of the predictions is probably because the absolute shear rate values obtained from the first half of the pulse neglected the effect of flow reversal on dissolution rate.

The predicted surface shear rate may not represent the true effect of the shear rate on the changing concentration gradient, due to limitations of the hydrodynamic simulation. These limitations include standard theoretical assumptions in input flow profile (section 2.2.1.3), the effect of residual flow on consecutive pulses, and the use of equation 3.3 in a cylindrical cell, in a 3-dimensional flow-field. One approach to improve the accuracy of the simulation may be to include the effect of density gradients from the dissolving surface on local hydrodynamics.

Table 3. 4 Predicted and experimental dissolution rate of BA at 8, 16 and 43 ml min^{-1}, LM at 8 ml min^{-1} in the flow through apparatus and predicted and experimental dissolution rate of BA and LM in the free convection system.

Different methods	BA 8 ml min^{-1}	BA 16 ml min^{-1}	BA 43 ml min^{-1}	LM 8 ml min^{-1}	BA	LM
Predicted dissolution rate based on calculated shear rate values over the whole pulse (mg min^{-1} cm^{-2}) (Equation 3.6)	-1.3×10^{-3}	-1.5×10^{-3}	-4×10^{-4}	-0.028	N/A	N/A
Predicted dissolution rate based on calculated shear rate values; FNCC method (mg min^{-1} cm^{-2}) (Equation 3.7)	0.122	0.135	0.159	4.372	N/A	N/A
Predicted dissolution rate based on absolute shear rate values over the whole pulse (mg min^{-1} cm^{-2}) (Equation 3.6)	0.124	0.157	0.217	2.622	N/A	N/A
Predicted dissolution rate based on absolute shear rate values; FNCC method (mg min^{-1} cm^{-2}) (Equation 3.7)	0.148	0.168	0.205	4.921	N/A	N/A
Experimental dissolution rate (mg min^{-1} cm^{-2})	0.094+/- 0.008	0.095+/- 0.007	0.102+/- 0.003	3.240 +/- 0.680	N/A	N/A
Predicted dissolution rate in the free convection system (mg min^{-1} cm^{-2}) (Equation 3.6)	N/A	N/A	N/A	N/A	0.147	6.744

Experimental dissolution rate in the free convection system ($mg\ min^{-1}\ cm^{-2}$) (Equation 3.6)	N/A	N/A	N/A	N/A	0.123+/- 0.003	6.889+/- 1.700

3.5 Conclusion

The observed dissolution rates of a BA compact at different flow rates were not consistent with the change in flow velocity. The boundary separation points at different flow rates were associated with the adverse pressure gradient following the decrease in input flow rate during the latter part of the semi-sinusoidal input flow profile. Flow reversal resulting from boundary separation reduced the shear stress on the compact surface and counteracted the upward flow. Consequently, this effect reduced the dissolution rate of the compact. Furthermore, the variation in shear rates at the different flow rates investigated may not be adequate to notably affect the dissolution rate within 22.6 mm cell. All of these factors resulted in the similar dissolution rates being observed at different flow rates in the flow-through apparatus. CFD was successfully used to simulate fluid flow and demonstrate the change of shear rates at different flow rates affecting the dissolution rate in the flow-through apparatus. However, the relationship of concentration gradient and fluid velocity could not be accurately demonstrated in the current model, and predicted dissolution rates were inaccurate, particularly as the predictions suggested an increase in dissolution rate with flow rate. A further study using species transfer, which includes the effects of density gradients on local hydrodynamics, will be discussed in chapter 4.

Chapter 4: Hydrodynamics and species transfer in the flow-through apparatus and free convection system: investigating variation in hydrodynamics with solubility of model drug.

4.1 Introduction

Effect of hydrodynamics on the dissolution rate was investigated in the Chapter 3. However, the effect of the density gradient resulting from solubility of the dissolving compounds on the hydrodynamics was not considered in the simulated model of Chapter 3. Therefore, the aim of this chapter is to study the effect of the hydrodynamic environment, including the effect of natural convection due to density gradients, on the dissolution rate of drugs of different solubilities under low velocity conditions. The two different solubility compounds, benzoic acid (BA, slightly soluble) and lactose monohydrate (LM, freely soluble) were used as model drugs.

Previous studies using numerical models which included the effect of density gradients in a very low-velocity flow-through environment reported that the effect of gravity on natural convection increased with increasing solubility of solute (Stevens and Missel 2006). However, the effect of local hydrodynamics resulting from pulsed semi-sinusoidal flow on density gradient was not investigated. It is possible to simulate the effect of the dissolution process on the local hydrodynamic environment using a species transfer model. Species transfer does not simulate the dissolution process itself, but rather is a method by which the effect of a more dense solution (the result of the dissolution process) at the surface on the surrounding hydrodynamics can be modeled.

Hydrodynamic features present in the low velocity environment of the flow through apparatus include boundary separation at the dissolving surface, leading to flow reversal, as demonstrated in Chapter 3. This flow reversal affects the local flow velocity surrounding the compact surface and consequently affects the dissolution rate (Chapter 3).

Although boundary layer separation was evident in the hydrodynamic simulation of flow around the compact at 8 ml min^{-1} (22.6 mm diameter cell) in the flow-through apparatus. Simulation of both species transfer and hydrodynamics within the dissolution system will give a more comprehensive prediction of both velocities and concentration gradients near the dissolving surface. Such simulations, however, are computationally expensive. There is a need to determine the effect of solubility, density and forced convection on the local hydrodynamics affecting dissolution in the low velocity environment of the flow through apparatus. This will enable prioritization of computational resources for those situations

where it would be of benefit to simulate both species transfer and forced convection hydrodynamics, and those situations where it would be adequate to simulate forced convection hydrodynamics alone.

The objectives of this chapter were:

(1) to examine the effects of different hydrodynamic regimes, influenced by both forced and natural convection effects, on dissolution of a slightly and a freely soluble model compound in the dissolution apparatuses investigated;

(2) to simulate, using CFD, the interacting effects of forced convection and natural convection, introduced by local density gradients, on hydrodynamics in the flow-through apparatus and a free convection system;

(3) to provide an informed hypothesis as to why the dissolution rate produced in the free convection system is higher than that in the flow-through apparatus at a low flow rate.

(4) to assess the combination of CFD velocity data and the convection-diffusion equation derived from Nelson and Shah (Equation 3.5) to predict dissolution rate in the flow-through apparatus.

4.2 Physicochemical properties and dissolution studies

4.2.1 Measurement of particle size of BA and LM

The particle size distributions of BA, LM and milled LM are shown in Table 4.1.

Table 4. 1 Particle size distribution of BA, LM and milled LM.

	d(0.1) μm	d(0.5) μm	d(0.9) μm
BA	3.952	17.832	59.092
LM	12.701	72.432	180.839
milled LM	4.175	22.218	49.905

The particle sizes of BA and LM (not milled) are not similar to each other. Different particle sizes could significantly affect the dissolution rate as the small particle size presented large surface area (Corrigan, Healy et al. 2006). The raw LM particles were milled before making compacts in order to reduce the effect from different particle sizes. After preparation of a fine powder of lactose using the ball-mill, the particle size distribution was very similar for the BA powder and the LM powder as shown in Figure 4.1. The particle size distribution demonstrated a similar profile for LM and BA.

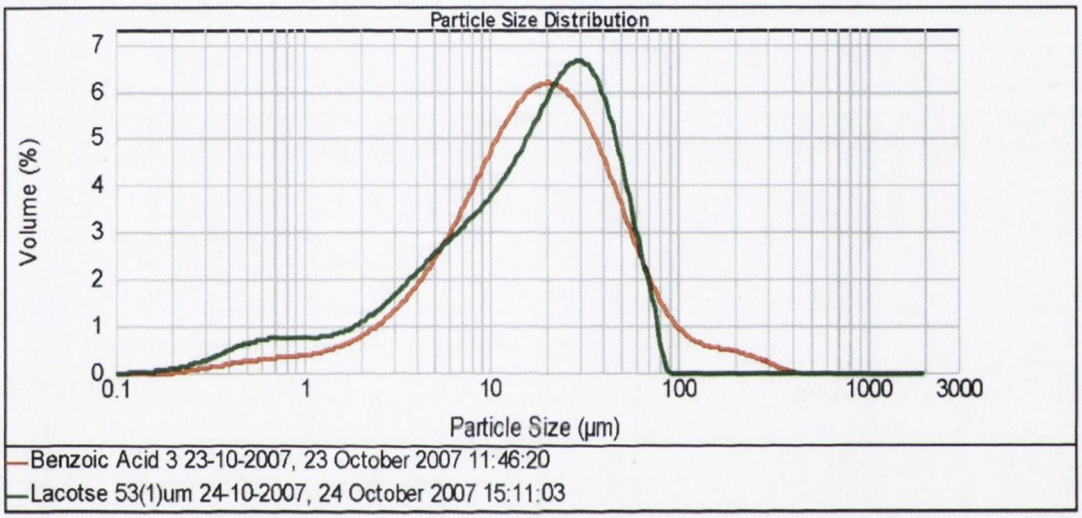


Figure 4. 1 Comparison of the BA particle size distribution and the milled LM particle size distribution.

4.2.2 Measurement of density

The densities of the saturated BA and the saturated LM solutions at 37 °C were 997.2+/-0.2 g L^{-1} and 1091.1+/-0.9 g L^{-1} respectively. In contrast, the density of the dissolution medium, 0.1M HCl, was 995.3 g L^{-1}.

4.2.3 Dissolution profile and dissolution rate

The dissolution results are shown in Table 4.2. The dissolution rate of BA was highest in the paddle apparatus, at 3.6 times that in the free convection system and 4.7 times that in the flow-through apparatus. The thickness of the effective diffusion boundary layer is calculated using the standard Nernst–Brunner equation (Equation 1.9) assuming sink conditions (C=0, Equation 4.1).

$$h_{eff} = \frac{SAC_s D}{\frac{dX}{dt}}$$

Equation 4. 1

The calculated parameter for h_{eff} illustrates that the effective diffusion boundary layer is thinner in the free convection system than in the flow through apparatus. As the effective diffusion boundary layer is proportional to the hydrodynamic boundary layer, these results suggest that the hydrodynamics in the vicinity of the dissolving surface are different in each apparatus. The thinner effective diffusion boundary layer within the same dissolution system (apparatus and geometry) is associated overall with higher local velocity values. The stronger agitation in the paddle apparatus contributed to the dissolution rate of BA in the paddle apparatus being highest overall for BA, with the smallest estimate for h in this system compared to the flow-through apparatus. Similarly, the dissolution results for LM demonstrate that the effective diffusion boundary layer was thinner, and therefore dissolution faster, in the free convection system. It is interesting to compare the effective diffusion boundary layer estimates for LM and BA. Despite being in the same dissolution apparatus at the same flow rate, the estimated h for LM is approximately 2.8 and 4.5 times less than BA in the flow-through apparatus and free convection systems respectively. These results imply that the process of LM dissolution can have a significant effect on the local hydrodynamics, in both the free convection system and in the low-velocity pulsed flow of the flow-through apparatus. This observation, together with the fact that for both the slightly soluble BA and freely soluble LM, the dissolution rate in the free convection system was higher than in the flow-through apparatus, indicates that there is a complex interaction between local hydrodynamics and natural convection in the dissolution apparatuses investigated. The local hydrodynamic environment generated by each combination of dissolution system and solute will be discussed in detail in the next section.

Table 4. 2 The dissolution rate of BA and LM (mg min^{-1} cm^{-2}), in the different dissolution apparatuses and the effective diffusion boundary layer thickness, h.

BA	G (mg min^{-1} cm^{-2}) +/- SD	h (m x 10^{6})
Free convection system	0.123 +/- 0.003	275
Flow-through apparatus (USP 4)	0.094 +/- 0.008	360
Paddle apparatus (USP 2)	0.441+/-0.036	76
LM	G (mg min^{-1} cm^{-2}) +/- SD	h (m x 10^{6})
The free convection system	6.89 +/- 1.69	61
The flow-through apparatus	3.24 +/- 0.68	130
Paddle apparatus (USP 2)	8.52 +/- 0.40	49

4.3 Comparison of 3-D simulation model to 2-D simulation in the region of interest.

Contours of velocity magnitude on a defined plane, alongside contours of velocity magnitude from the 2D model, from steady state simulations using the species transfer model of BA in each case, are shown in the Figure 4.2. The CFD simulation generated a similar profile of velocity magnitude from both the 3-D model and the 2-D model. The contours of velocity magnitude around the left and right side of the compact of the 3-D simulation model, displayed in Figure 4.2 (a), show regions of high velocity of approximately 1.5×10^{-3} m s^{-1}. This high velocity area was at the same location in each simulation, at either side of the compact on the plane displayed. The 2-D simulation also showed a high velocity magnitude of approximately 1.5×10^{-3} m s^{-1} in the same region. As the mesh of the 3-D model is much larger and more complex than in the 2-D model, it is considerably more expensive in terms of computational resources. From a quantitative and qualitative comparison of the simulated results, such as those shown in Figure 4.2, it can be considered that the 2-D simulated model is sufficient for the objectives of the current research. All of the results presented in the following sections are from 2-D simulations.

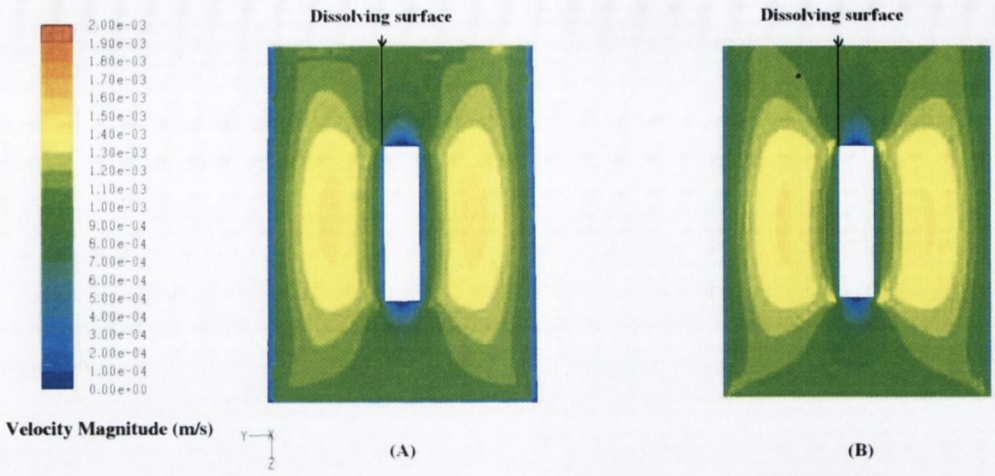
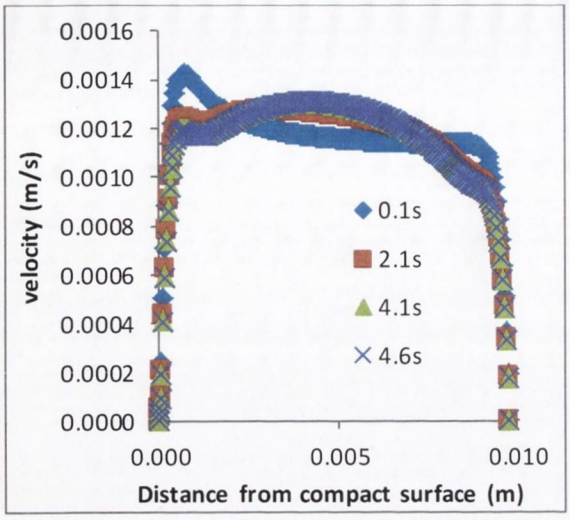


Figure 4. 2 Contours of velocity magnitude generated by Fluent™ of BA dissolution at 4.13s within 8 ml min^{-1} A. 3D simulated model B. 2D simulated model

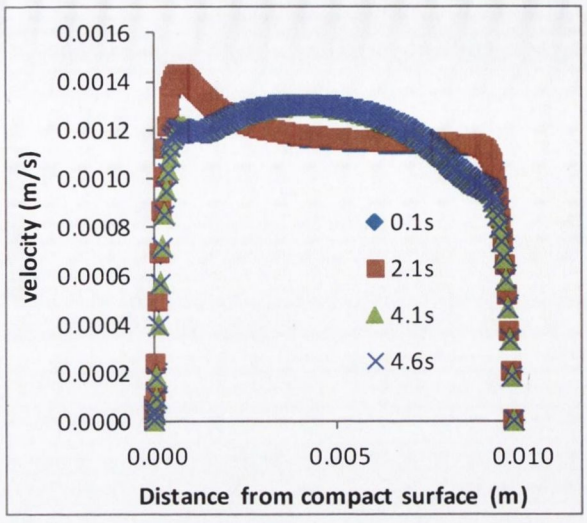
4.4 Hydrodynamic analysis of simulated 2-D hydrodynamic models including LM and BA species transfer in the flow-through apparatus and free convection system

4.4.1 Steady state of the BA and LM species transfer model in the flow-through apparatus and free convection system

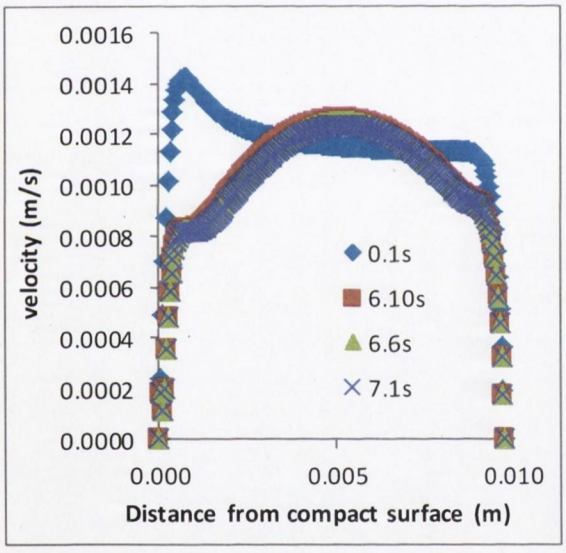
In the current work, simulations are presented from the initial state and steady state. The initial state is given by the simulation of the first pulse, where it is considered that species transfer will not have had the opportunity to significantly affect the local hydrodynamics. The method of judgment of steady state is outlined in section 2.2.1.2. The model simulating species transfer of BA in the flow through apparatus reached steady state during the 9th pulse commencing at 4.01 s (Figure 4.3 A and B), and that of LM during the 13th pulse commencing at 6.01s (Figure 4.3 C and D). In the free convection system, steady state was reached after 8.5 seconds for the simulation of BA species transfer (Figure 4.4 A and B), and after 6.5 seconds for the simulation of LM species transfer (Figure 4.4 C and D).



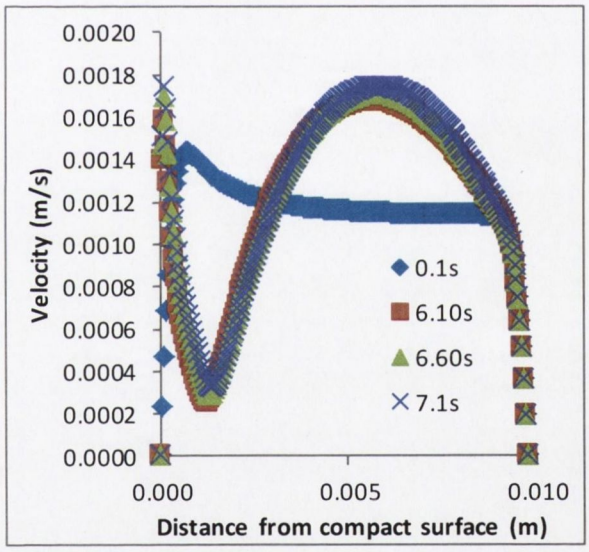
A



B

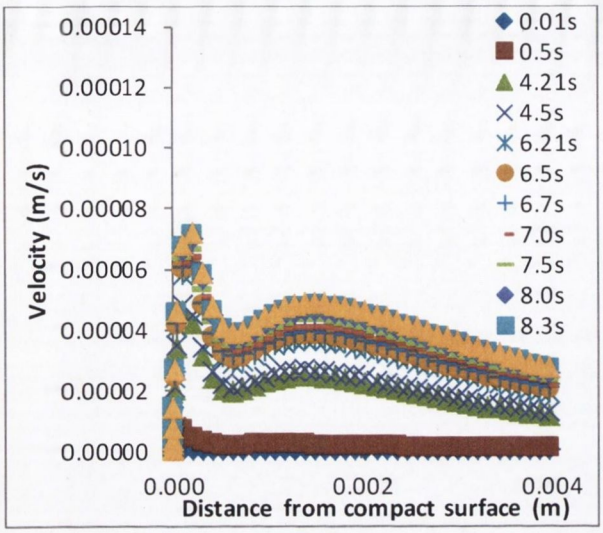


C

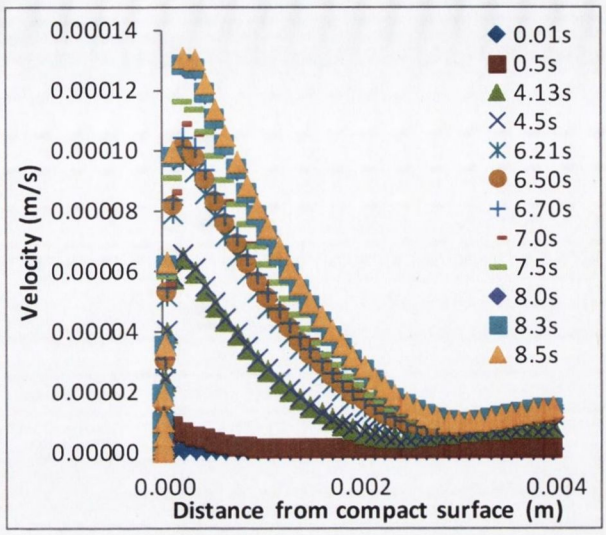


D

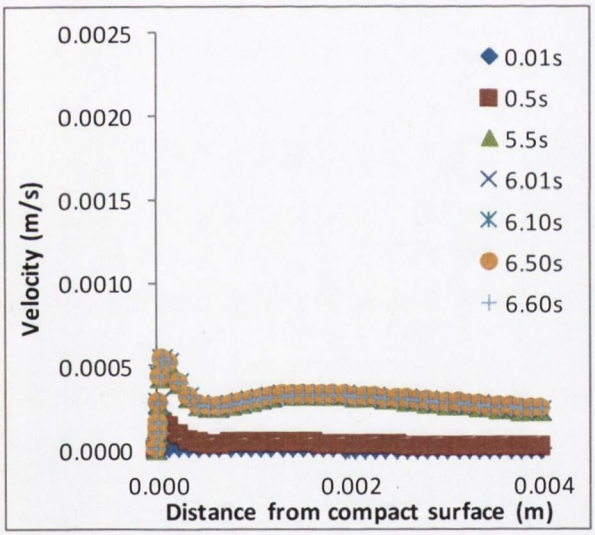
Figure 4. 3 Velocity magnitude distributions on different horizontal lines in the flow-through apparatus (Upper horizontal line(Figure 4.3 A,C) and lower horizontal line (Figure 4.3 B,D) referring to Lines A and C of Figure 2.5 (chapter 2)), demonstrating the overlapping velocity profiles on reaching steady state: A, Velocity distribution from BA species transfer simulation on upper line; B, Velocity distribution from BA species transfer simulation on lower line; C, Velocity distribution from LM species transfer simulation on upper line; D, Velocity distribution from LM species transfer simulation on lower line.



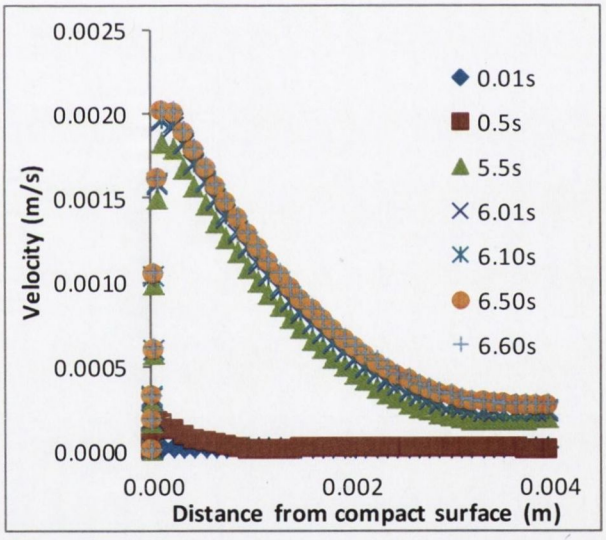
A



B



C



D

Figure 4. 4 Velocity magnitude distributions on different horizontal lines in the free convection system (Upper horizontal line(Figure 4.4 A,C) and lower horizontal line (Figure 4.4 B,D) referring to Lines A and C of Figure 2.6 (chapter 2)), demonstrating the overlapping velocity profiles on reaching steady state: A, Velocity distribution from BA species transfer simulation on upper line; B, Velocity distribution from BA species transfer simulation on lower line; C, Velocity distribution from LM species transfer simulation on upper line; D, Velocity distribution from LM species transfer simulation on lower line.

4.4.2 Hydrodynamics simulations including BA species transfer in the flow-through apparatus and free convection system from simulation including BA species transfer model

The vectors colored by velocity magnitude generated by Fluent™ from simulations of BA species transfer in the flow-through apparatus at different times of 0.03,0.13, 0.23, 4.03, 4.13 and 4.23s are illustrated in the Figure 4.5. These time points represent the accelerating inflow period (A, D), the peak inflow period (B, E) and the decelerating period just after flow reversal (C, F). Figure 4.5 A-C is taken from the simulations at the initial state, and D-F from the simulations at steady state.

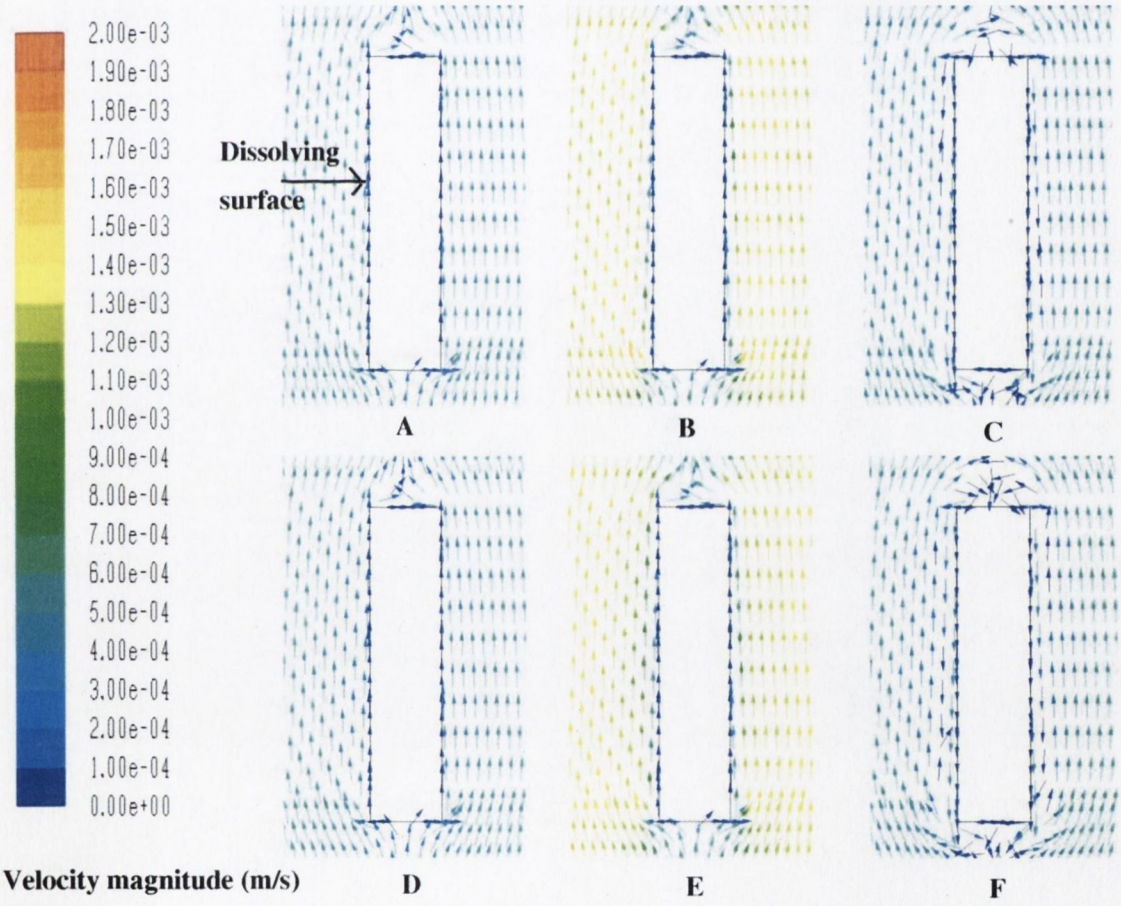
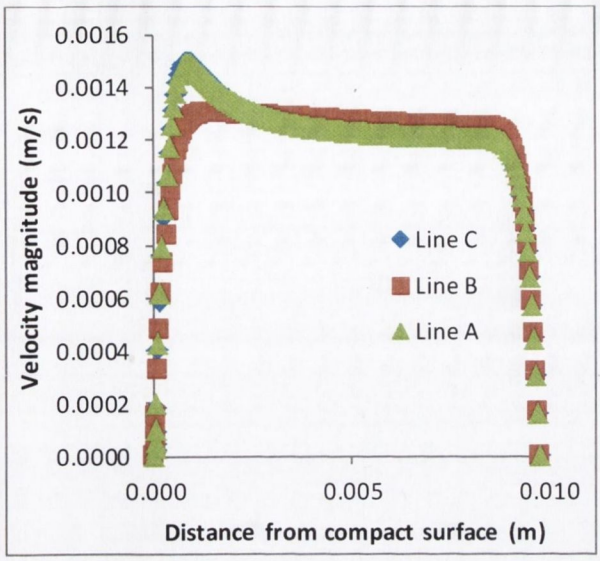
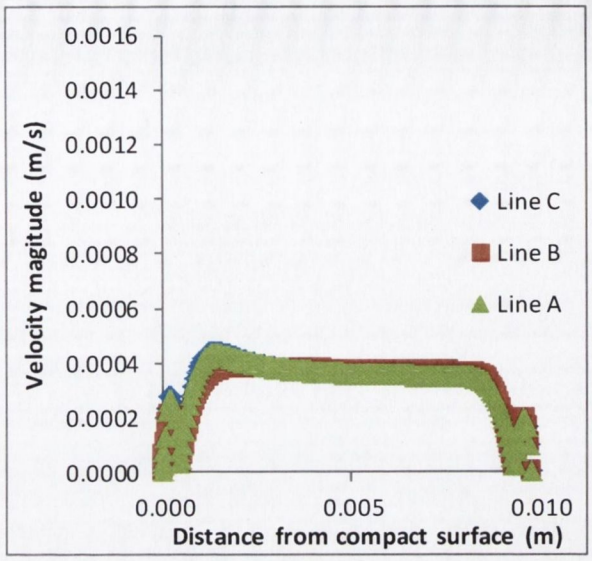


Figure 4. 5 The velocity vectors coloured by velocity magnitude generated by Fluent™ of BA species transfer simulation in the flow through apparatus at different times: A. 0.03s; B. 0.13s; C. 0.23s; D. 4.03s; E. 4.13s; F. 4.23s. A-C are defined as initial state and D-F are from the steady state simulation.

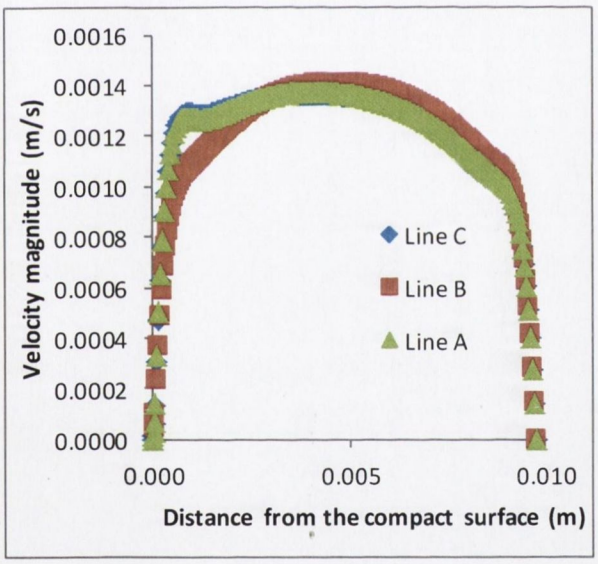
CFD generated vectors of velocity magnitude in the flow-through apparatus, incorporating the simulation of BA species transfer, demonstrated a notable hydrodynamic flow reversal adjacent to the compact surface, in both the initial (first pulse) and steady states, as shown in Figure 4.5 (C and F). CFD simulations of the 3-D model without species transfer demonstrated that flow reversal had already occurred during the decelerating period of the first pulse (0.20s) detailed in section 3.4 Chapter 3. In the current work, comparing the flow vector profiles of the BA species transfer model in the flow-through apparatus at the initial state and steady states, the separation of flow happened at the same time point in each case, at approximately 0.23s in each pulse. Due to different meshes of 2-D and 3-D model, the flow reversal occurred at different time. This indicates that the timing of flow separation is not affected by the species transfer. Rather, the adverse pressure gradient played the primary role in causing flow reversal, as described previously by Kakhi (Kakhi 2009). However, species transfer was not enabled in the study by Kakhi (Kakhi 2009; Kakhi 2009). The downward flow direction (flow reversal) following boundary separation is opposite to the bulk flow direction and counteracts the upward bulk flow induced by forced convection. Although the solubility and density of BA solution is not as high as that of the LM solution, there was a slight effect on the local hydrodynamics. This was manifest as a slight increase in the flow reversal at 4.23s (Figure 4.5 F) when the system was at steady state, in comparison to the corresponding time points in the initial state, Figure 4.5 C.



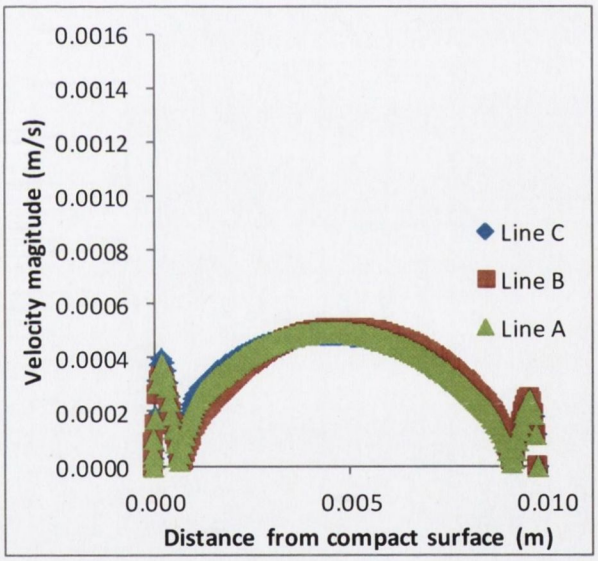
A



B



C



D

Figure 4. 6 Velocities in the flow-through apparatus BA species transfer simulation. Data from horizontal lines A-C referring to Figure 2.5 (Chapter 2) in the flow-through apparatus from the simulation using BA species transfer, showing velocity magnitude (m/s) vs. distance from compact surface at different times including: A.0.13s; B. 0.23s; C. 4.13s; D 4.23s.

The velocity magnitude distribution on each line was compared at 0.13s (Figure 4.6 A, maximum inflow, initial state) and 4.13s (Figure 4.6 C, maximum inflow, steady state). In terms of the bulk flow field (approximately 2-8 mm from the compact surface), the velocity magnitude distribution was similar on line A to C at 0.13s and 4.13s, with a maximum velocity of approximately 1.20×10^{-3} to 1.40×10^{-3} m s^{-1} at a distance of 2-8 mm from the compact surface, with a slightly increased velocity at 4.13 s. The overall picture therefore suggests that the relatively slow dissolution of BA does not influence the bulk region of the flow field. Therefore, a drug, with low solubility and similar saturated solution density as BA dissolving in 0.1 M HCl in the flow- through apparatus, will not significantly affect the bulk fluid flow in the flow-through apparatus.

In contrast, the quantitative analysis of the flow in the region of 0 to 2 mm from the compact surface reveals a minor change in flow velocity near the compact surface. There was a notable decrease in the velocity distribution curve in this region, as illustrated in Fig 4.6A and Fig 4.6c, between the initial and steady state. The difference in fluid velocity between the initial and steady state is most evident on lines A and C, which were near the top and bottom of the compact, respectively. The velocity profiles on these lines differ to those on line B in both the initial and steady state due to the more complex flow arising from edge effects near the top and bottom of the vertical compact surface. There is a decrease in velocity magnitude evident in this region near the compact surface on line B also (Figure 4.6 A versus C). The decrease in the flow velocity near the compact surface may be caused by gravitational effects on the more dense saturated solution of BA at the surface, slowing the upward forced convection at this point of maximal inflow of the pulsing flow. On the other hand, it is possible that there are some changes in local flow between the pulses at the initial and steady state independent of any natural convection effects, as each pulse at steady state will be affected by residual motion from the previous pulse, a condition not present in the initial state. Therefore, in order to investigate the nature of the flow direction and magnitude which can be induced by gravitational forces acting on the more dense bulk solution, a free convection system was simulated.

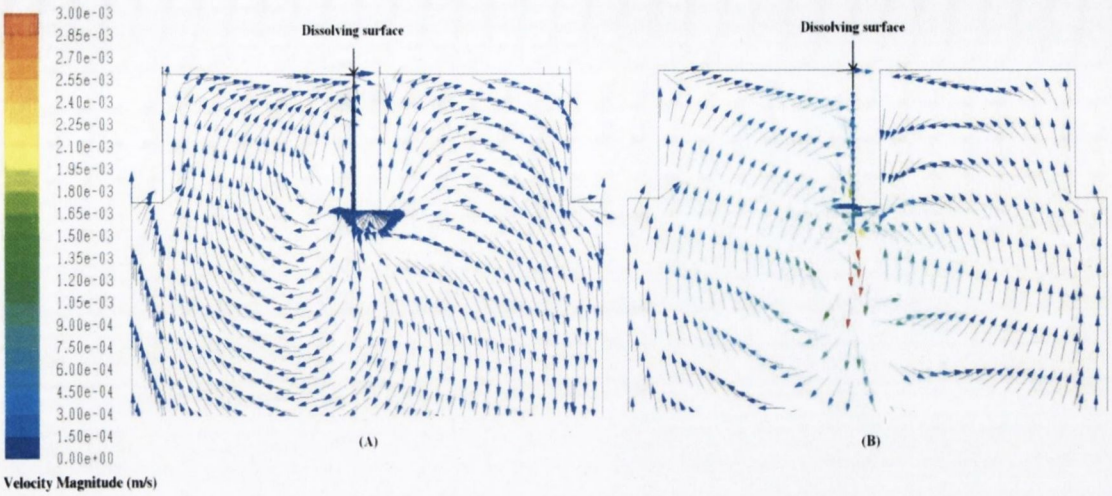


Figure 4. 7 Velocity vectors in the free convection system. Vectors colored by velocity magnitude (m s^{-1}) from (A) the BA species transfer simulation and (B) the LM species transfer simulation of hydrodynamics in the free convection system, at steady state.

The velocity vectors of BA and LM in the free convection system generated by CFD are shown in the Figure 4.7. The velocity range of 0 to 1.50×10^{-4} m s^{-1} (Figure 4.7 A) simulated in the free convection system is much lower than the velocity range of 0 to 1.4×10^{-3} m s^{-1} simulated in the flow-through apparatus (Figure 4.6). Furthermore, the diffusion of BA into the bulk flow field in the free convection system extended very slowly due to a low overall species transfer rate. Despite the low species transfer rate, the more dense BA solution induced a consistent downward flow near the dissolving surface due to natural convection. As there is no other force affecting or countering the flow direction or magnitude in the free convection system (unlike the opposing flows in the flow-through apparatus) the unobstructed downward flow of the BA solution formed, maintaining the concentration gradient at the dissolving surface, may explain the increased dissolution rate of BA in the free convection system compared to the flow-through apparatus (Table 4.2). In the free convection system, the highest velocity was below the surface of the BA compact exposed to the dissolution media, since the surface is a constant source of species. The BA will move from the saturated solution at the compact surface to the bulk dissolution media along a concentration gradient. However, as the saturated solution is more dense than the bulk medium, and the compact is fixed to the top of the free convection system, downward flow is also introduced along a density gradient under the influence of gravity. In terms of velocities generated at the dissolving surface, the

maximum velocity increased to approximately 1.3×10^{-4} ms^{-1}, near the upper edge of the compact. Although a velocity stream was generated due to natural convection, this is still a very low overall velocity, as illustrated in Figure 4.7 A. This was much lower than the bulk main stream velocity in the simulation of the flow-through apparatus with BA species transfer of approximately 1.4×10^{-3} $m\ s^{-1}$, as shown in Figure 4.6 C. These low velocity values generated in the free convection simulation suggests that the low velocity region produced by the BA dissolved in the free convection system could have, at most, a minor effect on the flow velocities near the dissolving surface in the flow-through apparatus at 8 ml min^{-1}. It is unlikely that gravitational effects on the more dense BA solution could overcome the upward flow, or completely reverse the flow, under the conditions simulated in the flow-through apparatus. The flow velocities in the flow-through apparatus under the conditions investigated during the dissolution of the BA compacts were predominantly controlled by forced convection and associated effects such as boundary layer separation and flow reversal. During the low- or zero velocity periods of the pulse in the flow-through apparatus, the simulations of the free convection system demonstrate that gravitational effects may have been able to influence local hydrodynamics, though flow reversal had already occurred at this point following hydrodynamic boundary layer separation.

Although the BA solution will not alter the hydrodynamics in the flow-through apparatus to the same extent as the more dense LM solution (section 4.4.3), it is possible that the denser BA solution (relative to the dissolution medium) increased the downward flow that was initially caused by flow reversal. The decrease in flow in the region close to the compact surface due to the boundary separation and/or flow reversal, with the effect enhanced by gravitational effects on the denser BA solution, affected the movement of BA from the surface to the bulk. The dynamic alteration between weak upward and downward flow near the dissolving surface will affect the effective diffusion boundary layer thickness and therefore the concentration gradient driving dissolution. As the flow slows and changes direction the boundary layer will increase, while flow reversal will increase the amount of solute present near the dissolving surface. Both of these effects will serve to inhibit dissolution in the flow-through apparatus.

4.4.3 Hydrodynamics simulations including LM species transfer in the flow-through apparatus and free convection system from simulation including LM species transfer model.

Velocity vectors coloured by velocity magnitude generated by Fluent™ from simulations of LM species transfer in the flow-through apparatus at different times of 0.03, 0.13, 0.23, 6.03, 6.13 and 6.23s are as shown in Figure 4.8. These time points represent the accelerating inflow period (A, D), the peak inflow period (B, E) and the decelerating period (C, F). Figure 4.8 A-C is taken from the simulations at the initial state, and D-F from the simulations at steady state. Flow reversal occurred over the whole pulse at steady state, despite boundary separation occurring at 0.23s in the initial state, indicating that the downward flow was driven by forces other than the adverse pressure gradient described in chapter 3.

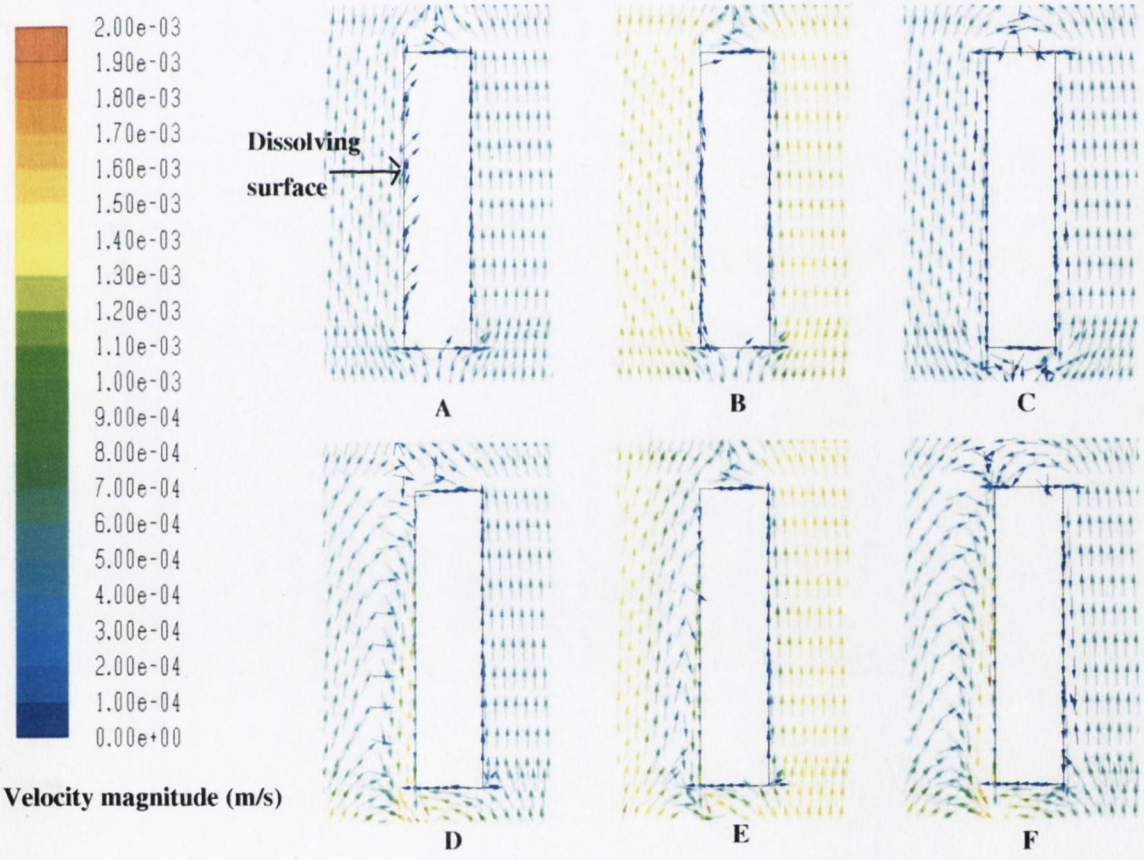
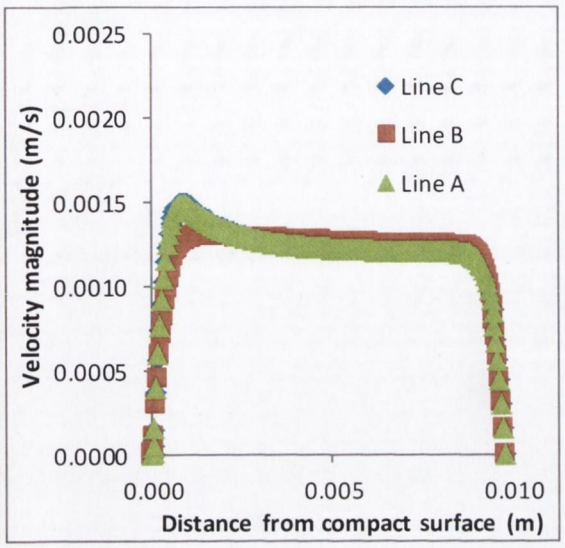


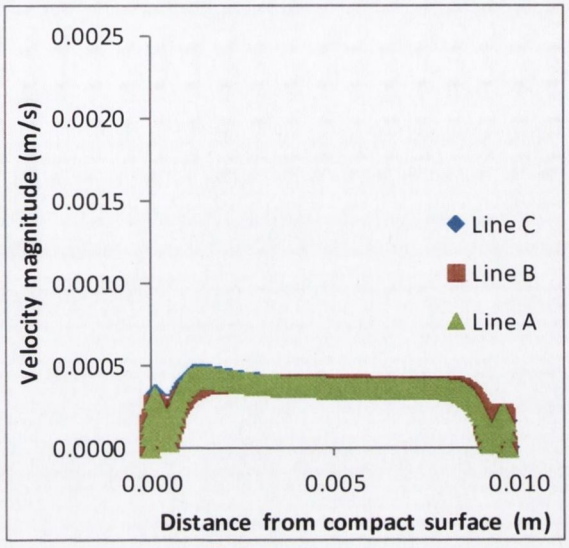
Figure 4. 8 Velocity vectors coloured by velocity magnitude generated by Fluent™ of LM species transfer simulation in the flow through apparatus at different time: A. 0.03s; B. 0.13s; C. 0.23s; D. 6.03s; E. 6.13s; F. 6.23s. A-C are defined as initial state and D-F are from steady state simulation.

The density of saturated LM solution is considerably higher than that of the dissolution medium (section 4.2.2). The ratio of the density difference ($\Delta\rho$, where ρ is density) between the saturated solution and bulk solution for LM and BA can be given as $\Delta\rho$LM: $\Delta\rho$BA. From the experimental data, this ratio was calculated to be approximately 50, which illustrates the more significant density gradient generated by the LM solution, enabling it to produce a stronger and more powerful downward flow based on gravity than the BA solution. Although flow reversal adjacent to the compact surface could be observed at 0.23s in the initial state (Figure 4.8 C), similar to that observed in the BA simulation (Figure 4.5 C), the flow pattern near the surface at steady state (6.23s, Figure 4.8 F) was quite different from the initial state. Downward flow was observed at different time points across the pulse including 6.03 and 6.23s at steady state (Figure 4.8 D and F), indicating that the downward flow of more dense LM solution was the dominant force near the surface of the dissolving LM compact. However, the upward bulk flow cannot be entirely neglected, as this counter-flow can reduce the dissolution rate of LM compared to that in the free convection system.

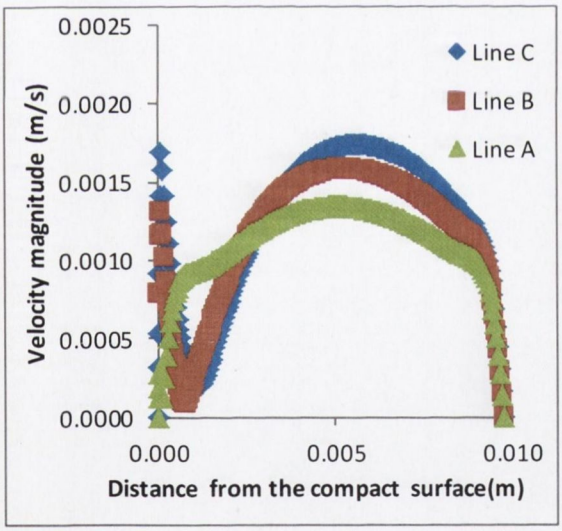
As the bulk velocity is determined by the pump, the bulk velocity vectors at the correspondent time of initial and steady state should be the same at 8 ml min^{-1}. However, it is interesting that the maximum flow velocity of approximately 7.5×10^{-3} m s^{-1} appeared at the centre to bottom of cell at 6.23 s. A similar phenomenon also occurred at 6.03 and 6.13s, which is obviously different to the initial state, where the maximum velocity is present at the two sides of the compact.



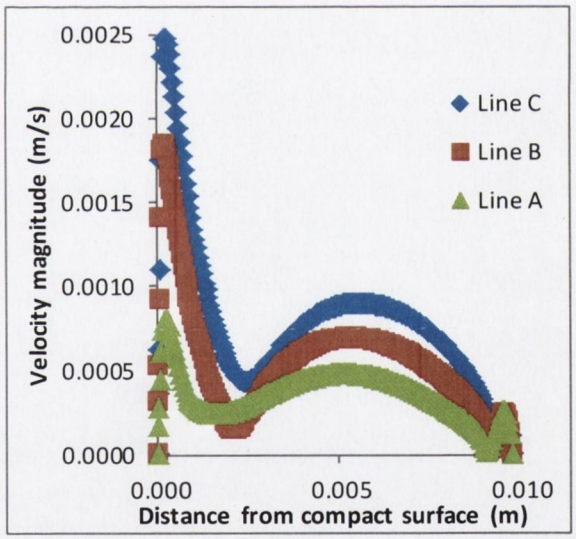
A



B



C



D

Figure 4. 9 Velocities in the flow-through apparatus LM species transfer simulation. Data from horizontal lines A-C referring to Figure 2.5 (Chapter 2) in the flow-through apparatus from the simulation using LM species transfer, showing velocity magnitude (m/s) vs. distance from compact surface at different times including, Initial sate: A.0.13s; B. 0.23s; Steady state: C. 6.13s; D 6.23s.

The velocity distributions of LM at 0.13, 0.23, 6.13 and 6.23 s are shown in the Figure 4.9, on upper, central and lower lines. The flow profiles on different lines were more distinguish able at steady state compared to those at the initial state. The velocity close to the compact surface on the lower line (Line C) of approximately 2.5×10^{-3} m s^{-1} at 6.23s was higher than that of approximately 1.7×10^{-3} ms^{-1} at 6.13s indicating that hydrodynamics close to the surface resulting from natural convection are affected less by upward flow at 0.23s than that at 0.13s. Furthermore, comparing the velocity distribution at 0.23s in the initial state and 6.23s at steady state, the downward flow resulting from density gradient of LM solution is the dominant force in the area close to the compact surface. The flow velocity close to compact surface is obviously higher than that of bulk flow. The estimated bulk velocity can be distinguishable at 0.13 and 0.23s (initial state, Figure 4.9 A, B) as well as between 6.13 and 6.23s (steady state, Figure 4.9 C, D), indicating that the bulk flow velocity was proportional to inflow velocity controlled by mechanical force (forced convection).

Quantitative analysis of velocity magnitude distribution during LM species transfer in the flow-through system at the initial state was consistent with the flow rate being initially controlled by forced convection, since velocity magnitude distribution of the models simulating BA species transfer and LM species transfer at initial state were similar, in Figure 4.5 A to C and Figure 4.8 A to C. When the species transfer of LM was at steady state (Figure 4.8 D to F), the region influenced by the LM dissolution process was significantly larger than that in the BA dissolution system, affecting a region up to 4 mm away from the compact surface. In this region, the velocity was complex, as shown in Figure 4.9 C, which is taken from the simulation at maximum inflow velocity, at 6.13 s. Figure 4.9 C shows that after the initial velocity increase moving away from the compact surface, there was a decrease to almost zero velocity at a position around 1 mm from the compact surface. This suggests that the downward flow produced by the LM species transfer counteracted the upward flow produced by the forced convection by an approximately equal force at this point, even at the point of maximum inflow velocity. This 1 mm position away from the tablet surface can be labelled as a transit point. From the surface of the compact to the transit point, the natural convection produced by the LM species transfer was dominant, with the highest velocity around 0.0017 m s^{-1}. In contrast, from the transit point to the wall of the flow-through cell, the flow produced by the forced convection was dominant, with the velocity reaching 0.0013 m s^{-1} to 0.0017 m s^{-1} (Figure 4.9 C) The velocity distributed on line A was different to the velocity

distribution on the other lines, with only a slight increase and decrease in velocity near the compact surface. The flow then increased to the velocity of the bulk flow region, which was established at a point nearer the compact surface in the region of this upper line than was apparent on the lower lines B and C. As Line A is close to the upper edge of the compact, there is little accumulation of LM solution at this position, due to the overall downward flow of LM. Compared to other positions on the compact surface, the effect from the density gradient was much smaller near this upper edge. The main force dominating the flow distribution profile at the position of line A, at the time points illustrated, was therefore forced convection, which is further compounded by the inward flow over the upper edge of the compact at this location (Figure 4.8).

The velocity vectors of the LM species transfer in the free convection system generated by the CFD are shown in Figure 4.7 B. The velocity of the BA species transfer simulation in the free convection system was obviously lower than that of the LM species transfer simulation. It is notable that the direction of the velocity vectors from both the BA and LM species transfer simulations in the free convection system are downward due to gravitational effects.

In addition, the LM dissolution rate was significantly higher than that of BA in the free convection system due to a higher density of saturated LM solution as well as a higher solubility of LM, as reflected in the h values presented in Table 4.2. When the LM species transfer simulation was at steady state, the region of the free convection system affected by LM species transfer (Figure 4.7 B) was notably larger than that of the BA species transfer (Figure 4.7 A).

The simulated maximum velocity in the free convection system when it reached steady state, was approximately 0.002 m s^{-1} near the lower edge of the compact. Comparing this velocity value to velocities present in the flow through apparatus (maximum about 0.0017 m s^{-1}, Figure 4.8), suggests that when LM dissolved in the flow-through apparatus, the natural convection produced by the LM dissolution could alter the hydrodynamics in the cell of the flow-through apparatus at 8 ml min^{-1}.

Contrary to the situation in the BA species transfer model of the flow through apparatus, the species transfer of LM was partly driven by the flow generated by the LM solution itself as it dissolved. This flow was countered by the upward forced convection, reducing the potential

for downward flow from the LM solution. The effect from the upward forced convection is a dynamic one, as the forced convection magnitude, and therefore the potential effect of natural convection on forced convection, changes over the course of the pulse. This repeated slowing, by upward forced convection, of the downward flow produced by the forming LM solution will affect the local concentration gradient, as the effective diffusion boundary layer broadens in a lower velocity field. The effect on concentration gradient is similar to that observed in the BA dissolution system, except that in that case the flow governing dissolution is the forced convection, with both boundary layer separation and local density gradients slowing the upward forced convection.

4.4.4 The effective diffusion boundary layer for BA and LM in the flow-through apparatus and free convection system

In order to examine the effect of flow on the boundary layer, its thickness was examined over the course of the pulse, on the upper, central and lower horizontal lines. The boundary layer thickness on the line extending horizontally from the centre of the compact surface in both the flow-through apparatus and free convection system, are shown in Figure 4.10.

The boundary layer was "thicker" at all time points at the lower edge of the BA compact than the upper edge (not shown). The boundary layer thickness on the central line, of approximately 4.5×10^{-4}m, was similar to that on the lower line. In contrast, in the free convection system, there was no change in boundary layer thickness between the lower, central and upper lines. The boundary layer thickness on the central line in the free convection system was approximately 4.3×10^{-4} m (Figure 4.10), and is less than that determined for the flow-through apparatus on the central line, at all time points over the pulse. Although the difference is small, the fact that the boundary layer is consistently thinner in the free-convection system than the flow-through apparatus is consistent with the higher dissolution rate for BA observed in the free convection system. Thus, the local hydrodynamics in the flow-through apparatus at this flow rate result in a system generating a lower dissolution rate, from a vertical surface of a compound with a solubility and density of BA in 0.1M HCl, than the dissolution rate observed in the free convection system.

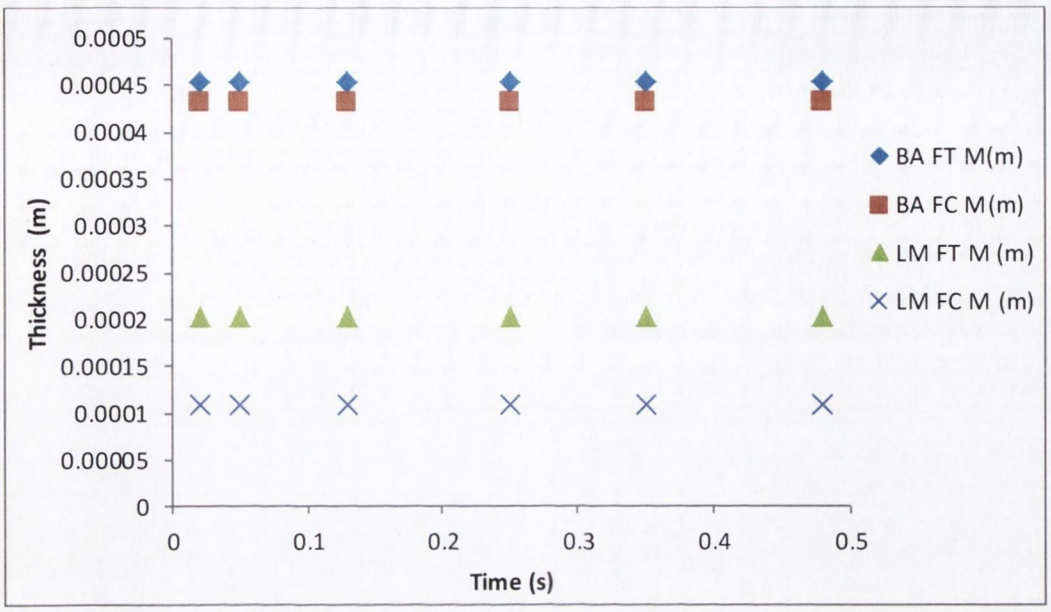


Figure 4. 10 Estimated boundary layer thickness along the central horizontal line at different time points of the pulse, from species transfer simulations in the flow-through (FT) apparatus (BA and LM) and free convection (FC) system

The diffusion boundary layer thickness of LM on the central horizontal line (Figure 4.10), revealed a thicker diffusion boundary layer in the flow-through apparatus (~2 x 10^{-4}m) than in the free convection system (~1.1 x 10^{-4}m), consistent with the lower dissolution rate in the flow through apparatus compared to the free convection system. It is worth noting that this central boundary layer thickness between the upper and lower lines in the flow-through apparatus was thinner than that in the BA species transfer model in the flow-through apparatus.

The difference between calculated boundary layer thickness on the lower and upper lines was greater in the free convection system than in the flow through apparatus (1.1 x 10^{-4} m (upper) versus ~2.2 x 10^{-4} m (lower) in the free convection system, and 1.1-1.5 x 10^{-4} (upper) versus ~2 x10^{-4} m (lower) in the flow through apparatus). The upper line in the flow through apparatus may have been affected by recirculation zones in the bulk flow generated by the flow reversal at the surface (Figure4.8 D-F), resulting in a thinner diffusion boundary layer in this region.

The boundary layer thicknesses on the central line do not change over the course of the pulse as shown in Figure 4.10. The thickness was noted to change along the lower line in the model simulating BA species transfer and the upper line in the LM species transfer model. In the BA

species transfer model, the boundary layer thickness increased during the second half of the pulse, consistent with the decrease in forced convection during this period. In the LM species transfer model, however, the boundary layer thickness on the upper line was reduced during the second half of the pulse. This can be attributed to a reduction in the upward forced convection, and therefore a reduction in the counterflow to the downward flowing natural convection. The constant boundary layer thickness over the course of the pulse on the central line depicted in Figure 4.10 may be due to the arbitrary definition of the "edge" of the boundary layer at the point where the concentration was less than 1% of the saturated concentration. On examination of the mass fraction of BA over the course of the pulse at varying distances from the compact surface, the concentration along this central line was noted to change over the course of the pulse. With the LM simulation, the concentration increased at the point where the forced convection increased, consistent with the observation that the counterflow of the forced convection decreased the natural convection induced by LM (Figure 4.8). With the BA simulation, the mass fraction along the central line was noted to continuously increase. This may be due to the continuous source of BA in the system, causing the concentration to increase overall before reaching an equilibrium with outflow. However it may also reflect the local buildup of BA at each location during the later part of the pulse when the forced convection had reduced.

4.4.5 Further consideration for practical dissolution

In each case, in the free convection system once a natural convective flow is established, there is no forced convection flow countering it to interfere with the local concentration gradient. Thus, with the velocities and solubilities investigated in the current work, the dissolution rates in the free convection system for both LM and BA were higher than in the flow-through apparatus. This observation is supported by the predicted differences in diffusion boundary layer thickness, and therefore concentration gradient driving dissolution, in particular in the central region of the compact, between the free convection and flow-through dissolution systems. Furthermore, particularly in the case of the more dense lactose solution, a density gradient develops within the flow-through cell over time, as the more dense solution is present towards the bottom of the cell. This would naturally be disrupted with each new pulse, however, overall it is possible that the effluent concentration might be less than the average concentration at the base of the cell. Nevertheless, over the course of the dissolution, an equilibrium should be established allowing quantitative comparison of

dissolution results from effluent concentration. The timescale required for such an equilibrium to develop is beyond the scope of the current simulations.

The current work used CFD to simulate hydrodynamics and velocity magnitudes within the flow-through apparatus dissolution cell. A recent study considering hydrodynamics in the 22.6 mm diameter cell used magnetic resonance imaging (MRI) as a method to determine the local fluid velocity magnitudes and overall hydrodynamic patterns in the flow-through apparatus(Shiko, Gladden et al. 2010). Dynamic flow movement was observed by MRI at a range of flow rates in both the 12 mm and 22.6 mm diameter cells. Although the compact dimension, orientation and location were different to that in the current work, the velocities observed were overall low, with notable variation across the cell. In particular, flow reversal was observed near the cell wall. The results also indicated that a change in tablet orientation in the flow-through apparatus would leads to a significant variation in flow velocity. The results presented in the current work can be interpreted with relevance to a compact positioned vertically at the centre of the cell. Furthermore, it can be concluded that the low and variable velocities present over the course of the pulse in the cell allow a potentially significant contribution from natural convection, depending on the solubility and position of the dissolving surface.

4.5 Prediction of dissolution rates of BA and LM in the flow-through apparatus based on the shear rate generated by Fluent™.

The dissolution rate was predicted using the most accurate dissolution prediction method from those investigated in chapter 3: forced-natural convection combination (FNCC) method (Equation 3.7) using calculated shear rate or absolute shear rate.

The shear rate generated by Fluent™ on the central line closest to compact surface (7.10×10^{-11} m from compact surface) was used as an estimate of shear rate on the compact surface. The prediction of BA and LM at initial state is slightly lower than the corresponding values obtained from Chapter 3 (Table 4.3), indicating that the difference between the 2D and 3D meshes could slightly affect the dissolution rate. Furthermore, the simulated dissolution rate of BA at steady state of 0.0965 mg min^{-1} cm^{-2} is very close to the observed dissolution rate of 0.0937+/-0.0078 mg min^{-1} cm^{-2}, (Table 4.3), suggesting that the species transfer has an effect on the dissolution rate. However, there was a higher simulated LM dissolution rate of 6.965

mg min^{-1} cm^{-2} using the same method. In other words, the FNCC method had a better agreement with the observed results for slightly soluble BA than that freely soluble LM. Although the surface shear rates were used to predict dissolution rate in both BA and LM cases, the flow velocity vectors are very different in these two cases (Figure 4.5 and 4.8). In the BA case, the directions of bulk flow and of the flow near the surface at most times at steady state are upward, except the boundary separation. However, the directions of bulk flow and of flow near the surface are opposite over the whole pulse at steady state in the LM case. Although magnitude of shear rate may be correct, directional effect on concentration gradient of the downward flow is not reflected by the equation. Therefore, the prediction of LM is overestimated using the FNCC method with calculated shear rate.

Additionally, the predicted result of LM of 6.965 mg min^{-1} cm^{-2} in the steady state based on FNCC method (Table 4.3) is comparable to the observed LM dissolution rate of 6.889+/- 1.700 mg min^{-1} cm^{-2} in the free convection system. This phenomenon is not in agreement with the effect of local hydrodynamics generated by the freely soluble LM on the dissolution rate as discussed above: the downward flow resulting from the density gradient counteracts upward forced flow and then decreases the dissolution rate in the forced convection part of the pulse.

Last but not least, it is notable that a disordered flow is produced near the compact surface in the LM case when strong upward forced flow meets the downward flow resulting from the density gradient (Figure 4.8 E). FNCC method will not account for effects of such disordered flow on dissolution rate.

Overall, the FNCC method is suitable for the slightly soluble drug with the simple and unidirectional forced convection.

Table 4. 3 All observed and predicted results of BA and LM in the flow-through apparatus within 22.6 mm cell at 8 ml min^{-1}

Different situations	BA (mg min^{-1} cm^{-2})	LM (mg min^{-1} cm^{-2})
Predicted dissolution rate based on calculated shear rates (initial state) distribution on the compact surface using FNCC method	0.119	4.226
Predicted dissolution rate based on calculated shear rate (steady state) distribution on the compact surface using FNCC method	0.096	6.965*
Predicted dissolution rate without species transfer based on calculated shear rate using FNCC method (chapter 3)	0.122	4.372
Experimental dissolution rate in the flow-through apparatus	0.094+/- 0.008	3.240+/-0.680

*As the calculated shear rates of LM at steady state have the same sign.

4.6 Conclusion

Both flow reversal following boundary separation and species transfer affect the local hydrodynamics and therefore the dissolution rate at 8 ml min^{-1} in the flow-through apparatus under the conditions investigated. For a freely soluble compound, such as LM, the denser flow could overcome upward inlet forced convection, with a downward counter-flow predicted over the course of the whole pulse at steady state. The notable effect of the species transfer from LM on the system hydrodynamics implies that simulation of both species transfer and hydrodynamics is necessary to interpret dissolution rates of a freely soluble compound under the low-velocity flow-conditions presented. For a slightly soluble compound, such as BA, the dissolution would have a minor effect on local hydrodynamics. The effects of flow-reversal due to the adverse pressure gradient during the deceleration phase of pulse inflow was the main factor affecting local hydrodynamics, causing a lower flow near the surface and consequently lower dissolution rate than the free convection system. A simulation, therefore, of hydrodynamics alone would be informative in interpreting dissolution rates of a slightly soluble compound in this low velocity pulsing flow. An estimate of boundary layer thickness from a simulation using species transfer should be able to predict the influence of the

hydrodynamic environment, accounting for both forced and natural convection, on dissolution rate. The variation in predicted boundary layer thickness at different locations and at different time points suggest possible non-uniform dissolution in low-velocity flow fields in the flow-through apparatus. The results indicate that the dissolution rate during a short time frame at locations near the dissolving surface may be more complex than regular effluent measurements would suggest. This is of relevance for situations where a dissolving surface may encounter non-sink conditions, for example during certain phases of its journey through the gastro-intestinal tract, where it may encounter low fluid volumes(Schiller, Frohlich et al. 2005). Furthermore, the results suggest that a freely soluble excipient, such as LM, may affect the local hydrodynamic environment during dissolution testing of a low solubility active ingredient.

The flow reversal resulting from density gradient for soluble LM notably affects hydrodynamics and shear rate distribution on the compact surface. The forced inflow does not change the hydrodynamics surround compact surface. Equation 3.7 does not sufficiently address the effect of countering flow direction on concentration gradient. However, Equation 3.7 can successful by predict the dissolution rate of slightly soluble BA with consideration of the effect of forced inflow on the concentration gradient.

Chapter 5 Investigation of dissolution rate of two-component compact systems of freely soluble component and slightly soluble component under low velocity conditions

5.1 Introduction

The freely soluble compound LM and the slightly soluble compound BA have been studied in the flow-through apparatus and free convection system in chapter 4. The flow resulting from the density gradient of LM counteracted the upward mechanical flow and subsequently reduced the dissolution rate of LM in the flow-through apparatus in a low velocity environment as detailed in Chapter 4. Additionally, the thickness of the diffusion boundary layer was affected by the flow resulting from the density gradient under the low velocity environment. However, the study in Chapter 4 is based on single component systems. Therefore, the study of multi-component system under low velocity conditions and the effect of the dissolution of freely soluble LM on the dissolution of slightly soluble BA in the same system were carried out in the current work.

The theory from Higuchi and coworkers (Higuchi, Mir et al. 1965) was used to predict the dissolution rate of two non-interacting compounds of BA and LM under a low velocity environment in 3 different systems: 1) the flow-through apparatus, 2) the free convection system and 3) the paddle apparatus. The solubility difference between the two components in the current study is higher than presented in the original work by Higuchi et al (1965) based on benzoic acid and salicylic acid. The reported experiments were carried out in 400 ml jacketed vessel with a glass stirrer at a rotation speed of 150 rpm. Furthermore, the freely soluble compound LM can affect the local hydrodynamics under low velocity environment as detailed in Chapter 4.

The aims of this chapter are:

- to investigate the effect of the highly soluble excipient LM on the dissolution rate of the slightly soluble model drug BA in low velocity environments.
- to develop a method to predict, *a priori*, the dissolution rate of non-interacting mixtures in the free convection system.

5.2 Validating composition and non-interacting of mixture systems

The measured content of BA in each mixture was used to validate whether the assumed ratio of BA in each mixture is appropriate as illustrated in Table 5.1. The observed contents were comparable to the corresponding theoretical value. (put it in the method part)

Table 5. 1 The content of BA in mixtures compacts of 25%, 50% and 75% BA.

Theoretical % w/v	25%	50%	75%
Experimental % w/v			
Average (n=3)	26.31%	51.11%	76.19%
S.D.	0.62%	0.82%	0.74%

As the solubility of LM in a saturated solution of BA in 0.1M HCl, and BA in a saturated solution of LM in 0.1M HCl were 232.39+/-9.254 and 4.598 +/-0.227 g L^{-1}, respectively, those values were comparable to the solubility of LM (219.64±22.2g L^{-1}) and BA (4.56 g L^{-1}) (Ramtoola and Corrigan 1987) alone in 0.1 M HCl. This confirmed that the LM and BA were non-interacting compounds.

5.3 Dissolution rate of BA and LM mixture systems in the different dissolution apparatuses

The experimental dissolution profiles of BA observed in the paddle apparatus at 50 rpm, the flow-through apparatus using a 22.6 mm cell at a flow rate of 8 ml min^{-1} and in the free convection system, are shown in Figure 5.1, 5.2 and 5.3, respectively and the correspond to the total amount of LM dissolved in 15 minutes and the dissolution rates as listed in Table 5.2 and Table 5.3, respectively.

The dissolution rates of both, BA and LM, in the paddle apparatus were higher than those in the flow-through apparatus and the free convection system (low velocity systems). In all testing systems, the dissolution rate of LM increased with increasing amount of LM in the mixture.

Furthermore, it was found that the dissolution rate of BA increased with increasing amount of LM in the mixture when using the flow-through cell or the free convection system, as shown in Table 5.4. This trend was not observed in the paddle apparatus with the exception of the compact containing 15% BA.

Therefore, the dissolution results obtained in the low velocity systems might be explained by changes in the local concentration of freely soluble LM resulting in changes of the local hydrodynamics due to natural convection induced by density gradients as detailed in chapter 4. These changes might become stronger with increasing amount of LM in the composite systems.

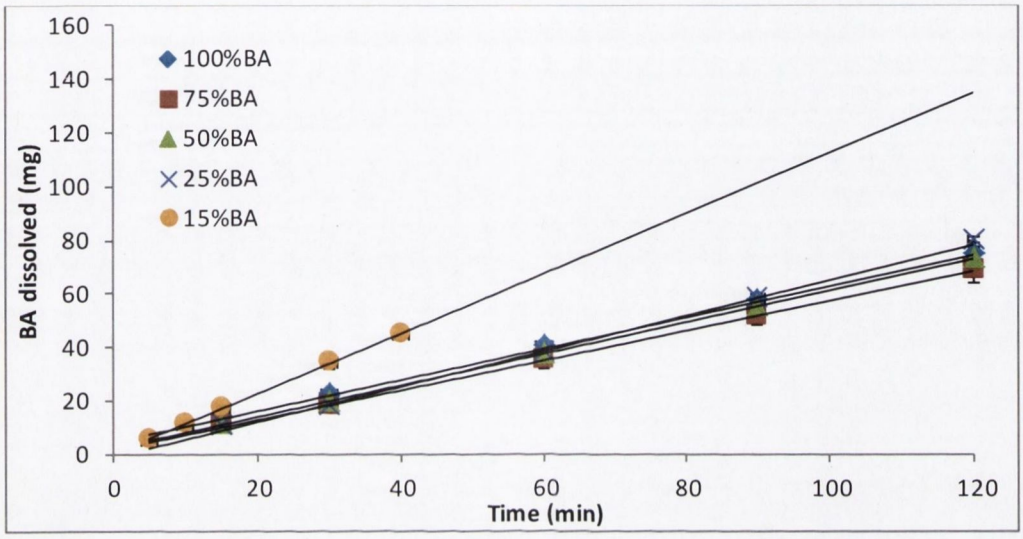


Figure 5. 1 The effect of composition on the dissolution rate of BA from BA-LM compacts in 0.1 M HCl in the paddle apparatus.

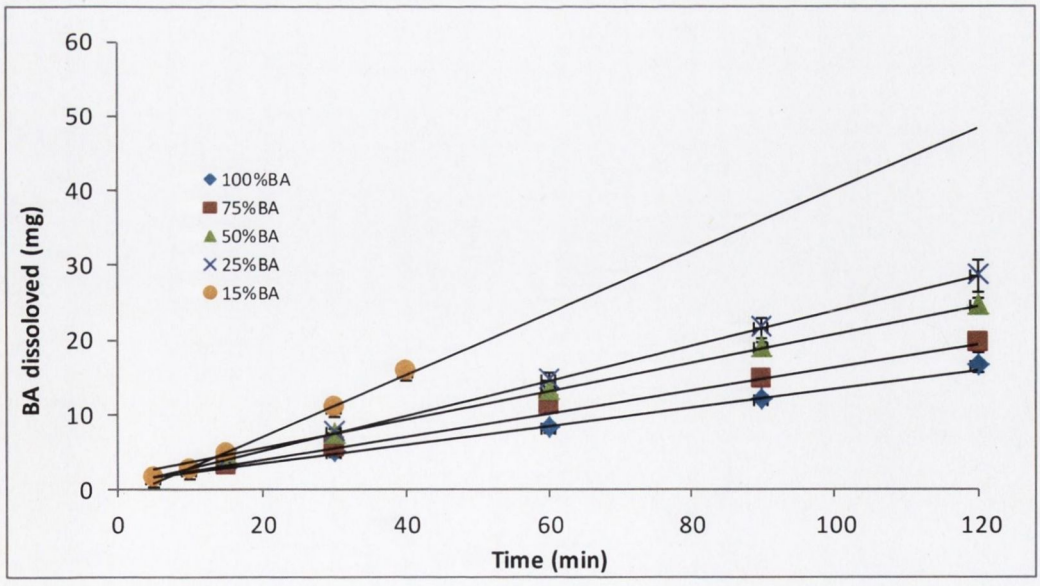


Figure 5. 2 The effect of composition on the dissolution rates of BA from BA-LM mixture compacts in 0.1M HCl in the flow-through apparatus.

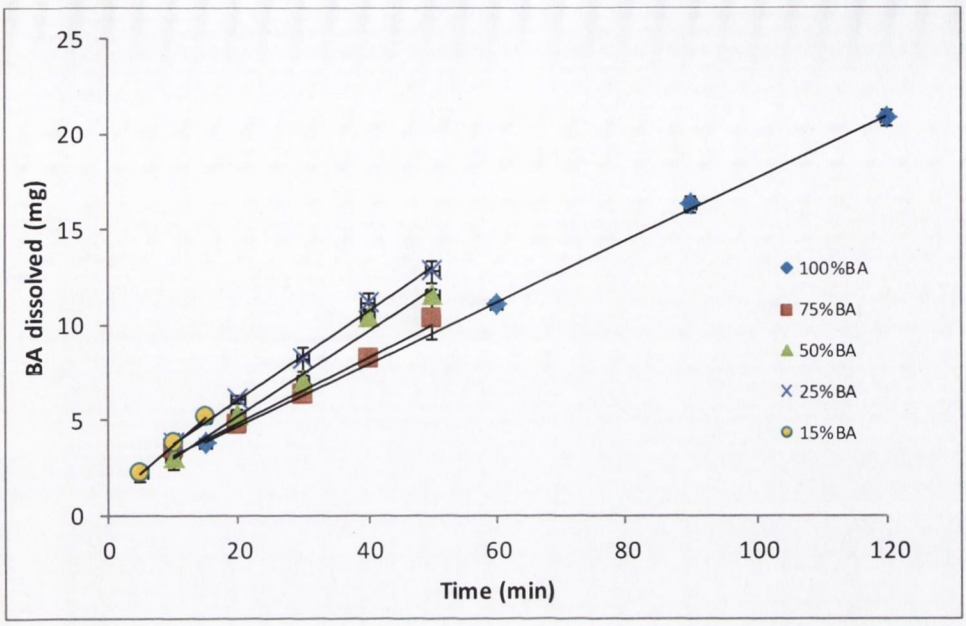


Figure 5. 3 The effect of composition on the dissolution rate of BA from BA-LM mixture compacts in 0.1 M HCl in the free convection system.

Table 5. 2 Total amount of LM dissolved in 15 minutes in different apparatuses.

LM in mixture	Total amount dissolved in 15 minutes (mg)		
	Paddle apparatus	Flow-through apparatus	Free convection system
25%	2.733+/-0.227	2.734+/-0.228	4.268+/-0.380
50%	8.276+/-0.573	5.543+/-0.263	9.697+/-1.468
75%	28.549+/-0.696	20.045+/-1.367	21.906+/-0.719
85%	86.862+/-8.217	38.268+/-3.156	45.109+/-3.179
100%	169.471+/-7.943	64.387+/-13.677	137.084+/-33.825

Table 5. 3 Dissolution rate of BA and LM in the different apparatus

LM in mixture	BA in mixture	Paddle apparatus (mg/min/cm2)		Flow-through apparatus (mg/min/cm2)		Free convection system (mg/min/cm2)	
		BA	LM	BA	LM	BA	LM
0%	100%	0.442 +/- 0.036	0	0.094 +/- 0.008	0	0.123 +/- 0.003	0
25%	75%	0.420 +/- 0.033	0.137 +/- 0.011	0.116 +/- 0.007	0.137+/- 0.011	0.130 +/- 0.012	0.215 +/- 0.019
50%	50%	0.446 +/- 0.043	0.416 +/- 0.029	0.143 +/- 0.002	0.279+/- 0.013	0.167 +/- 0.010	0.488 +/- 0.019
75%	25%	0.499 +/- 0.015	1.435 +/-0.035	0.177 +/- 0.014	1.007+/- 0.068	0.175 +/- 0.008	1.101 +/- 0.036
85%	15%	0.848 +/- 0.011	4.365 +/- 0.413	0.311 +/- 0.018	1.923+/- 0.159	0.220 +/- 0.027	2.267 +/- 0.160
100%	0	0	8.517 +/- 0.399	0	3.240 +/- 0.680	0	6.889+/- 1.700

Table 5. 4 The dissolution rate of BA at different BA-LM composition system comparing to the dissolution rate of BA at 100% mixture system in the different apparatus.

BA in mixture	Dissolution rate from a compact containing x% BA relative to the dissolution rate of the 100% BA compact		
	Paddle apparatus	Flow-through apparatus	Free convection system
100%	1	1	1
75%	0.95	1.24	1.06
50%	1.01	1.53	1.36
25%	1.13	1.89	1.42
15%	1.92	3.32	1.79

5.4 Investigation of factors affecting the dissolution rate of two-component systems.

5.4.1 Predicting dissolution rate from non-interacting two component systems

In order to investigate the effect of local hydrodynamics resulting from freely soluble LM in the mixture on the dissolution rate of BA, The theory from Higuchi and coworkers (Higuchi, Mir et al. 1965) was used to predict the dissolution rate of the non-interacting two component systems. The dissolution from a non-interacting mixture of A and B can follow one of three cases as illustrated in Figure 5.4.

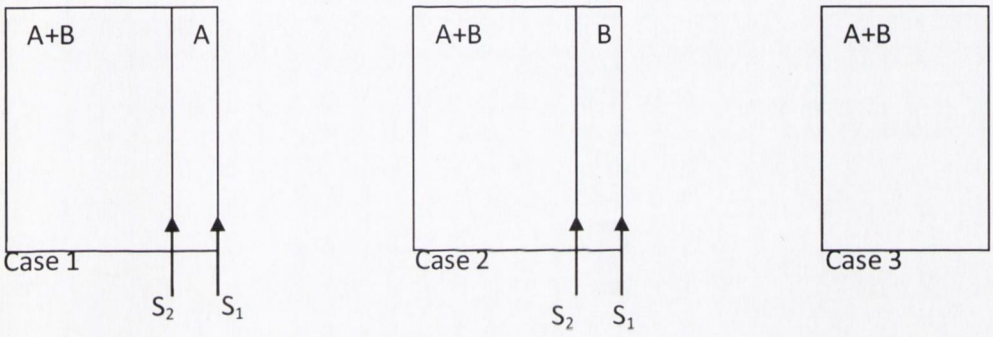


Figure 5. 4 Dissolution behavior of a two-phase mixture of A and B. In case 1 , phase B dissolves fast enough to leave a layer of pure A behind; in case 2, the reverse is true; while in case 3, dissolution rates of A and B are proportional to their relative amounts in the mixture.

Most cases would lead to Case 1 or 2, after one of the phases become depleted in the solid-liquid interface region, i.e. that either A or B would remain covering the compact surface at time t,>0 and only in case 3 do A and B coexist at the solid-liquid interface (Higuchi, Mir et al. 1965).

In case 1 and case 2, when case 1 and 2 are in the initial state (t=0), S_2=S_1=0. S_1 and S_2 are the coordinate values representing the phase A-solution boundary layer and the bulk mixture-phase A boundary layer, respectively.

When Case 1 and 2 are in the steady state (t>0), S_2-S_1 gives the thickness of the phase A or B layer. Before the system is in the steady state, the thickness of phase A or B layer will change

with time, and the theory from Higuchi and coworkers was based on the steady state. The calculation of S_1 and S_2 are illustrated in Equations 5.1 and 5.2 (Higuchi, Mir et al. 1965).

$$S_1 = \frac{D_A C_A}{A_A h} t$$

Equation 5. 1

$$A_B \frac{dS_2}{dt} = \frac{D_B C_B}{h + \left(\frac{\tau}{\varepsilon}\right)[S_2 - (D_A C_A / A_A h)t]}$$

Equation 5. 2

D_A is the diffusion coefficient of A; D_B is the diffusion coefficient of B; C_A is the saturated solubility of A; C_B is the saturated solubility of B; t is time; A_A is the amount per unit volume of A; A_B is the amount per unit volume of B; τ is tortuosity and ε is porosity; S_1 is the coordinate value representing the boundary between phase A and solution; S_2 is the coordinate value representing the boundary between bulk mixture and phase A.

When the system is in the steady state, the dissolution rate in each case can be predicted by the following equations 5.3 to 5.7.

In case 1, when the situation is that

$$\frac{N_A}{N_B} > \frac{D_A C_A}{D_B C_B}$$

Equation 5. 3

then

$$R_B = \frac{A_B D_A C_A}{A_A h} = \frac{N_B}{N_A} R_A$$

Equation 5. 4

In case 2, when the situation is that

$$\frac{N_A}{N_B} < \frac{D_A C_A}{D_B C_B}$$

Equation 5. 5

then

$$R_A = \frac{N_A}{N_B} R_B$$

Equation 5. 6

Where R_A is the dissolution rate of A per unit surface area; R_B is the dissolution rate of B per unit surface area; N_A: amount of A in the mixture and N_B: amount of B in the mixture.

In case 3, when the two phases always coexist at the solid-liquid interface, the critical mass fraction can be obtained from this Equation 5.7:

$$\frac{N_A}{N_B} = \frac{D_A C_A}{D_B C_B}$$

Equation 5. 7

The predicted dissolution rates obtained in the different apparatuses and modeled by Higuchi's Equations, are illustrated in Figures 5.5, 5.6 and 5.7 and Tables 5.5, 5.6 and 5.7. The prediction was based on the above equations and the diffusion boundary layer thickness (h) obtained from the dissolution rate of the 100% BA compact in the different apparatuses, using Equation 4.1.

For each mixture system, the predicted dissolution rate of BA was higher than the experimentally determined rate, except for the 15% BA compact. Additionally, a higher dissolution rate of LM was observed in the experiment than predicted in the case of a 15% and 0% BA compact (Figure 5.5, Table 5.5).

The predicted dissolution rates of mixture components in the flow-through apparatus and free convection system were less than the observed result, indicating that local hydrodynamics, resulting from LM density gradient, affect the dissolution rate in the low velocity environment. This effect on the dissolution rate of BA was stronger with increasing

amount of LM in the mixture. Compared to the observed dissolution rate of BA and LM in the paddle and the flow-through apparatus, the observed dissolution rate of 0.094+/-0.008 mg min^{-1} cm^{-2} from a 100% BA compact in the flow-through apparatus was nearly 5 fold lower that of 0.442+/-0.036 mg min^{-1} cm^{-2}, determined in the paddle apparatus, while the dissolution rate of 0.177+/-0.014 mg min^{-1} cm^{-2} from a 25% BA in the flow-through apparatus was only 2.8 fold lower than that of 0.499+/-0.015 mg min^{-1} cm^{-2}, observed in the paddle apparatus. With an increasing ratio of LM in the mixture compacts, the dissolution rate of BA apparently increased in the flow through apparatus. Therefore the difference between dissolution rates in each apparatus decreased as the ratio of LM: BA increased.

Furthermore, the difference between the predicted and observed dissolution rates of BA and LM was higher in the flow-through apparatus and the free convection system, compared to that in the paddle apparatus (Table 5.5, 5.6 and 5.7). This indicated that the theory from Higuchi and coworkers may not predict well in the low velocity environment.

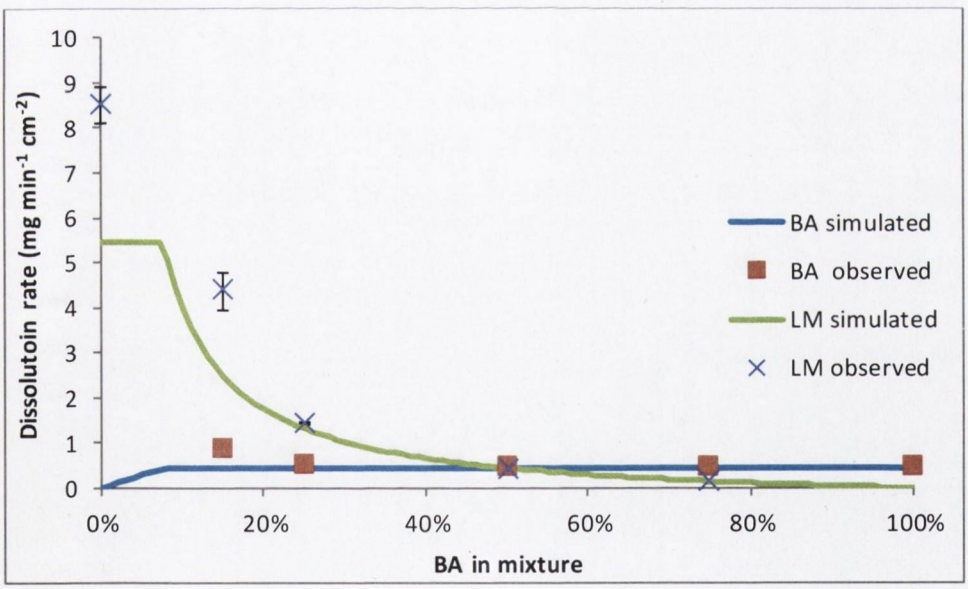


Figure 5. 5 Predicted and experimentally determined dissolution rates of BA and LM from different mixture composition in the paddle apparatus.

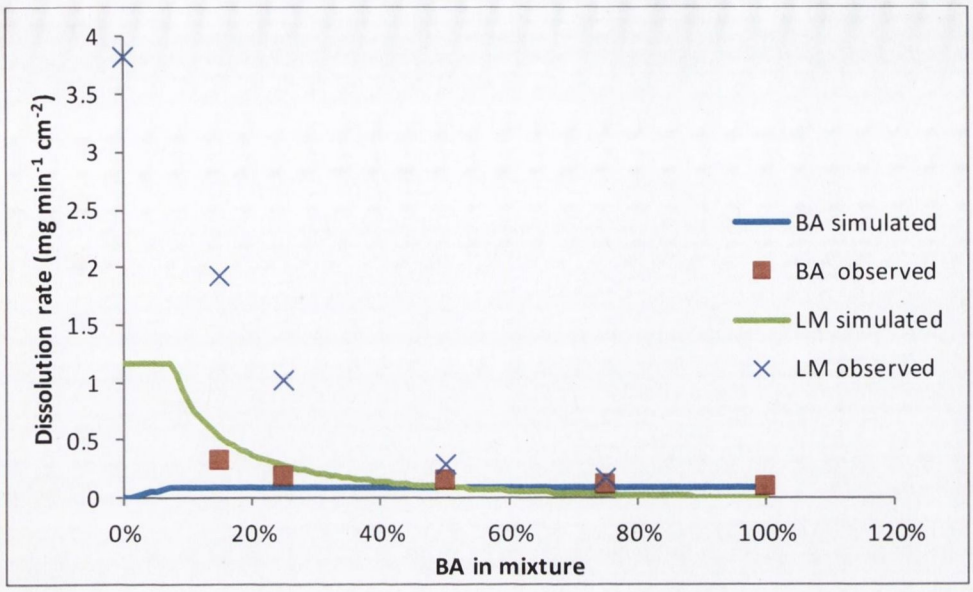


Figure 5. 6 Predicted and experimentally determined dissolution rates of BA and LM from different mixture compostition in the flow-through apparatus

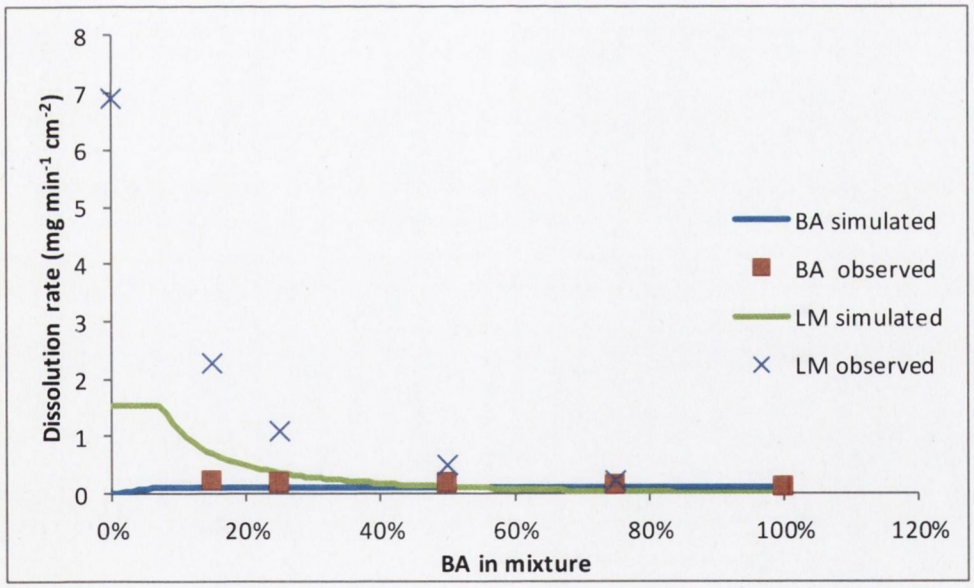


Figure 5. 7 Predicted and experimentally determined dissolution rates of BA and LM from different mixture composition in the free convection system.

Table 5. 5 Predicted and observed dissolution rate at different BA-LM composition in the paddle apparatus

BA in mixture	BA simulated (mg min^{-1} cm^{-2})	BA observed (mg min^{-1} cm^{-2})	Difference (Sim.-Obs.) /Obs.	LM simulated (mg min^{-1} cm^{-2})	LM observed (mg min^{-1} cm^{-2})	Difference (Sim.-Obs.) /Obs.
100%	0.439	0.442+/- 0.036	-0.70%	0	0	0
75%	0.439	0.420+/- 0.033	4.50%	0.146	0.137+/- 0.011	6.60%
50%	0.439	0.446+/- 0.043	-1.60%	0.439	0.416+/- 0.029	5.50%
25%	0.439	0.499+/- 0.015	-12.00%	1.317	1.435 +/- 0.035	-8.20%
15%	0.439	0.848+/- 0.011	-48.20%	2.488	4.365+/- 0.413	-43.00%
0%	0	0	0	5.46	8.517 +/- 0.399	-35.90%

Table 5. 6 Predicted and observed dissolution rate at different BA-LM composition in the flow-through apparatus.

BA in mixture	BA simulated ($mg\,min^{-1}\,cm^{-2}$)	BA observed ($mg\,min^{-1}\,cm^{-2}$)	Difference (Sim.-Obs.) /Obs.	LM simulated ($mg\,min^{-1}\,cm^{-2}$)	LM observed ($mg\,min^{-1}\,cm^{-2}$)	Difference (Sim.-Obs.) /Obs.
100%	0.0937	0.094+/-0.008	0	0	0	0
75%	0.0937	0.116+/-0.007	-19.20%	0.031	0.137+/-0.011	-77.20%
50%	0.0937	0.143+/-0.002	-34.40%	0.094	0.279+/-0.013	-66.40%
25%	0.0937	0.177+/-0.014	-46.90%	0.281	1.007+/-0.069	-72.10%
15%	0.0937	0.311+/-0.018	-69.90%	0.531	1.923+/-0.159	-72.40%
0%	0	0	0	1.165	3.240 +/-0.680	-64.00%

Table 5. 7 Predicted and observed dissolution rate at different BA-LM composition in the free convection system.

BA in mixture	BA simulated	BA observed (mg min^{-1} cm^{-2})	Difference (Sim.-Obs.) /Obs.	LM simulated (mg min^{-1} cm^{-2})	LM observed (mg min^{-1} cm^{-2})	Difference (Sim.-Obs.) /Obs.
100%	0.123	0.123+/- 0.003	0	0	0	0
75%	0.123	0.130+/- 0.012	-5.40%	0.041	0.215+/- 0.019	-81.00%
50%	0.123	0.167+/- 0.010	-26.30%	0.123	0.488+/- 0.019	-74.80%
25%	0.123	0.175+/- 0.008	-29.70%	0.368	1.101+/- 0.036	-66.60%
15%	0.123	0.220+/- 0.027	-44.10%	0.694	2.267+/- 0.160	-69.40%
0%	0	0	0	1.523	6.889+/- 1.700	-77.90%

The changes in the thickness of the diffusion boundary layer indicate changes in the local hydrodynamics. As shown in Figure 5.8, the thickness of the effective diffusion boundary layer (h) of different mixture compacts does not change significantly in the paddle apparatus, while the opposite is observed for the other testing apparatus. The slopes representing the BA dissolution rate at different BA-LM composition system in the flow-through apparatus and free convection system are 0.2605 and 0.1882, respectively, suggesting that h is very different at different BA-LM composition system. Additionally, the effective diffusion boundary layer thickness (h) of 100% LM compact was very different at different apparatuses (Figure 5.9). The h of 130 μm in the flow-through apparatus was the highest of the three apparatuses.

The h in the flow-through apparatus and the free convection system were initially different and increased with increasing amount of BA in the mixture compact (Figure 5.8). The

observed dissolution rates of LM were higher than the predicted result under low velocity condition (Table 5.6 and 5.7), as the same h was used in the original theory from Higuchi and coworkers (Higuchi, Mir et al. 1965). However, the dissolving of freely soluble LM can affect local density gradient and local hydrodynamics under low velocity condition as detailed in Chapter 4, indicating that h would be changed at different BA-LM composition under low velocity environment.

Moreover, the high ratio of LM: BA in the mixture compact could lead to a surface roughness as the LM dissolved, which may produce more eddies on the compact surface and increase the dissolution rate of BA. Therefore, it is necessary to consider the effect of natural convection in the current study.

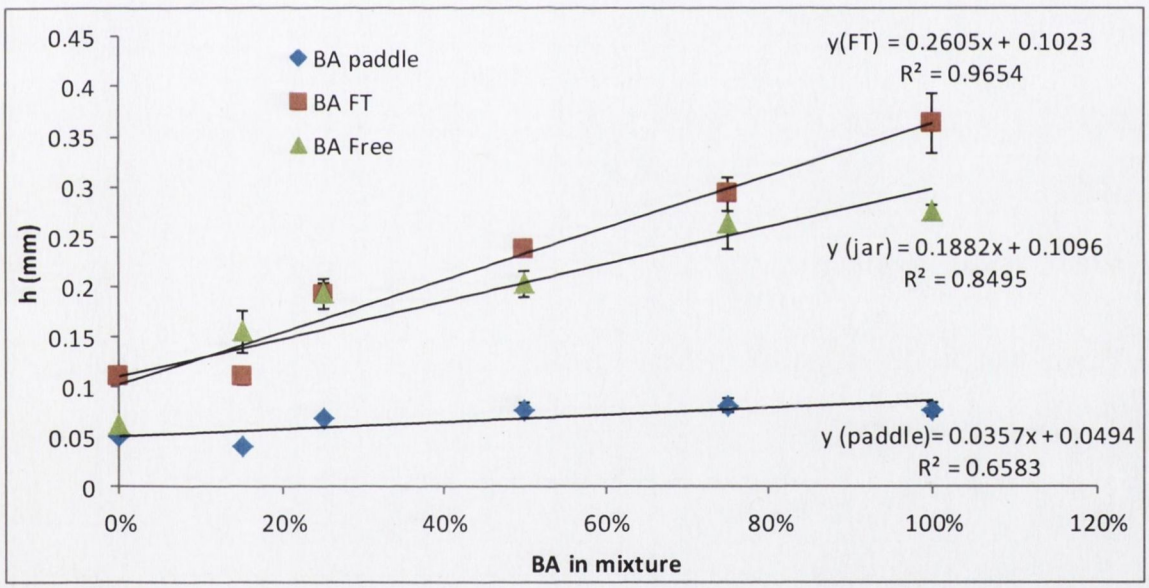


Figure 5. 8 Effective diffusion boundary layer thickness (h) of BA at 100%, 75%, 50% ,25% and 15% BA mixture compacts.

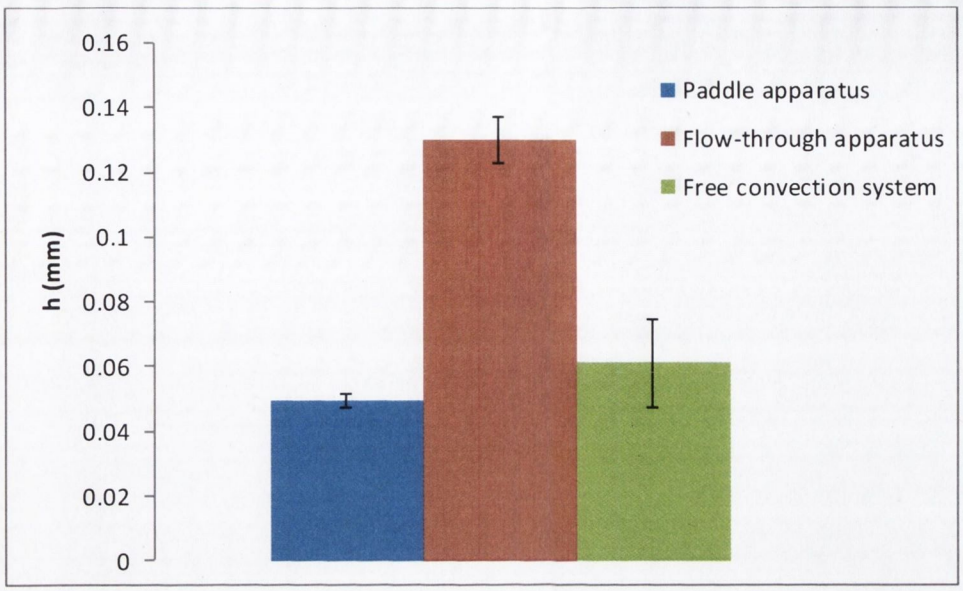


Figure 5. 9 The effective diffusion boundary layer thickness (h) of 100% LM compact.

5.4.2 Modification of the theory from Higuchi and coworkers by an empirical method to account for differing h value.

In order to address the issue of changing h values under low velocity conditions - which may result from natural convection, an empirical method was developed.

The relationship between the h and the amount of BA in mixture compact were obtained from the fitted lines, illustrated in Figure 5.8, and can be described by the following equations:

$$h' = 0.2605x + 0.1023$$

Equation 5. 8 (flow-through apparatus)

$$h' = 0.1882x + 0.1096$$

Equation 5. 9 (free convection system)

Where x is the percent of BA in the mixture and h' is the adapted h according to observed value

Furthermore mathematical modification using Equation 5.4 and 5.6, lead to the following expressions assuming 3 different cases:

1) When $N_{BA}/N_{LM}>(D_{BA}C_{BA})/(D_{LM}C_{LM})$, which described the situation where the critical mixture ratio is exceeded and LM dissolves fast enough to leave a layer of pure BA behind, the dissolution rate is only controlled by one of the components (Higuchi, Mir et al. 1965).

In this case, the BA layer controls the dissolution and the dissolution rates (R_{BA} and R_{LM}) can be estimated using the following two equations:

$$R_{BA} = \frac{D_{BA}C_{BA}}{h'}$$

Equation 5. 10

$$R_{LM} = \frac{A_{LM}D_{BA}}{A_{BA}h'} = \frac{N_{LM}}{N_{BA}}R_{BA}$$

Equation 5. 11

2) When $N_{BA}/N_{LM}<(D_AC_{SA})/(D_BC_{SB})$, component BA dissolves fast enough to leave a layer of pure LM behind and only the LM phase controls the dissolution. In this case, the dissolution rates can be calculated as described by Equation 5.12 and 5.13.

$$R_{BA} = \frac{A_{BA}D_{LM}}{A_{LM}h'} = \frac{N_{BA}}{N_{LM}}R_{100\%LM}$$

Equation 5. 12

When 0 was used to replace x in Equation 5.11, $h_{100\%LM}=0.1023$ and then

$$R_{100\%LM} = \frac{D_{LM}C_{LM}}{h_{100\%LM}}$$

Equation 5. 13

Where N_{BA} and N_{LM} are the original amounts of BA and LM in the mixture; D_{BA} and D_{LM} are the diffusion coefficient of BA and LM; C_{BA} and C_{LM} are the solubility of BA and LM; R_{BA} and R_{LM} are the dissolution rate of BA and LM; $h_{i\%BA}$ and $h_{100\%LM}$ are the thickness of effective diffusion boundary layer for BA at different BA-LM composition system and LM at 100 % LM system respectively.

Figure 5.10 and 5.11 and Table 5.8 and 5.9, respectively, illustrates the comparison between predicted and experimentally determined dissolution rates in the flow-through apparatus and free convection system

The empirical method (Figure 5.10, Table 5.8 and Figure 5.11, Table 5.9) agreed better than the original method (Figure 5.6, Table 5.6 and Figure 5.7, Table 5.7), as predicted dissolution results of BA and LM have a better agreement with observed results in the flow-through apparatus as well as that in the free convection system.

In the flow-through apparatus, it is notable that the predicted dissolution rate of BA from the 15% BA mixture compacts based on the empirical method is lower than the rate observed, suggesting that the hydrodynamics resulting from the high proportion of soluble LM in this compact may affect the dissolution rate detailed in Chapter 4.

This indicates that the empirical method can represent the effect of natural convection on the dissolution rate, as the changing of h resulting from the density gradient can be predicted by the empirical method. However, the empirical method is based on fitting a linear relationship of the experimental data at different proportion of LM in the mixture and the natural convection effect may result in a non-linear relationship at different BA-LM composition compact. Therefore, the empirical method may not be a precise prediction of the effect of the change in h with LM content.

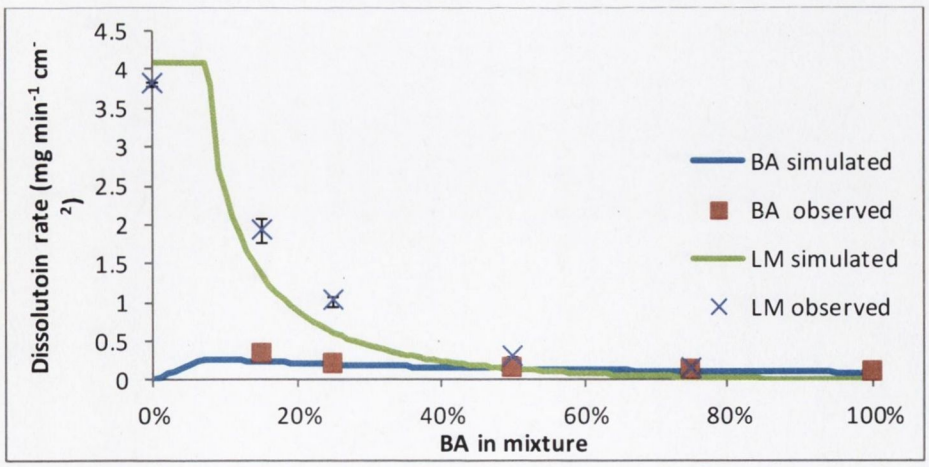


Figure 5. 10 Predicted (empirical method) and experimentally determined dissolution rates of BA and LM from different BA-LM composition compacts in the flow-through apparatus.

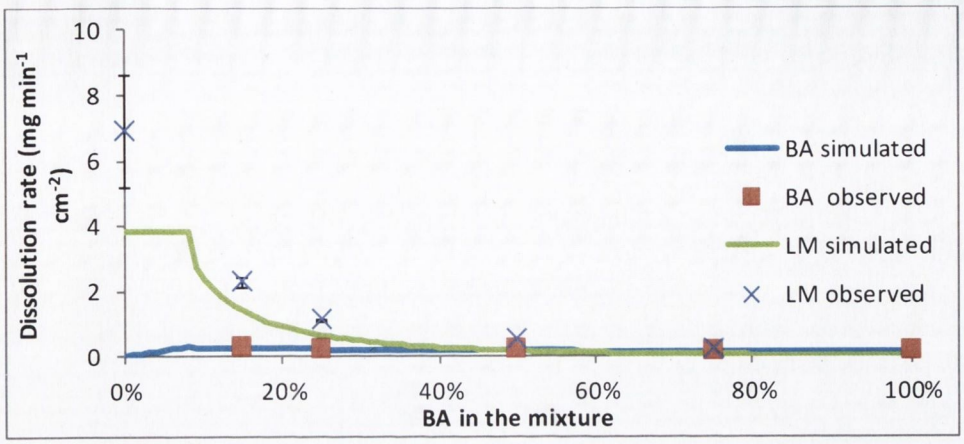


Figure 5. 11 Predicted (empirical method) and experimentally determined dissolution rates of BA and LM from different BA-LM composition compacts in the free convection system.

Table 5. 8 Predicted (empirical method) and experimentally determined dissolution rates of BA and LM from different BA-LM composition compacts in the flow-through apparatus.

BA in mixture	BA simulated ($mg\,min^{-1}\,cm^{-2}$)	BA observed ($mg\,min^{-1}\,cm^{-2}$)	Difference (Sim.- Obs.) /Obs.	LM simulated ($mg\,min^{-1}\,cm^{-2}$)	LM observed ($mg\,min^{-1}\,cm^{-2}$)	Difference (Sim.-Obs.) /Obs.
100%	0.093	0.0937+/-0.0078	-0.50%	0	0	0
75%	0.114	0.116+/-0.0071	-2.10%	0.038	0.137+/-0.0114	-72.3%
50%	0.145	0.1429+/-0.0017	1.80%	0.145	0.279+/-0.0132	-47.9%
25%	0.203	0.1767+/-0.0143	14.30%	0.606	1.007+/-0.0687	-39.8%
15%	0.239	0.3109+/-0.0183	-23.10%	1.355	1.923+/-0.1586	-29.5%
0%	0	0	0	4.097	3.240 +/-0.6799	26.5%

Table 5. 9 Predicted (empirical method) and experimentally determined dissolution rates of BA and LM from different BA-LM composition compacts in the free convection system.

BA in mixture	BA simulated ($mg\,min^{-1}\,cm^{-2}$)	BA observed ($mg\,min^{-1}\,cm^{-2}$)	Difference (Sim.-Obs.) /Obs.	LM simulated ($mg\,min^{-1}\,cm^{-2}$)	LM observed ($mg\,min^{-1}\,cm^{-2}$)	Difference (Sim.-Obs.) /Obs.
100%	0.114	0.123+/-0.0028	-7.30%	0	0	0
75%	0.135	0.130+/-0.0122	3.80%	0.045	0.215+/-0.0191	-79.1%
50%	0.166	0.167+/-0.0103	-0.60%	0.166	0.488+/-0.0191	-66.0%
25%	0.216	0.175+/-0.0081	23.40%	0.648	1.101+/-0.0361	-41.1%
15%	0.245	0.220+/-0.0274	11.40%	1.390	2.267+/-0.1598	-38.7%
0%	0	0	0	3.836	6.889+/-1.6997	-44.3%

As LM dissolution rates in low velocity environment were lower than the observed resulting, these may be caused by the unsteady state of control layer in the theory from Higuchi and coworkers (Higuchi, Mir et al. 1965).

5.4.3 The steady state assumption in the theory from Higuchi and coworkers.

The predicted thickness of the phase boundary (ΔS, S_2-S_1) vs. time (t) in the different apparatuses was illustrated in Figure 5.11, 5.12 and 5.13. As the smallest mass fraction of 15% BA in the images was higher than the critical mass fraction (8%), the BA layer (ΔS) is the controlled layer detailed in section 5.4.1. The following process introduces how to predict the porosity and these parameters were used to predict ΔS and the tortuosity of BA is a constant of 3 (Higuchi, Mir et al. 1965).

$$\varepsilon_{LM} = \frac{A_{LM}}{\rho_{LM}}$$

Equation 5. 14

Where ε_{BA} is the porosity of BA.

As A_{LM} was different at different BA-LM composition system, the corresponding porosity was different. The predicted results are illustrated in Table 5.10.

Table 5. 10 The predicted porosity and tortuosity of BA in different BA-LM composition system.

% BA in BA-LM compact	Porosity	Tortuosity
75% BA	0.20	3
50% BA	0.40	3
25% BA	0.60	3
15% BA	0.68	3

From the predicted tortuosity and porosity (Table 5.10) and further derivations by using the Equation 5.1 and 5.2 allow calculation of S_1 and S_2, and subsequently simulation of ΔS versus time (t) as illustrated in Figure 5.12, 5.13 and 5.14. It was found that in the paddle apparatus system, the ΔS versus time (t) simulation, for different ratios of BA, is close to or reached the steady state at 900 seconds (Table 5.11). However, the simulated results in the flow-through apparatus and free convection system were not in the steady state at 900 seconds. The predicted ΔS of BA at 900 seconds in the different apparatuses are illustrated in Table 5.11.

Table 5. 11 The predicted ΔS of BA at 900 seconds in the different apparatuses

% BA in BA-LM compact	ΔS of BA, paddle apparatus (m)	ΔS of BA, flow-through apparatus (m)	ΔS of BA, free convection system (m)
75% BA	$1.1x10^{-4}$	$1.3 x10^{-4}$	$1.3x10^{-4}$
50% BA	$9.2x10^{-5}$	$1.1x10^{-4}$	$1.1x10^{-4}$
25% BA	$4.8x10^{-5}$	$7.5 x10^{-5}$	$7.8 x10^{-5}$
15% BA	$2.1x10^{-5}$	$4.8x10^{-5}$	$4.9x10^{-5}$

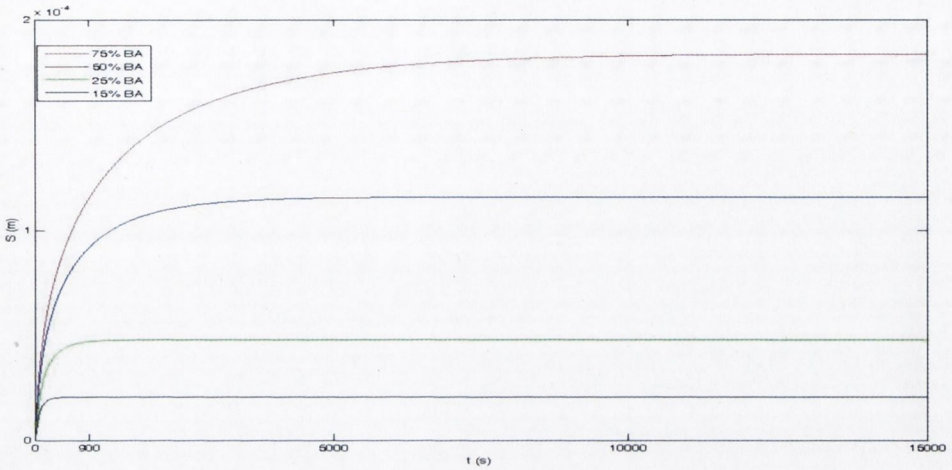


Figure 5. 12 The predicted (ΔS) vs. time at 75%, 50%, 25% and 15% BA in the paddle apparatus.

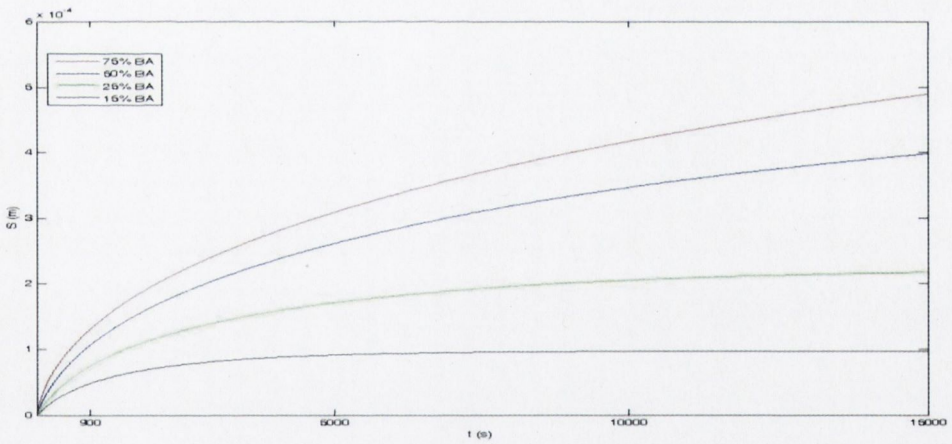


Figure 5. 13 The predicted (ΔS) vs. time at 75%, 50%, 25% and 15% BA in the flow-through apparatus.

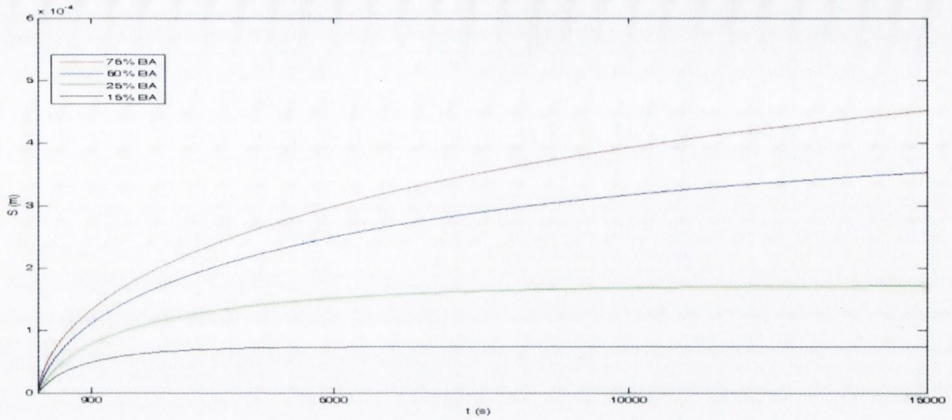


Figure 5. 14 The predicted (ΔS) vs. time at 75%, 50%, 25% and 15% BA in the free convection system.

The equation 5.15, was used to predict the dissolution rate of LM in the unsteady state in the low velocity system such as flow-through apparatus and free convection system.

When the ratio of BA in the mixture is more than 8.02% (critical point) the BA layer controls dissolution rate. As the system is not in the steady state, the predicted difference of S_1 and S_2 (Equation 5.8 and 5.9) was used to predict dissolution rate of LM using Equation 5.15.

$$R_{LM900} = \frac{D_{LM} C_{LM}}{h_{BA} + \left(\frac{\tau_{BA}}{\varepsilon_{LM}}\right)(S_2 - S_1)}$$

Equation 5. 15

Where R_{LM900} is the dissolution rate of LM at 900s; h_{BA} is the thickness of effective BA diffusion boundary layer.

The predicted results of LM at 15 minutes (900 seconds) in the flow through apparatus and free convection system are illustrated in Table 5.12 and Table 5.13, respectively.

The observed dissolution rate was the average dissolution rate over the first 15 minutes in the flow-through apparatus and free convection system as illustrated in Table 5.12 and 5.13. With time passed, ΔS was more close to steady state. This indicated that the dissolution rate was faster at the time point close to zero and slower at the time point closer to steady state. The time of 900 seconds was far from steady state at 75% and 50% BA-LM composition system,

indicating that the dissolution rate at 900 seconds may be higher than the average dissolution rate (Table 5.12) in the flow-through apparatus and dissolution rate at 900 seconds was slightly lower than the observed result in the free convection system. As the time of 900 seconds was close to steady state at 25% and 15% BA-LM composition system in the flow-through apparatus and free convection system, the dissolution rates were much lower than the average dissolution rate (Table 5.12 and 5.13).

Table 5. 12 The predicted dissolution rate of LM at 900 seconds in the flow-through apparatus.

BA in mixture	Predicted dissolution rate of LM ($mg\,min^{-1}\,cm^{-2}$)	Observed dissolution rate of LM ($mg\,min^{-1}\,cm^{-2}$)
75% BA	0.18	0.137+/- 0.0114
50% BA	0.35	0.279+/- 0.0132
25% BA	0.57	1.007+/- 0.0687
15% BA	0.73	1.923+/- 0.1586

Table 5. 13 The predicted dissolution rate at 900 seconds, surface concentration of LM and mass fraction of LM in the free convection system.

BA in mixture	Predicted dissolution rate of LM ($mg\,min^{-1}\,cm^{-2}$)	Observed dissolution rate of LM ($mg\,min^{-1}\,cm^{-2}$)
75% BA	0.19	0.215+/- 0.019
50% BA	0.38	0.488+/-0.019
25% BA	0.63	1.101+/-0.036
15% BA	0.85	2.267+/- 0.160

5.4.4 Using the adapted Higuchi equation to predict dissolution rate in the free convection system

The Equation 5.15 and 5.16 were used to predict surface concentration and mass fraction. The predicted dissolution rates from Equation 5.15 were input in Equation 5.16 in order to obtain the concentration of LM on the compact surface at 900s.

$$C_{LMsur} = \frac{R_{LM900} h_{BA}}{D_{LM}}$$

Equation 5. 16

Where C_{LMsur} is concentration of LM on the compact surface.

The mass fraction of LM on the compact surface was obtained from the surface concentration as illustrated in Equation 5.17. In addition the total mass of solution was assumed to be the total mass of dissolution media, as the mass of BA and LM only take small amount of total mass.

$$C'_{LM} = \frac{M_{LM}}{M_{total}} = \frac{C_{LMsur} V}{\rho_{HCl} V} = \frac{C_{LMsur}}{\rho_{HCl}}$$

Equation 5. 17

Where C'_{LM} is mass fraction of LM in the mixture; M_{LM} is the total mass of LM on the compact surface; M_{total} is the total mass on the compact surface; V is the volume of dissolution media on the compact surface; ρ_{HCl} is the density of dissolution media(0.1 M HCl).

The predicted results of surface concentration and mass fraction of LM is illustrated in Table 5.14 and these values were used to predict dissolution rates in the free convection system.

Table 5. 14 Predict surface concentration and mass fraction of LM in the free convection system.

BA in mixture	Surface concentration of LM (mg cm^{-3})	Mass fraction of LM
75% BA	27	0.03
50% BA	55	0.06
25% BA	91	0.09
15% BA	123	0.12

As discussed (Section 5.4.2), the observed dissolution rate of BA in the free convection system increased with an increase of LM fraction in the compact mixture, indicating that the local natural convection resulting from the density gradient of LM affecte d the dissolution rate. The dissolved LM on the compact surface can change the density gradient surrounding the

compact surface. Then resulting natural convection would further change the dissolution rate of BA. Therefore, the estimation of the concentration of LM on the compact surface is investigated in the current study to estimate the density gradient induced by LM.

The total density close to liquid solid interface in the free convection system is illustrated in Equation 5.18.

$$\rho_{mix} = \frac{1}{\frac{C'_{BA}}{\rho_{BA}} + \frac{C'_{LM}}{\rho_{LM}} + \frac{1 - C'_{BA} - C'_{LM}}{\rho_{HCl}}}$$

Equation 5. 18

Where ρ_{HCl} is the density of the pure dissolution medium (995 kg m^{-3}), ρ_{mix} is the density of the solution mixture of BA and LM; C'_{BA} is the mass fraction of BA on the compact surface. As there is a saturated BA diffusion film on the compact surface, the mass from of BA is from saturated solubility.

Thus the density difference of the mixture solution and the dissolution medium is illustrated in the following equation:

$$\Delta\rho = \rho_{mix} - \rho_{HCl}$$

Equation 5. 19

Substituting the Equation 5.19 in to the free convection Equation 3.3 in Chapter 3, the following equation (dissolution rate of BA) is obtained:

$$R_{BA} = 0.673 \left(\frac{g L_w^3 (\rho_{mix} - \rho_{HCl})}{D v \rho} \right)^{\frac{1}{4}} C_s \frac{D}{L_w}$$

Equation 5. 20

The predicted dissolution rate in the free convection system is detailed in Table 5.15. The predicted dissolution rate of BA was higher than the observed dissolution rate from different BA-LM composition systems. This was possibly because the effect of surface concentration of LM was overestimated in the current study. As the prediction based on 15 minutes (900

seconds) was not in the steady state and only obtained from one time point in the free convection system (Figure 5.14, Table 5.13), the predicted surface concentration of LM may not represent average concentration of LM over 15 minutes. Furthermore, the remaining slope of simulated dissolution rate of -0.132 was similar to that of the observed value of -0.128 (Figure 5.15), except simulated and observed dissolution rate of 100% BA, indicating the current model can interpret the trend of dissolution rate change at different BA-LM composition systems.

Table 5. 15 Predicted and observed dissolution rate at different ratio of compacts using natural convection

BA in mixture	BA simulated	BA observed ($mg\,min^{-1}\,cm^{-2}$)	Difference (Sim.-Obs.) /Obs.	LM simulated ($mg\,min^{-1}\,cm^{-2}$)	LM observed ($mg\,min^{-1}\,cm^{-2}$)	Difference (Sim.-Obs.) /Obs.
100%	0.147	0.123+/-0.0028	19.5%	0	0	0
75%	0.208	0.130+/-0.0122	60.0%	0.069	0.215+/-0.0191	-67.9%
50%	0.245	0.167+/-0.0103	46.7%	0.245	0.488+/-0.0191	-49.8%
25%	0.270	0.175+/-0.0081	54.3%	0.811	1.101+/-0.0361	-26.3%
15%	0.291	0.220+/-0.0274	32.3%	1.647	2.267+/-0.1598	-27.3%
0%	0	0	0	6.744	6.889+/-1.6997	-2.10%

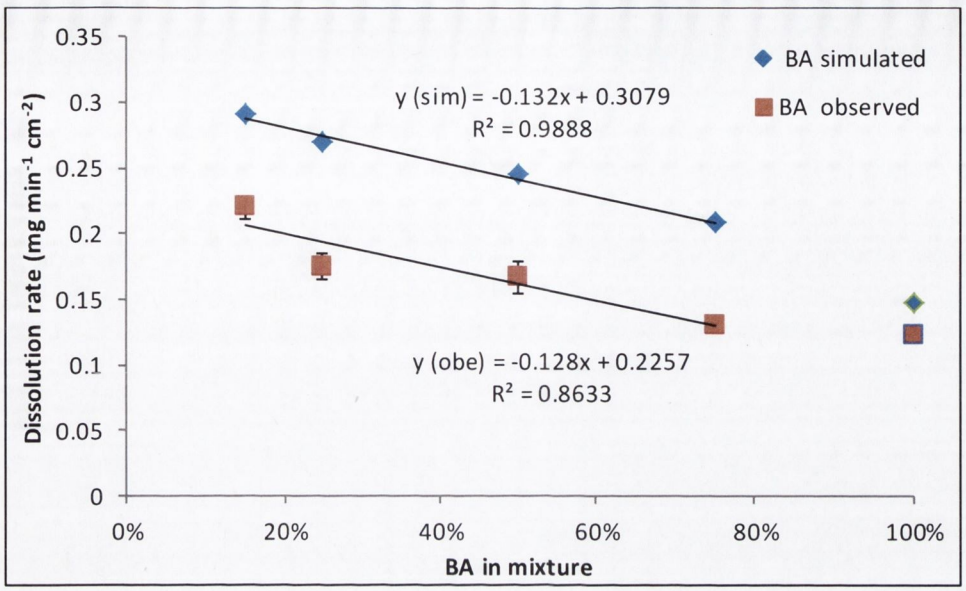


Figure 5. 15 Simulated and observed dissolution rate of BA in the free convection system

5.5 Conclusion

Compacts composed of mixtures of two compounds were tested in the paddle apparatus, the flow-through apparatus and the free convection system. The theory from Higuchi and coworkers predicted the dissolution rate of both compounds well in the paddle apparatus (Higuchi, Mir et al. 1965). An empirical method was developed to predict dissolution rate of BA and LM in the low velocity environment. Furthermore, a theoretical method based on the combination of the free convection theory and the theory from Higuchi and coworkers was attempted to predict dissolution rate in a low velocity environment. This method could be more effective, if the LM density gradient on the compact surface was accurately evaluated.

Chapter 6 *IVIVC* study of carbamazepine using the flow-through apparatus

6.1 Introduction

Carbamazepine (CBZ) is a drug widely used to treat epilepsy and trigeminal neuralgia that belongs to class II of biopharmaceutics classification system (BCS) (Jung, Milan et al. 1997; Lake, Olling et al. 1999; El-Massik, Abdallah et al. 2006; Kovacevic, Parojcic et al. 2008). In the current study, it was selected as a model drug to evaluate the correlation of *in vitro* dissolution data based on the flow-through apparatus and published *in vivo* data (Kovacevic, Parojcic et al. 2008). A BCS Class II drug is a substance with low solubility and high permeability and its absorption is controlled by the dissolution rate of the drug which in turn depends on different factors such as pH value, volume of the dissolution medium and the presence of surfactants. Therefore, a proper *in vitro* dissolution method is important for CBZ in order to achieve a better *in vitro in vivo* correlation (*IVIVC*) to predict the bioavailability of a CBZ formulation.

Due to the low solubility of CBZ (0.23 mg/ml at 37 °C) (Lee, Park et al. 2005), previous studies used different *in vitro* methods and dissolution media and high fluid agitation apparatus (Meyer, Straughn et al. 1992; Jung, Milan et al. 1997; Lake, Olling et al. 1999; Lee, Park et al. 2005; El-Massik, Abdallah et al. 2006; Kovacevic, Parojcic et al. 2008). An earlier dissolution test proposed by the FDA in 1987 used co-solvents containing 10.5% alcohol and 0.1% tween 20 as the dissolution medium and subsequently a dissolution test in the paddle apparatus using 900 ml 1% sodium lauryl sulfate (SLS) at 75 rpm was recommended by the USP XXII (1990). Additionally, the dissolution test of CBZ with 1% SLS demonstrated an inconsistency of *in vitro* and *in vivo* data in previous reports (Meyer, Straughn et al. 1992; Jung, Milan et al. 1997). The discrimination using the USP XXII method for different formulations of CBZ was not consistent with the observed plasma concentrations (Jung, Milan et al. 1997).

Furthermore, the SLS used in the dissolution test determined a different behaviour in terms of contact angle or surface tension to that of bile salt solution (Luner 2000). Therefore, the wetting behaviour of the bile salt solution was significantly different to that of the surfactant (Luner 2000). Thus, the *in vitro* dissolution method using 1% SLS may be not the best biorelevant method. As a result, a new *in vitro* dissolution test with less or no SLS at low agitation system is required to develop IVIVC in the current study. Furthermore, the low agitation system is more biorelevant as is detailed in section 1.4.4. Additionally, it is evident

that low flow rates can allow formulation effects on dissolution rate to be highlighted as detailed in section 5.3.

Kovacevic et al also carried out the *in vitro* dissolution test in 900 ml 1% SLS at 75 rpm and integrated these dissolution results into Gastroplus™ (Kovacevic, Parojcic et al. 2008). This is an unconventional method to develop an *IVIVC*. As Kovacevic et al used Tegretol IR and CR tablets in their investigation and thus those *in vivo* experimental data was available for these formulations. Therefore, these CBZ formulations were also investigated in the current study. Dissolution results at different rotation speeds from the Tegretol tablets used in the published study were obtained (J. Parojcic, personal communication). The same dissolution tests as reported from the tablets used in the published work were carried out in order to establish the similarity of the Tegretol tablets used in the current work. Moreover, a similar dissolution result was observed in the low rotation environment in the paddle apparatus, which could be comparable to the low velocity conditions in the flow-through apparatus. If the *in vivo* dissolution can be estimated by an *in vitro* dissolution method, it is is possible to establish an *IVIVC* in the current study. The different flow rates of 8, 16 and 32 ml min^{-1} in the 22.6 mm flow-through cell were considered in order to find an appropriate *in vitro* dissolution method.

The objectives of the current study are

to evaluate the use of the low velocity USP 4 dissolution apparatus with water as a dissolution medium, in the open loop system flow-through configuration, to generate an *IVIVC* with Tegretol IR and CR tablets. Both a conventional *IVIVC*, comparing fraction dissolved and fraction absorbed, and an unconventional *IVIVC*, using dissolution profiles with Gastroplus software, will be investigated.

6.2 *In vitro* dissolution study of Tegretol IR and CR tablets

6.2.1 The *in vitro* dissolution test of Tegretol IR in the paddle apparatus.

The *in vitro* dissolution data was provided by J. Parojcic (J. Parojcic, personal communication) as a control group. The dissolution under different pH dissolution media was carried out by J. Parojcic group. The CBZ release in the paddle apparatus was not affected by the pH value, since the release profiles were nearly overlapping in dissolution media of different pH values at 75 rpm (Kovacevic, Parojcic et al. 2008). Moreover, the dissolution under different ratio of

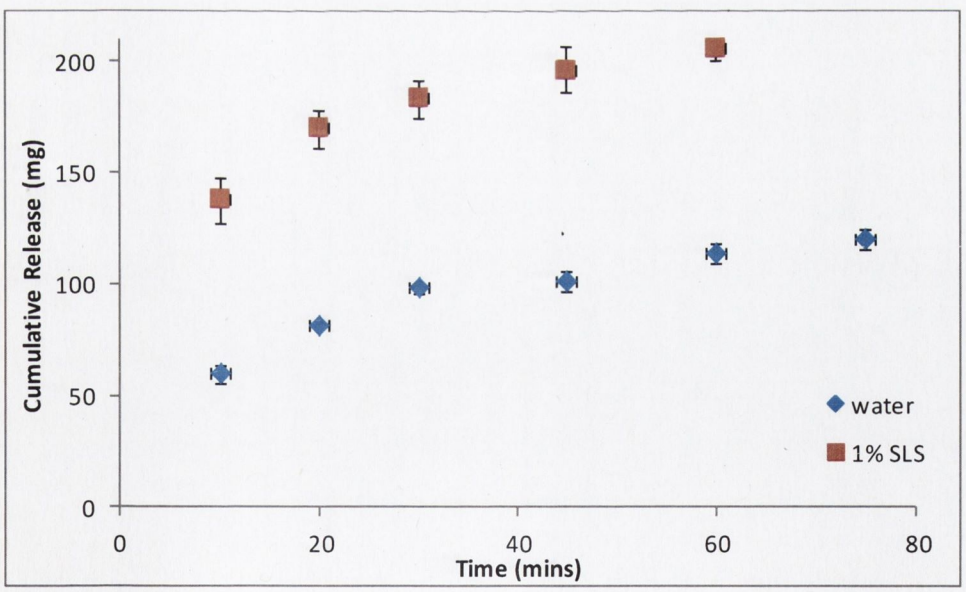
surfactant performed by J. Parojcic group was control value. In the current study, we also repeat the dissolution under different ratio of surfactant in the paddle apparatus. However, the *in vitro* release measured in the current work is faster than the control result at 50 and 75 rpm (Figure 6.1 A and B). A decreasing release profile with decreasing agitation rate was observed with a low release of about 5% at the first 10 minutes at low agitation conditions at 25 rpm (Figure 6.1C). The differing profiles with changing agitation rate indicated that the agitation degree would significantly affect the *in vitro* CBZ release.

As the Tegretol tablets used in the current study were from a different manufacturing site to that of the control group used for the *in vivo* experiments, the comparison of these *in vitro* dissolution results is necessary to ensure that the reported *in vivo* data could be utilized in the current work. The f_2 was used to assess similarity of the *in vitro* dissolution profiles of the Tegretol tablets as illustrated in Table 6.1. An f_2 value between 50 and 100 ensures equivalence. As the f_2 factors of 94.41, 99.43 and 88.58 in water, 0.1% and 1% SLS at 25 rpm, this indicated that the similarity of the dissolution profile was good at 25 rpm. The dissolution at 25 rpm determined a similar release in the current study and the data provided by J. Parojcic (J. Parojcic, personal communication). Moreover, it was interesting that the dissolution profile is similar with the dissolution media with 0.1% SLS and water at 25rpm. Additionally, the maximum flow velocity was approximately 0.006 m s^{-1} at the centre of the base of the vessel at 25 rpm in the paddle apparatus (D'Arcy 2007) which was similar to the simulated flow velocity of 7.5×10^{-3} ms^{-1} in the 2-D GI tract (Pal, Indireshkumar et al. 2004). Although this flow velocity at 25 rpm in the paddle apparatus was not too much different to that predicted in the GI tract, the way of mixing and exposing of particles in the dissolution medium in the paddle apparatus was different to that in the GI tract.

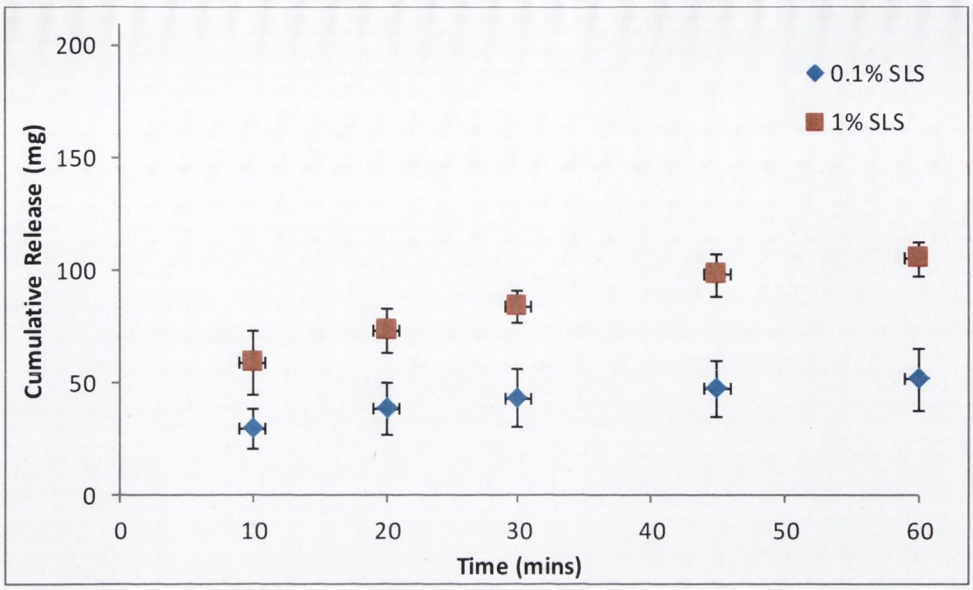
Table 6. 1 The f_2 factor was used to evaluate the observed dissolution profile compared to the reported result. ($50<f_2<100$ ensures sameness or equivalence)

rotation speed	25 rpm		
dissolution media	water	0.1% SLS	1% SLS
f_2	94.41	99.43	88.58

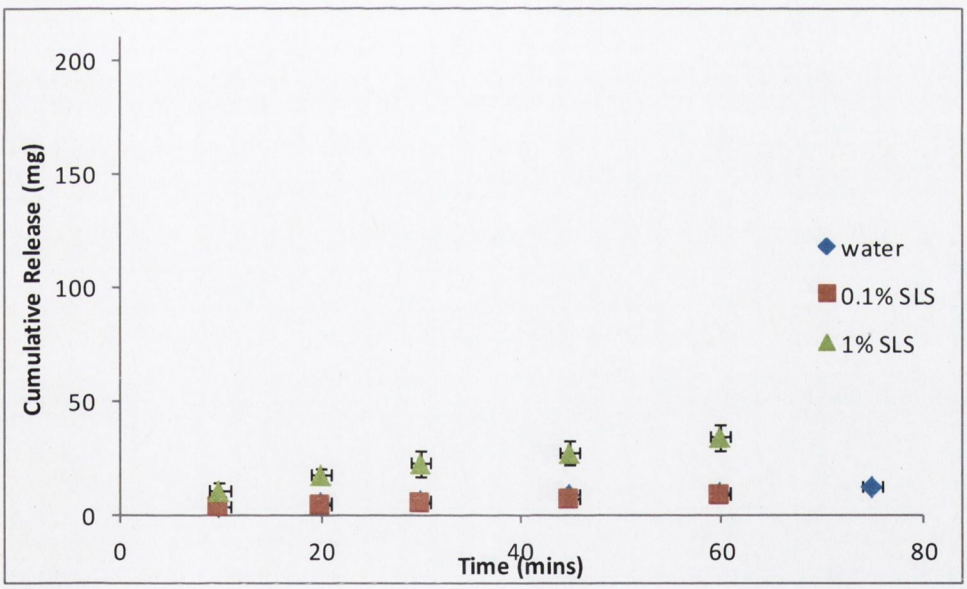
Furthermore, the release speed of Tegretol IR is much lower after 20 minutes in the paddle apparatus with water at 75 rpm compared to that in 1% SLS (Figure 6.1 A). After a two hour dissolution test, its release was no more than 60%. In addition the concentration of CBZ after 2 hours of dissolution in water was around 0.118 mg ml^{-1} which was the half of the solubility of CBZ (0.23 mg/ml in water at 37°C)(Lee, Park et al. 2005). This difference in the dissolution media of water and 1% SLS at 75 rpm indicated that the lack of sink conditions limits the dissolution of Tegretol IR in water and a surfactant was required if a dissolution test of Tegretol IR was conducted in the paddle apparatus. Due to the combined effect of 1% SLS at 75 rpm, the release at 10 minutes was around 65% during the current research. However, the drug dissolution in the Gastrointestinal (GI) tract is very different to that observed in the paddle apparatus. The paddle method based on high rotation speed and high concentration of surfactant may not be an optimal *in vitro* method to evaluate the release from Tegretol tablets as detailed in section 6.1. Therefore, a lower agitation system was investigated, to ensure sink conditions, without the need for a high concentration of surfactant, an open system configuration was used.



A



B



C.

Figure 6. 1 CBZ release in different conditions: A. CBZ release in water and 1% SLS at 75 rpm; B. CBZ release in 0.1% and 1% SLS at 50 rpm; C. CBZ released in water, 0.1% and 1 % SLS at 25 rpm.

6.2.2 Dissolution of Tegretol IR in the flow-through apparatus.

One of the advantages of the flow-through apparatus is to assure sink conditions with an unlimited use of dissolution media (Bhattachar, Wesley et al. 2002). When the flow-through apparatus was used in the Tegretol IR dissolution test with water as dissolution medium, sink conditions could be ensured.

The *in vitro* dissolution profile of Tegretol IR in the open loop of the flow-through apparatus at different flow rates is illustrated in Figure 6.2. The release of Tegretol IR is no more than 20% in the first 10 mins at flow rates from 8 to 32 ml min^{-1}. The dissolution rate of Tegretol IR increased with increasing flow rate. However, the difference in the dissolution profile between 16 ml min^{-1} and 8ml min^{-1} is more obvious than that between 32ml min^{-1} and 16ml min^{-1}.

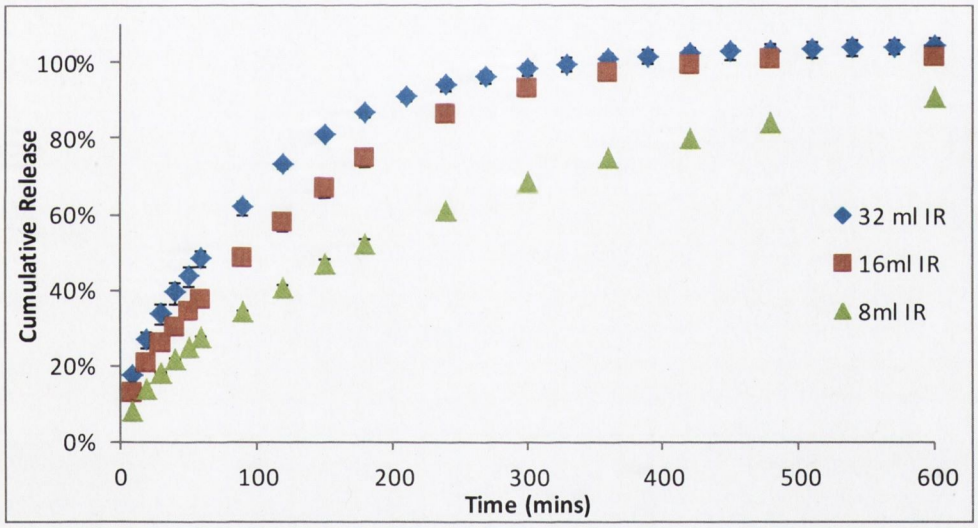


Figure 6. 2 Dissolution in the flow-through apparatus with different flow rates. Tegretol IR observed in 8, 16 and 32 ml min^{-1}.

The CBZ concentration in the dissolution medium at each time point in the open loop system is as shown in the Fig 6.2. The concentrations at 10 minutes (first sampling time) at 8, 16 and 32 ml min^{-1} were approximately 0.19, 0.15 and 0.10 mg ml^{-1}, respectively. As the sink condition is usually defined the volume of medium is at least three times great than that required to form saturated solubility (Dressman 2005) and the solubility of CBZ at 37°C is 0.23 mg ml^{-1}, the limit concentration is 0.077 mg ml^{-1}. The concentration at most sample times of Tegretol IR in the first hour at 8 and 16 ml min^{-1} were higher than that of the arbitary limit.

Thus, the best *in vitro* flow rate meeting the requirement of sink conditions is 32 ml min^{-1}, except the first sample point at 32 ml min^{-1}, which is a bit lower than the limit. However, when the fresh medium flows in the cell, the concentration in the cell during the dissolution is not constant and will always be periods where the concentration is lower than the sink conditions.

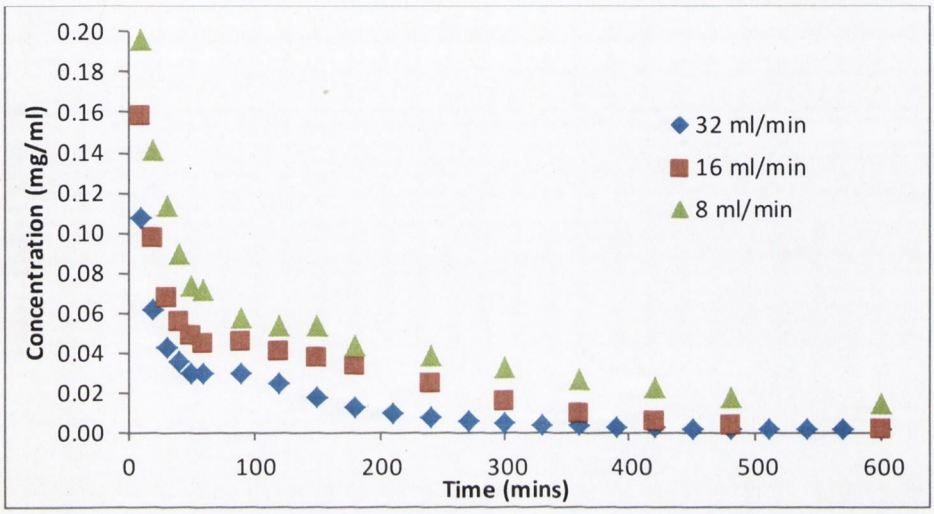


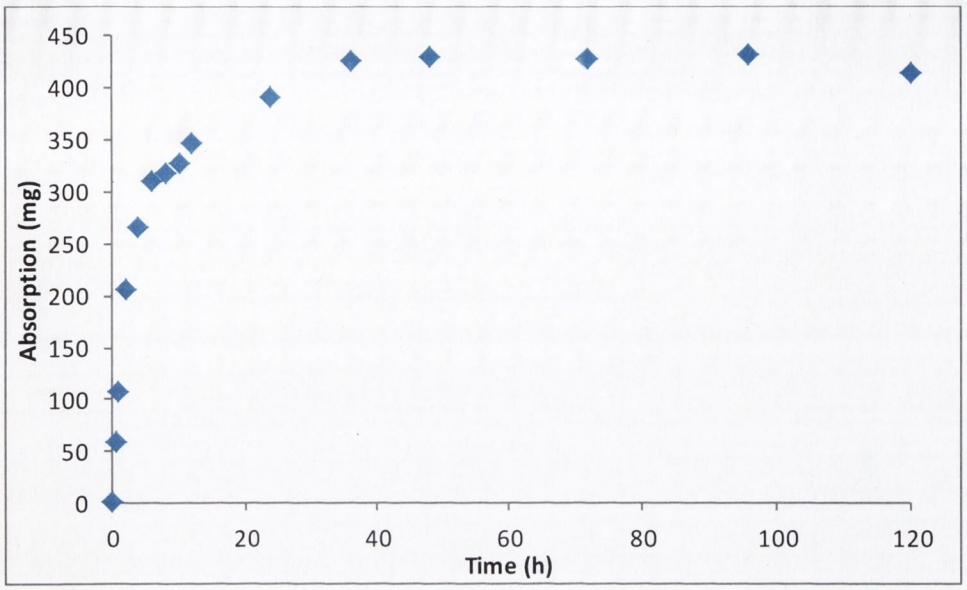
Figure 6. 3 The CBZ concentration at each sampling point for Tegretol IR and CR at different input flow rate. Tegretol IR at 8, 16 and 32 ml min^{-1}.

6.3 Using *in vitro* dissolution data to generate *IVIVC.*

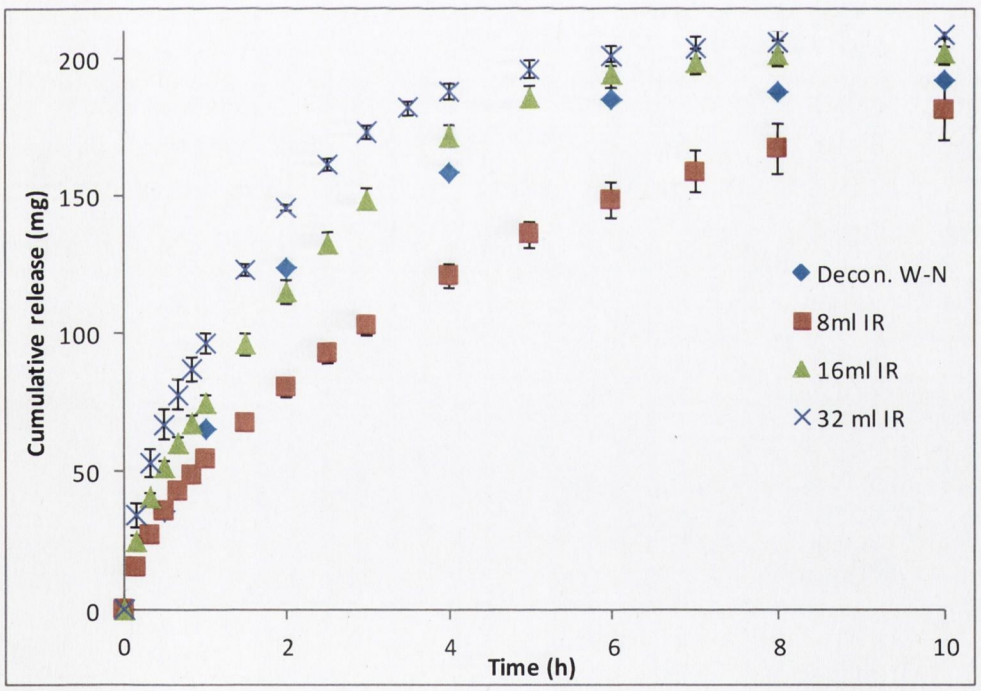
6.3.1 Deconvolution of observed plasma concentration profile of Tegretol IR based on Wagner-Nelson method

The Wagner-Nelson method (Wagner and Nelson 1963) was implemented to generate an absorption profile from the dissolution profile of Tegretol IR (Kovacevic, Parojcic et al. 2008). The method using the Wagner-Nelson equation was illustrated from Equation 1.21 to 1.23. The elimination rate of 0.0237 h^{-1} was obtained by fitting a line through the logged concentration-time data, using the last four points up to 96 hours, from the published *in vivo* data (Kovacevic, Parojcic et al. 2008).

The absorption profile of Tegretol IR and CR over 100 hours and absorbed plotted with dissolution profile at different flow rates are illustrated in Figure 6.4 and 6.5. The release was about 80% at approximately 12 hours for the Tegretol IR tablet.

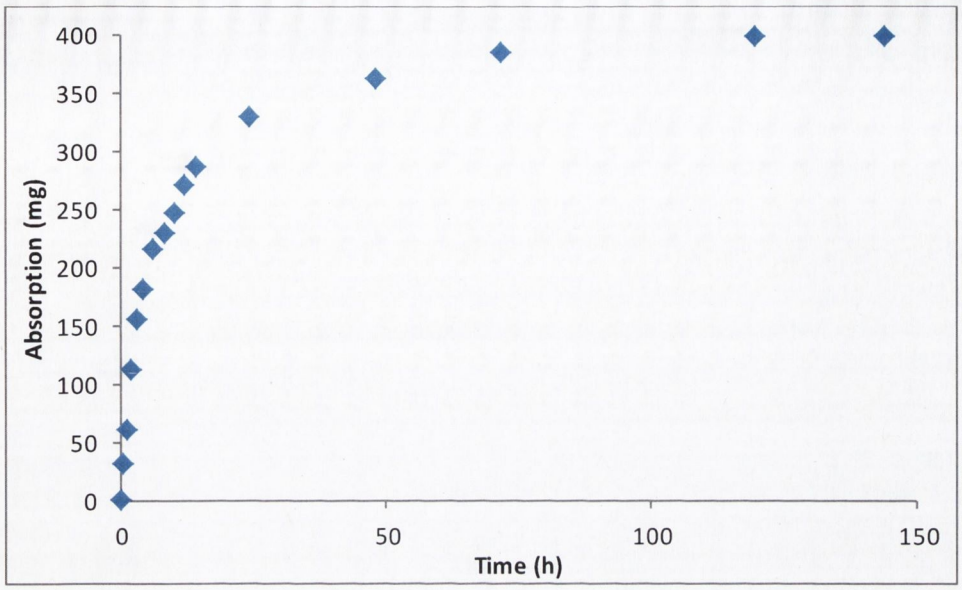


A

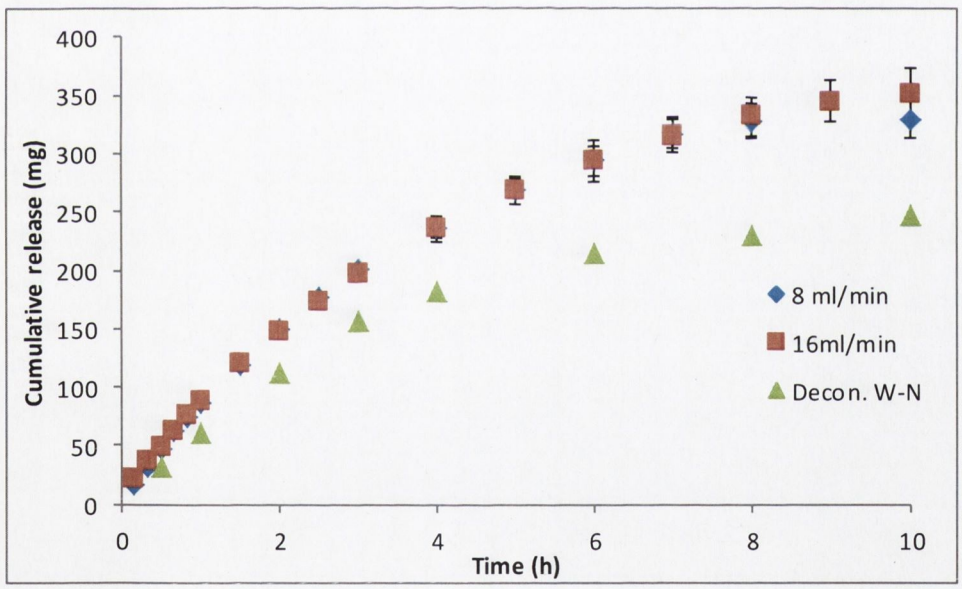


B

Figure 6. 4 The Tegretol IR profile absorption based on Wagner-Nelson equation, A. Absorption profile over 100 hours; B. absorption profile and *in vitro* dissolution profile at 8, 16 and 32 ml min^{-1}.



A



B

Figure 6. 5 The Tegretol CR absorption profile based on Wagner-Nelson equation, A. Absorption profile over 100 hours; B. absorption profile and *in vitro* dissolution profile at 16 ml min^{-1}.

The fraction absorbed of Tegretol IR plotted against the fraction dissolved is illustrated in Figure 6.6. When dissolution did not occur (x=0) at 8 ml min^{-1}, the positive intercept of

absorption of 0.0721 implied absorption is faster than dissolution which is impossible. Furthermore, the correlations at 16 of 0.9962 was similar to that of 0.9965 at 32 ml min^{-1}.

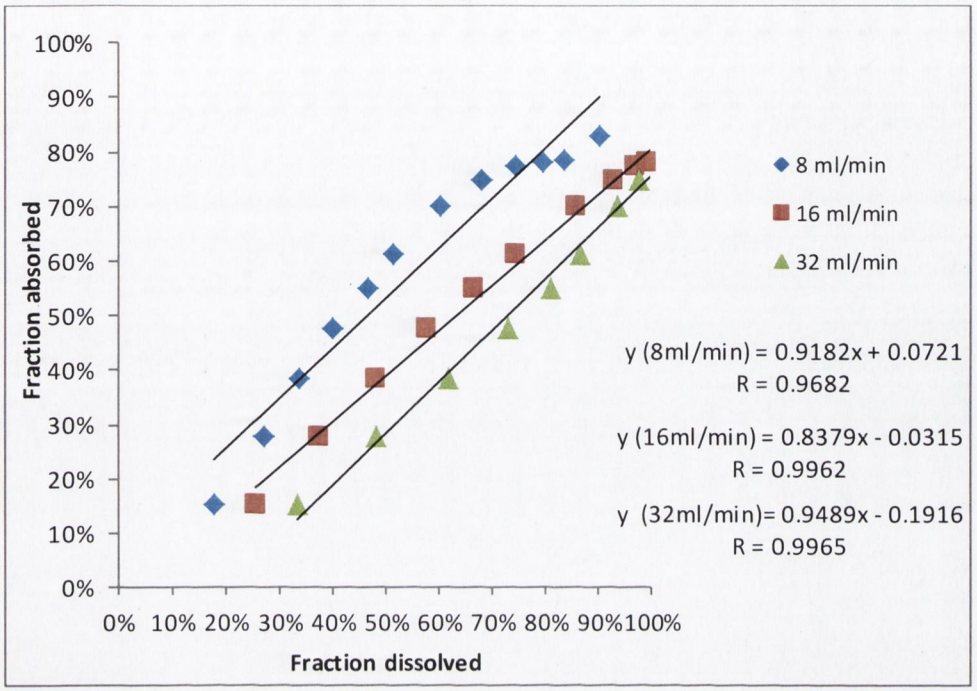


Figure 6. 6 The deconvoluted fraction absorbed based on the Wagner-Nelson method plotted against the fraction dissolved at inflow rate of 8, 16 and 32 ml min^{-1} in the flow-through apparatus for Tegretol IR.

As dissolution was also available from the Tegretol CR at 16 ml min^{-1}, this flow rate was selected to establish an *IVIVC* using both Tegretol IR and CR dissolution data. The *IVIVC* result of absorption profile plotted against *in vitro* cumulative release at 16 ml min^{-1} is illustrated in Figure 6.7. The correlation coefficient and the slope of the regression line were 0.9895 and 0.7963, respectively, indicating that the *in vitro* dissolution method at 16 ml min^{-1} using water as dissolution medium were biorelevant dissolution testing conditions for Tegretol IR, with a good correlation between fraction absorbed and fraction dissolved for two different CBZ formulations.

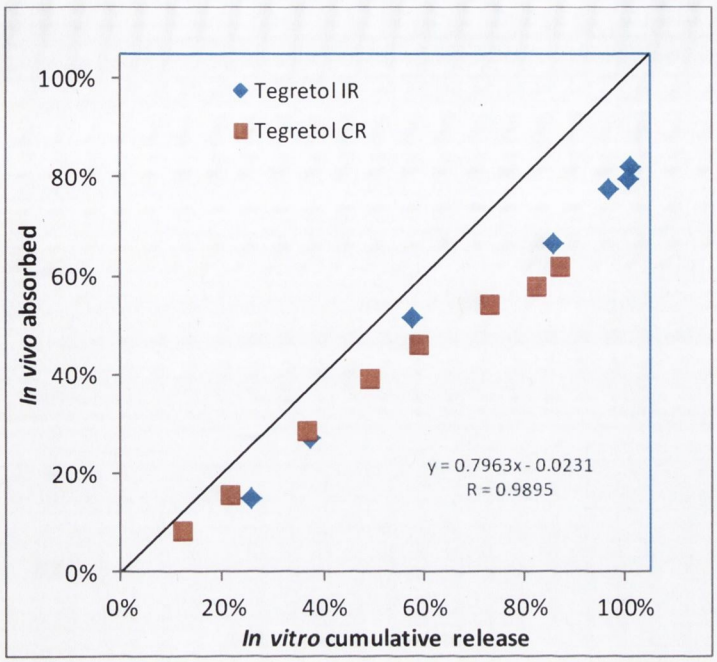


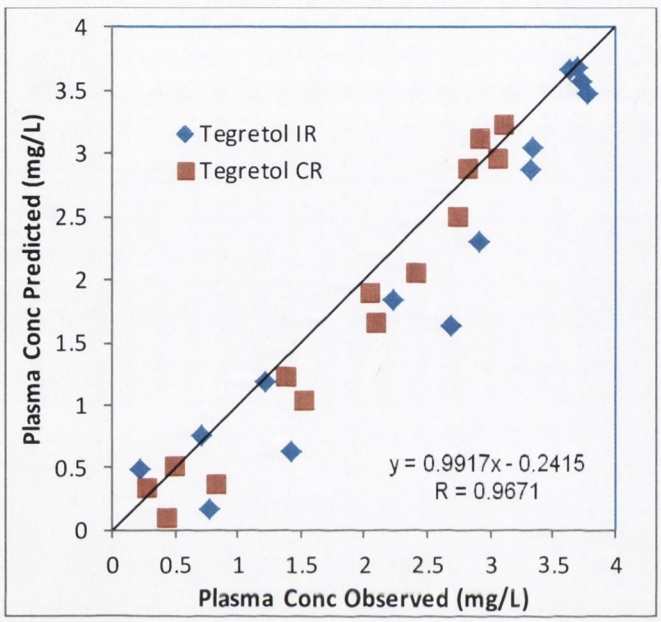
Figure 6. 7 *IVIVC* plot for the deconvoluted fraction absorbed dose based on the Wagner-Nelson method against the *in vitro* cumulative release at flow rates of 16 ml min^{-1} in the flow-through apparatus

6.3.2 *IVIVC* result based on simulated result of Gastroplus™ and observed *in vivo* result.

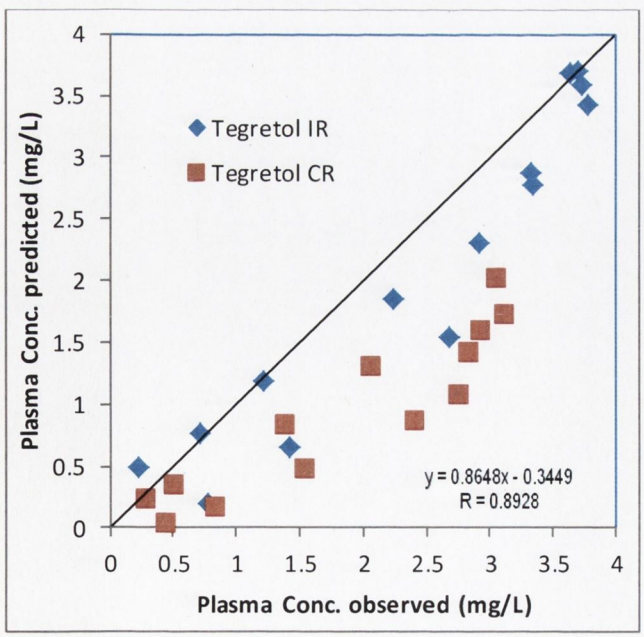
In the current study, Gastroplus™ was used to convolute the *in vitro* dissolution profile obtained from the flow-through apparatus into the *in vivo* absorption profile and establish an *IVIVC*, using this simulated *in vivo* result plotted against the absorbed *in vivo* data as illustrated in Figure 6.8A. This simulation was carried out by Parojcic et al. The published *IVIVC* result of Tegretol IR and CR in water and 1% SLS (Kovacevic, Parojcic et al. 2008) at 75 rpm in the paddle apparatus are illustrated in Figure 6.8 B and C.

The calculated correlation coefficients were 0.9671, 0.8928 and 0.9589 for the prediction based on the *in vitro* data observed in water at 16 ml min^{-1} (Flow-through apparatus), water at 75 rpm and 1% SLS at 75 rpm (Paddle apparatus) (Kovacevic, Parojcic et al. 2008), respectively. Corresponding slopes of the regression lines were 0.9917, 0.8648 and 1.042, respectively. This result suggested that the dissolution method of the flow-through apparatus in water at 16 ml min^{-1} in an open system was more biorelevant than that in paddle apparatus with water at 75 rpm. This dissolution method was comparable to the published method in 1%

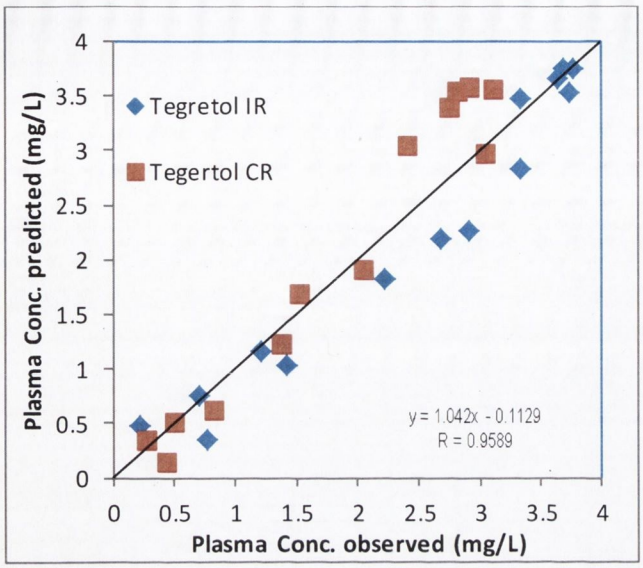
SLS at 75 rpm, in terms of generating an *IVIVC*. However, the lower agitation rate and lack of 1% SLS could be considered more biorelevant. Therefore, the *in vitro* dissolution at 16 ml min^{-1} in the flow-through apparatus using an open system which can be used to carry out the *in vitro* dissolution test of Tegretol IR and CR.



A.



B.



C.

Figure 6. 8 *IVIVC* plot for the simulated plasma concentration based on Gastroplus™ against the *in vivo* cumulative release using at. A. dissolution profile in the flow-through apparatus in water at 16ml min^{-1} as input to Gastroplus™; B. dissolution in the paddle apparatus in water at 75 rpm as input to Gastroplus™ (Kovacevic, Parojcic et al. 2008); C. dissolution in the paddle apparatus in 1% SLS at 75 rpm as input to Gastroplus™ (Kovacevic, Parojcic et al. 2008).

6.4 Conclusion

The *in vitro* dissolution of Tegretol using the USP 4 flow-through apparatus could be used to generate an *IVIVC* result which is comparable to that reported using *in vitro* dissolution in the paddle apparatus at 75 rpm, 1% SLS (Kovacevic, Parojcic et al. 2008). The dissolution in the flow-through apparatus at 16 ml min^{-1} without surfactant can be biorelevant method for Tegretol IR and CR. Furthermore, Gastroplus™ also demonstrated good capability to predict plasma concentration in the current study.

Chapter 7 Simulation of particle dissolution in the flow-through apparatus

7.1 Introduction

As the *IVIVC* result in chapter 6 indicated that hydrodynamic condition in the flow-through apparatus at 16 ml min^{-1} in the 22.6 mm cell was relevant to *in vivo* conditions, the dissolution rate predicted in the flow-through apparatus may imply the dissolution rate in the GI tract. Therefore, a model was established in the current study to predict the dissolution rate in the flow-through apparatus using Tegretol IR tablets as the model drug.

The Tegretol IR tablet disintegrates quickly to form particles in the dissolution test. The dissolution process of the Tegretol IR tablet could be considered as the dissolution of CBZ particles. Different particulate dissolution theories have been developed to predict the dissolution rate of particles (Noyes and Whitey 1897; Wang and Flanagan 1999; Wang and Flanagan 2002; Dokoumetzidis and Macheras 2006; Sugano 2008). The diffusion controlled model for solid dissolution developed by Noyes and Whitney (Noyes and Whitey 1897) was the basis for the above theories and subsequently modified by Nernst and Brunner (Dokoumetzidis and Macheras 2006). The diffusion controlled model suggests that the diffusion boundary layer adhering to the solid surface controls the dissolution rate in most drug dissolution scenarios. Based on the diffusion boundary layer theory , Wang and Flanagan assumes that the real hydrodynamic diffusion layer does not only depend on the particle size (Wang and Flanagan 1999; Wang and Flanagan 2002). The aforementioned models found that hydrodynamics has no significant effect on the dissolution rate for a smaller sized particle range (≤30μm), whereas different effective thicknesses of hydrodynamic diffusion layer was determined for a larger particle size range (≥30μm) (Sugano 2008). Based on Ranz-Marshall Correlation (Equation 1.11), a good agreement with observed dissolution rates in various dissolution conditions (Sugano 2008). Therefore, the diffusion boundary layer theory was used to predict CBZ dissolution rate in the current study.The objectives of the current study were:

to determine an appropriate particle size distribution to use in the particle dissolution simulation;

to examine variables in the dissolution simulation which could be adjusted to best reflect the experimental set-up;

to predict the effect of using the open vs. closed dissolution configurations.

7.2 Dissolution of Tegretol IR in the open and close loop configurations of the flow-through apparatus.

The dissolution at 8 and 16 ml min^{-1} using an open and closed loop system demonstrated very different dissolution profiles as illustrated in Figure 7.1. The total volume of dissolution media was 480 ml for the open system and 900 ml for the closed system at 8 ml min^{-1} over one hour, as well as 960 ml for the open system and 900 ml for the closed system at 16 ml min^{-1} in one hour.

The final concentration of CBZ after 60 minutes in the closed loop system was approximately 0.03 mg/ml at 8 ml min^{-1} and 0.069 mg/ml at 16 ml min^{-1} which was much lower than the saturated concentration (0.23mg/ml), suggesting that sink conditions were ensured whole dissolution test in the closed loop system. Theoretically, the dissolution rates should be the same in open and closed loop systems, if sink conditions can be ensured. However, the observed dissolution profiles from the open and closed loop systems were different at both 8 and 16 ml min^{-1} (Figure 7.1), despite the dissolution rate at 8 ml min^{-1} in the open system not being considered limited in terms of sink conditions, referring to section 6.2.2. Moreover, the dissolution profiles are different in both the open and closed loop systems at 16 ml min^{-1}. Thus the observed dissolution rate in the closed loop was lower than that in the open loop system at 16 ml min^{-1}. This issue will be revisited in section 7.4.3.

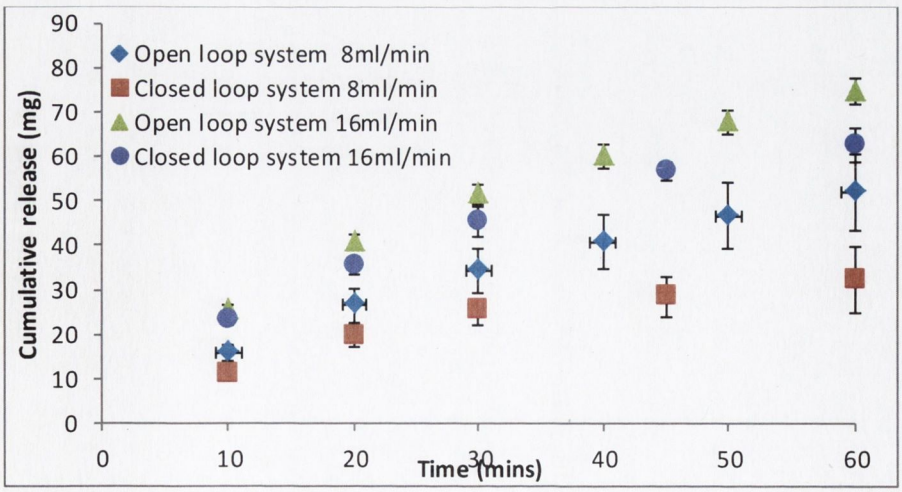


Figure 7. 1 Dissolution of Tegretol IR at 8 and 16 ml min^{-1} in open and closed loop systems.

7.3 Hydrodynamics considerations for Tegretol in the flow-through apparatus

The initial state of Tegretol IR is illustrated in Figure 7.2 A, E and I. After the Tegretol tablet disintegrated in the flow-through cell, the particles would settle down and form a "cake" covering the glass beads. The process of the Tegretol IR tablet dissolving in the flow-through cell consisted of three stages: first, the Tegretol tablet was fixed in the cell and flow filled the cell and covered the tablet (Figure 7.2 B, F and J), then the Tegretol began to disintegrate into small particles (Figure 7.2 C, G and K) which then sedimented to cover the glass beads (Figure 7.2 D, H and I). For the first stage, the tablet kept a round shape while the flow surrounded the tablet. The duration for the first stage was very short, no more than 1 min (Figure 7.2). In the disintegration process, the disintegrated particles would freely float in the flow-through cell and then settle down by gravitational effects. The duration of this process was no longer than 4 minutes. The last step was that the particle "cake" settled down on the glass beads. This was the predominant step in the flow-through cell during the whole dissolution process. Due to different flow rates being generated by the flow-through apparatus, the drag force was not the same in various flow conditions. The observed motion of the particle "cake" ceased on the top surface of the glass beads at 8 and 16 ml min^{-1}. In addition, the particle "cake" kept only a slightly synchronizated movement with the glass beads at 32 ml min^{-1} over the whole dissolution process. Therefore, the fluid velocity relevant to the dissolution process is the absolute fluid velocity value, or dose to the slightly synchronizated movement at 32 ml min^{-1}, rather than the relative velocity.

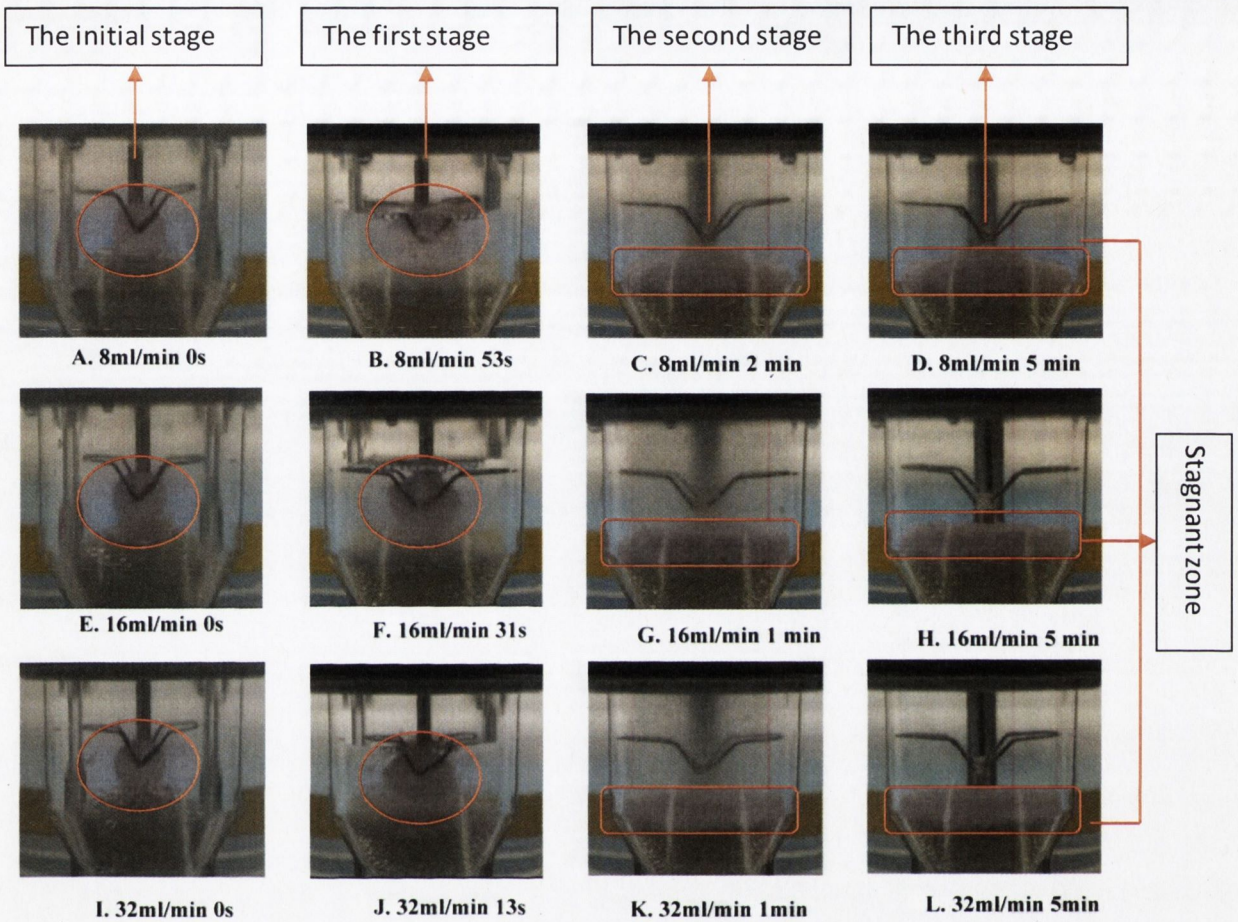


Figure 7. 2 The captured video of Tegretol IR dissolving in the flow-through cell at 8, 16 and 32 ml min^{-1}.

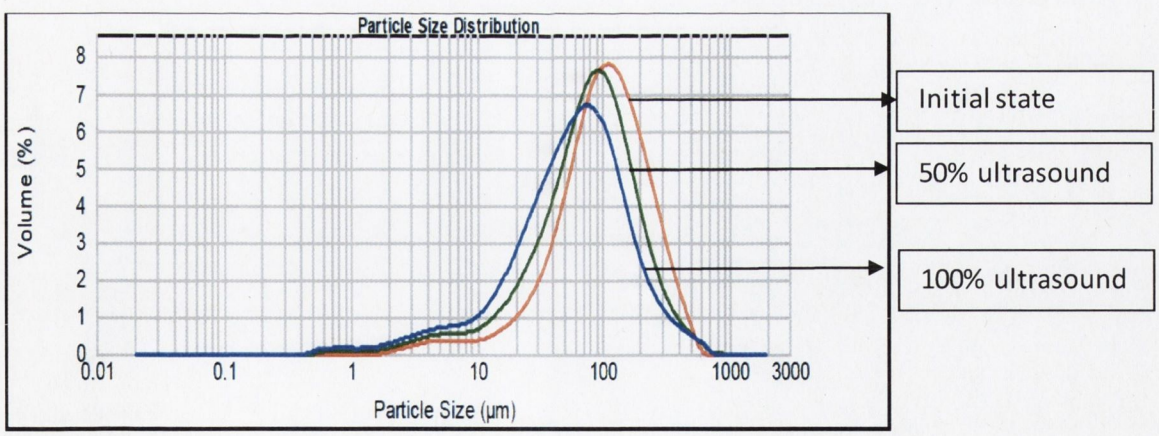
There was a "stagnant zone" defined as the area close to the upper surface of the bed of glass beads zone and under the lower edge of the compact, which was about 1 to 6 mm thick which could be changed with the input velocity change. In this "stagnant zone", the flow velocity was lower than the other zones in the flow-through cell and a particle "cake" could deposit at the bottom of the "stagnant zone". Additionally, the CBZ particles from the Tegretol tablet could descend towards the glass beads during the first stage. Most particles sedimented around the centre while the flow rate was at 8 ml min^{-1} as illustrated in Figure 7.2. During the third stage, flow caused the particle cake to form near the outer region of the cell at 16 and 32 ml min^{-1}, rather than in the centre as at 8 ml min^{-1} (Figure 7.2 D, H, L).

7.4 Prediction of dissolution rate of Tegretol IR

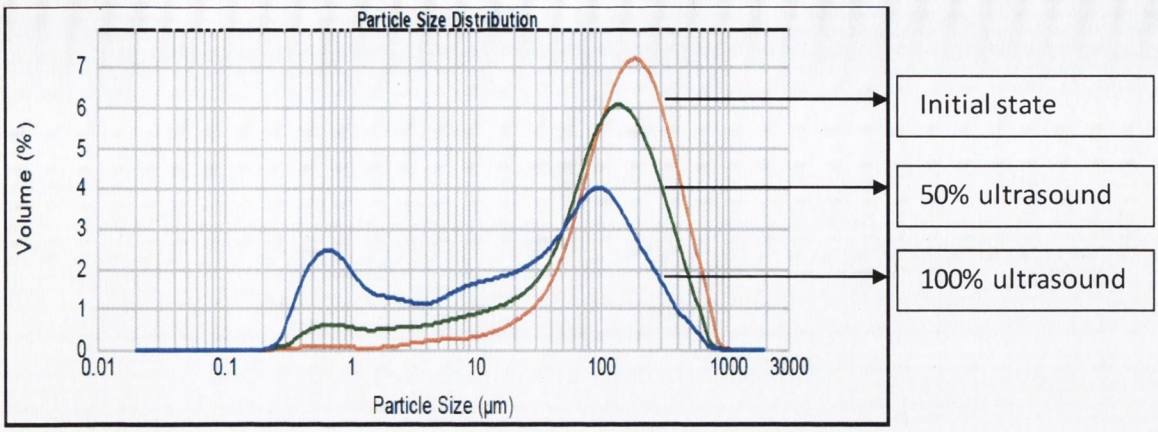
As Tegretol IR is a quickly disintegrating tablet, it could rapidly disintegrate into different sized particles in a very short time. If the disintegration time was not considered in the simulation, the whole dissolution process could be regarded as particle dissolution. The particle dissolution equations (Sugano 2008; D'Arcy and Persoons 2011) could be used to predict the dissolution rate of CBZ particles.

7.4.1 Particle size analysis.

In order to simulate dissolution from a particulate system, it is necessary to have an estimate of the initial particle size distribution. The particle size distribution of excipient particles and disintegrated particles from Tegretol tablets is illustrated in Figure 7.3. The particle sizes were determined for disintegrated Tegretol tablets (as would be present following disintegration in the dissolution test) and of excipients only (following dissolution of the CBZ) as described in section 2.26. The particle size distribution is illustrated in Figure 7.3. Adjusting the ultrasound effect on the excipients only did not result in a noticeable change of the median particle size distribution. However, the median particle size distribution of CBZ significantly reduced and the total volume of particles sized from 0.1 to 10 μm increased. This indicated that the small CBZ particles may be in an agglomerated state after initial disintegration.



A. Excipient only



B. Tegretol

Figure 7. 3 The particle size distribution using liquid chamber of Mastersizer 2000 with hydro attachment after Tegretol IR disintegration. A. Excipient only; B. Tegretol drug.

Therefore, the particle size distribution of Tegretol particles was examined. Firstly the particle distribution was divided into several particle size bins. According to the volume %, 5 groups with similar total volume were defined, as detailed in Figure 7.4.

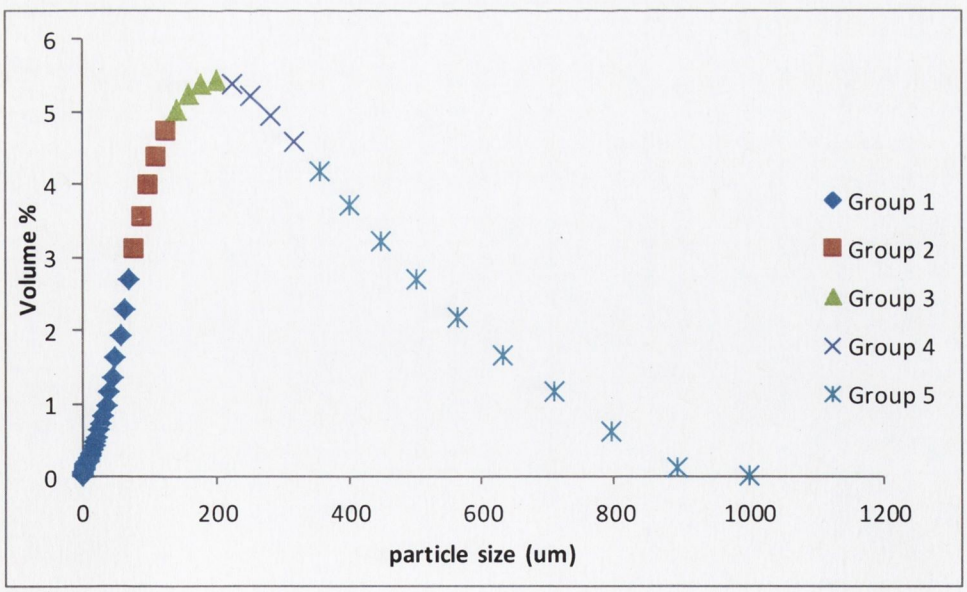


Figure 7. 4 Particle size distribution of Tegretol particles after disintegrated in water.

Although the excipient-only particle size distribution without ultrasound (Red curve, Figure 7.3A), was similar to the Tegretol particles without ultrasound (Red curve, Figure 7.3 B), the ultrasound there was required to separate small CBZ particles. Therefore, for the particulate

dissolution calculation, an assumption was made that the CBZ particle size distribution was separated by the Tegretol IR particle size distribution. It was considered that the force in the flow-through apparatus was not equivalent to the ultrasound from to separate the smaller particles, as distribution 10 μm particle would be much faster than the observed rates (Figure 7.1)

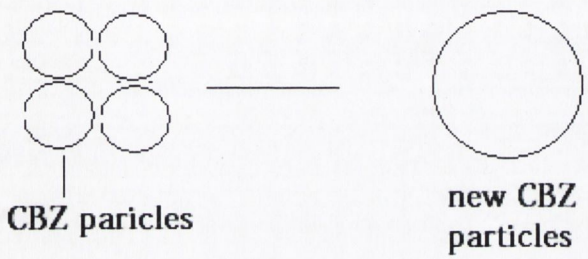


Figure 7. 5 New CBZ particle: agglomerate of smaller CBZ particles.

Each tablet has 200 mg CBZ. The mass was assumed to be proportional to volume % (Figure 7.4). Therefore the particle size bins was defined with almost equal mass. The particles in each bin were assigned the average particle diameter Table 7.1. From calculating the mass of each particle using the diameter, the no of particles in each bin was calculated. Particles were assumed to be spherical.

Table 7. 1 The CBZ particle size distribution and total mass for each group.

Category	Average particle size (μm)	Total volume (mg)
Bin 1	35.623	39.08
Bin 2	102.906	39.48
Bin 3	170.7945	42.16
Bin 4	270.6915	40.22
Bin 5	679.015	38.98

7.4.2 Consideration of effects from other parameters during the simulation.

From Ranz-Marshall Correlation (Equation 1.11), the Sherwoods number (Sh) was predicted. From this, the mass transfer coefficient was calculated ($Sh = \frac{K_{mass} d_p}{D_{eff}}$). The particle diameter was then used to calculate the surface area. The surface area, concentration gradient and mass transfer coefficient were used to calculate the mass transfer coefficient were used to calculate the mass transfer over time for each particle. Knowing the mass dissolved at each time step, a new particle size diameter was calculated, and the mass dissolved over the next time step was calculated. The mass dissolved multiplied by the number of particles in each bin gave the mass dissolved over time for each particle size bin.

7.4.2.1 Absolute and relative velocity

The absolute velocity is the same as flow velocity when the particle motion velocity is zero as described in Equation 7.1. In equation 1.11, the Reynolds Number (Re) was used to calculate the Sh. Therefore, the velocity parameters used in calculating the Re will affect the mass transfer prediction. The relative velocity is the velocity of the particle motion relative to the fluid velocity. The equations used to determine the relationship between relative and absolute velocity (D'Arcy and Persoons 2011) was demonstrated as below:

$$V=|U_f - U_p|$$

Equation 7. 1

$U_p=0$, $V=V_{abs}$

$U_p \neq 0$, $V=V_{rel}$

U_f: fluid velocity;

U_p: particle velocity;

V_{abs}: absolute velocity;

V_{rel}: relative velocity;

$$Re = \frac{d_p V}{\upsilon}$$

Equation 7. 2

The relative velocity was determined by the simultaneous solving of Equations 7.3, 7.4, 7.5, 7.6 and 7.7, due to the particle motion which was determined by the different force in the flow-through apparatus using a previously developed dissolution simulation code (Melling 1997; D'Arcy and Persoons 2011).

$$m_p \frac{dU_p}{dt} = F_{drag} + F_{buoy} + F_{fluidacc} + F_{Basset}$$

Equation 7. 3

$$F_{drag} = b(U_f - U_p)$$

Equation 7. 4

$$F_{buoy} = -(\rho_p - \rho_f)\frac{1}{6}\pi d_p^3 g$$

Equation 7. 5

$$F_{fluidacc} = \frac{3}{2}\rho_f \frac{1}{6}\pi d_p^3 \frac{dU_f}{dt}$$

Equation 7. 6

$$F_{Basset} = -\frac{3}{2} d_p^2 \sqrt{\pi \mu \rho_f} \int_{\xi=0}^{t} \frac{d(U_p - U_f)}{d\xi} \frac{d\xi}{\sqrt{t-\xi}}$$

Equation 7. 7

F_{drag}: drag force;

F_{buoy}: buoyancy;

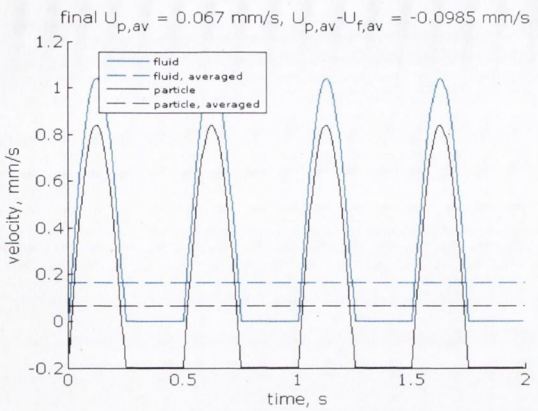
$F_{fluidacc}$: fluid acceleration force;

F_{Basset}: the resistance due to flow field unsteadiness;

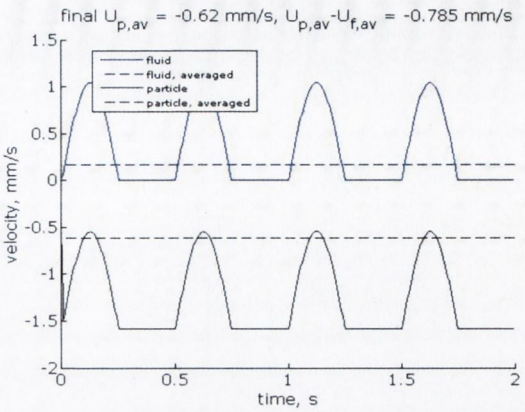
ρ_f: density of fluid;

m_p: the apparent particle mass;

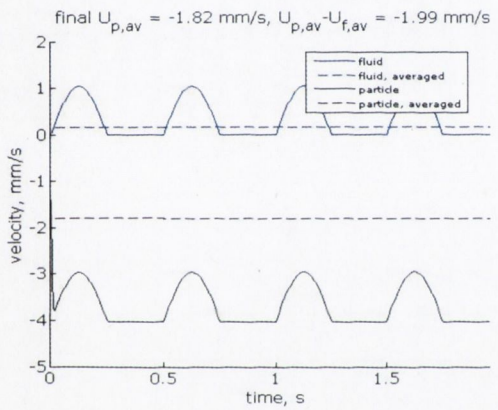
The effect of relative velocity on dissolution rate has been studied before (D'Arcy and Persoons 2011). When particles are held stationary at a cell boundary, the absolute velocity controls the dissolution of particles. The simulation of relative velocity assumed that there is no boundary for moving particles and thus those particles can keep moving upward or downward. With the exception of the average relative velocity of 35 µm particles, the average relative velocities ($U_f - U_p$) of the other particles were higher than the average flow velocity as illustrated in Figure 7.6. This relative velocity is negative, therefore results in downward motion, and that this negative motion must result in the particle depositing on the bottom of the cell. As the current dissolution was carried out in 22.6 mm cell at 8 ml min^{-1}, the flow velocity was lower than that used in the previous studies (D'Arcy and Persoons 2011) resulting in a low drag force. Furthermore, the density of CBZ particles is much higher than that of water leading to a high downward velocity. Thus most CBZ particles kept moving downward at a higher velocity than that of the fluid flow in the current model which resulted in the particles encountering the bed of glass beads in the cell, although smaller CBZ particles (35 µm) may take a slightly longer time to settle down with low relative velocity (0.0985 m s^{-1}). The motion of the particle matches the observed result (Figure 7.2) i.e. that the CBZ particles, after disintegration, rapidly settle down and form a "cake" in the bottom of cell after 5 minutes. Those CBZ particles, sedimenting on the glass beads bed, can be assumed to be stationary at 8, 16 and 32 ml min^{-1}, rather than freely moving particles as the relative velocity equation assumes. At this bounded point, the absolute velocity can be taken as the velocity of the particles, which simplifies the calculation process, rather than relative velocity (D'Arcy and Persoons 2011).



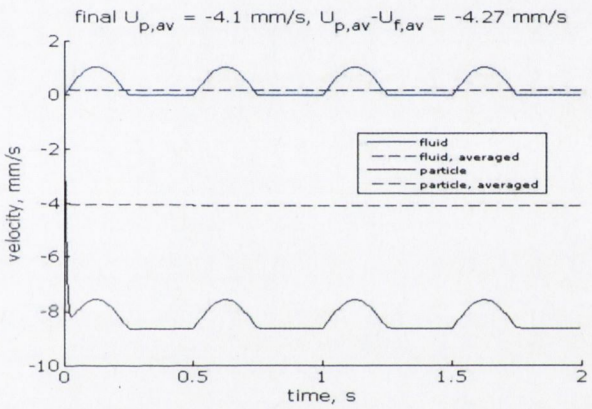
A



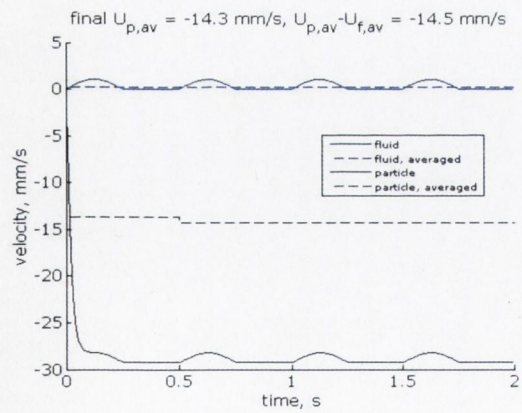
B



C



D



E

Figure 7. 6 The simulated relative velocity of different particle size: A. 35 μm; B.102 μm; C. 170 μm; D. 270 μm; E. 670 μm. The blue lines are fluid velocities and the black lines are particle move velocities.

7.4.2.2 Effective volume in the CBZ dissolution

Concentration gradient driving the dissolution process is affected by two factors: (1) Concentration at the cell inlet is zero in at open system configuration. (2) The concentration change in the cell over each pulse, from the amount being the cell through the outlet, and the amount dissolved into the cell, in each time step. Therefore, the volume defined into which mass dissolves will affect the bulk concentration and the dissolution rate.

The constant volume of the upper cylinder of the cell (22.6 mm cell) is approximately 12.035 cm^3, as the volume of lower part, filled with glass beads, could be neglected.

The volume through which the drug diffuses in particular, during the zero inflow period can be considered to be smaller than the cell volume. Even without any flow (Re=0), a particle fixed in the fluid space dissolves into the fluid and the maximum thickness of this layer is the radius of the particle, since Sherwood number (Sh) is 2, when Re is 0, for a spherical particle without any forced convection referring to Equation 1.12 (Sugano 2008). Therefore, the effective volume for each particle was assumed to be one layer, using the radius of the particle as the thickness of layer, surrounding the CBZ particle (Equation 7.8).

$$Vol_p = \frac{7}{6}\pi d_p^3$$

Equation 7. 8

Where Vol_p is the effective volume of each particle flow pattern.

7.4.3 Simulated dissolution results

The predicted CBZ dissolution rate in the open system using an absolute velocity parameter is evidently lower than that using a relative velocity as illustrated in Figure 7.7, as the CBZ particles subside and settle in the bottom of 22.6 mm cell, and are subjected to upward flow after disintegration of the Tegretol IR tablet. Furthermore, the relative velocity was higher than the absolute velocity in the current model detailed in the above discussion. Thus, the dissolution rate using the relative velocity was higher than that using absolute velocity during the initial dissolution period from 0 to 2000s. Therefore, the prediction based on the absolute velocity was close to the observed dissolution profile at 8 ml min^{-1}, compared that to relative velocity (Figure 7.7).

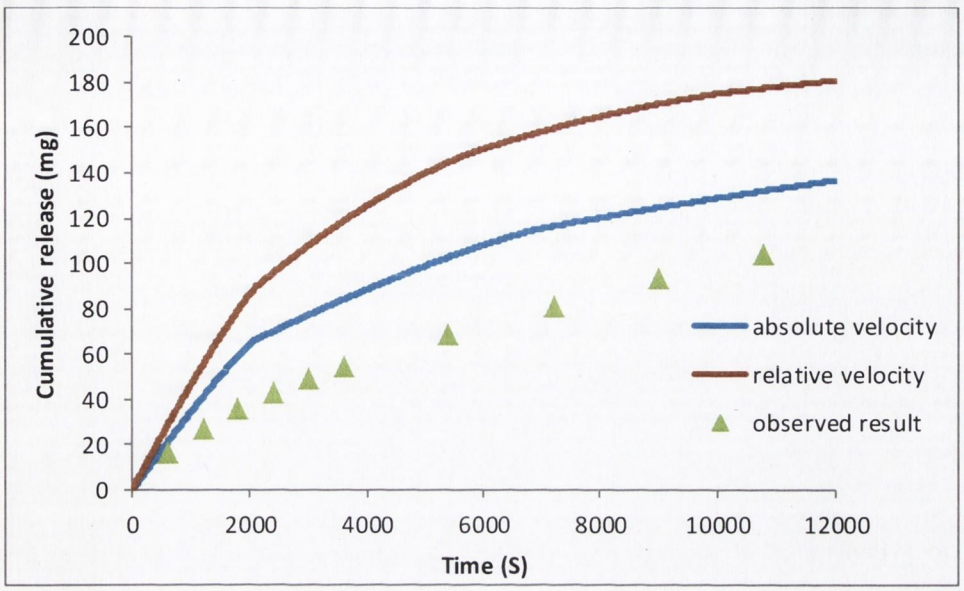


Figure 7. 7 The simulated dissolution profiles of CBZ at 8 ml min^{-1}, in the 22.6 mm cell in the open system using absolute and relative velocities.

The simulated dissolution profile based on an effective dissolution volume of a layer (thickness 1 radius) is slightly slower than that based on constant cell volume over 12000s as illustrated in Figure 7.8. The dissolution profile based on the layer volume was more close to the observed dissolution profile at the early phase, compared to the dissolution profile based on the constant cell volume. This was because smaller particles dissolve fastest in the early phase and therefore the effect of reduced effective volume (layer volume) was more notable than that of constant volume.

As a result, the layer volume and absolute velocity were selected as simulation conditions to finish the following simulations at different inflow rates.

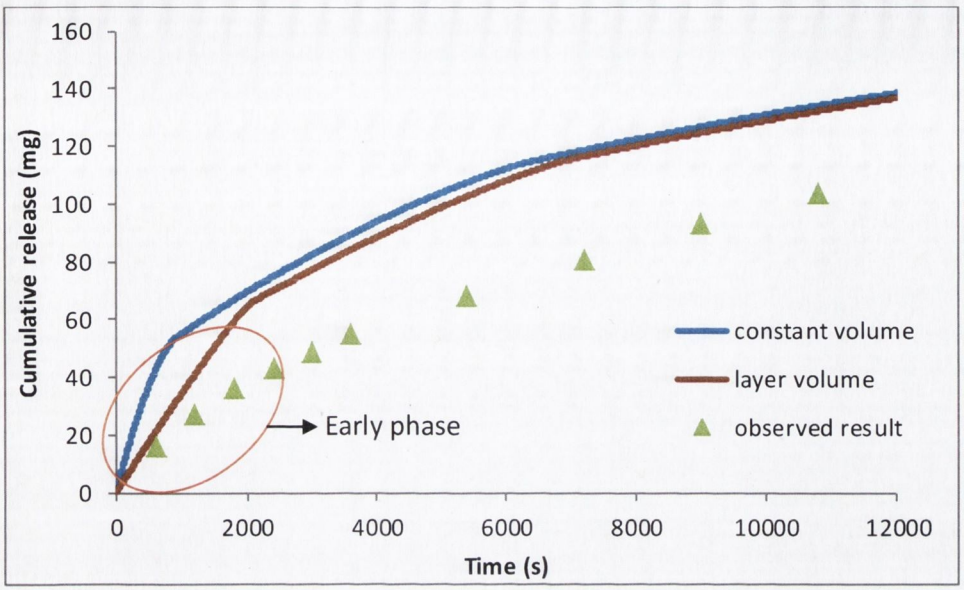


Figure 7. 8 The simulated dissolution profile of CBZ based on the cell volume and layer volume at 8 ml min^{-1} in the 22.6 mm cell in the open system.

The simulated dissolution profiles based on layer volume and absolute velocity at 16 and 32 ml min^{-1} have a better agreement with observed results (Figure 7.9), compared to the simulated dissolution profile at 8 ml min^{-1} (Figure 7.8). The simulated dissolution profile at 32 ml min^{-1} was marginally higher than that at 16 ml min^{-1}, despite the difference between the simulated dissolution profiles being less than that of the observed dissolution profiles, indicating that a similar trend to the observed dissolution profiles was simulated. Both simulated dissolution profiles at 16 and 32 ml min^{-1} are similar to observed dissolution profiles, respectively, at the early phase from 0 to 2000s, also verifying that the effective layer volume appropriately represents the diffusion region of CBZ at the initial stage at each flow rates. As the agglomerate of CBZ particles may break from 8000 to 12000s, more particles could be exposed in the dissolution medium. Thus, the observed dissolution profiles at both 16 and 32 ml min^{-1} are higher than the corresponding simulated dissolution profile from 8000 to 12000s and this trend is more obvious at 32 ml min^{-1}.

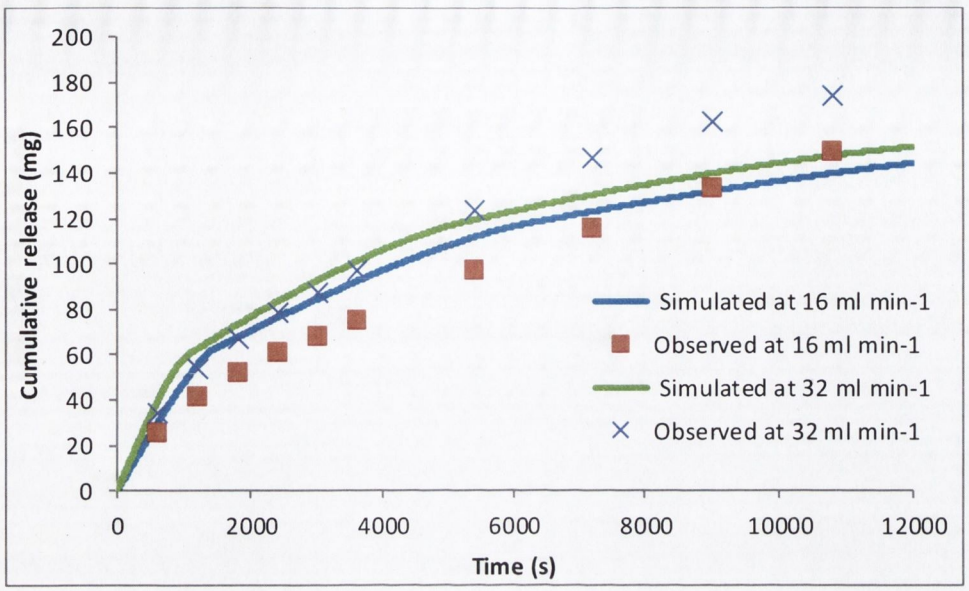


Figure 7. 9 The simulated dissolution profile of CBZ based on layer volume and absolute velocity at 16 and 32 ml min^{-1} in the 22.6 mm cell using the open system.

The prediction of the dissolution rate in the open and closed loop system also assumed the layer volume and used absolute velocity to calculate Re as the effective volume in both open and close loop (Figure 7.10). Comparing the simulated result in Figure 7.8 and 7.9, the simulated result was better at 16 ml min^{-1} than that at 8 ml min^{-1}. The simulated profiles in the open and closed systems had a good agreement with the observed dissolution profiles, in that a similar release was observed from 100 (6000s) to 180 minutes (10800s) and the difference increases from 0 to 100 minutes (6000s). The current simulation is based on the one median particle size (170.79 μm) which demonstrated a lower dissolution rate than that of the small particle size bins, as small particles would dissolve faster and larger particles will still be dissolving at later time points, giving a slower dissolution rate at later time points. Thus the simulated dissolution rate in both open and closed loop system is lower than the observed result. After 1 hour dissolution, the observed dissolution profile is more similar to the simulated dissolution profile as the small particles were completely dissolved or nearly dissolved. Furthermore, the dissolution profile in the sink (open loop system) and non-sink condition (closed loop system) can be distinguished in the current simulation, indicating that the current model is effective to simulate the effect of a closed loop configuration on the dissolution rate.

The dissolution under non-sink conditions is very complicated, since the concentration gradient is very different to that under sink conditions. Agata et al. suggested a model to predict the dissolution rate of sulfamethoxazole (SMX) in the paddle apparatus under non-sink conditions based on Fick's law, which had a good agreement with the observed results (Agata, Iwao et al. 2010). This model described the concentration gradient change under non-sink conditions and a reduction of particle size. A constant mass transfer coefficient, taken from experimental observation was used. However, the mass transfer coefficient is affected by hydrodynamic change (Sugano 2008), suggesting a limitation of the above reported model. In the current study, a dynamic mass transfer coefficient is used to predict the dissolution rate in the both open and closed loop systems which were calculated without use of experimental dissolution rate data. The current model can demonstrate a trend of particle dissolution in sink and non-sink conditions. Model needs to be refined to incorporate the effects of particle size distribution on dissolution in the closed system.

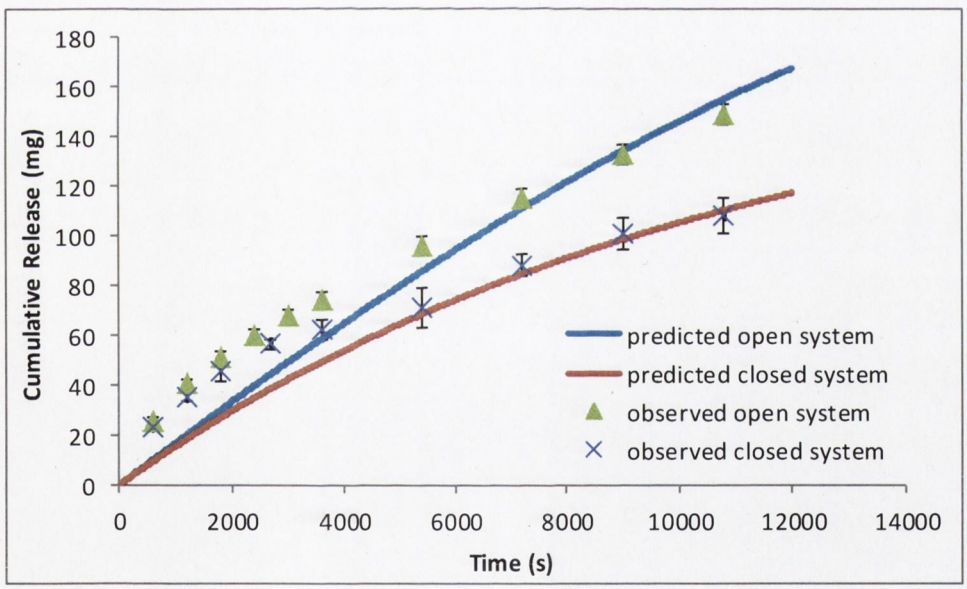


Figure 7. 10 The predicted dissolution rate based on open and close loop at 16 ml min^{-1} in flow-through apparatus (particle size 170.79 µm, 200 mg).

7.5 Conclusion

The *in silico* tool can simulate dissolution from particulate system in the flow-through apparatus, but reasonable estimate of initial particle size range is necessary. Additionally, the absolute velocity is the best velocity parameter as particles sediment to the bottom of the cell

for the current work, or "in simulation where the particles sediment and remain on the bottom of the cell". The effective layer volume was used over the whole pulse, which can interpret the effect of the local concentration on the dissolution rate. Furthermore, the effect of sink condition and non-sink condition simulation can be reproducible for the one particle size bin in the current study.

Chapter 8 General discussion

8.1 Comparing of particulate dissolution theories.

The simulated thickness of the effective diffusion boundary layer (h_{eff}) plotted against particle radius (r_p) using the Wang and Flanagan equation (Equation 1.10) and Fluid Dynamic (FD) equation (Equation 1.11) at different inflow rates is illustrated in Figure 8.1.

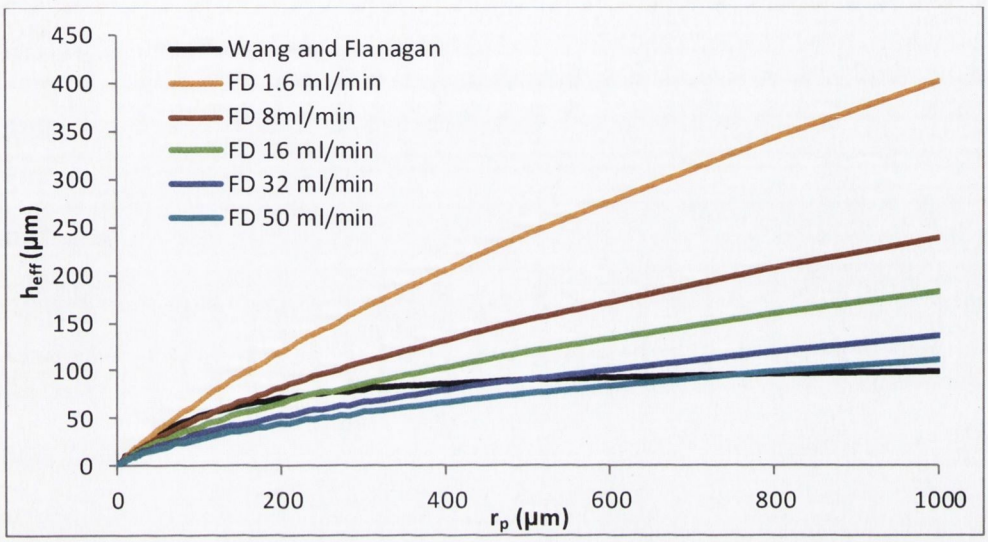


Figure 8. 1 The simulated thickness of the effective diffusion boundary layer (h_{eff}) plotted against particle radius (r_p) using Wang and Flanagan equation and Fluid Dynamic (FD) equation at different inflow rates

As introduced in Chapter 1, the Wang and Flanagan equation estimated the thickness of the effective diffusion boundary layer (h_{eff}) by using Equation 1.11 and 1.12. In the work reported by Wang and Flanagan, the relationship of dissolution rate and particle size was studied by using bezocaine ($D=1.40\times10^{-5}$ cm^2s^{-1}, solubility: 0.884 mg ml^{-1}) pellets dissolved in water and the value of $h_{c,wf}$ was estimated to be 110 µm. Therefore, the predicted h_{eff} using Wang and Flanagan equation was between 0 to 110 µm (Figure 8.1) and the predicted h_{eff} stayed almost constant with increasing particle size.

Different factors of pulsing flow, diffusion coefficient of CBZ and absolute velocity were evaluated in detail in Chapter 7. In order to simplify the calculation process of the h_{eff} estimated in Figure 8.1, a constant flow instead of a pulsing flow was used to predict the h_{eff} at different inflow rates. The h_{eff} decreased with increasing inflow rates and increased with increasing particle size at fixed inflow rate (Figure 8.1).

The h_{eff} predicted by Wang and Flanagan model was slightly higher than that predicted by the FD model when the particle size ranged from 0 to 30 μm. However, the h_{eff} predicted by the FD model was higher than that predicted by Wang and Flanagan model for particle radius of 30 to 1000 μm at inflow rate of 1.6 ml min^{-1}. Additionally the intersection of the h_{eff} curve predicted by the FD model and the Wang and Flanagan model moved to the right with increasing inflow rates.

Since the particle size could affect the relative velocity and consequently affect the Sherwoods number (Sh), an increase in Sh with particle size has demonstrated to be cancelled out by particle radius in the denominator (Sugano 2008). Thus , h_{eff} stayed constant when the particle size was greater than 100 μm when a prediction using relative velocity was used (Sugano 2008). Compared to a predicted result using relative velocity (Sugano 2008), the predicted result of h_{eff} based on the absolute velocity did not stay at a constant from 200 to 1000 μm particles (Figure 8.1). This is because the absolute velocity was used to predict h_{eff} in the current study, which was not affected by the particle radius change.

8.2 Comparing hydrodynamics effects in USP 2 and USP 4

Since designs of flow-through apparatus (USP2) and paddle apparatus (USP4) are different, the local flow hydrodynamics is different in these two systems. The inflow profile in the flow-through apparatus (USP 4) is an upward "semi-sinusoidal" flow because a piston pump push the flow (Kakhi 2009; Kakhi 2009; D'Arcy, Liu et al. 2010), while the flow is rotated in the paddle apparatus (USP 2).

Table 8. 1 Velocity range in the flow-through apparatus at 8 and 16 ml min^{-1}, at the centre of the base of the vessel and at the curved side of the vessel in the paddle apparatus at 25, 50 and 75 rpm.

Different conditions	USP 4 flow-through apparatus, velocity range (m s^{-1})	USP 2 paddle apparatus at the centre of the base of the vessel, velocity range (m s^{-1})	USP 2 paddle apparatus at curved side of the vessel, velocity range (m s^{-1})
8 ml min^{-1}	0 - 0.0014	N/A	N/A
16 ml min^{-1}	0 - 0.0027	N/A	N/A
25 rpm	N/A	0 – 0.006	0 – 0.03
50 rpm	N/A	0 – 0.03	0 – 0.078
75 rpm	N/A	0 – 0.06	0 – 1.2

The velocity range in the flow-through apparatus at 8 and 16 ml min^{-1}, at the centre base position and curved side of the vessel in the paddle apparatus at 25, 50 and 75 rpm (D'Arcy 2007) is illustrated in Table 8.1. The maximum velocities in the flow-through apparatus at 8 and 16 ml min^{-1} were comparable to those in the centre of the base of the vessel in the paddle apparatus at 25 rpm. These maximum velocities were much lower than the velocities in the paddle apparatus at 50 and 75 rpm. The maximum velocity in the centre of the base of the vessel in the paddle apparatus at 50 rpm was 22 times of the maximum velocity in the flow-through apparatus, indicating that the forced flow in the flow-through apparatus could be counteracted by the flow resulting from density gradient of a freely soluble compound such as LM. Furthermore, the maximum flow velocity of 2.7×10^{-3} m s^{-1} in the flow-through apparatus at 16 ml min^{-1} was also much lower than the maximum flow velocity in the paddle apparatus at 50 and 75 rpm. This indicated that the flow resulting from density gradient could not be negligible in the flow-through apparatus from 8 to 16 ml min^{-1}.

In the high agitation system such as at 75 rpm in the paddle apparatus, the maximum flow velocity at the side was nearly 850 times of the maximum velocity in the flow-through apparatus at 8 ml min^{-1}. Compared to the agitation of the forced flow, the effect of density gradient could be negligible in the high agitation system.

8.3 The dissolution of multi-component systems in a low velocity environment.

The dissolution rate of BA at different ratio of BA-LM composition compacts in the paddle apparatus, flow-through apparatus and free convection system is illustrated in Figure 8.2 and 8.3 and Table 5.3. The density gradient of LM results in a high velocity flow in the flow-through apparatus and free convection system are detailed in the chapter 4.

The dissolution rate of LM increased with increasing of LM proportion in the mixture in the flow-through apparatus and free convection system, indicating that there will be more LM dissolved per unit time from compacts containing a high ratio of LM: BA. As more LM dissolved in the flow-through apparatus or the free convection system, the density gradient effect on the dissolution rate increases due to the high LM proportion.

The ratio of BA dissolution rate in the flow-through apparatus versus that in the paddle apparatus is illustrated in Table 8.2. The ratio of BA dissolution rate increased with decreasing BA proportion in the mixture consistent with an increase in the density gradient from LM increasing the dissolution rate of BA, validating that increasing of density gradient of LM at different LM portion compact increased dissolution rate of BA. The effect of the density gradient on the dissolution rate is more notable in the flow-through apparatus at 8 ml min^{-1} than in the paddle apparatus. The difference in forced convection velocities and their effects on dissolution rate decrease with increasing LM properties.

Under a high agitation system such as paddle apparatus at 50 rpm, the dissolution rate of BA was constant from 100% to 25% BA composition compact, despite the fact that the dissolution rate of LM increases with the increase of LM portion in the mixture system. This indicates that the effect of the density gradient resulting from freely soluble excipient on the dissolution rate of slightly soluble BA is less under high velocity and agitation conditions.

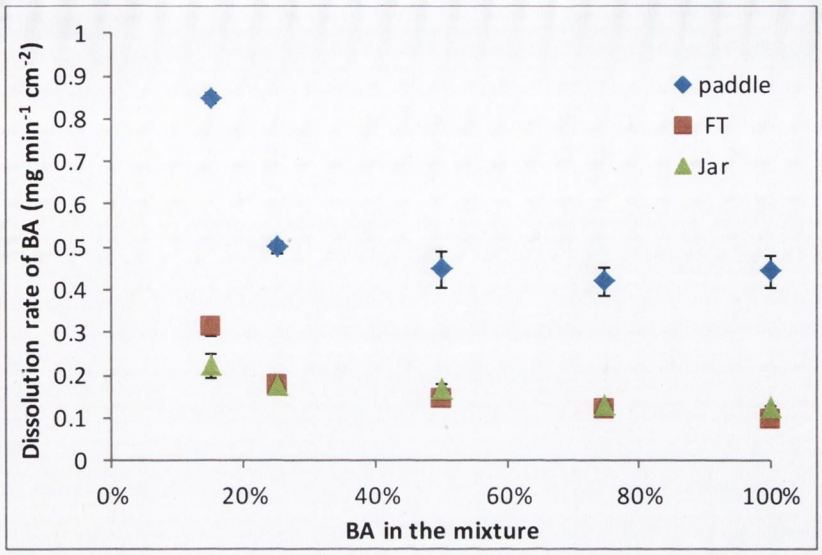


Figure 8. 2 The dissolution rate of BA at different BA-LM composition compacts in the paddle apparatus, flow-through apparatus and free convection system.

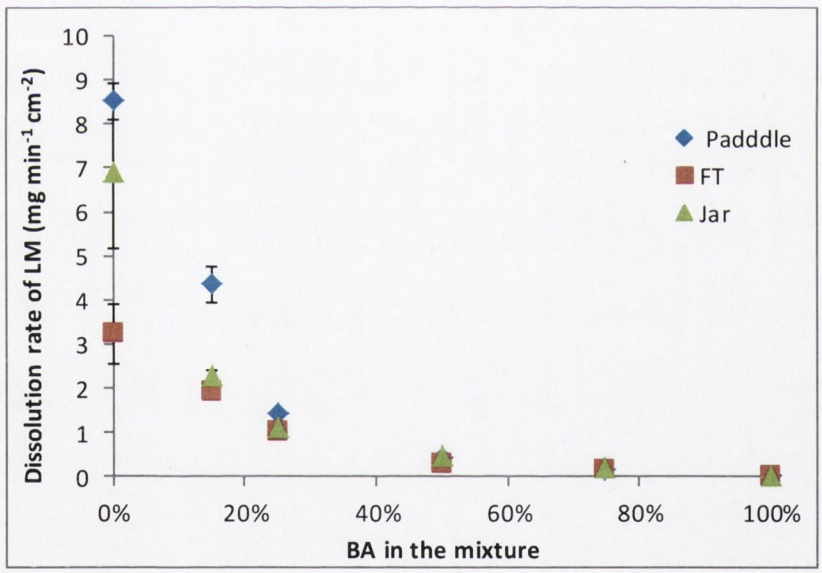


Figure 8. 3 The dissolution rate of LM at different BA-LM composition compacts in the paddle apparatus, flow-through apparatus and free convection system.

Table 8. 2 The ratio of BA dissolution rate in the flow-through apparatus versus that in the paddle apparatus

BA in the mixture	Relative dissolution rate of BA (FT vs Paddle)
100%	0.21
75%	0.28
50%	0.32
25%	0.35
15%	0.37

8.4 Comparing hydrodynamics in the USP4 dissolution apparatus to simulation of gastric hydrodynamics

Simulated gastric hydrodynamics using CFD have been investigated in many studies (Pal, Indireshkumar et al. 2004; Schulze 2006; Pal, Brasseur et al. 2007; Ferrua and Singh 2010; Kozu, Kobayashi et al. 2010; Ferrua, Kong et al. 2011). The highest viscosity value of 4.76 Pa s (Kozu, Kobayashi et al. 2010) measured from 75% starch syrup was used to simulate the fluid field in the stomach. A lower value of 7.3×10^{-4} Pa s was measured for the simulated gastric fluid (SGF; NaCl 0.2 wt.%+HCl 0.1 M) (Kozu, Kobayashi et al. 2010). The former high viscosity can be used to simulate the *in vivo* fed situation and the latter low viscosity can be used to simulate the *in vivo* fasted situation. In the current study, all of the simulations are carried out in the low viscosity solution of 6.943×10^{-4} Pa s at 37°C, since the dissolution media is 0.1 M HCl whose viscosity is similar to that of water. Thus, the current study would be more meaningful, if the result can be compared to the *in vivo* fasted situation.

As an antral contraction wave (ACW) progresses, the simulated maximum flow velocity is 0.011m s^{-1} at the centre axis of the cross-sectional stomach under different viscosity solutions at 7.3×10^{-4} Pa s (Kozu, Kobayashi et al. 2010). The simulated maximum velocity of 0.011m s^{-1} in the work by Kozu et al (Kozu, Kobayashi et al. 2010). These simulated velocities in the stomach were higher than the current simulated maximum velocity of 7.4×10^{-3} m s^{-1} in the 22.6 mm cell when the input flow rate was 43 ml min^{-1}.

Although the simulated maximum velocity in the USP 4 flow-through apparatus of 22.6 mm cell is lower than that in gastric simulation, the frequency of maximum velocity in the USP 4

flow-through apparatus (120 times/min) is greater than that in the gastric simulation (3 times/min) which may make up for the insufficient agitation of the flow velocity in the USP 4 apparatus. In addition, the maximum velocity of 7.4×10^{-3} m s^{-1} at an input flow rate of 43 ml min^{-1} is similar to the axis peak velocity of 0.011 m s^{-1} with a low viscosity solution of 7.3×10^{-4} Pa s, indicating that the agitation degree of agitation at a high inflow rate in the flow-through apparatus is similar to that in the stomach.

The simulated shear rate was approximate 20 s^{-1} in the occluded region of the modeled antrum (Kozu, Kobayashi et al. 2010). The maximum shear rates in the current hydrodynamic model were 7.51, 15.14 and 41.59 s^{-1} at 8, 16 and 43 ml min^{-1}, respectively. Furthermore, the shear rate of 15.14 s^{-1} on the compact surface at 16 ml min^{-1} is similar to that of 20 s^{-1} in the gastric simulation, indicating that shear rate affecting the compact surface in the flow-through apparatus at an inflow rate of 16 min^{-1} was similar to that in the stomach, despite the maximum flow velocity at 16 ml min^{-1} being lower than that in the stomach.

Furthermore, the deconvoluted fraction of Tegretol IR absorbed based on the Wagner-Nelson method plotted against the simulated fraction dissolved at inflow rate of 16 ml min^{-1} in the flow-through apparatus is illustrated in Figure 8.4. The correlation coefficient was 0.9933 indicating that the simulated flow hydrodynamics condition for Tegretol IR at 16 ml min^{-1} was a biorelevant dissolution condition.

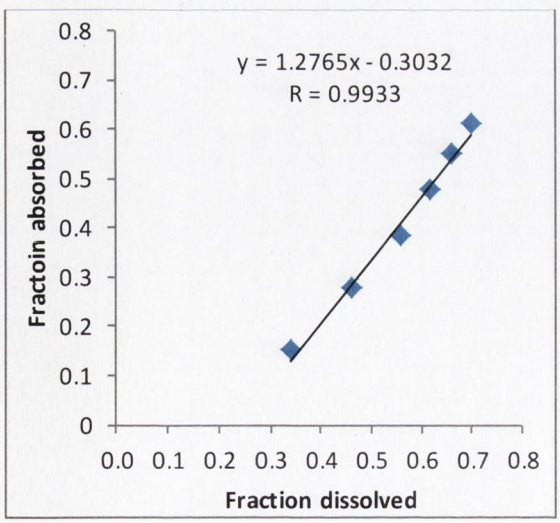


Figure 8. 4 The deconvoluted fraction absorbed based on the Wagner-Nelson method plotted against the simulated fraction dissolved at inflow rate of 16 ml min^{-1} in the flow-through apparatus

8.5 Dissolution of particles under physiological based hydrodynamic condition.

In the groundbreaking work reported by Amidon et al. (Amidon, Lennnernas et al. 1995), the BCS classification was suggested to interpret drug absorption in vivo. Yu et al. developed a compartmental absorption and transit (CAT) model to explain drug dissolution and absorption in different parts of GI tract (Yu and Amidon 1999; Yu, Amidon et al. 2002; Yu, Amidon et al. 2002). In the CAT model, the GI tract was divided into different compartments according different pH, different functions and different permeability. There was another model used to describe dissolution and absorption in the GI tract- advanced dissolution, absorption and metabolism (ADAM) model (Jamei, Turner et al. 2009), which also divided the GI tract into different compartments. However, none of these models considered hydrodynamic change in different compartments and that the thickness of the effective diffusion boundary layer would change at different inflow velocities (Figure 8.1). Therefore, the current study divided the GI tract into different compartments according to different hydrodynamics.

The simulated flow velocity in the 12 mm diameter cell of flow-through apparatus at 17 ml min^{-1} is approximately from 0 to 0.02 m s^{-1} (D'Arcy, Liu et al. 2010). The simulated flow velocity in the 12 mm diameter cell at 8 ml min^{-1} causes approximately from 0 to 0.01 m s^{-1} as the maximum flow velocity is proportional to the inflow rate as illustrate in Chapter 3. This velocity is comparable to the simulated velocity of 0.0075 to 0.012 m s^{-1} in the stomach (Ferrua and Singh 2010; Kozu, Kobayashi et al. 2010; Ferrua, Kong et al. 2011). Thus the hydrodynamics of the stomach could be similar to those in the flow-through apparatus in a 12 mm cell at 8 ml min^{-1}.

Furthermore, hydrodynamics in the duodenum is assumed to be similar to the flow-through apparatus with a 22.6 mm diameter cell at a flow rate of 8 ml min^{-1}. The transit rate of liquids in the intestine was estimated to range from 0.0002 to 0.0008 m s^{-1} (Diebold 2005). As the duodenum is in the upper intestine where the velocity is closed to the stomach, the flow velocity in the duodenum is assumed to be 0.0008 m s^{-1}. The predicted maximum velocity of 0.0013 m s^{-1} at 8 ml min^{-1} in 22.6 mm cell is comparable to the maximum assumed velocity in the duodenum. Additionally, the velocity is estimated to range from 0 to 0.00027 m s^{-1} at 1.6 ml min^{-1} in the 22.6 mm cell which is comparable to the lower end of the range of liquid transit rates estimated for the intestine (0.0002-0.0008 m s^{-1}) (Diebold 2005).

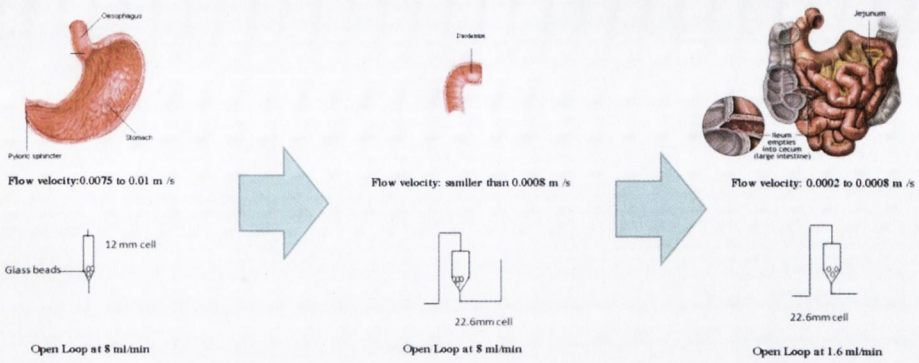


Figure 8. 5 The schematic view of the detailed hydrodynamic compartment of the GI tract.

The model drug was CBZ and particles with diameters of 10, 30, 50, 100 and 300 μm were used with the particle dissolution simulation described in Chapter 7 to evaluate the effect of different hydrodynamic environment on h_{eff} (obtained from Equation 1.11 and 1.12). The mass used in the simulation was 200 mg and the dissolution time was 30 minutes (1800 seconds). The flow rates and cell sizes used in the simulation were (1) 12 mm diameter cell, 8 ml min-1 to represent gastric hydrodynamics; (2) 22.6 mm diameter cell, 8 ml min^{-1} to represent duodenum hydrodynamics; (3) 22.6 mm diameter cell, 1.6 ml min-1 to represent intestine hydrodynamics. The predicted result of h_{eff} in different compartments for different particle sizes, is illustrated in Table 8.3.

Table 8. 3 The predicted result of h_{eff} in different compartment for different particle sizes

Particle size (μm)	h_{eff} in stomach (μm)	h_{eff} in duodenum (μm)	h_{eff} in remaining intestine (μm)
10	2.06×10^{-6}	2.07×10^{-6}	1.03×10^{-5}
30	1.93×10^{-5}	1.95×10^{-5}	9.26×10^{-5}
50	5.77×10^{-5}	5.90×10^{-5}	2.62×10^{-4}
100	2.98×10^{-4}	3.20×10^{-4}	1.14×10^{-3}
300	7.43×10^{-3}	9.42×10^{-3}	1.88×10^{-2}

The simulated results in Table 8.3 suggested that the h_{eff} of small particles of 10 and 30 μm do not change in the stomach and duodenum. However, this h_{eff} increased in the remaining

intestine, as the flow velocity in the intestine is much lower, resulting in an increased h_{eff} at 1.6 ml min^{-1} as illustrated in Figure 8.1. The h_{eff} of the big particles of 50, 100 and 300 μm were more sensitive to the hydrodynamic change, compared to the small particles of 10 and 30 μm. h_{eff} notably increased with decreasing flow velocity. The hydrodynamics in the stomach and duodenum determined a similar effect on the particle size smaller than 50 μm and the hydrodynamics in the remaining part of intestine would notably slow down the dissolution rate of the particles.

8.6 Conclusion and Future work.

8.6.1 Conclusion

CFD was used to simulate hydrodynamics and species transfer in the USP 4 flow-through apparatus which successfully interpreted the relationship of inflow rate and fluid velocity in different cells. CFD was also used to analyse the effects of compounds of different solubilities on the local hydrodynamics and local density gradient in a low velocity environment. Furthermore, CFD can be used to interpret the effect of velocity on dissolution rate.

The predicted dissolution rate of a non-disintegrating multi-component system using the Higuchi et. al equation has been investigated in the current study. A freely soluble excipient can affect the dissolution rate of a slightly soluble drug in a low velocity environment.

Furthermore, the simulations of hydrodynamics in the USP 4 flow-through apparatus demonstrated different fluid dynamics to the USP 2 paddle apparatus, suggesting a more similar fluid velocity in the USP 4 flow-through apparatus to that of the GI tract.

Based on the above understanding of the USP 4 flow-through apparatus, the simulation of particle dissolution in the flow-through apparatus had a good agreement with the observed results detailed in Chapter 7. Different dissolution profiles under sink and non-sink conditions were discussed. Furthermore, the *IVIVC* result demonstrated that the USP 4 flow-through apparatus was an effective *in vitro* dissolution test to establish a biorelevant dissolution method.

8.6.2 Future work

A more accurate simulation of freely soluble LM on the compact surface is required in order to interpret the effect of freely soluble compound on the slightly soluble compound in the low velocity environment.

The effect of freely soluble compound on the local concentration could be further studied in pulsing flow conditions to predict dissolution rate.

The current code can only simulate one particle size in non-sink conditions. Due to the inadequacy of combining the effect of dissolution from each particle size bin on the overall concentration gradient over time, further work is required to adapt the code to simulate dissolution of a particle size distribution under non-sink conditions.

A further study of dissolution under physiologically based hydrodynamic conditions is required with consideration of different pH conditions, different surfactants and biorelevant dissolution media.

The current dissolution model could be connected with an absorption model to predict drug dissolution and absorption in the GI tract.

References

Achanta, A. S., V. A. Gray, et al. (2005). "Evaluation of the performance of prednisone and salicylic acid USP dissolution calibrators." Drug Development and Industrial pharmacy 12: 35-36.

Adebayo, A. and O. Itiola (2003). "Effects of breadfruit and cocoyam starch mucilage binders on disintegration and dissolution behaviors of paracetomal tablet formulations." Pharmaceutical Technology 25: 78-90.

Agata, Y., Y. Iwao, et al. (2010). "Novel mathmatical model for predicting the dissolution profile of spherical particles under non-sink conditions." Chemical & Pharmaceutical Bulletin 58(4): 511-515.

Alvarez, D. G. (2006). "Comparison of acrylic and cellulose-based matrix formers for sustained drug release." Drug Delivery Technology 6: 61-65.

Amidon, G. L., H. Lennnernas, et al. (1995). "A theoretical basis for a biopharmaceutic drug classification: the correlation of in vitro drug product dissolution and in vivo bioavailability." Pharmaceutical Research 12(3): 413-420.

Anderson, J. D. (2005). "Ludwig Prandtl's Boundary layer." Physics Today: 42-48.

Ansari, M., M. Kazemipour, et al. (2004). "The development and validation of a dissolution method for clomipramine solid dosage forms." Dissolution Technologies August: 16-24.

Batchelor, G. K. (1956). "On steady laminar flow with closed streamlines at large Reynolds number." Journal of Fluid Mechanics 1(2): 177-190.

Baxter, J. L., J. Kukura, et al. (2005). "Hydrodynamics-induced variability in the USP apparatus II dissolution test." International Journal of Pharmaceutices 292: 17-28.

Bhattachar, S. N., J. A. Wesley, et al. (2002). "Dissolution testing of a poorly soluble compound using the flow-through cell dissolution apparatus." International Journal of Pharmaceutics 236: 135-143.

Bird, R. B., W. E. Stewart, et al. (2007). Transport Phenomena New York, John Wiley & Sons. Inc.

Bradshaw, L. A., A. Irimia, et al. (2006). "Biomagnetic characterization of spatiotemporal parameters of the gastric slow wave." Neurogastroenterology & Motility 18: 619-631.

Buhse, L. (2005). "Measruing and managing method variability." CDER Advisory Committee for Pharmaceutical Science 1: 184-219.

Buhse, L. (2006). Dissolution apparatus qualification. Challenges for dissolution testing for the 21st century. Arlington, VA.

Burmicz, J. (2005). "Observations of systemic errors in calibrator tablet testing." Dissolution Technologies 12: 33-34.

Cammarn, S. R. and A. Sakr (2000). "Predicting dissolution via hydrodynamices: salicylic acid tablets in flow through cell dissolution." International Journal of Pharmaceutices 201: 199-209.

Chowhan, Z. and L. Palagyi (1978). "Hardness increase induced by partial moisture loss in compressed tablets and its effect on *in vitro* dissolution." Journal of Pharmaceutical Sciences 67: 1385-1389.

Claes, J. and J. Hoffman (2011). "(2d) Pattern for separation with a no-slip boundary condition, URL: http://knol.google.com/k/ flow-separation-and-divorce-cost."

Corrigan, D. O., A. M. Healy, et al. (2006). "Preparation and release of salbutamol from chitosan and chitosan co-spray dried compacts and multiparticulates." European Journal of Pharmaceutics and Biopharmaceutics 62: 295-305.

Cortana Corporation (2011). "Description of drug, URL: http://www.cortana.com/Drag_Description.htm."

Crist, B. and D. Spisak (2005). "Evaluation of the induced variance of physical parameters on the calibrated USP dissolution apparatus 1 and 2." Dissolution Technologies 12: 28-31.

Currie, I. G. (2003). Fundamental mechanics of fluids. New York, Marcel Dekker, Inc.

D'Arcy, D. M. (2007). Use of computational fluid dynamics to investigate the relationship between hydrodyanmics and rates of dissolution rate. School of Pharmacy and Pharmaceutical Sciences. Dublin, Trinity College, Dublin. Doctor of Philosophy

D'Arcy, D. M., O. I. Corrigan, et al. (2005). "Hydrodynamic simulation (computational fluid dynamics) of asymmetrically positioned tablets in the paddle dissolution apparatus: impact on dissolution rate and variability." Journal of Pharmacy and Pharmacology 57: 1-9.

D'Arcy, D. M., O. I. Corrigan, et al. (2006). "Evaluation of hydrodynamics in the basket dissolution apparatus using computational fluid dynamics-Dissolution rate implications." European Journal of Pharmaceutical Sciences 27: 259-268.

D'Arcy, D. M., B. Liu, et al. (2010). "Hydrodynamic and species transfer simulations in the USP 4 dissolution apparatus: considerations for dissolution in a low velocity pulsing flow." Pharmaceutical Research 27(2): 246-258.

D'Arcy, D. M. and T. Persoons (2011). "Mechanistic modelling and mechanistic mointoring: simulation and shadowgraph imaging of particulate dissolution in the flow-through apparatus." Journal of Pharmaceutical Sciences DOI 10.1002/jps.

Diebold, S. M. (2005). Physiological paramteres relevant to dissolution testing: hydrodynamic considerations. Pharmaceutical Dissolution Testing. J. Dressman and J. Kramer. Boca Raton, Taylor and Francis Group.

Dodge, D. W. and A. B. Metzner (1959). "Turbulent flow of non-newtonian systems." AIChE Journal 5(2): 189-204.

Dokoumetzidis, A. and P. Macheras (2006). "A century of dissolution research: From Noyes and Whitney to the Biopharmaceutics Classification System." International journal of pharmaceutics 321: 1-11.

Dressman, J., Ed. (2005). Pharmaceutical Dissolution Testing. New York, Taylor & Francis Group.

Dressman, J., G. L. Amidon, et al. (1998). "Dissolution testing as a prognostic tool for oral absorption: immediate release dosage forms." Pharmaceutical Research 15: 11-22.

Dressman, J. and J. Kramer (2005). Pharmaceutical Dissolution Testing. Boca Raton, Taylor and Francis Group.

Dressman, J. and H. Lennernas (2000). Oral drug absorption prediction and assessment. New York, Marcel Dekker, Inc.

El-Massik, M. A., O. Y. Abdallah, et al. (2006). "Towards a universal dissolution medium for Carbamazepine." Drug Development and Industrial pharmacy 32: 893-905.

Emami, J. (2006). "In vitro - In vivo Correlation: From Theory to Applications." Journal of Pharmacy & Pharmaceutical Sciences 9(2): 169-189.

FDA CDER (1995). SUPAC-IR: Immediate-release solid oral dosage forms: Scale-up and post approval changes, and in vivo bioquivalence documentation: Guidance for industry. F. D. A. US Deparatment of Health and Human Services, Center for Drug Evaluation and Research. Rockville, MD., US Government Printing Office.

FDA CDER (1997). Dissolution testing of immediate release dosage forms: Guidance for industry. F. D. A. US Deparatment of Health and Human Services, Center for Drug Evaluation and Research. Rockville, MD, US Government Printing Office.

FDA CDER (1997). Guidance for industry, extended release oral dosage forms: development, evaluation and application of an in vitro/in vivo correlation. F. D. A. US Deparatment of Health and Human Services, Center for Drug Evaluation and Research. Rockville, MD.

FDA CDER (1997). Guidance for industry: Dissolution testing for immediate release solid oral dosage forms. F. D. A. US Deparatment of Health and Human Services, Center for Drug Evaluation and Research. Rockville, MD.

FDA CDER (1997). SUPAC-MR: Modified release solid oral dosage forms: scale-up and post-approval changes: Chemistry, manufacturing, and controls, in vitro dissolution testing and in vivo bioequivalence documentation: Guidance for industry. F. D. A. US Deparatment of Health and Human Services, Center for Drug Evaluation and Research. Rockville, MD, US Government Printing Office.

FDA CDER (2000). Guidance for Industry, Waiver of In Vivo Bioavailability and Bioequivalence Studies for Immediate-Release Solid Oral Dosage Forms Based on a Biopharmaceutics Classification System. F. D. A. US Department of Health and Human Services, Center for Drug Evaluation and Research. . Rock ville, MD, FDA, CDER.

FDA CDER (2000). Waiver of *in vivo* bioavailability and bioequivalence studies for immediate-release solid oral dosage forms based on a biopharmaceutics classfication system: Guidance for industry. F. D. A. US Department of Health and Human Services, Center for Drug Evaluation and Research. Rockville, MD, US Government Printing Office.

FDA CDER (2003). Q1A(R2) stability testing of new drug substances and products: Guidance for industry. F. D. A. US Deparatment of Health and Human Services, Center for Drug Evaluation and Research. Rockville, MD, US Government Printing Office.

Federal Register (2000). "International Conference on Harmnoization. Guidance on Q6A specifications: Test procedures and accepetance criteria for new drug substances and new drug products: Chemical substances." 65(251): 83041-83063.

Ferrua, M. J., F. Kong, et al. (2011). "Computational modeling of gastric digestion and the role of food material properties." Trends in Food Science & Technology: 1-12.

Ferrua, M. J. and R. P. Singh (2010). "Modeling the fluid dynamics in a human stomach to gain insight of food digestion." Journal of Food Science 75: R151-R162.

Fitzpatrick, S., J. F. McCabe, et al. (2002). "Effect of moisture on polyvinylpyrrolidone in accelerated stability testing." International Journal of Pharmaceutices 246: 143-151.

Fluent Inc (2004). Gambit 2.2 Tutorial Guide. Lebanon, NH, Fluent, Inc.

Fluent Inc (2006). Fluent 6.3 Documentation. Lebanon, NH 03766, Fluent Inc.

Foster, T. and W. Brown (2005). "USP dissolution calibrators: Re-examination and appraisal." Dissolution Technologies 12: 6-8.

Francis, J. R. D. (1975). Fluid mechanics for engineering student. London, Edward Arnold Ltd.

Gad-el-Hak, M. (2000). Flow control:passive, active, and reactive flow management, Cambridge University Press.

Galia, E., E. Nicolaides, et al. (1998). "Evaluation of various dissolution media for predicting in vivo performance of Class I and Class II drugs." Pharmaceutical Research 15(5): 698-705.

Gary, L. L. (1993). "Laminar Flow and Convective Transport Processes " Drying Technology 11(5): 1137-1138.

Gohel, M. C., R. K. Parikh, et al. (2007). "Improving the tablet characteristics and dissolutoin profile of Ibuprofen by using a novel coprocessed superdisintegrant: a technical note." AAPS PharmSciTech 8(1): E1-E6.

Goldberg, A. H. and W. I. Higuchi (1968). "Improved method for diffusion coefficient determinations employing the silver membrane filter." Journal of Pharmaceutical Sciences 57(9): 1583-1585.

Grady, L. T. (1980). "Persepctive on the history of dissolution testing URL: http://www.layloff.net/dissolution/1980Grady.pdf."

Graebel, W. P. (2007). Advanced Fluid Mechanics. San Diego, California, Elsevier Inc.

Gray, V., G. Kelly, et al. (2009). "The science of USP 1 and 2 dissolution: present challenges and future relevance." Pharmaceutical Research 26(6): 1289-1302.

Healy, A. M., L. G. McCarthy, et al. (2002). "Sensitivity of dissolution rate to location in the paddle dissolution apparatus " Journal of Pharmacy and Pharmacology 54(3): 441-444.

Higuchi, W. I. (1963). "Mechanism of Sustained-action medication: theoretical analysis of rate of release of solid drug dispersed in solid matrices." Journal of Pharmaceutical Sciense 52: 1145-1149.

Higuchi, W. I. (1967). "Diffusional Models Useful in Biopharmaceutics." Journal of Pharmaceutical Sciences 56(3): 315-327.

Higuchi, W. I., N. A. Mir, et al. (1965). "Dissolution Rates of Polyphase Mixtures." Journal of Pharmaceutical Sciences 54(10): 1405-1411.

Higuchi, W. I., E. I. Rowe, et al. (1963). "Dissolution rates of finely divided drug powders II. Micronized methylprednisolone. ." Journal of Pharmaceutical Sciences 52: 163-164.

Hixson, A. W. and J. H. Crowell (1931). "Dependence of reaction velocity upon surface and agitation -- Theoretical consideration." Industrial and Engineering Chemistry 23: 923-931.

Holland, F. A. and R. Bragg (1995). Fluid flow for chemical engineers. Jordan Hill, Oxford, Edward Amold.

Horter, D. and J. Dressman (2001). "Influence of physicochemical properties on dissolution of drugs in the gastrointestinal tract." Advanced Drug Delivery Reviews 46(1-3): 75-87.

Hussain, A. S. (2004). Quality by design and risk based regulatory scrutiny: connecting the dots. AAPS 39th Annual Pharmaceutical Technologies Conference. Arden House, Harriman, NY.

Ikegami, K., K. Tagawa, et al. (2003). "Prediction of in vivo drug release behavior of controlled-release multiple-unit dosage forms in dogs using a flow-through type dissolution test method." International Journal of Pharmaceutics 258(1-2): 31-43.

Jamei, M., D. Turner, et al. (2009). "Population-based mechanistic prediction of oral drug absorption." The AAPS Journal 11(2): 225-236.

Jung, H., R. C. Milan, et al. (1997). "Bioequivalence study of carbamzepine tablets: in vitro/in vivo correlation." International Journal of Pharmaceutices 152: 37-44.

Kakhi, M. (2009). "Classification of the flow regimes in the flow-through cell " European Journal of Pharmaceutical Sciences 37(5): 531-544.

Kakhi, M. (2009). "Mathematical modeling of the fluid dynamics in the flownext term-through cell " International Journal of Pharmaceutics 376(1-2): 22-40.

Katori, N., N. Aoyagi, et al. (1995). "Estimation of agitation intensity in the GI tract in humans and dogs based on in vitro/in vivo correlation." Pharmaceutical Research 12(2): 237-243.

Khan, K. and D. Rooke (1976). "Effect of disintegrant type upon the relationship between compressional pressure and dissolution efficiency." Journal of Pharmacy and Pharmacology 28: 633-636.

Khan, M. A., A. A. Karnachi, et al. (2000). "Stability characterization of controlled release coprecipitates and solid dispersions." Journal of Controlled Release 63: 1-6.

Kovacevic, I., J. Parojcic, et al. (2008). "Justification of biowaiver for Carbamazepine, a low soluble high permeable compound, in solid dosage forms based on IVIVC and gastrointestinal simulation." Molecular Pharmaceutics 6(1): 40-47.

Kozu, H., I. Kobayashi, et al. (2010). "Analysis of Flow Phenomena in Gastric Contents Induced by Human Gastric Peristalsis Using CFD." Food Biophysics 5: 330-336.

Kukura, J., P. E. Arratia, et al. (2003). "Engineering Tools for Understanding the Hydrodynamics of Dissolution Tests." Drug Development and Industrial pharmacy 29(2): 231-240.

Kukura, J., P. E. Arratia, et al. (2002). "Understanding pharmaceutical flows." Pharmaceutical Technology(10): 48-70.

Kukura, J., J. L. Baxter, et al. (2004). "Shear distribution and variability in the USP Apparatus2 under turbulent condition." International Journal of Pharmaceutics 279: 9-18.

Lake, O. A., M. Olling, et al. (1999). "In vitro/in vivo correlations of dissolution data of carbamazepine immediate release tablets with pharmacokinetic dat obtained in healthy volunteers." European Journal of Pharmaceutics and Biopharmaceutics 48: 13-19.

Langenbucher, F. D., W. Benz, et al. (1989). "Standarzized flow-cell method as an alternative to existing phamacopoeial dissolution testing." Pharmaceutical Industry 51(11): 1276-1281.

Lee, H., S. Park, et al. (2005). "Surfactant effects upon dissolution patterns of carbamazepine immediate release tablet." Archives of Pharmaceutical Research 28(1): 120-126.

Lerk, C. F. and K. Zuurman (1970). "The influence of pulsation on the dissolution rate measurements in column type apparatus." Journal of Pharmacy & Pharmacology 22: 319-320.

Levich, V. G. (1962). Physicochemical Hydrodynamics. Englewood Cliff, NY, Prentice-Hall.

Levins, D. M. and J. F. Glastonbury (1972). "Particle-liquid hydrodyanmics and mass transfer in a stirred vessel II. Mass transfer." Transactions of the Institution of Chemical Engineers 50: 132-146.

Levins, D. M. and J. F. Glastonbury (1972). "Particle-liquid hydrodyanmics and mass transfer in a stirred vessel. I. Particle-liquid motion." Transactions of the Institution of Chemical Engineers 50: 32-41.

Levy, G., J. M. Antkowiak, et al. (1963). "Effect of certain tablet formulation factors on dissolution rate of the active ingredient." Journal of Pharmaceutical Sciences 52: 1047-1051.

Lide, D. R., Ed. (2009). CRC handbook of chemistry and physics 89th edition. Boca Raton, FL., Taylor and Francis Group.

Luner, P. E. (2000). "Wetting properties of bile salt solutions and dissolution media." Journal of Pharmaceutical Sciences 89(382-395).

Macheras, P. and A. Iliadis (2006). Modeling in Biopharmaceutics, pharmacokinetics, and pharmacodynamics. New York, NY10013, USA, Springer Science+Business Media, Inc.

Manzo, R. H., M. E. Olivera, et al. (2006). "Biowavier Monographs for immediate release solid oral dosage forms: Amitriptyline Hydrochloride." Journal of Pharmaceutical Sciences 95(5): 966-974.

Marchais, H., G. Cayzeele, et al. (2003). "Cross-linking of hard gelatin carbamazepine capsules: Effect of moisture on polyvinylpyrrolidone in accelearted stability testing." European Journal of Pharmaceutical Sciences 19: 129-132.

Marciani, L., E. F. Cox, et al. (2010). "Postprandial changes in small bowel water content in healthy subjects and patients with irritable bowel syndrome." Gastroenterology 138: 469-U490.

Massey, B. and J. Ward-smith (2006). Mechanics of fluids. London and New York, Taylor & Francis.

McCarthy, L. G., G. Bradley, et al. (2004). "Computational Fluid Dynamics Modeling of the Paddle Dissolution Apparatus: Agitation Rate, Mixing Patterns, and Fluid Velocities." AAPS PharmSciTech 5(2): 31.

McCarthy, L. G., C. Kosiol, et al. (2003). "Simulating the hydrodynamic conditions in the United States Pharmacopeia paddle dissolution apparatus." AAPS PharmSciTech 4(2): 22-25.

Medicines.ie (2011). "http://www.medicines.ie/medicine/9619/SPC/Tegretol+Tablets+200mg/."

Melling, A. (1997). "Tracer particles and seeding for particle image velocimetry." Measurement Science and Technology 8(12): 1406-1416.

Merzkirch, W. (2005). Fluid mechanics of flow metering Berlin, Springer-Verlag Berlin Heidelberg.

Meyer, M. C., A. B. Straughn, et al. (1992). "The bioequivalence of carbamazepine tablets with a histroy of clinical failures." Pharmaceutical Research 9: 1612-1616.

MINITAB® (2003). Minitab Inc. .

Mirza, T., Y. Joshi, et al. (2005). "Evaluation of dissolution hydrodynamics in the USP, Peak™ and flat-bottom vessels using different solubility drugs." Dissolution Technologies 12(11-16).

Moore, J. W. and H. H. Flanner (1996). "Mathmatical comparision of dissolution profiles." Pharmaceutical Technology 20(6): 64-72.

Muzzio, F. J. and P. M. Armenante (2005). Action plan for the development of scientifically based bioavailability and dissolution testing systems. Drug Dissolution and Release Research Program Meeting. Piscataway, NJ (Rutgers University): 1-10.

Nelson, K. G. and A. C. Shah (1975). "Convective diffusion model for a transport-controlled dissolution rate process." Journal of Pharmaceutical Sciences 64(4): 610-614.

Nelson, K. G. and A. C. Shah (1977). "Application of a convection diffusion model to membrane transport." Journal of Pharmaceutical Sciences 66(1): 137-139.

Nelson, K. G. and A. C. Shah (1987). "Mass transport in dissolution kinetics I: convective diffusion to assess the role of fluid viscosity under forced flow conditions." Journal of Pharmaceutical Sciences 76(10): 799-802.

Nerurkar, J., H. Jun, et al. (2005). "Controlled-release matrix tablets of ibuprofen using cellulose ethers and carrageenans: Effect of formulation factors on dissolution rates." European Journal of Pharmaceutics and Biopharmaceutics 61: 56-68.

Nicolaides, E., J. M. Hempenstall, et al. (2000). "Biorelevant Dissolution Tests with the Flow-Through Apparatus?" Dissolution Technologies 2: 6-10.

Nicolaides, E., M. Symillides, et al. (2001). "Biorelevant dissolution testing to predict the plasma profile of Lipophilic drugs after oral administration." Pharmaceutical Research 18(3): 380-388.

Noyes, A., A. and W. Whitey, R. (1897). "The rate of solution of solid substances in their own solutions." Journal of American Chemical Society 19: 930-935.

O'Connor, J. J. and E. F. Robertson (2011). "MacTutor History of Mathematics archive URL: http://www-history.mcs.st-and.ac.uk/."

O'Hara, T., A. Dunne, et al. (1998). "A review of methods used to compare dissolution profile data." Pharmaceutical Science & Technology Today 1: 214-223.

Oberle, R. L. and G. L. Amidon (1987). "The influence of variable gastric emptying and intestinal transit rates on the plasma level curve of cimetidine: An explanantion for the double peak phenomenon." Journal of Pharmacokinetics and Biopharmaceutics

Pal, A., J. G. Brasseur, et al. (2007). "A stomach road or "Magenstrasse" for gastric emptying." Journal of Biomechanics 40: 1202-1210.

Pal, A., K. Indireshkumar, et al. (2004). "Gastric flow and mixing studied using computer simulation." Proceedings of the Royal Society B: Biological Sciences 271: 2587-2594.

Parr Instrument Company (2008). Certificate of Analysis Parr Instrument Company Benzoic Acid Calorimetric Standard.

Phadnis, N. V. and R. Suryanarayanan (2002). "Polymorphism in anhydrous theophylline-Implications on the dissolution rate of theophylline tablets." Journal of Pharmaceutical Sciences 86: 1256-1263.

Post, S. (2009). Applied and Computational Fluid Mechanics. Sudbury, MA, Jones and Bartlett Publishers, LLC.

Prandtl, L. (1904). Verhandlungen des dritten internationalen Mathematiker-Kongresses. Heidelberg.

Prandtl L. (1904). Uber Flussigkeitsbewegung bei sehr kleiner Reibung. 3rd International Mathmatical Congress. Heidelberg.

Qiu, Y., Y. Chen, et al. (2009). Developing solid oral dosage forms: pharmaceutical theory and practice. Burlington, Elsevier.

Qureshi, S. A. (2004). "A new crescent-shaped spindle for drug dissolution testing-but why a new spindle?" Dissolution Technologies 11: 13-18.

Qureshi, S. A., G. Caille, et al. (1994). "Application of flow-through dissolution method for the evaluation of oral formulations of Nifedipine." Drug Development and Industrial pharmacy 20(11): 1869-1882.

Radziemaska, E. and W. M. Lewandowski (2001). "Heat transfer by natural convection from an isothermal downward-facing round plate in unlimited space." Applied Energy 68: 347-366.

Ramtoola, Z. and O. I. Corrigan (1987). "Dissolution characteristics of benzoic acid and salicylic acid mixtures in reactive media." Drug Development and Industrial pharmacy 13: 170-1720.

Ramtoola, Z. and O. I. Corrigan (1987). "Dissolution characteristics of benzoic acid and slicylic acid mixture in reactive media." Drug Development and Industrial pharmacy 13(9-11): 1703-1720.

Reynolds, O. (1883). "An experimental investigation of the circumstances which determine whether the motion of water shall be direct or sinuous, and of the law of resistance in parallel channels." Philosophical Transactions of the Royal Society 174: 935-982.

Reynolds, O., A. W. Brightmore, et al. (1900). Papers on mechanical and physical subjects Volume: 1, University of California Libraries.

Rott, N. (1990). "Note on the history of the Reynolds number." Annual Review of Fluid Mechanics 22: 1-11.

Sayers, A. T. (1992). Fluid mechanics: an introduction. Oxford.

Schiller, C., C. P. Frohlich, et al. (2005). "Intestinal fluid volumes and transit of dosage forms as assessed by magnetic resonance imaging." Alimentary Pharmacology & Therapeutics 22: 971-979.

Schlichting, H. and K. Gersten (2000). Boundary layer theory 8th revised and enlarged edition. Berlin, Springer.

Scholz, A., B. Abrahamsson, et al. (2002). "Influence of hydrodynamics and particle size on the absorption of felodipine in labradors." Pharmaceutical Research 19(1): 42-46.

Schulze, K. (2006). "Imaging and modelling of digestion in the stomach and the duodenum." Neurogastroenterology & Motility 18: 172-183.

Scott, P. (2005). "Geometric irregularities common to the dissolution vessel." Dissolution Technologies 12: 18-21.

Shah, A. C. and K. G. Nelson (1975). "Evaluation of a convective diffusion drug dissolutoiin rate model." Journal of Pharmaceutical Sciences 64(9): 1518-1521.

Shah, A. C. and K. G. Nelson (1987). "Mass transport in dissolution kinetics II: convective diffusion to access role of viscosity under conditions of gravitational flow." Journal of Pharmaceutical Sciences 76(12): 910-913.

Shah, A. S. and E. L. Parrott (1976). "Dissolution of two-component solids." Journal of Pharmaceutical Sciences 65(12): 1784-1790.

Shah, V. P., Y. Tsong, et al. (1998). "*In vitro* dissolution profile comparison-Statistics and analysis of the similarity factor, f_2." Pharmaceutical Research 15(6): 889-896.

Shiko, G., L. F. Gladden, et al. (2010). "MRI studies of the hydrodynamics in a USP 4 dissolution testing cell." Journal of Pharmaceutical Sciences DOI 10.1002/jps.

Sirisuth, N. and N. D. Eddington "In vitro-in vivo correlation definitions and regulatory guidance." International Journal of Generic Drugs.

Sonin, A. (2001) Fundamental laws of motion for particles. Material volumes and control volumes, http://web.mit.edu/2.25/www/pdf/fundamental_laws.pdf

Sotax Inc (2006). Sotax CE7 smart Operating Instruction.

Steingoetter, A., M. Fox, et al. (2006). "Effects of Posture on the Physiology of Gastric Emptying: A Magnetic Resonance Imaging Study." Scandinavian Journal of Gastroenterology 41: 1155-1164.

Stevens, L. E. and P. J. Missel (2006). "Impact of density gradients on flow-through dissolution in a cylindrical flow cell." Pharmaceutical Development and Technology 11: 529-534.

Stokes, G. (1851). "On the effect of the internal friction of fluids on the motion of pendulums." Transactions of the Cambridge Philosophical Society 9: 8-106.

Sugano, K. (2008). "Theoretical comparisonof hydrodynamic diffusion layer modles used for dissolution simulation in drug discovery and development." International Journal of Pharmaceutics 363: 73-77.

Sugano, K., A. Okazaki, et al. (2007). "Solubility and dissolution profile assessment in drug discovery." Drug Metabolism and Pharmacokinetics 22(4): 225-254.

Sunada, H., I. Shinohara, et al. (1989). "Changes of surface area in the dissolution process of crystalline substances. II. Dissolution and simulation curves for mixed systems of sieved particles." Chemical & Pharmaceutical Bulletin 37: 467-470.

Sunesen, V. H., B. L. Pedersen, et al. (2005). "In vivo in vitro correlation for a poorly soluble drug, danazol, using the flow-through dissolution method with biorelevant dissolution media." European Journal of Pharmaceutical Sciences 24: 305-313.

Swichtenberg, W. (2006). "Dissolution testing in 21st century, hot topic minutes. AAPS National Meeting." Retrieved 25/11, 2008.

The United States Pharmacopeial Convention (2007). United States Pharmacopeia and National Formulary USP 30-NF 25. Rockville, MD,, The United States Pharmacopeial Convention, Inc.

The United States Pharmacopeial Convention (2008). United States Pharmacopeia–National Formulary Rockville, Maryland, USA.

Tingstad, J., J. Dudzinski, et al. (1973). "Dissolution rate studies IV: Solvent flow patterns in a column-type apparatus." Journal of Pharmaceutical Sciences 62: 1527-1530.

Tingstad, J., E. Gropper, et al. (1973). "Dissolution rate studies III: Effect of type and intensity of agitation on dissolution rate." Journal of Pharmaceutical Sciences 62(293-297).

Tsume, Y. and G. L. Amidon (2010). "The Biowaiver Extension for BCS Class III Drugs: The Effect of Dissolution rate on the Bioequivalence of BCS Class III Immediate-Release Drugs Predicted by Computer Simulation." Molecular Pharmaceutics 7(4): 1235-1243.

Urdinola, C., V. Gray, et al. (1981). "Effects of packaging and storage on the dissolution of model prednione tablets." American Journal of Hospital pharmacy 38: 1322-1327.

Venancio, A. and J. A. Teixeira (1997). "Characerization of sugar diffusion coefficients in alginate membranes." Biotechnology Techniques 11(3): 183-186.

Vliet, E. B. (1957). Letter sent to the USP Subcommittee on Tablets (August 23).

Wagner, J. and E. Nelson (1963). "Percent absorbed time plots derived from blood level and/or urinary excretion data." Journal of Pharmaceutical Sciences 52(6): 610-611.

Wang, J. and D. R. Flanagan (1999). "General solution for diffusion-controlled dissoluton of spherical particles. 1. Theory." Journal of Pharmaceutical Sciences 88: 731-738.

Wang, J. and D. R. Flanagan (2002). "General solution for diffusion-controlled dissolution of spherical particles. 2. Evaluation of experimental data." Journal of Pharmaceutical Sciences 91(534-542).

Wei, H. and R. Lobenberg (2006). "Biorelevant dissolution media as a predictive tool for glyburide a class II drug." European Journal of Pharmaceutical Sciences 29(1): 45-52.

White, F. M. (1991). Viscous fluid flow. New York, McGraw-Hill, Inc.

Woodcock, J. (2004). "The concept of pharmaceutical quality." Journal of American Pharmacetical Review 7: 10-15.

Yu, L. X. and G. L. Amidon (1999). "A compartmental absorption and transit model for estimating oral drug absorption." International Journal of Pharmaceutices 186: 119-125.

Yu, L. X., G. L. Amidon, et al. (2002). "Biopharmaceutics classification system; the scientific basis for biowaiver extensions." Pharmaceutical Research 19(7): 921-925.

Yu, L. X., G. L. Amidon, et al. (2002). "Biopharmaceutics classfication system: the scientific basis for biowaiver extensions." Pharmaceutical Research 19(7): 921-925.

Zhang, G. H., W. A. Vadino, et al. (1994). "Evaluation of the flow-through cell dissolution apparatus: effects of flow rate, glass beads and tablet position on drug release from different type of tablets." Drug Development and Industrial Pharmacy 20(13): 2063-2078.

Zhang, H. and L. Yu (2004). "Dissolution testing for solid oral drug products: Theoretical consideration." Journal of American Pharmaceutical Review 7: 26-31.

Appendices

Appendix 1 Calibration curve

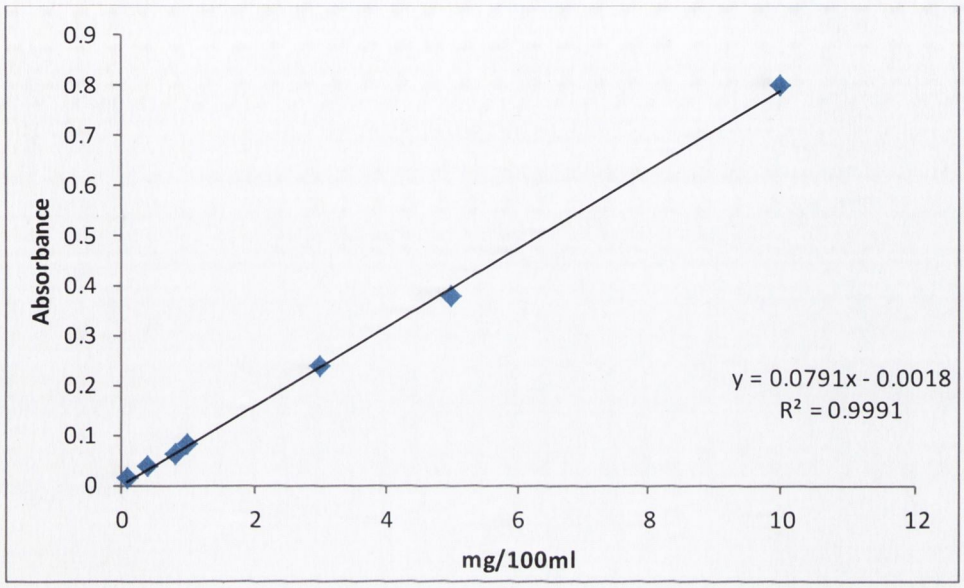


Figure A1. 1 The Calibration curve of BA in 0.1 M HCl.

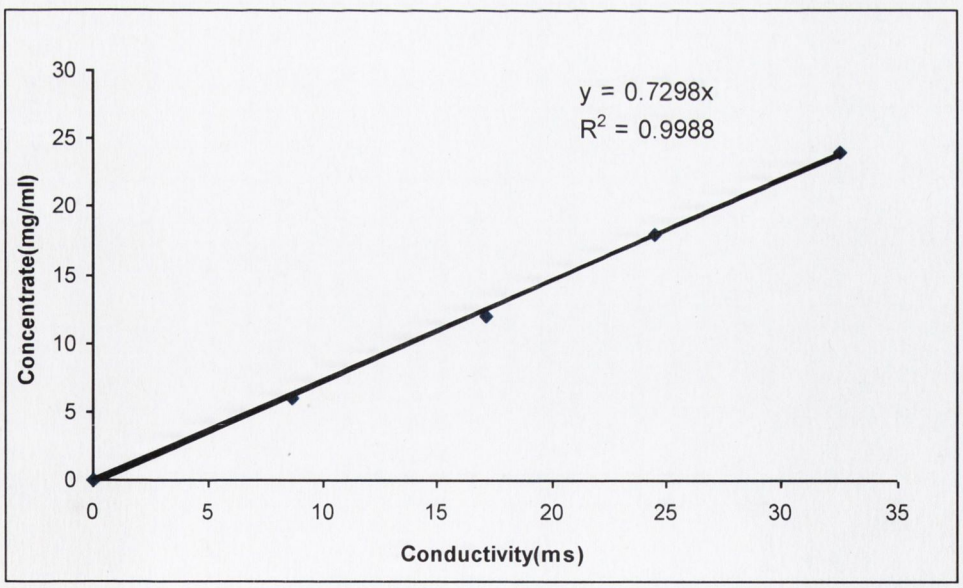


Figure A1. 2 The calibration curve of KCl in water.

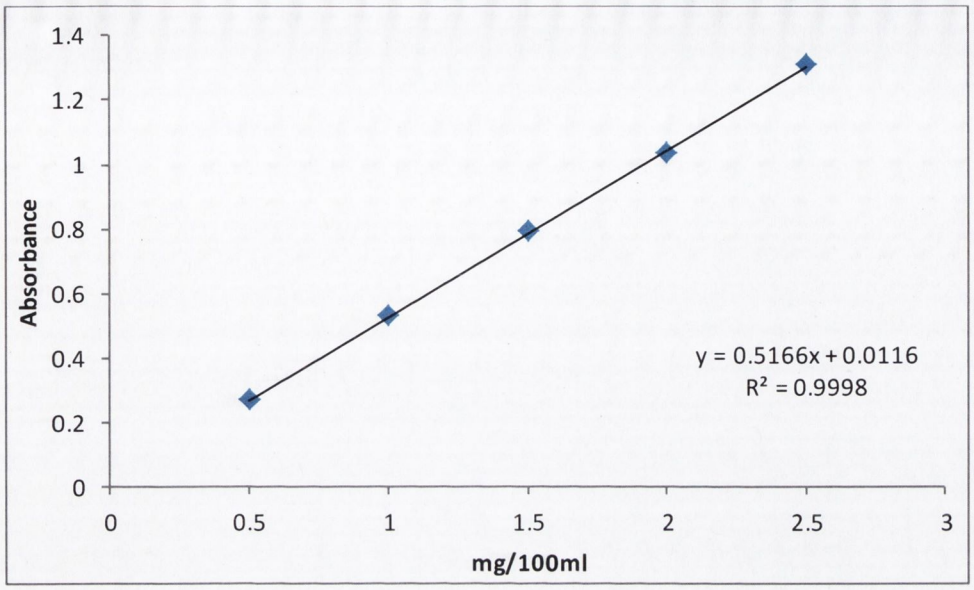


Figure A1. 3 The calibration curve of CBZ in water.

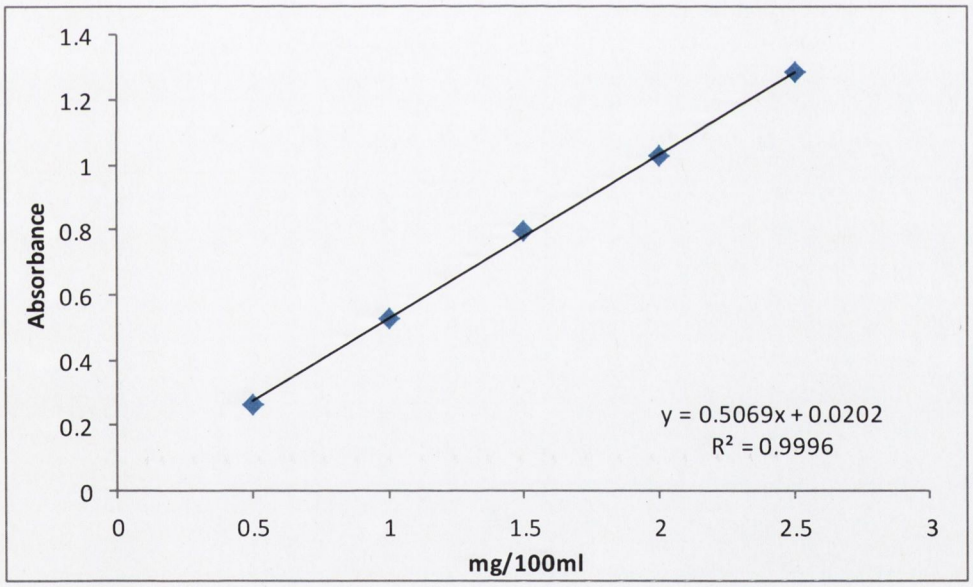


Figure A1. 4 The calibration curve of CBZ in 0.1% SLS.

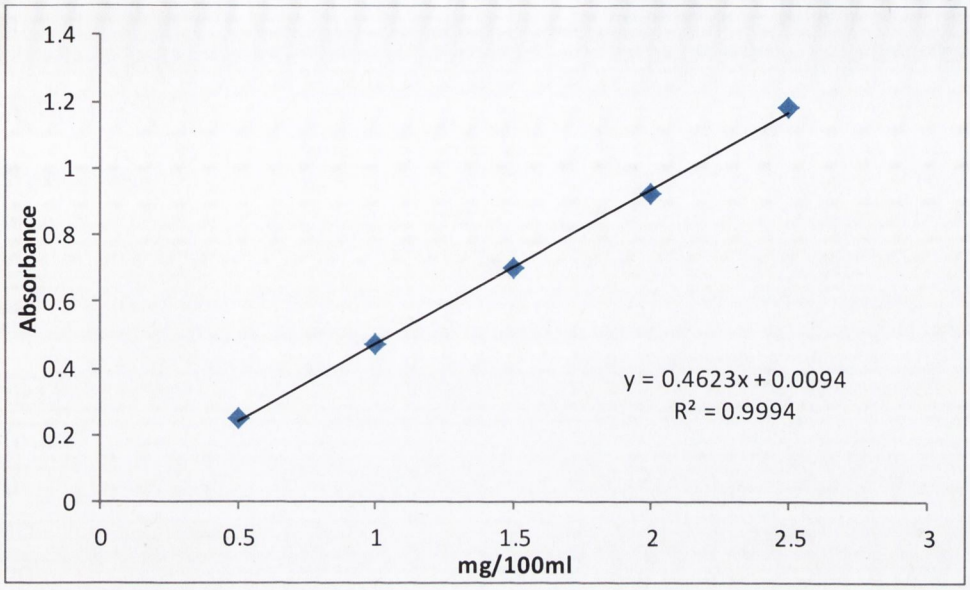


Figure A1. 5 The calibration curve of CBZ in 1% SLS.

Appendix 2 Dissolution data from J. Parojcic group (Provided by J. Parojcic).

	75 rpm, 900 ml CBZ IR									
	% CBZ dissolved									
time	water		0.1% SLS		0.25% SLS		0.5% SLS		1% SLS	
(min)	%	Sd	%	Sd	%	Sd	%	Sd	%	Sd
0	0		0		0		0		0	
10	21.05	5.55	22.49	0.93	38.17	2.2	34.51	1.6	42.83	6.21
20	28.26	4.56	29.5	1.65	44.8	3.91	47.6	2.09	58.91	5.81
30	32.72	4	37.94	1.82	54.56	3.55	58.52	3.87	70.04	5.33
45	39.12	4.23	43.5	2.89	59.07	2.89	69.68	3.06	79.59	2.19
60	44.1	3	47.94	2.63	64.97	4.16	75.94	4.15	84.41	3.54
75	48.93	2.11	51.56	1.44	67.28	4.44	82.18	3.66	88.51	1.99
90	50.98	3.01	53.19	3.85	72.32	2.8	84.25	5.07	89.73	1.25
105	52.45	1.15	56.67	3	74.47	1.53	85.31	3.89	90.59	3.44
120	55.62	1.63	58.36	3.15	75.43	0.97	87.1	3.66	91.32	5.06

Appendix 3 Code used to calculate ΔS in paddle apparatus, flow-through apparatus and free convection system.

A3.1. The Code used to calculate ΔS in paddle apparatus

```
hA  = 0.000076; %m
hB  = 0.000076;
D_A = 1.236*10^(-9); %  m2/s
D_B = 3.189*10^(-10);%  m2/s
C_A = 4.56;          %  kg m-3
C_B = 219.64;        %  kg m-3
E_1   = 0.20;        %  75%BA
T_1   = 3;          %  75%BA
E_2   = 0.40;        %  50%BA
T_2   = 3;          %  50%BA
E_3   = 0.60;        %  25%BA
T_3   = 3;          %  25%BA
E_4   = 0.68;        %  15%BA
T_4   = 3;          %  15%BA
delta=0.1;
t=0:delta:15000;

% Group 1
A_A_1 = 942;          %  kg m-3
A_B_1 = 314;            %  kg m-3

S2=zeros(size(t));
S1=zeros (size(t));
S_1=zeros (size(t));
for idx=2:length(t)
    sub1=D_B*C_B;
    sub2=T_1/E_1;
    sub3=D_A*C_A/(A_A_1*hA);
```

```
    sub4=hB+sub2*(S2(idx-1)-sub3*t(idx));
    S2(idx)=S2(idx-1)+sub1/(sub4*A_B_1)*delta;
    S1(idx)=sub3*t(idx);
    S_1(idx)=S2(idx)-S1(idx);
end


% Group 2
A_A_2 = 628;          %  kg m-3
A_B_2 = 628;            %  kg m-3

S2=zeros(size(t));
S1=zeros (size(t));
S_2=zeros (size(t));
for idx=2:length(t)
    sub1=D_B*C_B;
    sub2=T_2/E_2;
    sub3=D_A*C_A/(A_A_2*hA);
    sub4=hB+sub2*(S2(idx-1)-sub3*t(idx));
    S2(idx)=S2(idx-1)+sub1/(sub4*A_B_2)*delta;
    S1(idx)=sub3*t(idx);
    S_2(idx)=S2(idx)-S1(idx);
end


% Group 3
A_A_3 = 314;          %  kg m-3
A_B_3 = 942;            %  kg m-3

S2=zeros(size(t));
S1=zeros (size(t));
S_3=zeros (size(t));
for idx=2:length(t)
    sub1=D_B*C_B;
    sub2=T_3/E_3;
    sub3=D_A*C_A/(A_A_3*hA);
    sub4=hB+sub2*(S2(idx-1)-sub3*t(idx));
```

```
    S2(idx)=S2(idx-1)+sub1/(sub4*A_B_3)*delta;
    S1(idx)=sub3*t(idx);
    S_3(idx)=S2(idx)-S1(idx);
end



% Group 4
A_A_4 = 188.4;          %  kg m-3
A_B_4 = 1067.6;            %  kg m-3

S2=zeros(size(t));
S1=zeros (size(t));
S_4=zeros (size(t));
for idx=2:length(t)
    sub1=D_B*C_B;
    sub2=T_4/E_4;
    sub3=D_A*C_A/(A_A_4*hA);
    sub4=hB+sub2*(S2(idx-1)-sub3*t(idx));
    S2(idx)=S2(idx-1)+sub1/(sub4*A_B_4)*delta;
    S1(idx)=sub3*t(idx);
    S_4(idx)=S2(idx)-S1(idx);
end

plot (t,S_1);
xlabel('t (s)');
ylabel(' S (m)');
hold on;
plot (t, S_2);
hold on;
plot(t, S_3);
hold on;
plot(t, S_4);
```

A3.2. The Code used to calculate ΔS in flow-through apparatus

```
hA  = 0.000360; %m
hB  = 0.000360;
D_A = 1.236*10^(-9); %  m2/s
D_B = 3.189*10^(-10);%  m2/s
C_A = 4.56;          %  kg m-3
C_B = 219.64;        %  kg m-3
E_1   = 0.20;        %  75%BA
T_1   = 3;         %  75%BA
E_2   = 0.40;        %  50%BA
T_2   = 3;         %  50%BA
E_3   = 0.60;        %  25%BA
T_3   = 3;         %  25%BA
E_4   = 0.68;        %  15%BA
T_4   = 3;         %  15%BA
delta=0.1;
t=0:delta:15000;

% Group 1
A_A_1 = 942;          %  kg m-3
A_B_1 = 314;            %  kg m-3

S2=zeros(size(t));
S1=zeros (size(t));
S_1=zeros (size(t));
for idx=2:length(t)
    sub1=D_B*C_B;
    sub2=T_1/E_1;
```

```
    sub3=D_A*C_A/(A_A_1*hA);
    sub4=hB+sub2*(S2(idx-1)-sub3*t(idx));
    S2(idx)=S2(idx-1)+sub1/(sub4*A_B_1)*delta;
    S1(idx)=sub3*t(idx);
    S_1(idx)=S2(idx)-S1(idx);
end


% Group 2
A_A_2 = 628;          %  kg m-3
A_B_2 = 628;            %  kg m-3

S2=zeros(size(t));
S1=zeros (size(t));
S_2=zeros (size(t));
for idx=2:length(t)
    sub1=D_B*C_B;
    sub2=T_2/E_2;
    sub3=D_A*C_A/(A_A_2*hA);
    sub4=hB+sub2*(S2(idx-1)-sub3*t(idx));
    S2(idx)=S2(idx-1)+sub1/(sub4*A_B_2)*delta;
    S1(idx)=sub3*t(idx);
    S_2(idx)=S2(idx)-S1(idx);
end


% Group 3
A_A_3 = 314;          %  kg m-3
A_B_3 = 942;            %  kg m-3

S2=zeros(size(t));
S1=zeros (size(t));
S_3=zeros (size(t));
for idx=2:length(t)
    sub1=D_B*C_B;
    sub2=T_3/E_3;
    sub3=D_A*C_A/(A_A_3*hA);
```

```
    sub4=hB+sub2*(S2(idx-1)-sub3*t(idx));
    S2(idx)=S2(idx-1)+sub1/(sub4*A_B_3)*delta;
    S1(idx)=sub3*t(idx);
    S_3(idx)=S2(idx)-S1(idx);
end



% Group 4
A_A_4 = 188.4;          %  kg m-3
A_B_4 = 1067.6;             %  kg m-3

S2=zeros(size(t));
S1=zeros (size(t));
S_4=zeros (size(t));
for idx=2:length(t)
    sub1=D_B*C_B;
    sub2=T_4/E_4;
    sub3=D_A*C_A/(A_A_4*hA);
    sub4=hB+sub2*(S2(idx-1)-sub3*t(idx));
    S2(idx)=S2(idx-1)+sub1/(sub4*A_B_4)*delta;
    S1(idx)=sub3*t(idx);
    S_4(idx)=S2(idx)-S1(idx);
end

plot (t,S_1);
xlabel('t (s)');
ylabel(' S (m)');
hold on;
plot (t, S_2);
hold on;
plot(t, S_3);
hold on;
plot(t, S_4);
```

A3.3. The Code used to calculate ΔS in free convection system

```
hA  = 0.000275; %m
hB  = 0.000275;
D_A = 1.236*10^(-9); %  m2/s
D_B = 3.189*10^(-10);%  m2/s
C_A = 4.56;          %  kg m-3
C_B = 219.64;        %  kg m-3
E_1   = 0.20;        %  75%BA
T_1   = 3;         %  75%BA
E_2   = 0.40;        %  50%BA
T_2   = 3;         %  50%BA
E_3   = 0.60;        %  25%BA
T_3   = 3;         %  25%BA
E_4   = 0.68;        %  15%BA
T_4   = 3;         %  15%BA
delta=0.1;
t=0:delta:15000;

% Group 1
A_A_1 = 942;          %  kg m-3
A_B_1 = 314;            %  kg m-3

S2=zeros(size(t));
S1=zeros (size(t));
S_1=zeros (size(t));
for idx=2:length(t)
    sub1=D_B*C_B;
    sub2=T_1/E_1;
    sub3=D_A*C_A/(A_A_1*hA);
```

```
    sub4=hB+sub2*(S2(idx-1)-sub3*t(idx));
    S2(idx)=S2(idx-1)+sub1/(sub4*A_B_1)*delta;
    S1(idx)=sub3*t(idx);
    S_1(idx)=S2(idx)-S1(idx);
end



% Group 2
A_A_2 = 628;          %  kg m-3
A_B_2 = 628;            %  kg m-3

S2=zeros(size(t));
S1=zeros (size(t));
S_2=zeros (size(t));
for idx=2:length(t)
    sub1=D_B*C_B;
    sub2=T_2/E_2;
    sub3=D_A*C_A/(A_A_2*hA);
    sub4=hB+sub2*(S2(idx-1)-sub3*t(idx));
    S2(idx)=S2(idx-1)+sub1/(sub4*A_B_2)*delta;
    S1(idx)=sub3*t(idx);
    S_2(idx)=S2(idx)-S1(idx);
end



% Group 3
A_A_3 = 314;          %  kg m-3
A_B_3 = 942;            %  kg m-3

S2=zeros(size(t));
S1=zeros (size(t));
S_3=zeros (size(t));
for idx=2:length(t)
    sub1=D_B*C_B;
    sub2=T_3/E_3;
    sub3=D_A*C_A/(A_A_3*hA);
    sub4=hB+sub2*(S2(idx-1)-sub3*t(idx));
```

```
    S2(idx)=S2(idx-1)+sub1/(sub4*A_B_3)*delta;
    S1(idx)=sub3*t(idx);
    S_3(idx)=S2(idx)-S1(idx);
end


% Group 4
A_A_4 = 188.4;          %  kg m-3
A_B_4 = 1067.6;            %  kg m-3

S2=zeros(size(t));
S1=zeros (size(t));
S_4=zeros (size(t));
for idx=2:length(t)
    sub1=D_B*C_B;
    sub2=T_4/E_4;
    sub3=D_A*C_A/(A_A_4*hA);
    sub4=hB+sub2*(S2(idx-1)-sub3*t(idx));
    S2(idx)=S2(idx-1)+sub1/(sub4*A_B_4)*delta;
    S1(idx)=sub3*t(idx);
    S_4(idx)=S2(idx)-S1(idx);
end

plot (t,S_1);
xlabel('t (s)');
ylabel(' S (m)');
hold on;
plot (t, S_2);
hold on;
plot(t, S_3);
hold on;
plot(t, S_4);
```